

Space-VLBI studies of the parsec-scale jet in the quasar 3C 345

INAUGURAL-DISSERTATION

zur
Erlangung des Doktorgrades
der Mathematisch-Naturwissenschaftlichen Fakultät
der Universität zu Köln



vorgelegt von

Felix Pötzl

aus Bonn, Deutschland

Köln 2021

Berichterstatter:

Prof. Dr. J. Anton Zensus
Prof. Dr. Andreas Eckart

Tag der letzten mündlichen Prüfung: 04.03.2021

“After sleeping through a hundred million centuries we have finally opened our eyes on a sumptuous planet, sparkling with color, bountiful with life. Within decades we must close our eyes again. Isn’t it a noble, an enlightened way of spending our brief time in the sun, to work at understanding the universe and how we have come to wake up in it?”

- Professor Richard Dawkins

Abstract

Supermassive black holes in the centres of radio-loud active galactic nuclei (AGN) can produce collimated relativistic outflows (jets). Magnetic fields are thought to play a key role in the formation and collimation of these jets, but the details are much debated. Very-long-baseline interferometry (VLBI) is a powerful tool to observe the innermost regions of AGN jets and shed light on the physical processes responsible for the formation, collimation, and the emission in those jets.

The main goal of this thesis is to expand the knowledge about AGN with a detailed case study of the archetypical quasar 3C 345 with state-of-the-art high-resolution space-VLBI observations. The flat-spectrum radio quasar 3C 345 was observed over several decades by VLBI, single-dish radio monitoring as well as in X rays and γ -rays. The curved jet structure and bending of the jet led to proposed helical motions of jet components and possibly a precessing accretion disk as their origin.

I study the jet in 3C 345 with *RadioAstron*, where a VLBI ground-array is complemented by a 10-m radio antenna in space on the *Spektr-R* spacecraft. This allows me to image the source at an unprecedented resolution of 300 microarcseconds at 1.6 GHz. On the ground, a similar resolution is reached only at 22 GHz. Both total intensity and polarised intensity maps are produced, revealing the complex jet structure in high detail. The electric vector position angles (EVPAs) seems to be aligned with the jet direction. A likely shock-dominated region is identified as the total and polarised intensity peak downstream of the self-absorbed, depolarised VLBI core.

A further study of these data in conjunction with a multi-wavelength dataset from ground-based VLBI at 5, 8, 15 and 43 GHz reveals an optically thick core through the steep spectrum, that is visible for all frequencies. The spectral index declines along the jet direction as expected for a self-absorbed jet. The spectral index between 1.6 GHz and 15 GHz, with the highest available resolution, reveals an increase in the spectral index in the peak intensity region, solidifying the shock-type scenario.

In addition, I investigate the possible Faraday rotation in the source. A moderately high rotation measure (RM) of several tens up to a hundred rad m^{-2} is obtained, which appears to change the EVPA direction from parallel to almost perpendicular to the local jet direction around the peak emission region, while it becomes parallel in the core. An increase of the RM is seen going upstream in the jet, which reflects the increase in particle density and magnetic field strength. Interestingly, a flip in sign of the RM along the jet indicates the presence of a poloidal magnetic field component.

The study of the frequency-dependend shift of the VLBI core reveals that the shift measured from the *RadioAstron* data is most likely underestimated, and that the overall shift is consistent with an equipartition between particle and magnetic energy density in the core. The derived magnetic field and particle density are consistent with earlier VLBI observations. Comparing the particle density obtained from the core shift and RM hints at an external Faraday screen around the jet being responsible for the observed Faraday rotation.

In general, a consequence of the self-calibration procedures in VLBI observations is the loss of the absolute positional information of the source. This is why in these cases, the alignment of images at different frequencies is only possible with the presence of optically thin features in the jet, whose position should not change with frequency. This method is thus prone to systematic uncertainties, which drive the errors in the derived physical parameters of the jets.

A solution to this problem are phase referencing (PR) observations. A nearby calibrator is observed in conjunction with the target source to apply the calibrator phase solutions to the target, effectively removing the atmospheric phase errors without the need of self-calibration. With the superior alignment from phase referencing, the core shift can be more reliably estimated in AGN jets. However, PR observations are limited to lower frequencies due to the rapid atmospheric fluctuations at higher frequencies and need close-by, bright calibrators to be available. Observations at higher frequencies can be used to constrain jet parameters close to the central engine from high-precision core-shift measurements.

In this thesis I present the concept for PR observations at higher frequencies of 22 GHz and 43 GHz. The work makes use of the observations at lower frequencies to calibrate the phases at the higher frequencies, which enables PR at short mm-wavelengths. In conjunction with conventional phase-calibration with a suitable calibrator, this technique is termed source-frequency phase referencing (SFPR).

I proposed the first SFPR observations with intercontinental baselines between the Korean VLBI network and the Yebes telescope in Spain. Due to unforeseen delays in the observations, in this work I will focus in detail about the principles of SFPR, the source sample selection, and the observational procedures, providing an outlook on the unique capabilities of this observing mode.

Zusammenfassung

Supermassive schwarze Löcher in den Zentren von radio-lauten aktiven galaktischen Kernen (AGN) können relativistische, kollimierte Plasma-Ausflüsse (Jets) produzieren. Dabei spielen Magnetfelder eine zentrale Rolle bei der Entstehung und Kollimation dieser Jets. Die Details sind jedoch noch immer umstritten. Very-long-baseline interferometry (VLBI) ist ein mächtiges Werkzeug zur Beobachtung der innersten Regionen von Jets in AGN und können Aufschluss geben über die physikalischen Prozesse, die die Bildung, Kollimation und die Emission in Jets antreiben.

Das Hauptziel dieser Arbeit ist es, das Wissen über AGN anhand des Quasars 3C 345 zu erweitern, mithilfe von hochmodernen Weltraum-VLBI-Beobachtungen. 3C 345 wurde über mehrere Jahrzehnte hinweg kontinuierlich beobachtet, sowohl mit VLBI als auch mit einzelnen Radioteleskopen, sowie auch im Röntgen- und Gammastrahlungs-Bereich. Die allgemein gekrümmte Struktur und die beobachtete Biegung des Jets wurden bereits auf spiralförmige Bewegung einzelner Jet-Komponenten und damit auf eine mögliche präzedierende Akkretionsscheibe um das zentrale schwarze Loch zurückgeführt.

Ich untersuche den Jet in 3C 345 mit *RadioAstron*, wobei ein VLBI-Netzwerk von einem 10-m Radioteleskop auf dem *Spektr-R*-Satelliten im Weltraum unterstützt wird. Dadurch kann ich die Quelle bei bisher unerreichter Auflösung von 300 Mikrobogensekunden bei 1.6 GHz kartieren. Für VLBI-Netzwerke auf der Erde ist dies in der Regel nur bei 22 GHz möglich. Es werden Karten sowohl in Gesamt- wie auch linear polarisierter Intensität erstellt. Diese offenbaren die komplexe Struktur des Jets in hohem Detail. Die Positionswinkel der Vektoren des elektrischen Felds (EVPAs) scheinen mit der lokalen Richtung des Jets weiterstehend parallel zu verlaufen. Eine Region stromabwärts des Jets wird identifiziert, die sowohl in Gesamt- wie auch polarisierter Intensität das Maximum der Karte bildet. Wahrscheinlich zeigt dieses eine Schockfront, die sich stromabwärts des scheinbaren Anfangs des Jets (des VLBI-Kerns) befindet, der selbst absorbiert und depolarisiert ist.

Im Weiteren untersuche ich die Daten in Verbindung mit einem Multifrequenz-Datensatz von erdgebundenen VLBI-Netzwerken bei 5, 8, 15, und 43 GHz. Aus diesen ergibt sich durch das beobachtete steile Spektrum ein optisch dicker Kern bei allen Frequenzpaaren. Der Spektralindex nimmt wie erwartet entlang des Jets ab. Im speziellen zeigt die Spektralindexkarte zwischen 1.6 und 15 GHz, die die höchste Auflösung in dieser Studie hat, einen Anstieg des Spektralindex an der Position der höchsten Intensität, was die Annahme eines Schocks unterstützt.

Dazu untersuche ich mögliche Faraday-Rotation in der Quelle. Dabei wird ein mäßig hohes Rotation Measure (RM) gezeigt, das in der Größenordnung etwa zwischen 10 und 100 rad m^2 liegt. Dies rotiert die beobachteten EVPAs bei 1.6 GHz so weit, dass sie nun an der Stelle des Schocks eher senkrecht zur Ausbreitungsrichtung des Jets stehen, während sie im Kern parallel sind. Ein Anstieg des RM stromaufwärts des Jets wird ersichtlich, was den Anstieg in Teilchendichte und magnetischer Flussdichte widerspiegelt. Interessanterweise wird zudem ein Vorzeichenwechsel des RM beobachtet, was für einen poloidalen Anteil des Magnetfeldes spricht, und auf ein spiralförmiges Magnetfeld hindeuten könnte.

Die Untersuchung der räumlichen Verschiebung des VLBI-Kerns mit der Frequenz zeigt, dass die Verschiebung, die von den *RadioAstron*-Daten gemessen wurde, höchstwahrscheinlich methodisch unterschätzt wird. Die anderen Frequenzen zeigen Verschiebungen, die gut mit der Gleichverteilung der Teilchen- und Magnetfeldenergie in der Kernregion vereinbar sind. Die hieraus hergeleiteten magnetischen Flussdichten stimmen mit früheren Studien überein. Ein Vergleich der Teilchendichten, die aus der Kern-Verschiebung und der *RM*-Analyse berechnet werden, deutet auf externe Faraday-Rotation von Materie um den Jet herum hin.

Im Allgemeinen führt die Anwendung von Selbst-Kalibration in VLBI-Beobachtungen zum Verlust der absoluten Raumkoordinaten der so erhaltenen Karte. Deshalb erfordert eine Ausrichtung von Karten bei verschiedenen Frequenzen die Präsenz von optisch dünnen Komponenten im Jet, deren Position sich nicht mit der Frequenz ändert. Diese Methode neigt allerdings zu systematischen Unsicherheiten, die die Genauigkeit der Bestimmung der Kern-Verschiebung maßgeblich beeinflussen.

Eine Lösung bieten Phase-Referencing(PR)-Beobachtungen. Dabei wird eine am Himmel in der Nähe befindliche Kalibrationsquelle mit der Zielquelle zusammen beobachtet, um später die Phasenkorrekturen der Kalibrationsquelle auf die Zielquelle zu übertragen. Damit können die Phasenfehler durch die atmosphärischen Schwankungen korrigiert werden, ohne dass es der Selbst-Kalibration bei der Zielquelle bedarf. Mit dieser Methodik kann die Verschiebung des Kerns besser bestimmt werden. Allerdings ist die Anwendung von PR-Beobachtungen auf niedrige Frequenzen limitiert, durch die schnelleren atmosphärischen Schwankungen und die limitierte Verfügbarkeit von Kalibrationsquellen bei hohen Frequenzen. Beobachtungen bei hohen Frequenzen werden jedoch benötigt, um die Kern-Verschiebung und damit physikalische Parameter nahe des zentralen schwarzen Lochs zu bestimmen.

In dieser Arbeit präsentiere ich daher das Konzept für PR-Beobachtungen bei höheren Frequenzen, nämlich bei 22 und 43 GHz. Dabei werden die schnellen atmosphärischen Schwankungen zum Teil dadurch ausgeglichen, dass die Phasen von der niedrigeren Beobachtungsfrequenz für die höhere Frequenz angewandt werden. Damit sind grundsätzlich PR-Beobachtungen bei mm-Wellenlängen möglich. Zusammen mit konventionellen PR-Beobachtungen nennt sich das Verfahren source-frequency phase referencing (SFPR).

Ich habe einen Beobachtungsantrag für die ersten SFPR-Beobachtungen mit interkontinentalen Basislinien gestellt, der vom Korean VLBI network in Korea und dem Yebes-Telescope in Spanien angenommen wurde. Durch unvorhergesehene Ereignisse verzögerten sich die Beobachtungen, jedoch gehe ich im Detail auf den Beobachtungsplan ein, der die Auswahl der Quellen und die Beobachtungsprozeduren beinhaltet. Ich gebe dabei einen Ausblick auf die Möglichkeiten, die diese Beobachtungen als Wegbereiter eröffnen.

Contents

1	Introduction	1
1.1	Active Galactic Nuclei	1
1.1.1	A brief history	1
1.1.2	The unified scheme	2
1.2	Relativistic Jets	4
1.2.1	Jet launching	4
1.2.2	Collimation and acceleration	5
1.2.3	Jet composition	6
1.3	Emission mechanisms	6
1.3.1	Synchrotron emission	8
1.3.2	Synchrotron self-absorption	10
1.3.3	Inverse Compton emission	11
1.3.4	Relativistic effects	12
1.4	Polarisation	14
1.4.1	Polarisation states of an electromagnetic wave	14
1.4.2	Polarised synchrotron emission	16
1.4.3	Faraday rotation	17
1.4.4	Depolarisation effects	19
1.5	Opacity effects: Core shift	20
1.5.1	Jet parameters from core shift	20
1.6	The flat-spectrum radio quasar 3C 345	23
2	Very-long-baseline interferometry	27
2.1	Fundamentals of radio astronomy	27
2.2	Basic principles of interferometry	29
2.3	VLBI	32
2.4	Correlation	33
2.5	Amplitude calibration	34
2.6	Fringe fitting	34
2.7	Imaging	35
2.7.1	Deconvolution	35
2.7.2	Self-calibration	35
2.8	Space VLBI	36
2.9	Polarisation measurements	37
3	Observations, calibration and data reduction	39
3.1	Observations of 3C 345	39
3.2	Calibration	39
3.2.1	Amplitude calibration	39
3.2.2	Fringe fitting	42
3.2.3	Bandpass calibration	44

3.2.4	Data averaging	45
3.2.5	Polarisation calibration	45
4	RadioAstron images of 3C 345 at 1.6 GHz	51
4.1	Imaging	51
4.2	Total intensity images	54
4.2.1	Model fitting	56
4.3	Linear polarisation images	58
5	Analysis of the physical properties of the parsec-scale jet in 3C 345	63
5.1	Complementary data	63
5.1.1	VLBA data	63
5.1.2	MOJAVE data	63
5.1.3	BU blazar program data	64
5.2	Brightness temperature	66
5.2.1	Refractive substructure	71
5.2.2	Comparison with brightness temperatures from MOJAVE data . . .	75
5.3	Variability timescale	75
5.4	Core shift	76
5.5	Spectral index	81
5.6	Rotation Measure	82
5.7	Estimating the electron density	93
5.8	Component evolution	95
5.9	Possible counter-jet emission	96
6	Core-shift studies with long-baseline source-frequency phase referencing	99
6.1	Phase referencing	99
6.2	Source-frequency phase referencing (SFPR)	100
6.3	Observations	102
6.4	Outlook	107
7	Concluding remarks and outlook	109
A	Map alignment	111

Chapter 1

Introduction

This chapter shall provide the necessary scientific context for the understanding of the analysis presented in the following chapters of this thesis.

1.1 Active Galactic Nuclei

1.1.1 A brief history

Until the early 20th century, astronomers were still debating about the nature of diffuse nebulae in the sky, that were clearly not stars. Only with the discovery of variable stars in NGC 6822, Edwin Hubble could argue in 1925 that many of these objects are actually too distant to be of galactic origin (Hubble 1925). He later published his famous “Hubble sequence”, classifying these nebulae into spirals, ellipticals and irregulars (Hubble 1926). That was followed up by his “Hubble sequence”, relating the velocity with which the nebula is receding from us to its distance, $v = H_0 d$ (Hubble 1929). This defines the Hubble constant H_0 . The spectra of the observed nebulae, now known to be other galaxies, contained mostly absorption lines from the stars in them.

However, already in the early 20th century, emission lines were detected in the nebula NGC 1086 by Fath (1909), and were later shown to be very broad by Slipher (1917), already hinting at very fast gas motions of 3600 km s^{-1} in the centre of this galaxy. This was also observed for NGC 4151 (Campbell and Moore 1918), with even faster gas motions ($7500 \text{ km s}^{-1} = 0.025 c$, with c being the speed of light).

In 1943, Seyfert (1943) presented data from more galaxies with broad emission line spectra, where the emission came from a notably small region in the centre. To date, millions of those objects have been found, and are termed Seyfert galaxies. It was later shown that there are two distinct classes of Seyfert galaxies, termed type-1 and type-2 Seyfert galaxies. The former show both broad and narrow emission lines, while for the latter, they show only narrow emission lines ($500 - 1000 \text{ km s}^{-1}$). It was already argued that the narrower emission lines should come from a region some 100 pc away from the central radiation source, while the broader emission lines have to come from much closer ($< 0.01 \text{ pc}$). The central radiation source had to be even smaller in size, and radiate power in the range of $(10^{43} - 10^{45}) \text{ erg s}^{-1}$ ($1 \text{ erg} = 10^{-7} \text{ J}$). All this suggested exceptionally high dynamical masses ($\sim 10^6 M_\odot$) in the centres of these galaxies.

In the 1960s, a number of bright, unresolved sources in the optical were discovered, and due to their brightness and variability were thought of as stars, termed QSOs (quasi stellar object). During the same time, the number of detected radio sources increased by a large amount with the third Cambridge catalogue. 3C 273 was the first object where a cross-identification between the unresolved QSO in the optical and the quasi-stellar radio source (quasar) was done (Schmidt 1963). Due to the highly redshifted emission lines, it

became obvious that the source lies at a cosmological distance. Only about 10 % of QSOs were observed to have radio counterparts, and were termed radio-loud.

Advances in technology resulted in the emergence of radio interferometers, which increased the originally poor resolution and the sensitivity of radio telescopes by orders of magnitude. One of the most prominent and archetypical radio sources is Cygnus A. It was discovered in 1944 by Grote Reber, one of the pioneers of radio astronomy. It is the second brightest radio source on the sky after the supernova remnant Cassiopeia A. Fig. 1.1 shows an image observed with the Very Large Array (VLA) in the 1980s. The double structure could only be seen with radio interferometers, and only with the sensitivity of the VLA, the stream of emission between the “radio lobes” could be seen.

This phenomenon was soon connected to much earlier observations of the galaxy Messier 87, where Curtis (1918) observed a collimated jet emanating from the nucleus of the galaxy (see Fig. 1.4). Baade (1956) then observed the polarisation properties in this jet, supporting the scenario that the emission is synchrotron radiation. Later observations revealed that the optical jet is actually part of a much larger radio jet (see Fig. 1.3).

All these phenomena were later connected to the same kind of physical objects in the framework of the unified scheme of AGN.

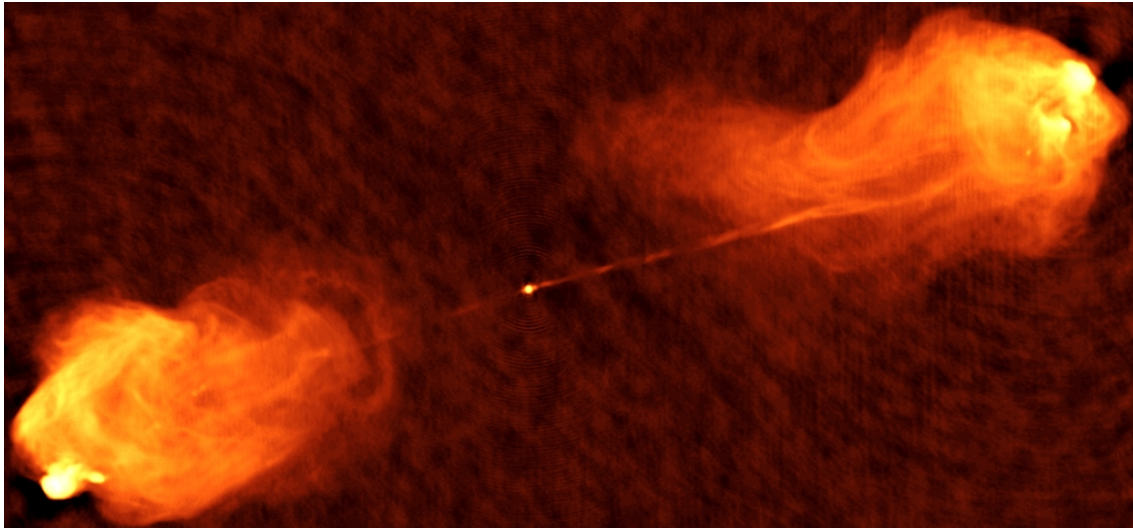


Figure 1.1: Cygnus A observed with the VLA at 5 GHz (Perley et al. 1984). The image clearly shows the double structure of the source, with the kpc-scale jets connecting the central engine with the radio lobes (Credit: Chris Carilli, NRAO/AUI).

1.1.2 The unified scheme

In the unified scheme (Urry and Padovani 1995), the different sources described in the previous section are tied to the same kind of physical object, where its orientation with respect to the observer explains the different observed properties. I will outline the basic constituents of these *active galactic nuclei* (AGN), which can be seen in Fig. 1.5.

Nowadays, the centres of the majority of, if not all, galaxies of sufficient mass are thought to host in their centre a supermassive black hole (SMBH), a black hole (BH) with mass roughly between 10^6 and $10^9 M_{\odot}$. Infalling matter, due to its own angular momentum will form an accretion disc around the black hole and gets heated up to temperature of millions of Kelvin due to friction. The disc shines bright in optical up to X-ray energies. The luminosity is limited by the Eddington luminosity, which limits the luminosity of any accreting object:

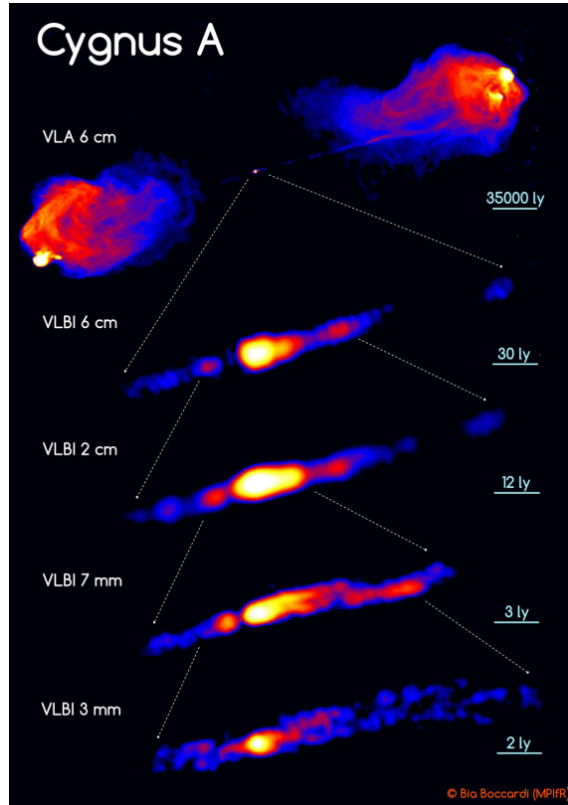


Figure 1.2: Composite image of Cygnus A at different scales and radio frequencies (Boccardi et al. 2017).

$$L_{\text{edd}} = \frac{4\pi G c m_p M}{\sigma_T}. \quad (1.1)$$

Here, M denotes the mass BH mass, G is the gravitational constant, m_p is the proton mass and σ_T is the Thomson cross section. This limit effectively states that if the radiation pressure gets too high due to increasing luminosity, it becomes stronger than the gravitational pull of the central object, terminating the accretion and thus decreasing the luminosity again. The limit on luminosity ultimately sets a limit on the mass accretion rate as well. Still, accretion onto a SMBH is the most efficient mechanism to convert rest-mass into energy known to date.

The SMBHs are generally thought to rotate, i.e. they can be fully described by the Kerr metric, with their mass and their dimensionless spin parameter $a = J_{\text{obs}}/J_{\text{max}}$. The maximum spin for a Kerr black hole is $J_{\text{max}} = GM^2/c$, then $a = 1$. Here, G is the gravitational constant, M is the mass of the central object, and c is the vacuum speed of light. Close to the BH, the accretion disk aligns with the direction and rotational axis of the BH spin due to frame dragging effects.

Surrounding the accretion disk is a dusty torus, the exact geometry and composition of which is still not well understood. It consists of gas and dust, and obscures the radiation from the BLR for type-2 Seyfert galaxies, so only the emission from the NLR is visible. It has been argued that the torus has a more clumpy shape than what is depicted in Fig. 1.5 (Elitzur 2007).

Only a fraction of about 10% of AGN is observable in the radio as stated in the previous section. Their "radio-loudness" or "radio-quietness" is most likely tied to the existence or absence of a relativistic jet (see Sect. 1.2) (Urry and Padovani 1995; Padovani

2017). When the jet of an AGN is closely aligned with the line of sight to the observer, the objects are referred to as *blazars*. They are further categorised in BL Lac objects (named after the progenitor, BL Lac) and flat-spectrum radio quasars. They mainly differ in the appearance or lack of emission lines and their luminosity (see Fig. 1.8).

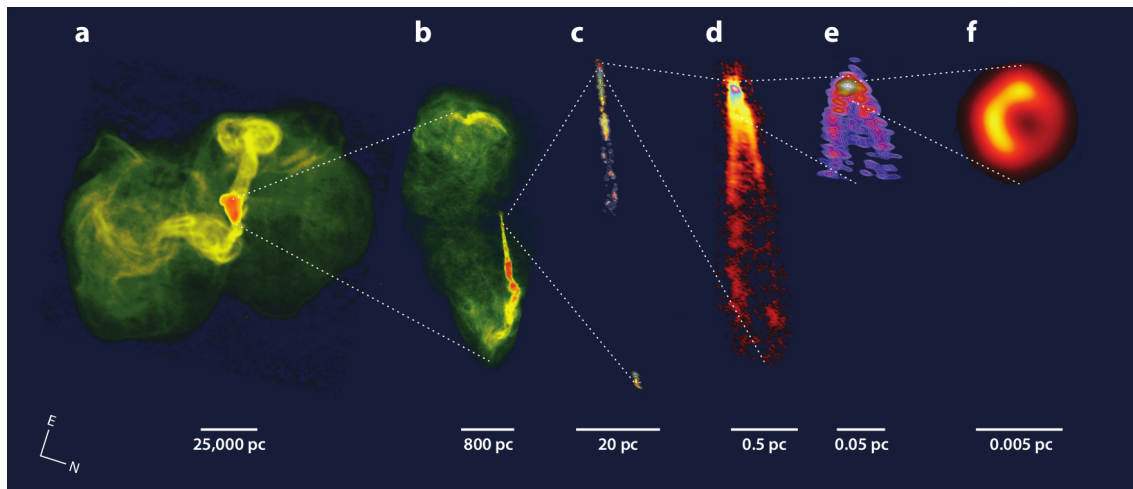


Figure 1.3: Radio view of M87 at different scales and radio frequencies (Composite image taken from Blandford et al. 2019). Credits from left to right: (a) NRAO, 90-cm Very Large Array (VLA); (b) NRAO, 20-cm Very Large Array (VLA); (c) NRAO, 20-cm VLBA (Cheung et al. 2007); (d) NRAO, 7-mm Very Long Baseline Array (VLBA) (Walker et al. 2018); (e) 3-mm Global Millimeter VLBI Array (GMVA) (Kim et al. 2018); (f) 1.3-mm Event Horizon Telescope (EHT) (Event Horizon Telescope Collaboration et al. 2019b).

1.2 Relativistic Jets

Relativistic jets refer to a collimated outflow of relativistic particles. The term “collimated” is not uniquely defined, but one can think of it as the jet having a sufficiently small opening angle ϕ , where the transverse width of the flow R is much smaller than the length of the flow r ($\phi = \arctan(R/r)$). AGN jets have total power between 10^{43} and 10^{48} erg s $^{-1}$, and this power can even exceed that provided by the gravitational potential of the central object (Ghisellini et al. 2014).

Jets are observed in different astrophysical environments, such as protostars or X-ray binaries, but I will focus solely on the basic properties of AGN jets here. For a recent, more detailed review, the reader is referred to e.g., Blandford et al. (2019).

1.2.1 Jet launching

The formation of jets is tied to the AGN in the centre of galaxies. They are thought to be produced close to the central engine, the SMBH, on scales of a few 100 gravitational or Schwarzschild radii, $r_g = 2GM/c^2$. To date, single models of jet launching have difficulties explaining all the observed properties of AGN jets. In general, accelerating particles to relativistic speeds requires strong pressure gradients, for which thermal pressure is not sufficient. Therefore, jet launching models include magnetic pressure gradients (see e.g., Meier et al. 2001; Zamaninasab et al. 2014)). For an illustration of these processes, see Fig. 1.7. The basic principle is the extraction of energy via a magnetic torque and its conversion to Poynting flux. For many of the jet launching scenarios, a large-scale helical magnetic field is then expected around the jet (Fig. 1.7). The two main jet formation mechanisms that have emerged in the last decades are:

- The Blandford-Payne (BP) mechanism: Blandford and Payne (1982) introduced that relativistic jets may be launched from the accretion disc surrounding a SMBH. A poloidal magnetic field can be anchored in the rotating, conductive accretion disk. Due to the differential rotation, the magnetic field lines are wound up, effectively creating a magnetic torque that can accelerate particles along the field lines.
- The Blandford-Znajek (BZ) mechanism: Blandford and Znajek (1977) described the scenario where the jet is launched from the rotating magnetosphere, also termed ergosphere, of the SMBH itself. They showed that energy can be efficiently extracted from the rotation of the SMBH via the Lense-Thirring mechanism or the Penrose-mechanism (Penrose and Floyd 1971). The BZ mechanism results in a narrower jet compared to the BP-mechanism.

The formation mechanisms are not mutually exclusive. In fact, recent observations provide hints that in some sources, both mechanisms may be at play (see e.g. Giovannini et al. 2018). The formation of jets is also tightly coupled to the physical conditions in the accretion flow.

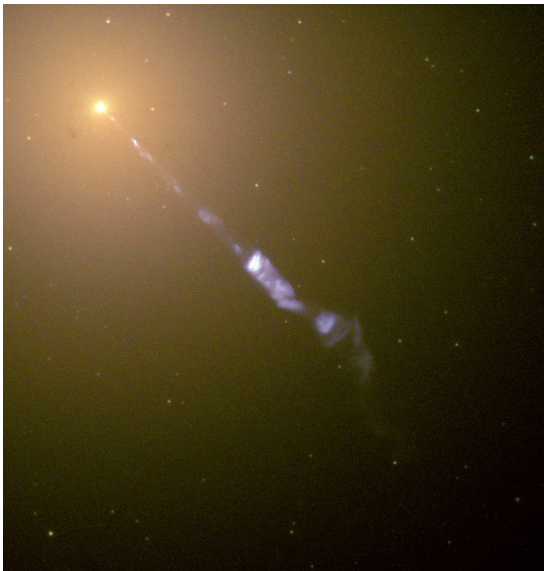


Figure 1.4: The elliptical galaxy M87 and its optical jet as observed by the Hubble Space Telescope. The image size is $\sim 2300 \times 2300$ pc (Credit: NASA and The Hubble Heritage Team).

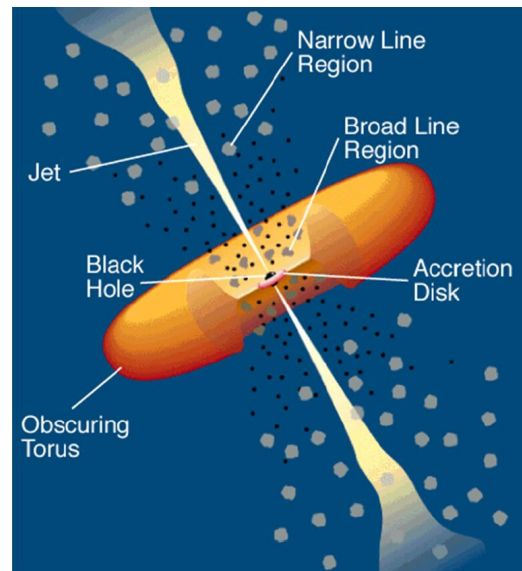


Figure 1.5: Unified scheme of AGN (original by Urry and Padovani 1995, taken from Klein and Fletcher 2015).

1.2.2 Collimation and acceleration

After the initial formation of the jet, the material propagates down the jet direction. The jet can be assumed to be a stationary, adiabatic flow propagating within some ambient medium. Close to the black hole, the jet is likely confined by either an ion-supported torus, or by gas winds from the accretion disk (Blandford et al. 2019). If the jet consists of charged particles, a toroidal magnetic field will form due to the axial current that can also support the jet confinement. As the jet gradually expands adiabatically, the pressure in it drops and a point is reached where the jet turns supersonic, at the so-called (magneto-)sonic point. After this point, the Poynting flux is gradually converted to bulk kinetic energy as the jet propagates and expands further (Blandford and Rees 1978). At this point, the jet is mostly confined by ambient gas pressure in the host galaxy. Most jets

show a conical expansion profile, however very-high-resolution observations, e.g. in M87 (Nakamura and Asada 2013) show that the jet may expand with a parabolic shape in the inner ~ 100 pc, and later transition to conical expansion.

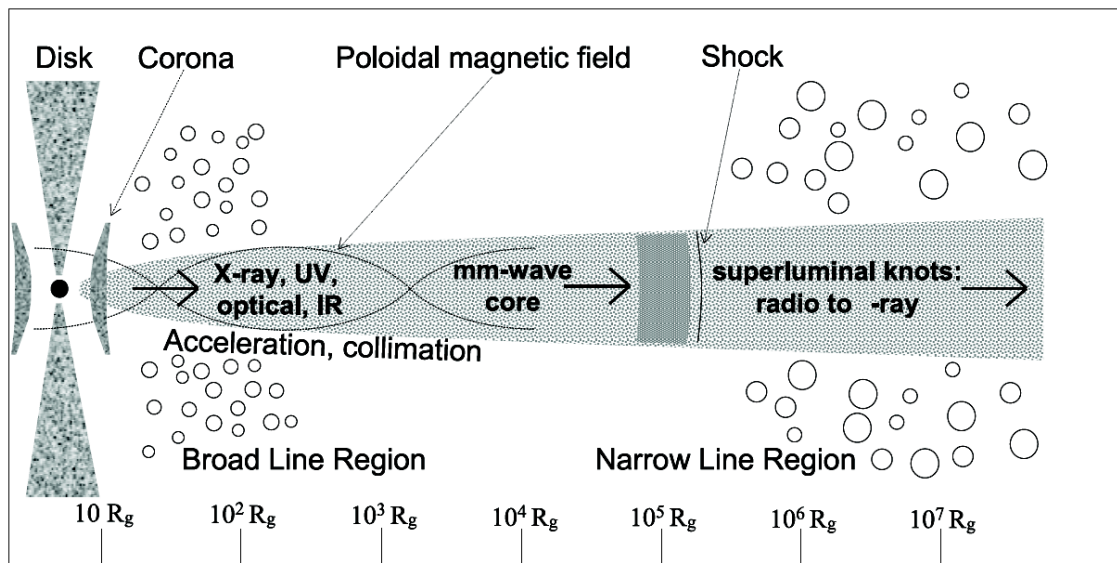


Figure 1.6: A jet model illustrating the jet launching and collimation and acceleration regions with a logarithmic scale in gravitational radii R_g (Lobanov 2007).

On larger scales, when the jet slows down, it may show substantial interaction with the interstellar medium (ISM) or intergalactic medium (IGM). This interaction is what likely causes the Fanaroff & Riley dichotomy, where radio galaxies with twin jets are divided into FR-I and FR-II sources (Fanaroff and Riley 1974). FR-II sources show jets that are still collimated on large scales (as Cygnus A shown in Fig. 1.1) and have high luminosities in the radio lobes where the jets terminate and dissipate their energy into the IGM. FR-I sources show greater disturbances in their jets and their brightness decreases with the distance along the jet (an example is M87, as depicted in Fig. 1.3).

1.2.3 Jet composition

Jets could in principle contain either protons and electrons, or electrons and positrons (pair plasma). Protons are more difficult to accelerate to relativistic speeds due to their higher rest mass compared to electrons, although the required energies might be present in AGN (e.g. Ghisellini et al. 2014). Relativistic protons would also be necessary for hadronic processes leading to γ -ray production. In most cases, pair-plasma dominated jets are favoured (e.g., Wardle et al. 1998; Hirovani 2005). However, this is challenged by the recent neutrino detections from blazars, which requires hadronic processes to take place (e.g., Kadler et al. 2016; Ros et al. 2020). In any case, it has been proposed that the jets could, in some cases, consist of an inner jet composed of a highly relativistic pair plasma, which is surrounded by a mildly relativistic e^-p jet (Sol et al. 1989; Klein and Fletcher 2015).

1.3 Emission mechanisms

As charged particles are accelerated, they will emit radiation as described in classical electro-magnetic theory. For details the reader is referred to any book about classical electrodynamics (e.g. Jackson 1999).

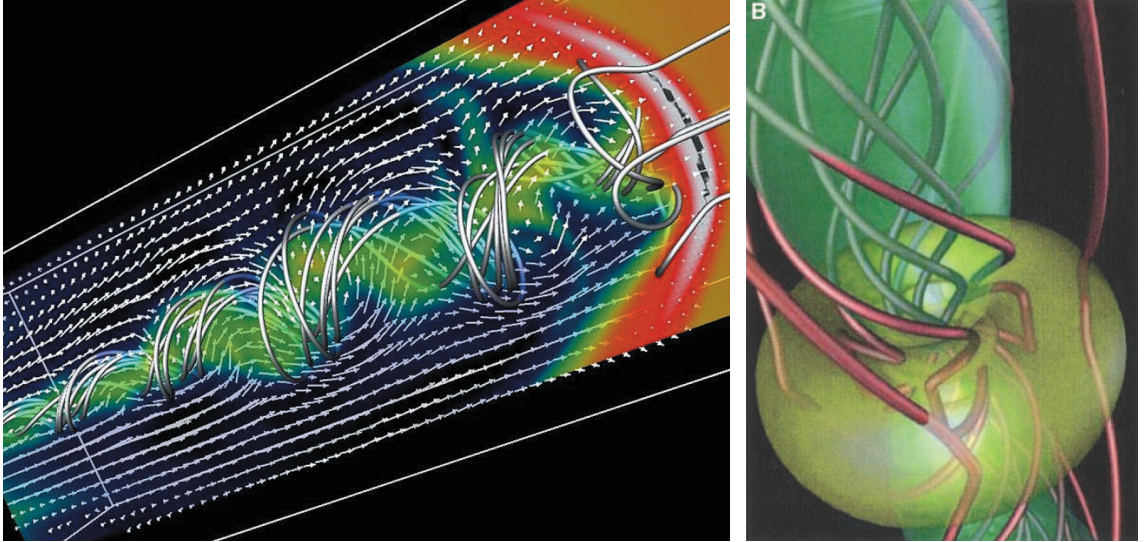


Figure 1.7: *Left:* A three-dimensional simulation of a magnetised jet. The flow velocity is depicted with arrows, while the magnetic field is displayed with metallic tubes (taken from Meier et al. 2001). *Right:* An MHD (magneto-hydrodynamic) simulation highlighting the magnetic field lines. After being initially poloidal, the accretion flow around the black hole drags the field lines, which produces a magnetic torque that can efficiently accelerate particles (taken from Meier et al. 2001).

This acceleration may be caused by the electron moving at thermal speeds (meaning they have a Maxwellian velocity distribution described by a temperature T) in an ionized region, where it is accelerated by the electric field of the surrounding ions. This free-free radiation or Bremsstrahlung has a distinct spectral shape, yielding $I_\nu \propto \nu^2$ for the optically thick ($\tau_\nu \gg 1$) and $I_\nu \propto \nu^{-0.1}$ for the optically thin ($\tau_\nu \ll 1$) case. I denote with I_ν the *intensity* or *surface brightness* of a source, which is equal to the power P radiated into a solid angle Ω per unit surface A and unit frequency ν :

$$I_\nu = \frac{P}{d\nu d\Omega dA}. \quad (1.2)$$

The optical depth τ_ν is defined in the equation of radiative transfer,

$$I_\nu = S_\nu(T) \cdot (1 - e^{-\tau_\nu}), \quad (1.3)$$

and is the line of sight integrated absorption coefficient κ_ν : $\tau_\nu = \int \kappa_\nu ds$. S_ν denotes the source function and is described by emission and absorption according to Kirchhoff's law

$$S_\nu = \frac{\epsilon_\nu}{\kappa_\nu}, \quad (1.4)$$

where ϵ_ν describes the emissivity. In case of local thermodynamic equilibrium, S_ν takes the form of a blackbody spectrum B_ν following Planck's law:

$$B_\nu = \frac{2h\nu^3}{c^2} \frac{1}{e^{\frac{h\nu}{k_B T}} - 1}, \quad (1.5)$$

and in the low-frequency limit $h\nu \ll k_B T$

$$B_\nu = \frac{2k_B\nu^2}{c^2} T. \quad (1.6)$$

In radio astronomy, the temperature in Eq. 1.6 is often referred to as brightness temperature, and is used as a proxy for the source brightness. In case the radiation is non-thermal, the term temperature loses its physical meaning, but is nevertheless commonly used to describe the brightness of a source. In the following I will focus on non-thermal emission mechanisms.

1.3.1 Synchrotron emission

Synchrotron emission is produced when relativistic particles are accelerated in a magnetic field. Particles are considered relativistic when their velocity v approaches the speed of light c : $\beta = v/c \lesssim 1$. They then have Lorentz factors $\gamma = (1 - (v^2/c^2))^{-0.5} \gg 1$.

For an accelerated electron with velocity $\vec{\beta}$ with an angle θ between $\vec{\beta}$ and the normalised line of sight vector $\vec{n} = \vec{R}/R$, its electric field is given by

$$\vec{E} = \frac{e}{c} \cdot \frac{\vec{n} \times ((\vec{n} - \vec{\beta}) \times \dot{\vec{\beta}})}{R(1 - \beta \cos \theta)^3}, \quad (1.7)$$

where e is the electron charge, $\dot{\vec{\beta}}$ is the particle acceleration and $R = |\vec{R}|$ (see Klein and Fletcher 2015). Note that here and in the following Chapters, I stick to cgs units (Gaussian system), which are commonly used in astrophysics. The radiation flux is given by the Poynting vector

$$\vec{S} = \frac{c}{4\pi} \cdot \vec{E} \times \vec{B} = \frac{c}{4\pi} \cdot |\vec{E}^2| \times \vec{n} \quad (1.8)$$

Then, the power P that is radiated into a solid angle Ω per frequency and time is

$$\frac{dP_\nu(t)}{d\Omega} = |\vec{S}| \cdot (1 - \beta \cos \theta) R^2 = \frac{e^2}{4\pi c} \cdot \frac{|\vec{n} \times ((\vec{n} - \vec{\beta}) \times \dot{\vec{\beta}})|}{(1 - \beta \cos \theta)^5}. \quad (1.9)$$

Integrating this power over the whole solid angle of a sphere and taking into account the distance to the observed particle, the radio flux density S_ν would be

$$P_\nu = 4\pi R^2 S_\nu. \quad (1.10)$$

From Eq. 1.9, what is called *relativistic boosting* or *Doppler boosting* already becomes clear: For $\beta \lesssim 1$ and small θ , the radiated power can become exceedingly large.

For a charged particle moving with a pitch angle χ_p with respect to the magnetic field \vec{B} , it will be subject to the Lorentz force:

$$m\dot{\vec{v}} = m \cdot (\vec{v} \times \omega_L \vec{e}_\perp) = -\frac{e}{c} \cdot (\vec{v} \times \vec{B}), \quad (1.11)$$

where $m = \gamma m_0$ is the particle mass (m_0 being the rest mass). Here, ω_L is the Larmor frequency (or gyration frequency) in the centrifugal force because of the circular motion of the particle in a (uniform) magnetic field. This is illustrated in Fig. 1.9. With ϕ now being the angle between \vec{n} and $\dot{\vec{\beta}}$, as $\vec{\beta} \perp \dot{\vec{\beta}}$, Eq. 1.9 can be rewritten as

$$\frac{dP_{\text{synch}}(t)}{d\Omega} = \frac{e^2 \dot{v}^2}{4\pi c^3} \cdot \frac{1 - \frac{\sin^2 \theta \cos^2 \phi}{\gamma^2 (1 - \beta \cos \theta)^2}}{(1 - \beta \cos \theta)^3}. \quad (1.12)$$

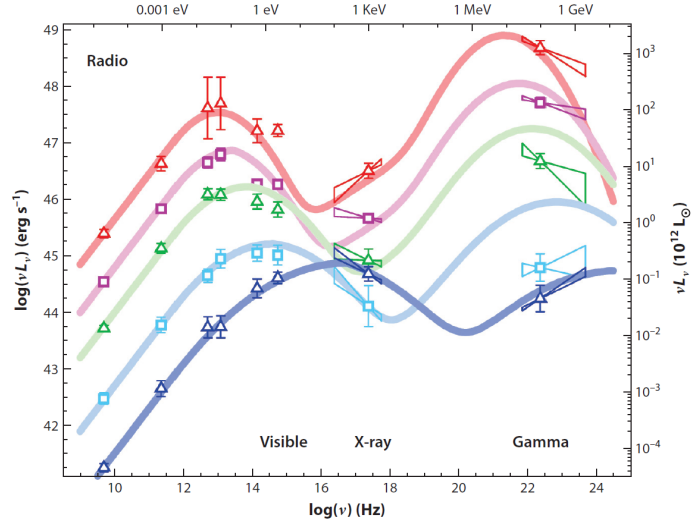


Figure 1.8: Energy spectra of different AGN. The y -axis shows the monochromatic luminosity. The plot illustrates the “blazar sequence” (see text for details), showing, from top to bottom: a high-powered flat-spectrum radio quasar (red), a low-energy peaked BL Lac object (BLL) (LBL, pink), a medium-luminosity intermediate-energy peaked BLL (IBL, green), high-energy peaked blue BLL (HBL, light blue), and a low-powered extreme HBL/TeV (dark blue) blazar. After Fossati et al. (1998), taken from Blandford et al. (2019).

The integration over solid angle then yields

$$P_{\text{synch}}(t) = \frac{2}{3} \cdot \frac{e^2 \dot{v}^2}{c^3} \gamma^4 = \frac{2}{3} \frac{e^4}{3m_0^2 c^3} \gamma^2 \beta^2 B^2 = 2\sigma_T c \gamma^2 \beta^2 u_B. \quad (1.13)$$

Here I defined both the magnetic field energy density $u_B = \frac{B^2}{8\pi}$ and the Thompson cross-section $\sigma_T = 8\pi r_e/3$ with the electron radius $r_e = \frac{e^2}{m_0 c^2}$.

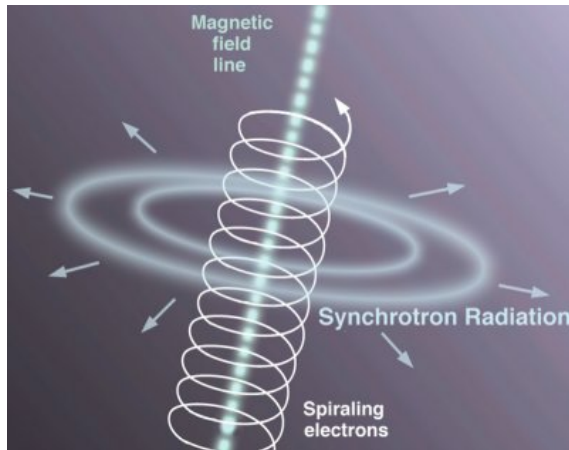


Figure 1.9: Artistic representation illustrating a charged particle gyrating in a magnetic field (Credits: Jon Lomberg/Gemini Observatory).

With a proper Fourier analysis one arrives at the frequency dependence of the radiated power:

$$P_{\text{synch}}(t) = \frac{\sqrt{3}e^3}{mc^2} \cdot B \sin \chi_p \cdot \frac{\nu}{\nu_c} \int_{\nu/\nu_c}^{\infty} K_{5/3}(x) dx, \quad (1.14)$$

where $v_c = \frac{3\gamma^2 eB}{4\pi mc} = \frac{1}{2/3\Delta t'}$ is the critical frequency, and $K_{5/3}$ is the modified Bessel function. $\Delta t'$ is the time width of the pulse of radiation in the *observer's* frame, which relates to the one in the source frame as

$$\Delta t' = \frac{\Delta t}{\gamma^2}. \quad (1.15)$$

Equation 1.15 shows that the synchrotron frequency spectrum is shifted to higher frequencies by a factor of γ^2 , which is why synchrotron radiation can be observed at radio wavelengths for particles with γ ranging from a few 100 to a few 10000.

Now let us consider that the radiation is coming from an ensemble of particles. The energy spectrum of such an ensemble in an energy range between E_{\min} and E_{\max} is assumed to have a power-law distribution:

$$N(E)dE = A \cdot E^{-g}dE \quad (1.16)$$

where N is the particle number density, E the particle energy and A is a normalisation constant. The power-law distribution is well-established, e.g. by measurements of cosmic ray energy spectra on Earth, with $g = 2.4$ (Klein and Fletcher 2015). This may differ in different physical environments. For example, the spectrum steepens in regions of lacking constant energy supply.

The total emissivity of an ensemble of particles is then

$$\epsilon_\nu = \frac{1}{4\pi} \int_{E_{\min}}^{E_{\max}} P(\nu) \cdot E^{-g}dE. \quad (1.17)$$

First, I consider the optically thin case, with $\tau_\nu \ll 1$. Then one can approximate Eq. 1.3 to

$$I_\nu = S_\nu(T) \cdot \tau_\nu \quad (1.18)$$

In this case, with the important assumption that the absorption does not depend on location, the absorption coefficients cancel, and

$$I_\nu = \int_0^{s_0} \epsilon_\nu ds = \frac{1}{4\pi} \int_0^{s_0} \int_{E_{\min}}^{E_{\max}} P(\nu) \cdot E^{-g} ds dE \quad (1.19)$$

Solving this integral then yields the synchrotron spectrum:

$$I_\nu \propto B_\perp^{1-\alpha} \cdot \nu^\alpha \quad \text{for } \tau_\nu \ll 1, \quad (1.20)$$

with $\alpha = (1 - g)/2$ being the spectral index and B_\perp is the magnetic field component perpendicular to the particle motion.

1.3.2 Synchrotron self-absorption

In general, one has to consider absorption as well, where for synchrotron radiation, synchrotron-self-absorption (SSA) might play a role in the emitting region. In this case, $\tau_\nu \gg 1$, and one can equate I_ν with the source function S_ν . This requires a definition of the Einstein coefficients of absorption and stimulated emission, and after some algebra, one arrives at

$$I_\nu \propto B_\perp^{-1/2} \cdot \nu^{5/2} \quad \text{for } \tau_\nu \gg 1, \quad (1.21)$$

The resulting spectrum is displayed in Fig. 1.10. In addition to the above calculations, any synchrotron spectrum will display a cutoff frequency above which the spectrum falls off exponentially. This is a natural consequence of the finite particle energy spectrum, and variations in this cutoff frequency can show particle energy losses.

One can quantify the radiation losses by setting $P_{\text{synch}} = -\frac{dE}{dt}$ and integrating to define the time where the particles have lost half of their energy:

$$t_{1/2} \propto B^{-2} E^{-1}, \quad (1.22)$$

where E is the initial particle energy. For an electron with $\gamma = 2000$ in a magnetic field of 1 G, which are typical for relativistic jets, the electron will lose half of its energy within three days. Therefore substantial particle re-acceleration is needed to sustain the particle energies up to kiloparsec scales.

It is important to revisit the concept of brightness temperature at this point. From Eq. 1.6 one defines the brightness temperature T_b as

$$T_b = \frac{\lambda^2}{2k_B} \cdot I_\nu. \quad (1.23)$$

Relativistic particles are not in a thermal equilibrium, so that their velocity distribution is not Maxwellian and at first glance, a temperature can not be assigned to such an ensemble of particles. However, one can still define the temperature for a relativistic Maxwellian distribution as

$$T_k = \frac{\gamma mc^2}{3k_B}, \quad (1.24)$$

where this kinetic temperature is assigned to particles with an energy $E = \gamma mc^2$. This can be used because the spectrum of these particles is peaked at the critical frequency, so the emission and absorption processes at a frequency ν are associated with particles of about the same energy. A relativistic electron gas will reach an equilibrium state only after a long time because particle densities are low and interactions not frequent. For low enough frequencies, one expects the brightness temperature T_b to reach the kinetic temperature as defined in Eq. 1.24 as self-absorption becomes important.

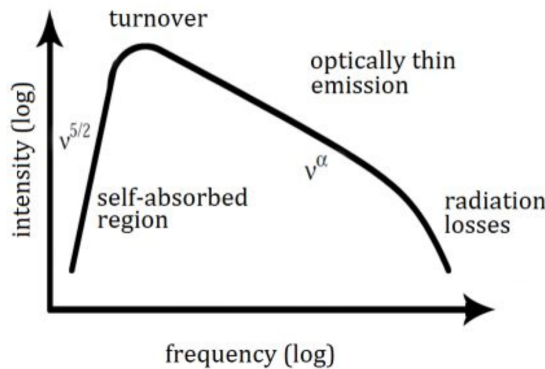


Figure 1.10: Synchrotron spectrum resulting from an ensemble of electrons with a power-law energy distribution (taken from Angioni 2018). The spectral index α will take values around -0.7 .

1.3.3 Inverse Compton emission

Given an initial radiation field with energy density u_{rad} , the photons can get up-scattered to higher energies by charged particles. This is the inverse of the Compton scattering,

where a photon scatters off an electron. On average, the photon will increase its energy by a factor of the order of γ^2 of the electron. The radiative energy density is given by integrating the intensity over all solid angles and frequencies,

$$u_{\text{rad}} = \frac{1}{c} \int_{\nu} \int_{\Omega} I_{\nu} d\nu d\Omega. \quad (1.25)$$

The derivation of the radiated power of a single particle in the inverse-Compton (IC) process is similar to the one explained in Sect. 1.3.1, and is given by

$$P_{\text{IC}} = \frac{4}{3} \sigma_{\text{T}} c \gamma^2 \beta^2 u_{\text{rad}}, \quad (1.26)$$

where one can see again the Thomson cross section σ_{T} defined in Eq. 1.13. The initial radiation field can be produced in different environments. For example, the radiation field could come from the synchrotron radiation explained in Sect. 1.3.1. The photons in it are then inverse-Compton scattered by the very particles that give rise to the synchrotron radiation. This process is therefore termed as the synchrotron self-Compton (SCC) process. The radiation field can also be external, coming from the accretion disk, the dust torus or the BLR, in which external IC takes place.

From Eq. 1.26 and 1.13 one can see that P_{synch} and P_{IC} have the same dependencies and

$$\frac{P_{\text{synch}}}{P_{\text{IC}}} = \frac{u_{\text{B}}}{u_{\text{rad}}}. \quad (1.27)$$

Deriving the intensity emitted by an ensemble of particles yields the same frequency dependence as the synchrotron spectrum. The IC emission is visible as the second peak at higher frequencies in Fig. 1.8, and can be the cause for emission up to γ -ray energies. However, at very high energies, hadronic processes might also play a role, as indicated by recent neutrino detections (see Kadler et al. 2016; Ansoldi et al. 2018; Britzen et al. 2019; Plavin et al. 2020, 2021; Ros et al. 2020). I refer the interested reader to the aforementioned sources, as in this thesis, hadronic processes are not treated.

1.3.4 Relativistic effects

We already saw the time dilation effect in Sect. 1.3.1, but there is a multitude of relativistic effects like relativistic beaming and boosting. In general, relativistic effects start to be significant when particles have velocities $v > 0.1c$.

In the following, when referring to the jet bulk motion, the Lorentz factor is denoted by a capital Γ , while for single particles it is denoted by γ . The bulk jet speed I denote with a subscript β_{j} , while the particle velocity is denoted as β .

In special relativity, when a particle is moving close to the speed of light with respect to an observer, the time dilation and length contraction will lead to an observer seeing a different radiation pattern than what is seen in the source frame. The radiation pattern is then strongly beamed into the direction of the particle's movement, with a critical angle

$$\theta_{\text{crit}} \approx \frac{1}{\gamma}. \quad (1.28)$$

This also leads to a boosting or de-boosting of the flux density for an ensemble of particles approaching or receding from the observer. I again denote quantities in the

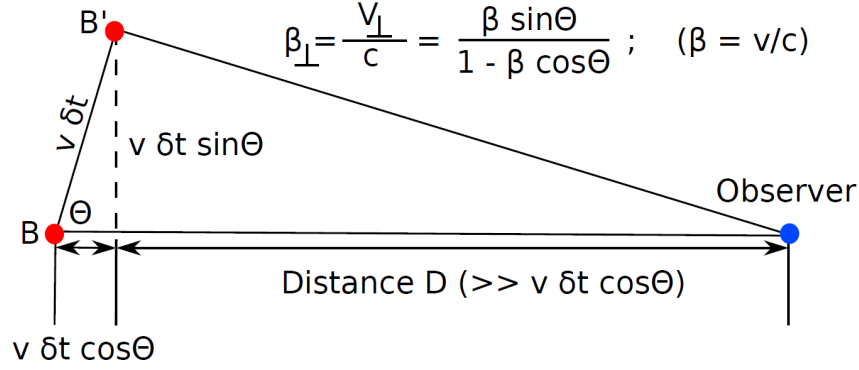


Figure 1.11: Geometry of apparent superluminal motion (Schinzel 2011).

source frame as primed, and the quantities in the observer's frame without prime. Then for the solid angle

$$\Omega' = \frac{\Omega}{\delta^3}, \quad (1.29)$$

with the *Doppler factor* $\delta = (\Gamma(1 - \beta_j \cos \theta))^{-1}$. To transform the time t , one has to consider the time dilation as $\Delta t = \Gamma \Delta t'$. In addition, one has to incorporate the fact that the emitting source of radiation will have moved in the time interval between emitting the photon and the observer measuring the photon. Then it is imperative

$$t' = \frac{t}{\delta}, \quad (1.30)$$

and thus

$$\nu' = \delta \nu. \quad (1.31)$$

Following that,

$$I'_{\nu} = \delta^3 I_{\nu}. \quad (1.32)$$

The flux density S_{ν} is the intensity integrated over the source solid angle, and thus

$$S_{\nu} = S'_{\nu} \delta^{3-\alpha}, \quad (1.33)$$

where α accounts for the shape of the spectrum from Eq. 1.20.

Another effect are apparent superluminal velocities of source components moving at relativistic speeds with small angles with respect to the line of sight to the observer, as is the case for blazars. If one considers a source of radiation moving between points B and B' towards an observer (see Fig. 1.11), then for the time interval between those points measured by an observer it is apparent that

$$\Delta t = t_{B'} - t_B, \quad (1.34)$$

with

$$t_{B'} = \frac{D}{c} - \frac{v \delta t \cos \theta}{c} \quad \text{and} \quad (1.35)$$

$$t_B = \frac{D}{c} - \delta t, \quad (1.36)$$

where the time interval δt is given in the source frame. Here the distance D from the observer to the source is assumed to be much larger than the distances covered by the source moving in the covered time ranges. Then

$$\Delta t = \delta t(1 - \beta \cos \theta), \quad (1.37)$$

Consequently, the apparent velocity as projected on the sky is:

$$\beta_{\text{app}} = \beta_{\perp} = \frac{v \delta t \sin \theta}{c \Delta t} = \frac{\beta \sin \theta}{1 - \beta \cos \theta}. \quad (1.38)$$

The geometry is illustrated in Fig. 1.11 and the magnitudes of the relativistic effects are shown in Fig. 1.12.

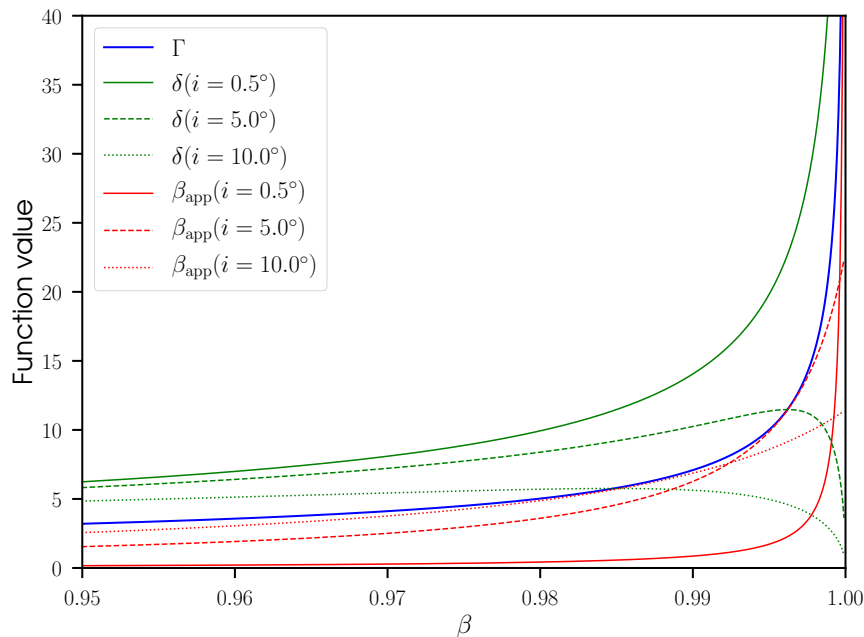


Figure 1.12: Values of the Lorentz factor Γ , Doppler factor δ and apparent speed β_{app} as a function of the speed β , for different source viewing angles.

1.4 Polarisation

1.4.1 Polarisation states of an electromagnetic wave

For an electromagnetic wave with an electric field vector \vec{E} propagating in a direction z , its components in the x - y -plane can be written as

$$E_x = E_{x_0} \cdot \cos(kz - \omega t + \delta_1) \quad (1.39)$$

$$E_y = E_{y_0} \cdot \cos(kz - \omega t + \delta_2), \quad (1.40)$$

where k denotes the wave vector, $\omega = 2\pi\nu$ the frequency and δ_1 and δ_2 are arbitrary phase shifts. One can already see that \vec{E} will produce a helical motion in the wave propagation direction, depending on the phase difference $\delta = \delta_2 - \delta_1$. The most general form is an ellipse with the ellipse equation

$$\left(\frac{E_x}{E_{x_0}}\right)^2 + \left(\frac{E_y}{E_{y_0}}\right)^2 - 2\frac{E_x \cdot E_y}{E_{x_0} \cdot E_{y_0}} \cdot \cos \delta = \sin^2 \delta. \quad (1.41)$$

Different polarisation states arise from the phase difference δ . In general, its value describes elliptical polarisation. For $\delta = n \cdot \pi$ with $n \in \mathbb{Z}$, the ellipse collapses to a single line and one speaks of linear polarisation. For $\delta = m \cdot \frac{\pi}{2}$ with $m \in \mathbb{Z} \wedge m \neq 0$, one has circular polarisation, with the sign determining the handedness. For $m > 0$, the polarisation circle rotates in a clockwise sense as seen from an observer towards whom the wave is propagating. In this case, one speaks of right-hand circular polarisation (RCP). On the other hand, for $m < 0$, the polarisation circle rotates in a counter-clockwise sense, and in that case, one speaks of left-hand circular polarisation (LCP).

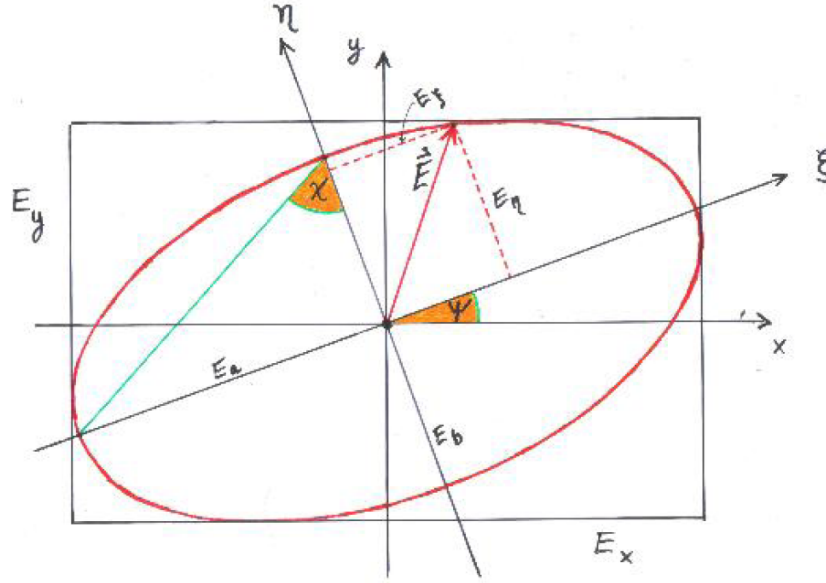


Figure 1.13: Polarisation ellipse (from Klein and Fletcher 2015).

The resulting polarisation ellipse is shown in Fig. 1.13. One can transform to another more convenient coordinate system along the directions of the ellipse's major and minor axis, ξ and η . It is then described by the amplitudes E_ξ and E_η as well as the angle ψ (the rotation angle of the ellipse) and χ (defining the ellipticity):

$$E_\xi = E_{\xi_0} \cdot \cos(kz - \omega t + \delta) = E_x \cdot \cos \psi + E_y \sin \psi \quad (1.42)$$

$$E_\eta = E_{\eta_0} \cdot \cos(kz - \omega t + \delta) = -E_x \cdot \sin \psi + E_y \cos \psi. \quad (1.43)$$

One can redefine this coordinate system using the convenient description with the Poincaré sphere (see Fig. 1.14) and the four Stokes parameters I , Q , U and V , as follows:

$$I = S = E_a^2 + E_b^2, \quad (1.44)$$

$$Q = S \cdot \cos 2\chi \cos 2\psi, \quad (1.45)$$

$$U = S \cdot \cos 2\chi \sin 2\psi \quad \text{and} \quad (1.46)$$

$$V = S \cdot \sin 2\chi, \quad (1.47)$$

where S denotes the Poynting flux again (equalling the total intensity I). Every point on the Poincaré sphere describes a unique polarisation state of the electromagnetic wave. If the wave is in the (Q, U) -plane, it is linearly polarised with a polarisation angle of 2ψ . The poles are circularly polarized, with the northern hemisphere corresponding to RCP and the southern one to LCP, and all the other states correspond to elliptical polarisation with an amount of circular polarisation defined by χ .

In this convenient polarisation base, the Stokes parameters are given in terms of the quantities defined in Eq. 1.40:

$$I = E_{x_o}^2 + E_{y_o}^2, \quad (1.48)$$

$$Q = E_{x_o}^2 - E_{y_o}^2, \quad (1.49)$$

$$U = 2 \cdot E_{x_o} E_{y_o} \cdot \cos \delta \quad \text{and} \quad (1.50)$$

$$V = 2 \cdot E_{x_o} E_{y_o} \cdot \sin \delta. \quad (1.51)$$

Or rather, in terms of superposition of the RCP and LCP components:

$$I = E_{l_o}^2 + E_{r_o}^2, \quad (1.52)$$

$$Q = 2 \cdot E_{l_o} E_{r_o} \cdot \sin \delta', \quad (1.53)$$

$$U = 2 \cdot E_{l_o} E_{r_o} \cdot \cos \delta' \quad \text{and} \quad (1.54)$$

$$V = E_{l_o}^2 - E_{r_o}^2. \quad (1.55)$$

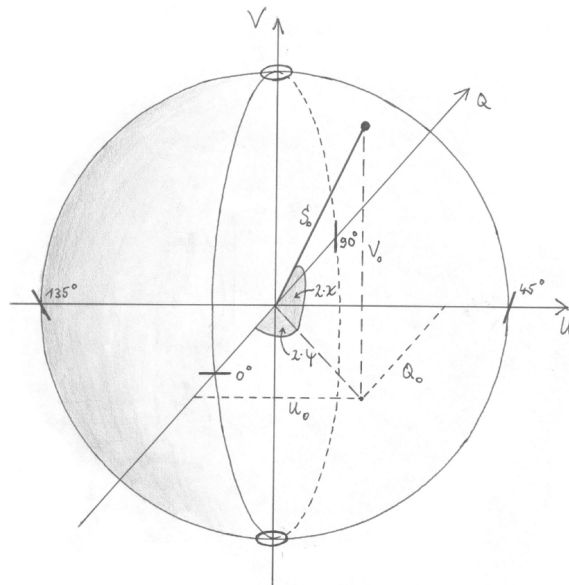


Figure 1.14: Poincaré sphere (from Klein and Fletcher 2015).

In the following, I define I as the total intensity, while $P = \sqrt{Q^2 + U^2}$ is the linearly polarised intensity, and V is the circularly polarised intensity. In the course of this work, I will refer to the fractional linear polarisation as $m = P/I$.

1.4.2 Polarised synchrotron emission

In the following, I will give a brief explanation of the concepts of polarisation of synchrotron emission. For a detailed treatment I refer the reader to Longair (2011).

First I consider non-relativistic particles gyrating in a magnetic field, which have a broad radiation pattern, and an observer will observe linear polarisation if $\vec{B} \perp \vec{n}$. As before, \vec{n} denotes the line-of-sight vector. Circular polarisation will be observed if $\vec{B} \parallel \vec{n}$, and elliptical polarisation for angles in between.

Now if one considers that the particles are highly relativistic, then one particle will form a velocity vector in the form of a velocity cone, the opening angle of which is twice the pitch angle χ_p . The angular width of the velocity cone will be $1/\gamma$. This is illustrated in Fig. 1.15. Significant radiation is only observed if the velocity vector has a small angle

with respect to the line of sight to the observer, so if approximately $\vec{v} \parallel \vec{n}$. In case it exactly coincides with the line of sight, an observer will see linear polarisation. The geometry is illustrated in Fig. 1.16.

This is because in this case, the wave vector $\vec{k} \parallel \vec{v}$, and so $\vec{E} \perp \vec{v} \times \vec{B}$. This can also be clearly seen from Eq. 1.7. The radiation pulse is only observed for a short time $\propto 1/\gamma^2$, so the acceleration vector does not change significantly while one observes it, as the time is much shorter than the gyration frequency. If $\vec{k} \not\parallel \vec{v}$, then there will be a component of \vec{E} parallel to \vec{B} . Subsequently, one will observe elliptical polarisation, as E_{\parallel} and E_{\perp} have different time dependencies within each radiation pulse. The handedness then depends on whether the line of sight lies inside or outside of the velocity cone. However, for an ensemble of particles, those will contribute equally with velocity cones on both sides of the line of sight, effectively cancelling out the elliptical component (which is only true because the beam is very narrow, $\theta \propto 1/\gamma$). In the end, the polarisation is linear, with a degree of polarisation (Longair 2011):

$$m = \frac{g+1}{g+\frac{7}{3}} = \frac{1-\alpha}{\frac{5}{3}-\alpha}, \quad (1.56)$$

for the optically thin case. On the other hand, for the optically thick case

$$m = \frac{1}{2g+\frac{13}{3}} = \frac{1}{\frac{19}{3}-4\alpha}. \quad (1.57)$$

The dependence on α in Eq. 1.56 is not too strong, with $m = 75\%$ for $\alpha = -1$ and $m = 60\%$ for $\alpha = 0$. One expects a theoretical maximum in the range of these values, so in principle, $m > 75\%$ is not possible. Here the case of a uniform magnetic field is assumed. If the field has a random component as well, the degree of polarisation will decrease accordingly.

For the optically thick case in Eq. 1.57, one expects $m = 6\%$ with $\alpha = 5/2$. In an optically thick region, synchrotron photons are much more likely to be absorbed. If one considers the linearly polarised wave as a superposition of a component perpendicular and parallel to the magnetic field, the parallel component then has a higher chance of being absorbed. In this case, the perpendicular component will be left, resulting in the fact that the observed electric field is parallel to the magnetic field.

1.4.3 Faraday rotation

When a linearly polarised electromagnetic wave passes through a magnetised plasma with some magnetic field component parallel to the propagation direction, B_{\parallel} , the wave will experience a rotation $\Delta\chi$ of its linear polarisation angle χ_0 by

$$\chi = \chi_0 + \Delta\chi = \chi_0 + \frac{e^3}{2\pi m^2 c^4} \lambda^2 \int_0^{s_0} n_e B_{\parallel} ds = \chi_0 + RM \cdot \lambda^2, \quad (1.58)$$

where I have defined the rotation measure RM , in cgs units. n_e is the electron density, and the integral is performed along the line of sight s_0 through the plasma. The rotation is due to the fact that one can view the linearly polarised wave as a superposition of two circularly polarised waves, RCP and LCP. Both components will experience a different phase shift due to their handedness, and will thus produce a net linear polarisation angle change. The RM in Eq. 1.58 can also be given in convenient astronomical units:

$$RM = 8.1 \cdot 10^5 \int_0^{s_0} \left(\frac{n_e}{\text{cm}^{-3}} \right) \left(\frac{B_{\parallel}}{\text{G}} \right) \left(\frac{dr}{\text{pc}} \right) \text{rad m}^{-2}, \quad (1.59)$$

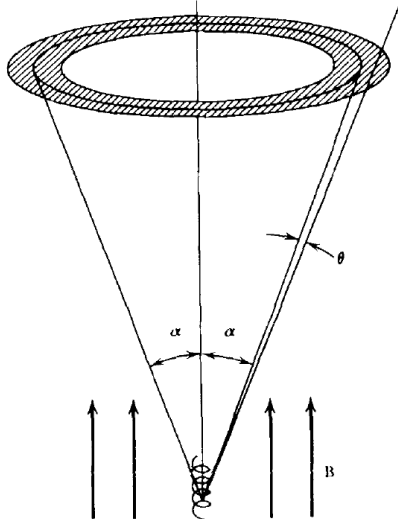


Figure 1.15: Velocity cone formed by a relativistic particle (from Rybicki and Lightman 1979). Note that the pitch angle is denoted as α here, while I denote it as χ_p .

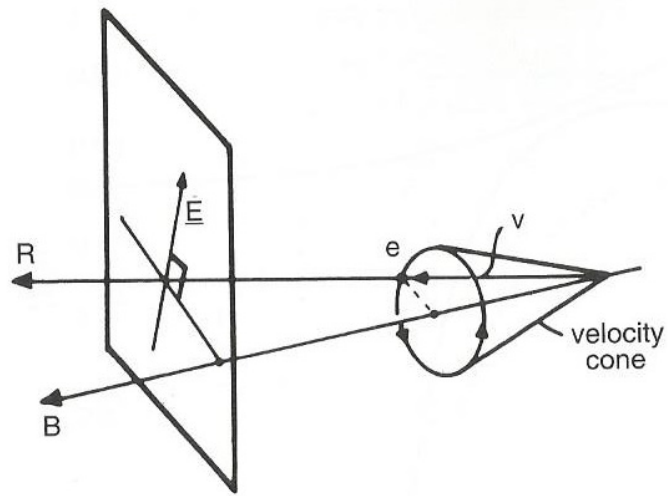


Figure 1.16: Geometry of the velocity cone of a relativistic particle moving in a magnetic field (from Longair 2011).

where the magnetic field strength is given in Gauss and the distance in parsec.

Polarisation vectors are in fact not proper vectors, as they have a $n\pi$ degeneracy. In other words, a polarisation vector can not be distinguished from one that is rotated by 180° . Subsequently, determining the RM requires measurements at at least three wavelengths to avoid the degeneracy. The problem is illustrated in Fig. 1.17. If the polarisation vectors are shifted by a certain amount of rotations, one can substantially change the estimated RM .

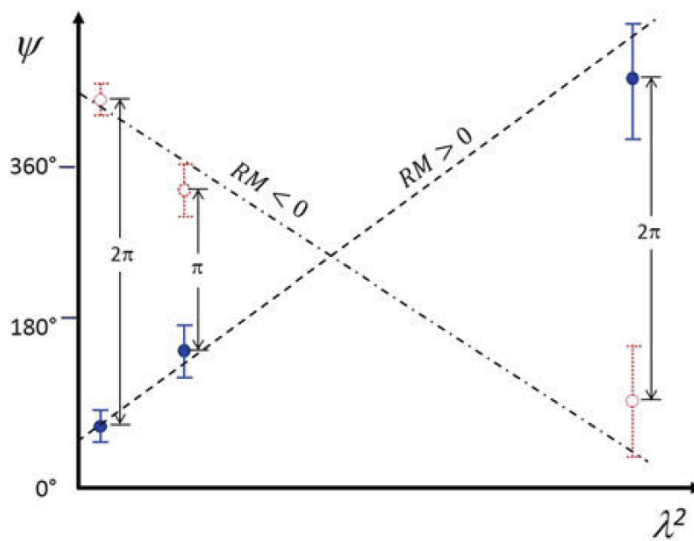


Figure 1.17: Measurements of the polarisation vectors can be rotated by an arbitrary amount of rotations by 180° to yield a different RM value (from Klein and Fletcher 2015).

1.4.4 Depolarisation effects

Due to the nature of Faraday rotation, significant depolarisation might happen in a source, so that the actual theoretical limit imposed by Eq. 1.56 is almost never reached.

In the following, it is useful to define the Faraday depth Φ as

$$\Phi = \frac{e^3}{m^2} \lambda^2 \int_0^{\vec{r}} n_e \vec{B} \cdot d\vec{r}. \quad (1.60)$$

The Faraday depth can be understood as a generalisation of the RM as defined in Eq. 1.58. The complex degree of polarisation is then

$$P(\vec{r}) = p(\vec{r}) \cdot e^{2i\chi_0(\vec{r})}. \quad (1.61)$$

As a function of the Stokes parameters, the complex polarisation can also be written as $P = Q + iU$. The *observed* degree of polarisation is then the emissivity-weighted integral of the degree of polarisation along the path \vec{r} :

$$P_{\text{obs}}(\lambda) = \frac{\iint p(\vec{r}) \cdot \epsilon(\lambda, \vec{r}) \cdot e^{2i(\chi_0(\vec{r}) + \Phi(\vec{r})\lambda^2)} d\vec{r} d\Omega}{\iint \epsilon(\lambda, \vec{r})}. \quad (1.62)$$

One can distinguish between different scenarios where depolarisation can occur:

- **Internal depolarisation:** Depolarisation might happen within a source, especially if it is optically thick. The degree of depolarisation will depend greatly on the source geometry and the degree of uniformity of the magnetic field. So far, the assumption of a uniform magnetic field has been made throughout Sect. 1.3 and 1.4, which is generally not the case in nature. There will also be a random component of the magnetic field. For simplicity, let us still consider observing a slab along which the magnetic field is uniform. Then it can be shown, following from Eq. 1.62, that the degree of polarisation is (Burn 1966; Klein and Fletcher 2015)

$$m(\lambda) = m_0 \cdot \frac{\sin(\Phi\lambda^2)}{\Phi\lambda^2}, \quad (1.63)$$

where m_0 refers to the theoretical limit defined in Eq. 1.56. One could now assume that the source geometry is made up out of slabs as described above, each contributing to the depolarisation according to Eq. 1.63. In reality, complex source geometries could make the actual degree of depolarisation difficult to assess.

- **Beam depolarisation:** If the telescope beam encompasses multiple polarised emission regions with different polarisation angles, they might partly cancel, thus diminishing the observed polarised intensity.
- **Unresolved Faraday screen:** In case there is an unresolved Faraday screen in the foreground of the source extending over R along the line of sight, there are components of different Faraday depths contributing differently to the overall Faraday rotation. In this case, the dependence on λ^2 does not hold anymore. Instead, if one assumes the unresolved elements of this screen sufficiently small with size d , the fluctuations can be represented by a Gaussian, and the degree of polarisation will decrease exponentially as (Klein and Fletcher 2015)

$$m(\lambda) = m_0 \cdot e^{-2K^2 \langle n_e B_{\parallel} \rangle d R \lambda^4}, \quad (1.64)$$

with K being the constant in Eq. 1.58 and $\langle n_e B_{\parallel} \rangle$ being the variance of the product of the electron density and magnetic field in an element of the screen.

- **Bandwidth depolarisation:** In the presence of Faraday rotation and a finite bandwidth in the observations, $\Delta\nu$, the polarisation angle might rotate significantly across the bandwidth. This will lead to a rotation of the polarisation angle

$$\Delta\chi = -2\lambda_0^2 \cdot RM \frac{\Delta\nu}{\nu_0}, \quad (1.65)$$

where ν_0 and λ_0 denote the central observing frequency and wavelength. Resultant from that is the potential partial cancellation of polarisation vectors across the bandwidth and thus a decrease in the degree of polarisation. It can be shown that, again for the simple source geometry of a uniform slab, that the degree of polarisation diminishes as

$$m(\Delta\nu) = m_0 \cdot \frac{\sin \Delta\chi}{\Delta\chi}. \quad (1.66)$$

1.5 Opacity effects: Core shift

In many cases for high-resolution radio observations, on scales probed by very-long-baseline interferometry (VLBI, see Chapter 2), one observes a bright feature at the jet base, which is referred to as the VLBI core. In the picture of a self-absorbed jet (Blandford and Königl 1979), the position of the core will change with observing frequency, if the core is thought of as the surface where the jet turns optically thick ($\tau = 1$). This picture is illustrated in Fig. 1.18. In most jets, the VLBI core is observed as the brightest feature in the jet, but this does not have to be the case necessarily. Regions of enhanced plasma density caused by shocks travelling down the jet can also be the cause for bright features in the jet, so care has to be taken when identifying the core.

The absolute position of the VLBI core will depend on frequency as (Königl 1981; Marcaide and Shapiro 1984; Lobanov 1998):

$$r_{\text{core}} \propto \nu_{\text{obs}}^{-1/k_r}, \quad (1.67)$$

where $k_r = ((3 - 2\alpha)m + 2n - 2)/(5 - 2\alpha)$, with

$$B = B_1 \left(\frac{r_1}{r}\right)^m \quad \text{and} \quad (1.68)$$

$$N = N_1 \left(\frac{r_1}{r}\right)^n \quad (1.69)$$

being the particle density N and the magnetic field B along the jet axis r , which decrease due to the adiabatic expansion of the jet.

1.5.1 Jet parameters from core shift

In the following, I adopt the approach by Lobanov (1998). The opacity as a function of the distance along the jet, r , is given by (Rybicki and Lightman 1979):

$$\tau(r) = C_2(\alpha) N_1 \left(\frac{eB_1}{2\pi m_e}\right)^{3/2-\alpha} \frac{\delta^{3/2-\alpha} \phi}{r^{(3/2-\alpha)m+n-1} \nu^{5/2-\alpha}}, \quad (1.70)$$

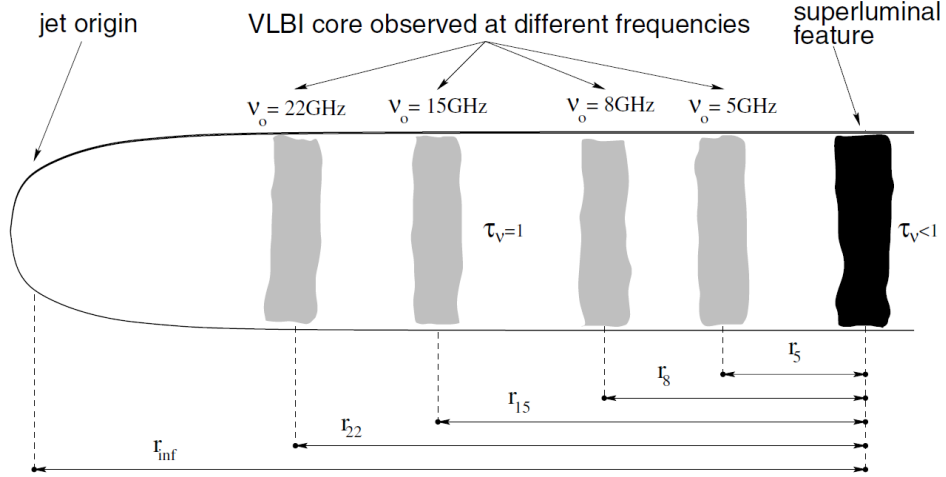


Figure 1.18: Positional shift of the VLBI core with frequency in a self-absorbed jet (Lobanov 1996).

where ϕ is the jet opening angle, and $C_2(\alpha)$ is given in Blumenthal and Gould (1970), with $C_2(-0.5) = 8.4 \cdot 10^{10}$. When setting $\tau(r)$ to unity, as is the case for the VLBI core, one can calculate the distance between the core and the central engine as

$$r_{\text{core}} = \left(\frac{B_1^{k_b} F}{\nu} \right)^{1/k_r}, \quad (1.71)$$

where $k_b = (3 - 2\alpha)/(5 - 2\alpha)$ and

$$F = (1 + z)^{-1} (6.2 \cdot 10^{18} C_2(\alpha) \delta^{3/2-\alpha} N_1 \phi)^{1/(5/2-\alpha)}. \quad (1.72)$$

Now the core-shift measure $\Omega_{r\nu}$ is defined as

$$\Omega_{r\nu} = 4.85 \cdot 10^{-9} \frac{\Delta r_{\text{mas}} D_L}{(1 + z)^2} \cdot \frac{\nu_1^{1/k_r} \nu_2^{1/k_r}}{\nu_2^{1/k_r} - \nu_1^{1/k_r}}, \quad (1.73)$$

with r_{mas} being the measured offset between core positions between the frequencies ν_1 and ν_2 with $\nu_2 > \nu_1$. $\Omega_{r\nu}$ should not vary with frequency unless k_r changes along the jet. With that, one can calculate the magnetic field at 1 pc from the central engine as:

$$B_1 = \left(\frac{\Omega_{r\nu}}{\sin \theta} \right)^{k_r/k_b} F^{-1/k_b}. \quad (1.74)$$

Inserting this into Eq. 1.71, we arrive at

$$r_{\text{core}} = \frac{\Omega_{r\nu}}{\nu^{1/k_r} \sin \theta}. \quad (1.75)$$

And, with $B_{\text{core}} \approx B_1 \cdot r_{\text{core}}$, it follows that

$$B_{\text{core}} \approx \nu^{m/k_r} \left(\frac{\Omega_{r\nu}}{(1 + z) \sin \theta} \right)^{k_r/k_b - m} F^{-1/k_b}. \quad (1.76)$$

In Eq. 1.75, the distance formally refers to the distance between the core and the sonic point. Since the distance between the sonic point and the central engine can be assumed much smaller than the distance between the core and the sonic point, one can take Eq. 1.75

as the distance from the core to the central engine. Hence this method can provide an effective measure of the field profile along the jet, when one measures the core shift at three or more frequencies. With the assumption of equipartition between particle and magnetic field energy, which means $\alpha = -0.5$ and $k_r = 1$, it follows:

$$B_1 \approx 0.016 \left(\frac{\Omega_{r\nu}^3 (1+z)^3}{\delta_j^2 \phi \sin^5 \theta} \right)^{0.25}. \quad (1.77)$$

Here, $\Omega_{r\nu}$ is expressed in more convenient units of pc GHz. Hirotani (2005) also assume equipartition, but express the magnetic field derived from the core shift in terms of the particle energy spectrum with minimum and maximum Lorentz factors, γ_{\min} and γ_{\max} (see also Fromm et al. 2013):

$$B_1 \approx \frac{2\pi m_e^2 c^4}{e^3} \left[\frac{e^2}{m_e c^3} \left(\frac{\Omega_{r\nu}}{r_1 \sin \theta} \right)^{k_r} \right]^{\frac{5-2\alpha}{7-2\alpha}} \times \left[\pi C_1(\alpha) \frac{r_1 m_e c^2}{e^2} \frac{-2\alpha}{\gamma_{\min}^{2\alpha+1}} \frac{\phi}{\sin \theta} K(\gamma, \alpha) \left(\frac{\delta}{1+z} \right)^{3/2-\alpha} \right]^{\frac{-2}{7-2\alpha}}, \quad (1.78)$$

with

$$C_1(\alpha) = \frac{3^{1-\alpha}}{8} \sqrt{\pi} \hat{\Gamma} \left(\frac{7-2\alpha}{4} \right) \hat{\Gamma} \left(\frac{5-6\alpha}{12} \right) \hat{\Gamma} \left(\frac{25-6\alpha}{12} \right) \hat{\Gamma} \left(\frac{9-2\alpha}{4} \right)^{-1} \quad (1.79)$$

and

$$K(\gamma, \alpha) = \frac{2\alpha + 1}{2\alpha} \frac{(\gamma_{\max}/\gamma_{\min})^{2\alpha} - 1}{(\gamma_{\max}/\gamma_{\min})^{2\alpha+1} - 1}, \quad (1.80)$$

where $\hat{\Gamma} = \int_0^\infty x^{z-1} e^{-x} dx$ is the complete Euler- Γ function, defined for $z \in \mathbb{C}$ and $\Re(z) > 0$. In this picture, the magnetic field at 1 pc can be expressed as (Fromm et al. 2013):

$$B_1 \approx 0.025 \left(\frac{\Omega_{r\nu}^3 (1+z)^2}{\delta_j^2 \phi \sin^2 \theta} \right)^{0.25}. \quad (1.81)$$

With the aforementioned assumptions, one can also express the particles density at 1 pc distance (in cm^{-3}):

$$N_1 = \frac{K(\gamma, \alpha)}{8\pi m_e c^2} \gamma_{\min}^{-1} B_1^2. \quad (1.82)$$

In the equipartition case, Eq. 1.82 can be rewritten as (Fromm et al. 2013):

$$N_1 = 7 \cdot 10^3 \gamma_{\min}^{-1} \cdot B_1^2 \quad \text{for } \gamma_{\max}/\gamma_{\min} = 10^3 \quad (1.83)$$

$$N_1 = 4.2 \cdot 10^3 \gamma_{\min}^{-1} \cdot B_1^2 \quad \text{for } \gamma_{\max}/\gamma_{\min} = 10^5. \quad (1.84)$$

When jets are observed with low-resolution radio telescopes, many of them exhibit a flat spectrum ($\alpha \approx 0$). This is readily explained in the framework of the self-absorbed jet, where the overall spectrum is obtained as a superposition of the VLBI cores at different frequencies, each with a different spectrum with different turnover frequency (Marscher 1996). This is illustrated in Fig. 1.19.

As we will see in Chapter 2, the position of the core is not always readily determined from VLBI observations. A way to circumvent this is phase referencing, which is explained

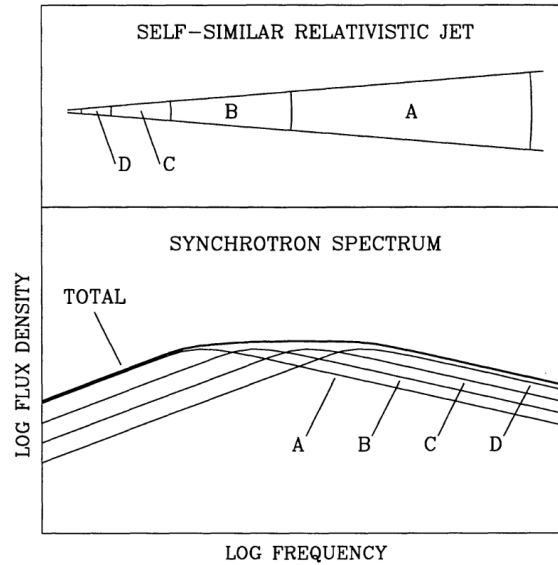


Figure 1.19: The superposition of different components in a self-similar, self-absorbed jet leads to a flat integrated spectrum (Marscher 1996).

in Sect. 6.1. Determining the core shift at the highest frequencies is possible with source frequency phase referencing, which I introduce in Chapter 6. This way the magnetic field can be determined in the core regions at millimetre wavelengths, closer to the central engine than with conventional cm-VLBI.

1.6 The flat-spectrum radio quasar 3C 345

The quasar 3C 345 (J1642+3948, 1641+399) was first listed in the third Cambridge catalogue of radio sources (Edge et al. 1959), from which the name derives. The source is a compact, bright flat spectrum radio quasar (FSRQ) that has been observed with VLBI over several decades. It shows structure in the radio from parsec (pc) (see Fig. 1.20) to kiloparsec (kpc) (see Fig. 1.21) scales, and also emits in the X rays (Unwin et al. 1997; Sambruna et al. 2004) and γ -rays (see e.g., Schinzel et al. 2012). It shows compact structure on pc scales (Zensus et al. 1995; Ros et al. 2000), and is known to exhibit superluminal motion with speeds of $\sim 3\text{--}20 c$ (e.g., Shaffer et al. 1977; Zensus et al. 1995; Schinzel et al. 2012; Lister et al. 2019). Jorstad et al. (2017) find an average of about $10 c$.

The jet propagates with a viewing angle of $\sim 5^\circ$ (Pushkarev et al. 2009; Schinzel et al. 2012). The source has been regularly monitored over some decades by several programs, e.g., by the Metsähovi Radio Observatory in Finland at 37 GHz ¹, the Owens Valley Radio Observatory (OVRO), or the MOJAVE (see Sect. 5.1.2) survey, which observes at 15 GHz with the VLBA. In these surveys, 3C 345 showed several flaring episodes, illustrated in Fig. 1.22 for the radio, but also flared in the optical and γ -rays (Schinzel et al. 2012).

The jet is observed to propagate first westwards within the first parsecs, and then downstream bend to the north-west, as observed at lower frequencies, with the bending being less prominent at higher frequencies (see Fig. 1.20). The outer jet at pc scales then continues in the direction of the kpc-scale jet, as seen in Fig. 1.21. The source showed to be core dominated, with the flux density of the core component having more than 60% of the total flux density as measured with VLBI (Hovatta et al. 2009). Relativistic shocks dominate the jet emission on scales of up to $\sim 100 \text{ pc}$ (Zensus et al. 1995; Lobanov and

¹<http://www.metsahovi.fi/opendata/>

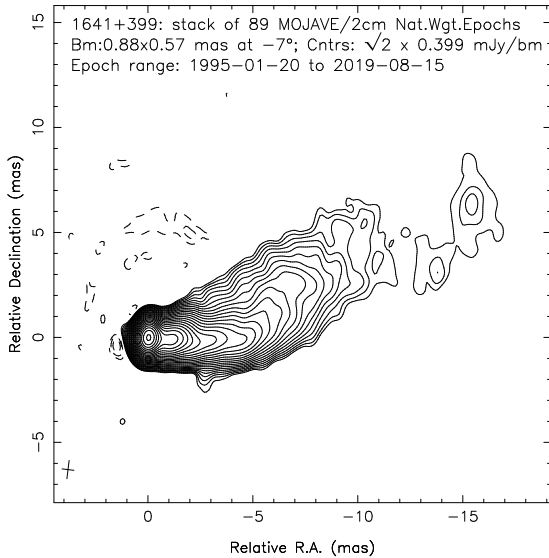


Figure 1.20: Stacked VLBI image at 15 GHz from epochs between 1995 and 2019 (Credit: MOJAVE survey, Pushkarev et al. 2017b)

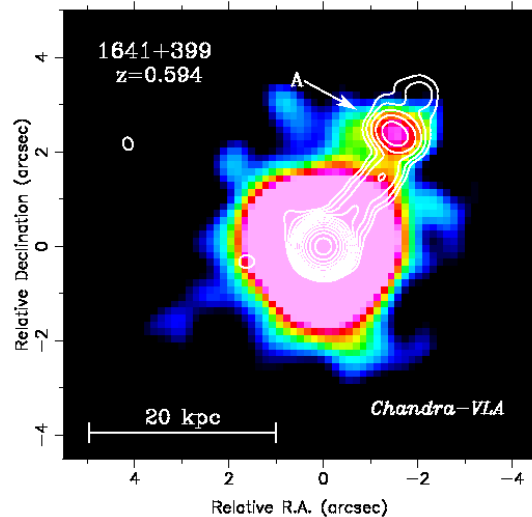


Figure 1.21: The FSRQ 3C 345 observed with the VLA at 5 GHz (logarithmic contours), overlaid onto a Chandra X-ray image (colour) (Sambruna et al. 2004).

Zensus 1999) and are responsible for a major fraction of the X-ray (Unwin et al. 1997) and γ -ray (Schinzel et al. 2012) emission.

3C 345 is known to be strongly variable. This behaviour was first noted at 8 GHz (Aller and Haddock 1967) with the 26 m Peach Mountain Radio Telescope. In addition, extensive observations over a five year period at 408 MHz using the Northern Cross in Bologna, revealed that 3C 345 undergoes significant low-frequency variability (Fanti et al. 1981), along with a number of other flat-spectrum ultra-compact sources. 3C 345 is amongst the top 15% of sources in terms of its 15 GHz modulation index, $m_5 = 0.254$, in the OVRO 15 GHz monitoring program in terms of its overall long-term variability, along with all of the MASIV strong scintillators (Richards et al. 2014). The parameter m_5 describes the flux density variations in terms of their standard deviation with respect to the mean over a certain time period (see Liu et al. 2018). The OVRO light curve is shown in Fig. 1.22. The observations presented in Chapter 3 are close to a local maximum in flux density, although the source is generally in a lower state compared to previous flaring episodes.

Long-term studies (Schinzel 2011; Klare 2003) have linked the observed radio variability to the ejection of new components from the core on VLBI scales. Klare 2003 found a quasi-periodicity of ejected components on scales of 8-10 years, matching the observed flaring timescale. The variability in 3C 345 can possibly be explained by a precessing accretion disc, introduced by a binary black hole system (Lobanov and Roland 2005; Klare 2003). This scenario was also proposed for other AGN, e.g., PKS 0420-014 (Britzen et al. 2001), or OJ 287 (Valtonen et al. 2008). In general, precession in AGN can also be produced by frame-dragging near the central SMBH in the form of the Lense-Thirring effect (Bardeen and Petterson 1975). Schinzel (2011) showed that there is significant variation in the magnitude and direction of apparent speeds of different jet components, possibly explained by intrinsic acceleration as well as changes in the respective viewing angles. Also the core position was shown to vary with time, which was connected to the overall jet viewing angle and variations in the core brightness.

In the following, a flat Λ CDM cosmology with $\Omega_m = 0.3$, $\Omega_\Lambda = 0.7$ is assumed, and $H_0 = 70 \text{ km s}^{-1} \text{ Mpc}^{-1}$ (Planck Collaboration et al. 2014), so that 1 milliarcsecond (mas)

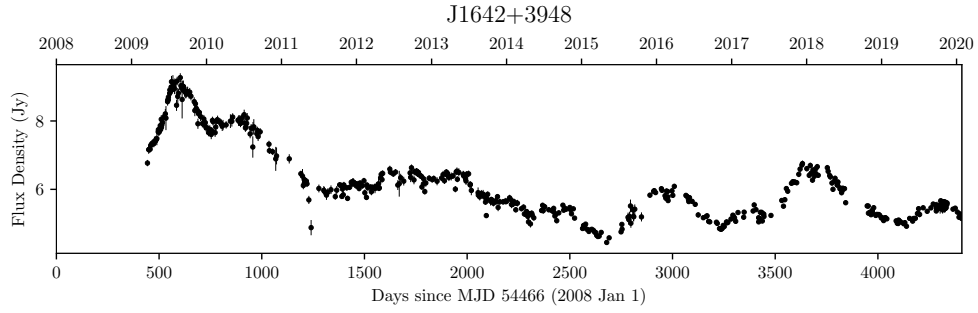


Figure 1.22: 15 GHz light curve of 3C 345 (see the OVRO archive: https://www.astro.caltech.edu/ovroblazars/data.php?page=data_return&source=J1642+3948). The observations presented in Chapter 3 were carried out in March 2016.

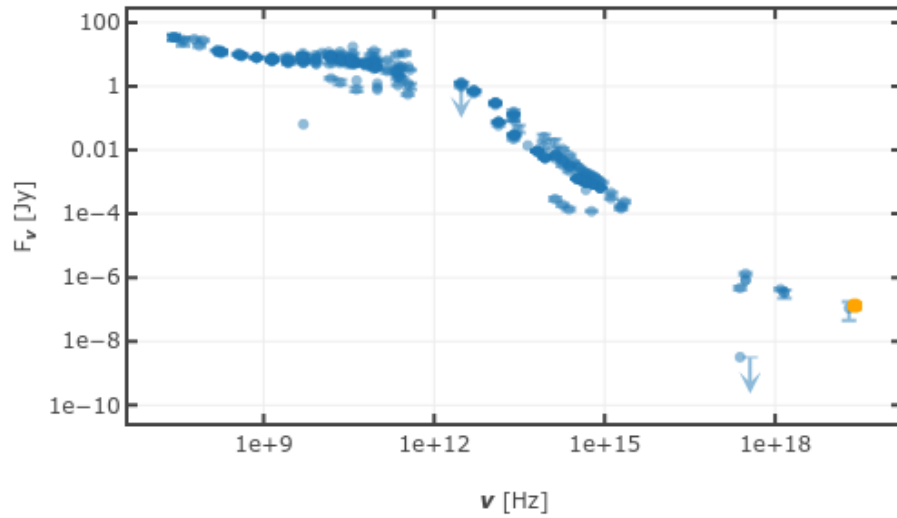


Figure 1.23: Spectral energy distribution (SED) of 3C 345. The flat spectrum at radio wavelengths is evident (from the NASA extragalactic database, visited on October 8, 2020).

corresponds to 6.6 pc projected distance for a redshift of $z = 0.593$ ($D_A = 1.37$ Gpc) (Marziani et al. 1996) for 3C 345.

Chapter 2

Very-long-baseline interferometry

In this chapter I will give an overview over the basic principles of data acquisition and processing in very-long-baseline interferometry (VLBI), which is the main observational technique used for this thesis. For a more extensive treatment of the topic, which is beyond the scope of this work, I refer the reader to e.g., Felli and Spencer (1989) or Thompson et al. (2017, Chapter 9).

2.1 Fundamentals of radio astronomy

Radio astronomy is the branch of astronomy that studies celestial objects in the radio frequency regime of the electromagnetic spectrum. As is shown in Fig. 2.1, the radio regime provides the advantage that the atmosphere is not opaque at this frequencies, so one can observe celestial bodies using facilities on the ground. The limit at lower frequencies is set by the ionosphere, where absorption and scattering makes observations below ≈ 10 MHz impossible. In addition, at lower frequencies, radio-frequency interference (RFI) from artificial, man-made signals disturb radio observations. At higher frequencies, molecular absorption in the troposphere is limiting the observing window at > 300 GHz. Between those frequencies, one still has to cope with the atmospheric contribution to the observed signal. At mm-wavelengths, water vapour and oxygen absorption lines already contribute significantly (see Fig. 2.2).

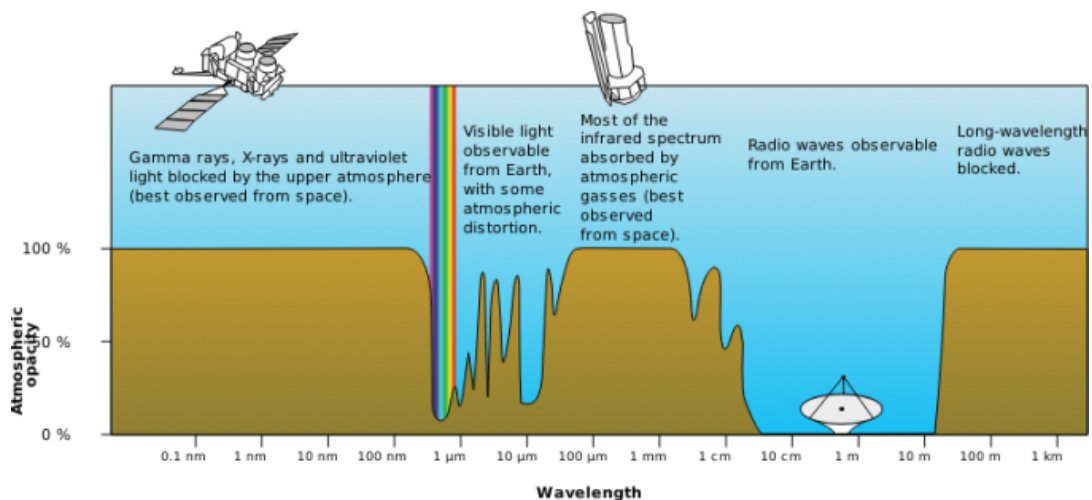


Figure 2.1: Atmospheric transparency as a function of wavelength. Radio waves are largely unaffected (Credit: <https://gisgeography.com/atmospheric-window/>).

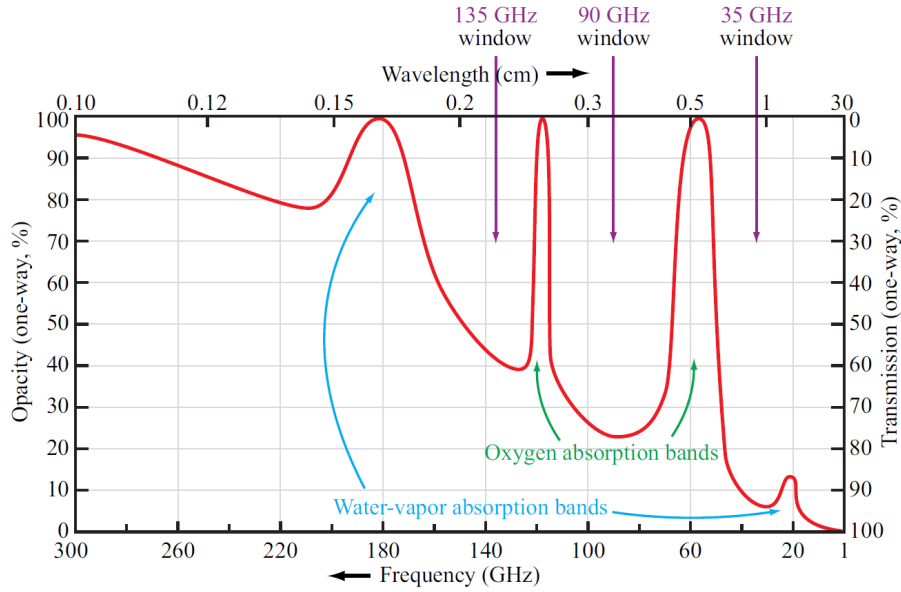


Figure 2.2: Atmospheric transparency in the radio frequency regime (from Ulaby et al. 2014).

Fundamentally, a radio telescope will measure the radiated power from a source, where the energy is given by the magnitude of the Poynting flux $|\vec{S}| \propto |\vec{E}|^2$.

This energy is measured per unit time, unit surface, and unit frequency, which defines the flux density

$$S_\nu = \frac{E}{dt dA d\nu} \quad (2.1)$$

The term density refers to a spectral density in this case. Signals in radio astronomy are usually small, so for the flux density the unit Jansky is used, where $1 \text{ Jy} = 10^{-26} \text{ W m}^{-2} \text{ Hz}^{-1}$. The power density P_ν is then:

$$P_\nu = S_\nu \cdot A_{\text{eff}}, \quad (2.2)$$

where A_{eff} is the effective telescope area. Ideally, it would correspond to the geometrical surface area, but it will be reduced by the aperture efficiency, limited by several factors. Integrating over the bandwidth $\Delta\nu$, it yields:

$$P = 0.5 \cdot S_\nu \cdot A_{\text{eff}} \cdot \Delta\nu, \quad (2.3)$$

where the factor 0.5 comes in as one integrates over all polarisation states, assuming the receiver is a dipole (which is only sensitive to one polarisation). In the Rayleigh-Jeans limit, the receiver measuring a power P will behave as a black-body with temperature T_A :

$$P = k_B \cdot T_A \cdot \Delta\nu. \quad (2.4)$$

This is the Nyquist law, describing the noise power of a resistor with temperature T_A . Taking Eq. 2.3 and 2.4, we get:

$$S_\nu = \frac{2k_B}{A_{\text{eff}}} \cdot T_A. \quad (2.5)$$

In other words, a radio receiver measures an increase in temperature due to the incoming radiation.

Generally, T_A will also encompass any contribution of signals that are received by the telescope. The total *system temperature* T_{sys} is given as

$$T_{\text{sys}} = T_{\text{R}} + T_A \quad (2.6)$$

$$T_{\text{sys}} = T_{\text{R}} + T_{\text{S}} + T_{\text{atm}} + T_{\text{g}}, \quad (2.7)$$

where T_{R} is the receiver temperature. T_A is composed of the source brightness temperature T_{S} , the atmospheric temperature T_{atm} and the ground temperature T_{g} . Radio receivers can be cooled down to some tens of Kelvin with cryogenics to minimise thermal noise. The contribution of the ground and the atmosphere greatly depends on the general observing conditions and the observing frequency. To give an example of the contribution of the source to the signal, at 1 Jy it will increase the temperature of a receiver on a 76 m telescope by about 1 K. So detect such sources, one has to integrate the signal over time. The signal strength will increase compared to the noise terms, which in turn decrease according to the radiometer formula:

$$\Delta T = \frac{T_{\text{sys}}}{\sqrt{\Delta\nu \cdot \tau}}, \quad (2.8)$$

where τ is the integration time. When estimating the noise level, Eq. 2.8 is often also given as the baseline sensitivity ΔS , depending on the system equivalent flux density (SEFD):

$$\Delta S = \frac{\text{SEFD}}{\sqrt{\Delta\nu \cdot \tau}}. \quad (2.9)$$

It is necessary to define the telescope gain G . Any receiver has a directional sensitivity, with the simplest receiver being a dipole. The telescope gain is defined as the ratio between the power that is radiated in a certain direction to the power radiated in that direction by an isotropic radiator. This translates to the ratio of the solid angle covered by a whole sphere to the solid angle of the antenna beam. Any optical system is diffraction-limited, giving rise to a specific antenna beam pattern for a radio telescope, visualised in Fig. 2.3. The angular resolution is given by the FWHM of the main lobe of the beam pattern:

$$\theta = \frac{\lambda}{D}, \quad (2.10)$$

where D is the diameter of the optical system, in our case the telescope diameter. The telescope gain thus becomes:

$$G = \frac{4\pi}{\theta} = \frac{4\pi D^2}{\lambda^2} = \frac{4\pi}{\lambda^2} \cdot A_{\text{eff}}. \quad (2.11)$$

So the telescope gain effectively modifies the effective telescope area used in Eq. 2.5. For a more detailed review of radio astronomical receivers, see Klein (2014).

2.2 Basic principles of interferometry

The resolution of a single radio telescope is limited by Eq. 2.10. Due to the large wavelengths and the engineering limit on the telescope size, a maximum angular resolutions of the order of tens of arcseconds (") can be achieved. This is comparable to the capabilities of the unaided human eye for visible light. With the earliest observations of quasars, it became clear that their variability indicates very small angular sizes of these sources, that could not be resolved with conventional radio telescopes. To increase the resolution at radio wavelengths, and to make it comparable to the resolution of optical telescopes

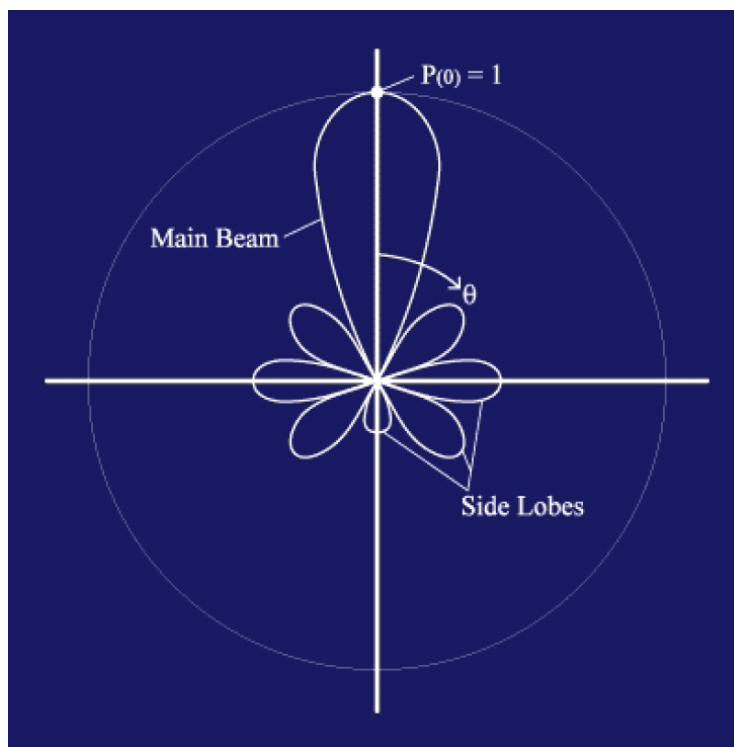


Figure 2.3: Two-dimensional beam pattern of a radio telescope. The principal resolution is defined by the FWHM θ of the main lobe in the centre (Credit: <http://www.ras.ualgary.ca/radiotel/calibration.html>, visited Sep 16th, 2020).

(about $0.015''$ with adaptive optics), radio interferometry was developed. Radio interferometry started with simple two-element interferometers with solar observations (Ryle and Vonberg 1946) and was improved in the following years. Another interesting concept that was developed at this time was the sea interferometer, where the second interferometer element was provided by the reflection of the signal from the sea's surface (Bolton and Slee 1953).

The underlying principle of this technique can be seen using the example of the basic double slit experiment, performed for the first time by Thomas Young in 1801. This was one of the first experiments to prove that light is a wave phenomenon. If one considers two wave fronts which each pass through one of the slits, they will interfere either destructively or constructively on a surface where the arriving signal is measured. This depends on their geometric delay, which in turn depends on the geometry of the experiment. For this, it is assumed that the signal is observed far away from the source of light, i.e. $D > d^2/\lambda$, with D being the object distance and d the size of the slit. This assumption is generally valid for observations of astrophysical objects that are farther away than one light year, when d is the Earth's diameter (as is the case for VLBI), at $\lambda = 1$ cm (Felli and Spencer 1989). With this interferometric technique, Michelson and Pease (1921) were able to obtain the diameters of some nearby stars from the observed interference, or fringe patterns.

This principle can be used with radio telescopes. The geometry is illustrated in Fig. 2.4. Two incoming light rays will have a geometrical delay between the two observing telescopes, which depends on the angle of the incoming light. The light rays can be assumed parallel with the far-field assumption. The time delay is then given by

$$\tau_g = \frac{\vec{b} \cdot \vec{s}}{c} = \frac{b}{c} \cos \theta \quad (2.12)$$

with θ being the angle between \vec{b} and \vec{s} . This delay causes a phase difference of $\phi = 2\pi\nu\tau_g$ between the signals. Thus, when combining the signals of the telescopes, one will observe an interference pattern. The two light signals are given by

$$V_1 = V \cdot \cos(2\pi\nu t) \quad (2.13)$$

$$V_2 = V \cdot \cos(2\pi\nu(t + \tau_g)), \quad (2.14)$$

where V_2 is delayed by τ_g . Multiplying the signals yields

$$V_1 \cdot V_2 = \frac{V^2}{2} [\cos(4\pi\nu t) + \cos(2\pi\nu(t + \tau_g))] \quad (2.15)$$

We observe a time-integrated signal, where the integration time $t_{\text{int}} \gg 1/\nu$, so that

$$\langle V_1 \cdot V_2 \rangle = \frac{V^2}{2} \cos\left(\frac{2\pi b \sin \theta}{\lambda}\right) \quad (2.16)$$

In essence, for radio interferometers, the process of multiplying and integrating is the work of the correlator, which will be explained in more details in Sect. 2.4.

Radio interferometry took off with the development of the aperture synthesis principle (Ryle and Hewish 1960; Ryle 1962), acknowledged by the first Nobel prize for astronomical research in 1974. It utilises Earth's rotation in conjunction with a multi-element interferometer. Normally, a two-element interferometer will observe a one-dimensional interference pattern. Using Earth's rotation, the angle of this simple interferometers with respect to the source will change, so one is able to measure the interference with different rotations.

Let us define these concepts mathematically. Effectively, an interferometer measures the cross-correlation of electric fields at different positions in the observer's plane, called the (u, v) -plane. u and v denote the two spatial coordinates in this plane, most times expressed in units of the observing wavelength. The eventual image, i.e., the intensity distribution I_ν in the source plane, can be obtained from Fourier transforming those complex cross-correlation coefficients, that are called visibilities, or also referred to as spatial coherence function. As in general for complex numbers, each visibility V has an amplitude A and a phase ϕ . The following relation can be derived from the van-Cittert-Zernicke theorem, where for the derivation I point the reader to Thompson et al. (2017, Chapter 15) or Taylor et al. (1999):

$$V(u, v) = \iint I_\nu(\alpha, \delta) e^{-i2\pi(u\alpha + v\delta)} d\alpha d\delta. \quad (2.17)$$

Here α and δ denote rectangular coordinates on the sky (e.g., right ascension and declination) and $i = \sqrt{-1}$ in the exponential. For the visibility measured between two telescopes with index i and j , the measured visibility V_{ij}^{obs} is

$$V_{ij}^{\text{obs}}(t, \nu) = G_i(t, \nu) G_j^*(t, \nu) V_{ij}^{\text{true}} + \sigma_{ij}, \quad (2.18)$$

where V_{ij}^{true} is the true source visibility modified by some terms. The G are the complex gains for each antenna, and σ_{ij} denotes a thermal noise term. Note that an important assumption has been made here: there is no baseline-dependent gain factor, and all gain factors are antenna-dependent. The goal of VLBI calibration is to determine those complex gain factors and retrieve the true underlying visibility. The G contain information about a multitude of factors affecting the data. These will be described in more detail in the following sections.

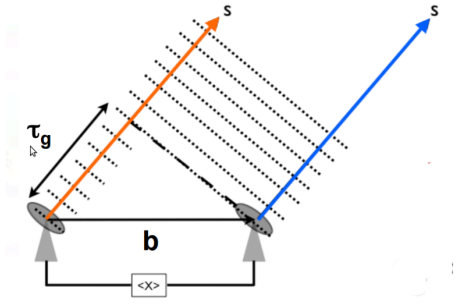


Figure 2.4: Illustration of the geometry of a two-element interferometer (Credit: IMPRS Blackboard Lectures 2014, Hans-Rainer Klöckner. Taken from Boccardi (2015)).



Figure 2.5: Very Large Array in Socorro, New Mexico, USA (Credit: Dave Finley courtesy of NRAO/AUI).

A simple two-dimensional baseline is sensitive to only one Fourier component of a given source, i.e. it is sensitive to only one spatial scale. In a multi-element interferometer with measurements at a multitude of baselines (numbering $n(n-1)/2$, where n is the number of telescopes), the (u, v) -plane can be filled to a degree that the source brightness distribution can be reconstructed. Due to the Earth's rotation, baseline projections also rotate in the (u, v) -plane, which is crucial for proper image reconstruction. An ideal interferometer would fill the whole (u, v) -plane, but in reality telescopes are not placed everywhere. This leads to gaps in the (u, v) -coverage, and thus uncertainties in the image reconstruction. The implications of those drawbacks will be further explained in Sect. 2.7.

2.3 VLBI

VLBI is the extension of conventional radio interferometry using connected element interferometers. It uses arrays of telescopes around the world on different continents, providing baselines up to $\lesssim 1 D_{\oplus}$ (i.e., $\sim 12,000$ km). As for any other interferometer, the angular resolution θ only depends on the observing wavelength λ and the maximum distance between telescopes, or baselines (D) as $\theta \approx \lambda/D$. The major difference to conventional interferometers is that, for VLBI, the telescopes operate without any communication in real time among each other, as they are not physically connected. Rather, their signals are recorded on hard drives with accurate time stamps for later correlation at a central computing facility.

The first successful VLBI observations have been conducted as early as 1967 by US and Canadian groups. This was only possible due to the development of precise clocks and tape recording systems at that time. With that, baselines up to 3000 km were reached, allowing for an angular resolution of $0.02''$. Since then, substantial improvements have been made in instrumentation and techniques. Today there are several dedicated VLBI arrays, e.g. the Very Long Baseline Array (VLBA) in the USA, which has been build between 1986 and 1993 and consists of ten equal 25-m antennas. To improve on angular resolution, the VLBI technique has been further developed over decades to work in the mm-wavelength regime, e.g., with the Global Millimeter VLBI array (GMVA) at 86 GHz, and with the state-of-the-art Event Horizon Telescope (EHT) at 230 GHz (soon expected at 345 GHz), which produced the first image of a black hole shadow (Event Horizon Telescope Collaboration et al. 2019a). VLBI arrays such as the GMVA or the EHT work with the contribution of individually run telescopes, which operate together for VLBI in sessions, but are used for other purposes as well.

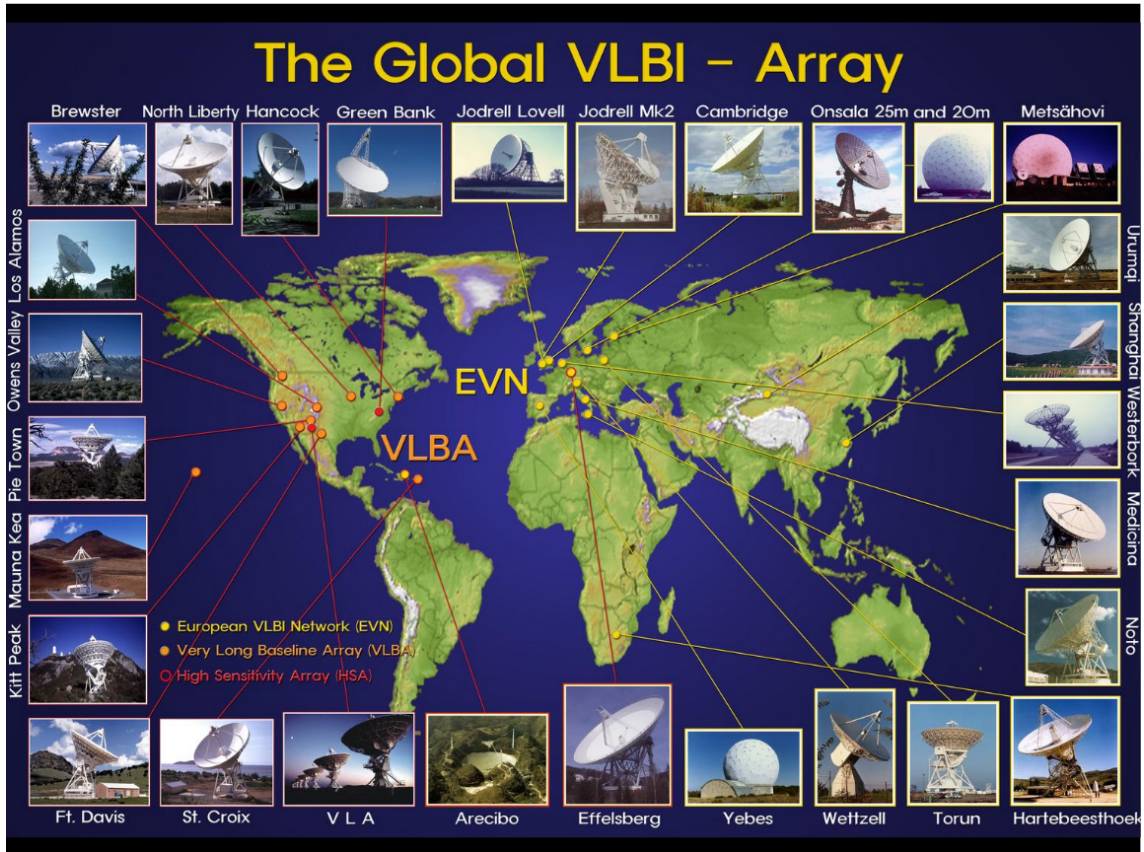


Figure 2.6: Two global VLBI arrays (the VLBA in the USA and the European VLBI network) depicting many of the different radio telescopes used for VLBI around the world (Credit: T. Krichbaum, MPIfR).

2.4 Correlation

For VLBI, after the data have been acquired at each telescope, the signals are post-processed at a special-purpose computer, called correlator. It takes the digitized signals (i.e., voltages) from the telescopes and multiplies them with each other, which then outputs the complex correlation coefficients as a function of time and frequency. No substantial averaging in neither frequency nor time is made at this point because slopes of the phase as function of time and frequency still exist. This is due to uncertainties in the initial correlator model that searches the two-dimensional space of delay and rate for the signal, or fringes. The delay is the derivative of the phase with frequency:

$$\tau = \frac{d\phi(t, \nu)}{d\nu} \quad (2.19)$$

and is visible as a phase slope when looking at the visibility phases as a function of frequency. This delay corresponds to the geometrical delay as explained in Sect. 2.2. The delay rate, or fringe rate, or short just rate, is defined as the derivative of the phase with time:

$$r = \frac{d\phi(t, \nu)}{dt}. \quad (2.20)$$

The delay τ has values of the order of ns, while the rate r is usually measured in mHz. Fringes will appear as isolated peaks in this two-dimensional space. For this initial fringe search at the correlation stage, one needs a bright source as fringe finder, so that fringes

can be detected in real time to determine the relative station clock-offsets a priori. To find the fringes, the correlator assumes a correlator model which includes the geometry of the array and several other parameters.

Errors in the initial correlator model include factors such as errors in the telescope or source positions, residual atmospheric delays or uncertainties caused by different frequency standards used at each telescope. The slopes in phase as function of phase and time prevent coherent averaging of the data, which is important to detect weaker sources and to make the data easier to handle for later imaging. These slopes can be removed by post-processing of the data during the fringe fitting stage.

2.5 Amplitude calibration

The amplitudes of the correlator output are the ratios of correlated power to noise power. Generally, for VLBI observations, these amplitudes can not be converted to flux density in Jy with observations of calibrators as it is done for single-dish telescopes and connected interferometers. This is because virtually all sources observed are resolved by VLBI. Instead, the amplitudes are calibrated using the system temperatures T_{sys} recorded at each telescope. For weak sources, T_{sys} is dominated only by source-independent quantities and can therefore be used for calibration of the measured amplitudes. For strong sources, the zero-spacing flux density should be known and set during the calibration as T_{S} may start so contribute significantly.

For the visibility V_{ij} with amplitude A_{ij} , similarly to Eq. 2.5, it holds:

$$S_{ij} = A_{ij} b \sqrt{\frac{T_{\text{sys},i} T_{\text{sys},j}}{G_i G_j}}, \quad (2.21)$$

where S_{ij} now is the correlated flux density in Jy, and G is the telescope gain in K/Jy, as defined with the factor preceding T_{A} in Eq. 2.5. The parameter b is a factor that accounts for additional digitization losses, bandpass effects, etc. So, given the T_{sys} and gain curves measured at each telescope, one can calibrate the amplitudes.

2.6 Fringe fitting

In the first stage of fringe fitting, the space of delay and rate is searched more exhaustively for the fringe peaks. Generally, one searches for fringes within a specified search range in both delay and rate, which has been more broadly constrained during the correlation stage. One chooses a time interval over which to search for solutions, and this time interval has to characterise the phase variations sufficiently. In general, this time interval is limited by the atmospheric coherence time. The signal-to-noise ratio (SNR) of solutions will increase with solution interval, but only until the coherence time is reached.

The solutions from this first coarse fringe search will then be used as priors for a least-squares fit. For this, an initial model of the source is required. Then one can make use of Eq. 2.18, substituting the true visibilities with the assumed model. In most cases, a point source model is assumed, but one can use more sophisticated source models, if available.

The fringe fitting solves for the parameters of $N - 1$ antennas, as there is no absolute reference for the phases. One of the antennas is then used as a reference antenna, where the phases are set to an arbitrary value, usually zero for convenience. Because of this arbitrary shift in phases, the absolute positional information of the source is lost in the process. For a more detailed insight into fringe fitting, I refer the reader to Schwab and Cotton (1983).

2.7 Imaging

After the data have been calibrated so that residual phase slopes in both time and frequency have been removed, the data can be coherently averaged in frequency. After reducing the file size significantly, the data are ready for being imaged.

For imaging, two problems have to be taken care of: There are still residual complex gain errors present in the data, and the image will contain noise added by the convolution with the *dirty* beam. The dirty beam refers to the beam of the interferometer, which is obtained by Fourier transforming the (u, v) -sampling. If this sampling is sparse, the Fourier transform will cause strong sidelobes in the dirty beam.

To address both of these issues, a *hybrid imaging* approach is applied. It consists of sequential steps of deconvolution and self-calibration.

2.7.1 Deconvolution

One of the most successful and widely used deconvolution algorithms is the **Clean** algorithm (Högbom 1974; Clark 1980). For calculating the true brightness distribution $I(\alpha, \delta)$ from the visibilities, one needs a non-linear deconvolution algorithm because the number of samples of the visibility function is incomplete. In the following, I describe the use of **Clean** as it is incorporated into the software **Difmap** (Shepherd 1997), which was mainly used for this thesis.

Clean first finds the pixel of the dirty map with the highest flux density, where it will not care whether this maximum is positive or negative. The pixel value of this δ component is multiplied by a **Clean** gain factor, convolved with the dirty beam, and then subtracted from the map. This way the component is effectively removed from the dirty map and stored in the model, leaving a residual map with which the process can be repeated. This is done until the residual map looks uniform and the residual map noise is approaching the expected thermal noise. In reality, the thermal noise level is normally not reached due to uncertainties in the antenna gains. An obvious disadvantage of **Clean** in comparison to other deconvolution algorithms is that it is not very sensitive to extended structure, and due to the nature of extracting δ components it might introduce artificial substructure in the image.

In between **Clean** runs, when some of the flux has been extracted from the map, a step of self-calibration is applied.

2.7.2 Self-calibration

Even after the calibration steps explained in Sect. 2.5 to 2.6, residual gain errors are still present in the data. These are compensated for by using self-calibration. In this step the visibilities are calibrated against a fiducial source model, so that the difference

$$S = \sum_k \sum_{ij} w_{ij}(t_k) [V_{ij}^{\text{obs}}(t_k) - g_i(t_k) g_j^*(t_k) V_{ij}^{\text{mod}}(t_k)] \quad (2.22)$$

is minimised. One can set the weights w_{ij} during self-calibration to e.g., weigh down poorly calibrated stations, so that their visibilities affect less the calibration of the other telescopes.

Self-calibration will calibrate the complex visibilities with constraints on the closure quantities with the current model of the source. Following Eq. 2.18, the phases between two antennas will be given by

$$\phi_{ij}^{\text{obs}} = \phi_{ij}^{\text{true}} + \phi_i - \phi_j + \sigma_{ij}^{\phi}. \quad (2.23)$$

For any closed loop of three antennas, the antenna-dependent quantities in Eq. 2.23 will cancel, defining the closure phase Φ as

$$\Phi = \phi_{ij}^{\text{obs}} + \phi_{jk}^{\text{obs}} + \phi_{ki}^{\text{obs}} \quad (2.24)$$

$$= \phi_{ij}^{\text{true}} + \phi_{jk}^{\text{true}} + \phi_{ki}^{\text{true}}. \quad (2.25)$$

So the closure quantities are robust against the phase errors of individual antennas. In any observation with n antennas, there will be $(n-1)(n-2)/2$ closure phases, which constrains a source model well for sufficiently large n . During cleaning and self-calibration, the closure quantities work as a constraint, although they are not used for imaging directly in `Difmap`. Other imaging algorithms exist that make explicit use of only closure quantities for imaging¹. It is possible to introduce false structure in the data, by cleaning side lobes in the image and freezing that into the model by self-calibration. Therefore, special care has to be taken during self-calibration. One way to avoid false structure is to monitor how well the model fits the closure quantities.

In the case that all residual gain errors can be corrected for, the noise in the resulting image will approach the theoretical thermal noise limit:

$$\sigma_{\text{I}} = \frac{\text{SEFD}}{\eta \sqrt{N_{\text{pol}} N (N-1) \tau \Delta\nu}}. \quad (2.26)$$

The factor η denotes the correlator efficiency (accounting mainly for digitisation losses), N_{pol} is the number of polarisations observed (see Sect. 2.9) and N is the number of antennas.

In general, solving for these complex gains using self-calibration requires high SNR , so for weak sources, another method can be used, which is referred to as phase referencing. This will be explained in more detail in Sect. 6.1.

2.8 Space VLBI

In the quest for increasing angular resolution, the idea to use a space radio telescope (SRT) in conjunction with ground-based telescopes first arose as early as in the 1970s. Already in 1980, the foundations for the planning of the *RadioAstron* project were made.

The first dedicated space-VLBI program was the VLBI Space Observatory Program (VSOP), that operated from 1997 until 2003. It used the *HALCA* satellite that was equipped with an 8-m antenna. The satellite was in an elliptical orbit around Earth with a period of 6.3 h and a major axis of 28,000 km. It observed at wavelengths of 6 and 18 cm (Hirabayashi et al. 1998; Hirabayashi et al. 2000).

RadioAstron was the successor of VSOP. It used the *Spektr-R* spacecraft (see Fig. 2.7), which was launched from the Baikonur cosmodrome on July 18, 2011, and was equipped with a 10-m dish. The observing frequencies were centred at 0.32, 1.6, 4.8, and 22 GHz, and at 0.32, 1.6, and 22 GHz the antenna can observe in full polarisation. It followed a highly elliptical orbit with a major axis of $\sim 360,000$ km corresponding to $\sim 30 D_{\oplus}$. The SRT was tracked by ground tracking stations such as the Pushchino Radio Astronomy Observatory (PRAO), as the orbital parameters of the spacecraft have to be known to a high enough precision to detect fringes. The tracking station sent a phase-stable reference signal synchronized by a hydrogen maser to the spacecraft, and received the coherently converted response signal from it. This way the phase difference and residual Doppler shift could be measured. The tracking stations were also used to establish the data link to the SRT for the acquisition of the data on the ground.

¹An example is `eht-imaging` (<https://github.com/achael/eht-imaging/>)

Among many compact radio-emitting objects such as pulsars or molecular maser sources, *RadioAstron* aimed at probing the innermost regions of AGN jets, that are not accessible with ground-based VLBI. Bruni et al. (2020) describe the different imaging programs with *RadioAstron*. First test observations began in September 2011. During the Early Science Program, Lobanov et al. (2015) first showed the unique polarization capabilities of the spacecraft by imaging the high-redshift quasar TXS 0642+449.

As of February 2019, the spacecraft stopped responding, and after several failed attempts to re-establish communication, the observations officially ended in May 2019.



Figure 2.7: *Spektr-R* spacecraft with 10-m antenna (From the *RadioAstron* user handbook).

2.9 Polarisation measurements

For VLBI, mostly receivers are used that are sensitive to circular polarization. When calibrating and analysing VLBI data, the four different correlations of right hand (*R*) and left hand (*L*) circularly polarized feeds are used. We also conveniently call back on the four Stokes parameters (see Sect. 1.4) here, which completely define any polarization state of an electromagnetic wave as a function of the receiver responses:

$$I = 0.5 (RR + LL) \quad (2.27)$$

$$Q = 0.5 (RL + LR) \quad (2.28)$$

$$U = 0.5 i(LR - RL) \quad (2.29)$$

$$V = 0.5 (RR - LL) \quad (2.30)$$

Here *RR* and *LL* denote the autocorrelation of *R* (RCP) and *L* (LCP), *RL* and *LR* their cross-correlations, and $i = \sqrt{-1}$. For details I refer to Felli and Spencer (1989).

If one wants to calibrate all polarisation states in an observation, Eq. 2.18 takes the form of:

$$\mathbf{V}_{ij}^{obs} = \mathbf{J}_i \cdot \mathbf{V}_{ij}^{true} \cdot (\mathbf{J}_j)^H, \quad (2.31)$$

where H is the Hermitian transpose of the matrix, J is the Jones matrix \mathbf{J} defined as:

$$\mathbf{J} = \begin{pmatrix} G_R & 0 \\ 0 & G_L \end{pmatrix} \cdot \begin{pmatrix} 1 & D_R \\ D_L & 1 \end{pmatrix} \cdot \begin{pmatrix} e^{i\phi} & 0 \\ 0 & e^{-i\phi} \end{pmatrix}. \quad (2.32)$$

The gains G summarize all gains for *R* and *L* in a diagonal matrix (meaning they commute), the second matrix is for the polarisation leakage terms, and the third one is for parallactic angle (ϕ) correction. The latter is only diagonal for circular feeds, which is one of the reasons that VLBI observations generally make use of those instead of linear feeds. The true visibility matrix in Eq. 2.31 is the Fourier transform of the brightness matrix \mathbf{S} :

$$\mathbf{V}_{ij}^{true} = \int \mathbf{S} \cdot e^{-\frac{2\pi}{\lambda}(u\alpha + v\delta)} d\alpha d\delta, \quad (2.33)$$

where \mathbf{S} is, for linear feeds

$$\mathbf{S} = \begin{pmatrix} I + Q & U + iV \\ U - iV & I - Q \end{pmatrix}, \quad (2.34)$$

or, for circular feeds

$$\mathbf{S} = \begin{pmatrix} I + V & Q + iU \\ Q - iU & I - V \end{pmatrix}. \quad (2.35)$$

The major issue with polarimetric data calibration is the leakage matrix in Eq. 2.32. The matrix is not diagonal and thus does not commute with the other gain matrices. For that reason it has to be corrected for at the end of the calibration pipeline. Several methods exist for determining the leakage (or D -terms), and I will briefly describe the one that will be used for the calibration described in Chapter 4. A more extensive description can be found in e.g., Smirnov (2011).

First a source model in Stokes I is needed, that is then subdivided into several sub-components. Then one makes the important assumption of self-similarity: namely that the fractional polarisation in each of those sub-components is constant. That means:

$$Q = \sum_i^N q_i I_i \quad \text{and} \quad (2.36)$$

$$U = \sum_i^N u_i I_i, \quad (2.37)$$

with N being the number of sub-components. Then Eq. 2.31 is minimised with the assumptions just made, with the parameters being the complex leakage terms D_L and D_R in Eq. 2.32 for each antenna, and the q_i and u_i in Eq. 2.36 and 2.37. So effectively, with the other gains calibrated, the function to be minimised reduces to:

$$\chi^2 = \sum_m^N w_m |RL_{kl,m} - (Q + iU)_m|^2 + \sum_m^N w_m |LR_{kl,m} - (Q - iU)_m|^2, \quad (2.38)$$

where w_m are the visibility weights. The implicit assumption of Stokes $V = 0$ is made here. In the vast majority of cases, this assumption is valid, as Stokes V is a small fraction of Stokes I of less than 1%. For example, Thum et al. (2018) find average levels of 0.5% at mm-wavelengths in a sample of 37 AGN, arguing that this fractions should not depend strongly on wavelength. In general, determining Stokes V depends much more on calibration errors due to its small magnitude in AGN jets, and the observations presented here do not provide sufficient quality for such an analysis. Thus I will not go into further details about circular polarisation in this thesis.

It should be noted that for complex polarised structure, the self-similarity assumption might break down, and introduce more uncertainties in the D -terms. This might happen when sources are resolved with VLBI, so care must be taken in the determination of the appropriate sub-models in Stokes I .

Chapter 3

Observations, calibration and data reduction

Parts of this Chapter have been published in Pötzl et al. (2018) and Pötzl et al. (2021).

This chapter provides an overview of the observations, data acquisition, and the necessary steps in calibrating the data. After these data reduction steps, the data are ready for imaging, which will be described in Chapter 4.

3.1 Observations of 3C 345

The quasar 3C 345 was observed with *RadioAstron* on March 30th and 31st, 2016, where the SRT complemented an array of eighteen ground antennas. The participating antennas are listed in Table 3.1 with some of their basic properties. Six more stations should have been observing, but had technical problems (Badary (BD), Mauna Kea (MK), Onsala (ON25), Sheshan (SH), Urumqi (UR) and Westerbork (WB1)).

The data were recorded in dual-polarisation mode (Right-hand circular (RCP) and Left-hand circular (LCP) polarisation), with four intermediate frequency bands (IFs) of 16 MHz bandwidth each, yielding 64 MHz total bandwidth for the ground stations, and two IFs for the SRT, yielding 32 MHz bandwidth. The data were correlated with the space-VLBI dedicated version of the DiFX software correlator, developed and run at the MPIfR in Bonn (Bruni et al. 2016).

3.2 Calibration

After correlation, the data were further processed and calibrated in AIPS¹ (Greisen 2003), which is comprised of different *tasks* for the individual calibration and imaging purposes. The overall calibration procedure can be examined in Fig. 3.1, and a more detailed description of the most important steps will be presented in this section.

3.2.1 Amplitude calibration

The T_{sys} measurements have been collected from the different telescopes together with their gain curve values, and were then used to produce a file that could be read by the task ANTAB. This created TY and GC tables, which can subsequently be used by the task APCAL. This task calibrates the amplitude according to the values in the TY and GC tables.

¹Astronomical Image Processing Software of the National Radio Astronomy Observatory, USA; <http://www.AIPS.nrao.edu/index.shtml>

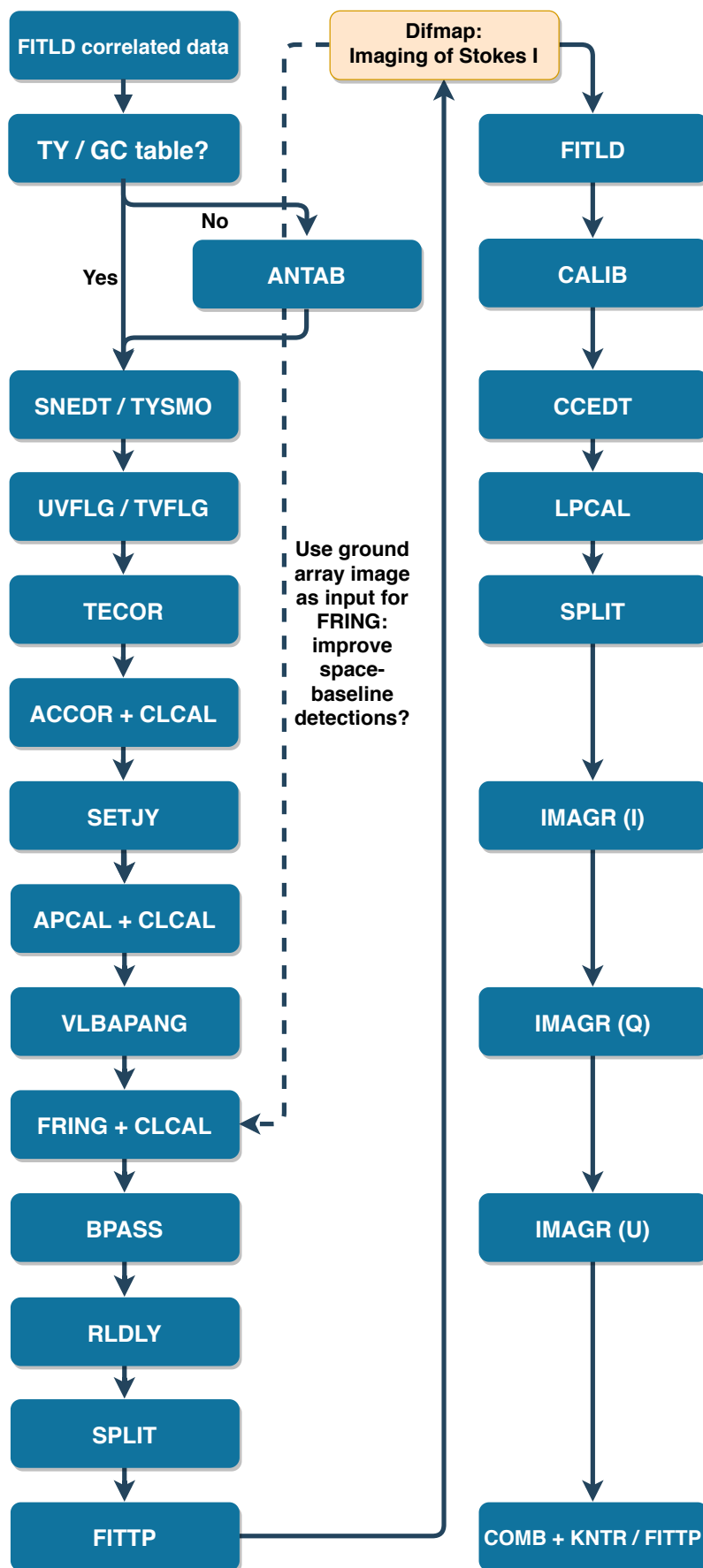


Figure 3.1: Calibration scheme for *RadioAstron* (and other VLBI) data in AIPS and Difmap. For ground-array only data, the intermediate step of first imaging the ground array and then doing a second fringe-fit for the space baselines is naturally omitted.

Table 3.1: List of antennas participating in the *RadioAstron* observations.

(1) Antenna	(2) Abbreviation	(3) Location	(4) Array	(5) SEFD [mJy]	(6) Diameter [m]
Brewster	BR	USA	VLBA	282	25
Effelsberg	EF	Germany	EVN	19	100
Fort Davis	FD	USA	VLBA	314*	25
Green Bank	GB	USA	...	10	100
Hartebeesthoek	HH	South Africa	EVN	430	26
Hancock	HN	USA	VLBA	324	25
Jodrell Bank Mark II Telescope	JB	UK	EVN	320*	38
Kitt Peak	KP	USA	VLBA	271	25
Los Alamos	LA	USA	VLBA	314*	25
Medicina	MC	Italy	EVN	700	32
North Liberty	NL	USA	VLBA	324	25
Ovens Valley	OV	USA	VLBA	354	25
Pie Town	PT	USA	VLBA	281	25
<i>Spekt-R</i> SRT	R2	USA	...	2840	10
Robledo	RO	Spain	EVN	35*	70
Saint Croix	SC	USA	VLBA	304	25
Svetloe	SV	Russia	EVN	360	32
Torun	TR	Poland	EVN	300	32
Zelenchukskaya	ZC	Russia	EVN	300	32

NOTE: Columns indicate (1) Antenna name, (2) name abbreviation, (3) Antenna Location, (4) Array Name, (5) System Equivalent Flux Density (from Lobanov et al. (2015) and Vega-García et al. (2020), and *the EVN calculator) and (6) Antenna Diameter.

For most antennas, T_{sys} measurements were made at sufficiently short time intervals to give a good a-priori calibration of the amplitudes. Nevertheless, I encountered several problems in the amplitude calibration. For many VLBA stations, there was considerable scatter in T_{sys} for IF 1. For Jodrell Bank, T_{sys} ranging from a few 100 to a few 1000 K were found with large scatter, which is unrealistic, and points to some problems in the T_{sys} measurements at the telescope. For Green Bank (GB), about 10 times higher values for LCP were seen compared to RCP. The origin of this issue was clarified with the GB telescope later. On January 26, 2016, a change in the receiver backend was made, apparently requiring the installation of longer cables on January 29. After that, they noted T_{sys} of several 100 K in LL correlation. They found that to be due to the cables introducing a 90° phase shift, leading to almost zero values of LL. This problem lasted until May 5, 2016, so it was existent at the time of our observations. It was tried to compensate that by using the T_{sys} values for RCP also for LCP.

The data from Robledo (RO) also showed some interesting behaviour, as the amplitudes for RR and LR showed virtually zero amplitude for IF 2 and 3, while for LL and RL the same was true for IF 1 and 4. In addition, no T_{sys} values were available, so default values of 35 K were used. This is also what may have led to the amplitude problems. Subsequently, these IFs were flagged in the respective polarisation product, and the station would show to not be usable overall in the subsequent analysis.

For Svetloe (SV) and Zelenchukskaya (ZC) the cadence of T_{sys} measurements was too low, so median values were used. The a-priori amplitude calibration of these two stations was particularly insufficient, as the imaging stage showed later. At all stations, some clear outliers in T_{sys} could already be flagged with the task `SNEDT` or smoothed out with `TYSMO` at this stage.

After the inspection of T_{sys} , the data were corrected for digitisation losses by the AIPS task ACCOR. These amplitude corrections were within a few %, as expected. Then the source zero-spacing flux is set with the task SETJY to 6.67 Jy as measured at the Effelsberg telescope on the day of the *RadioAstron* observations (see Table 4.1). This compensates for the contribution of the source to T_{sys} as outlined in Chapter 2.5.

Subsequently, APCAL was run, where one has the option to correct for atmospheric opacity. This correction was found to be minor, and I could proceed to the fringe fitting stage.

3.2.2 Fringe fitting

The delay-rate space was searched for fringes first for the ground-array only with the task FRING. At 1.6 GHz, this usually is pretty straightforward for VLBI, and standard parameters were used. As has been done for *RadioAstron* data previously (e.g., Gómez et al. 2016; Giovannini et al. 2018), I used the ground-array data to create a preliminary image of the source. This image was then used as further input for FRING. In addition, the fully gain-calibrated visibility data from the ground array were used. Then the parameter DOFIT was set to search for fringe solutions only for the SRT baselines. One could expect a better SNR and thus an increasing number of good fringe solutions for the SRT, as has been reported previously. However, no significant improvements were observed in my results. For both cases, a limit for accepted solutions of SNR = 6 was set. Finally, it was decided to use the results from the initial global fringe fit, which provides good solutions for baselines up to nine earth diameters ($9 D_{\oplus}$) with a solution interval of 7 min. The reference antenna used was Effelsberg (EF), as it is one of the most sensitive telescopes in the array and was present during the whole observing time. Only for two of the 7 min intervals there were no fringe detections, showing SNR ~ 3 . Different solution intervals, reference antennas and delay/rate windows were tried, but this result could not be improved. Figures 3.3 and 3.4 show the amplitudes and phases as a function of frequency before and after fringe fitting for selected ground-space baselines.

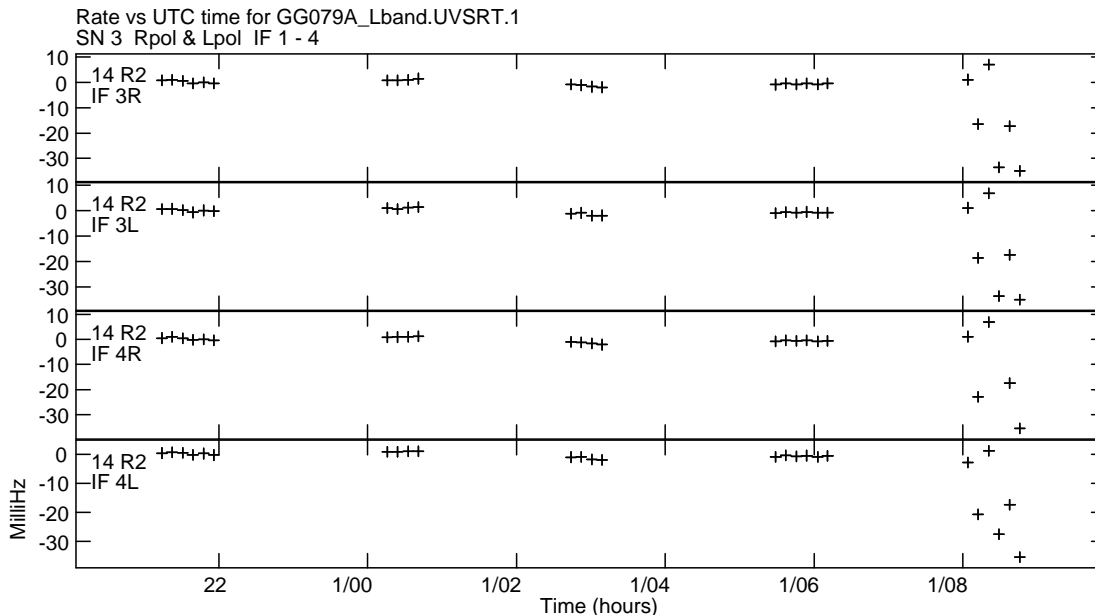


Figure 3.2: Fringe rate as a function of time during the observations for the SRT. Note the stronger time-dependence of the rate during the later scans, which corresponds to the perigee of the SRT. A solution interval of 7 min allowed the detection of fringes for the longest baselines, while at the same time not observing significant decorrelation at the short baselines due to the non-modelled acceleration terms of the SRT.

Since the space antenna is accelerating quickly during the perigee, there might be a time-dependent phase rate. For long solution intervals, one might notice decorrelation of the signal as the phase changes become too rapid due to the non-modelled acceleration term. Figure 3.2 shows the rate changes during perigee at the last scans of the observations. Due to the described effect, different and increasing solution intervals were tested, and increasingly more fringes were detected for the earlier scans with larger intervals. With the finally chosen solution interval of 7 min, no significant decorrelation was observed during the later scans close to the SRT perigee.

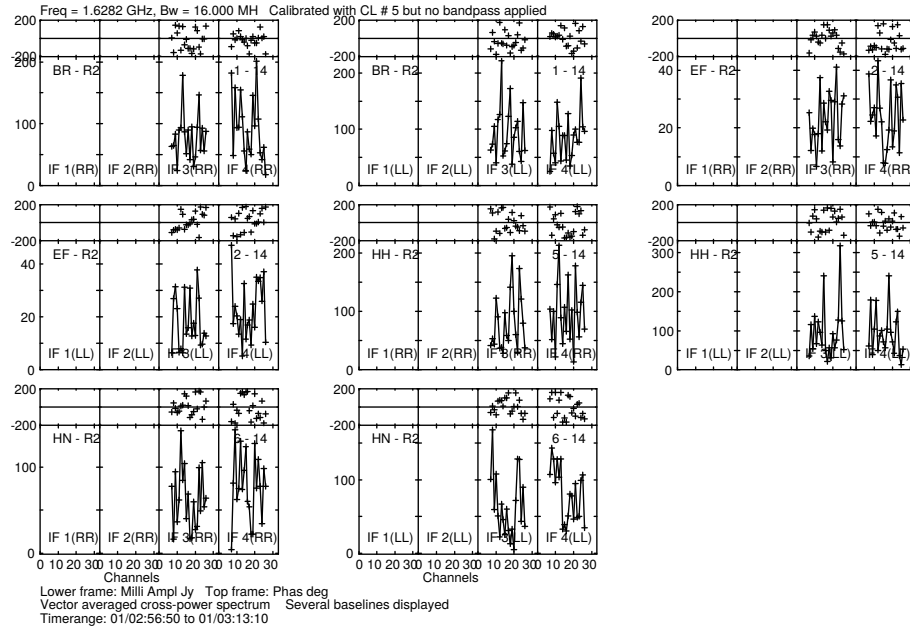


Figure 3.3: Frequency dependence of the amplitudes and phases (bottom and top panel of each individual plot, respectively) *before* fringe fitting for a few selected ground-space baselines. Compare with Fig. 3.4.

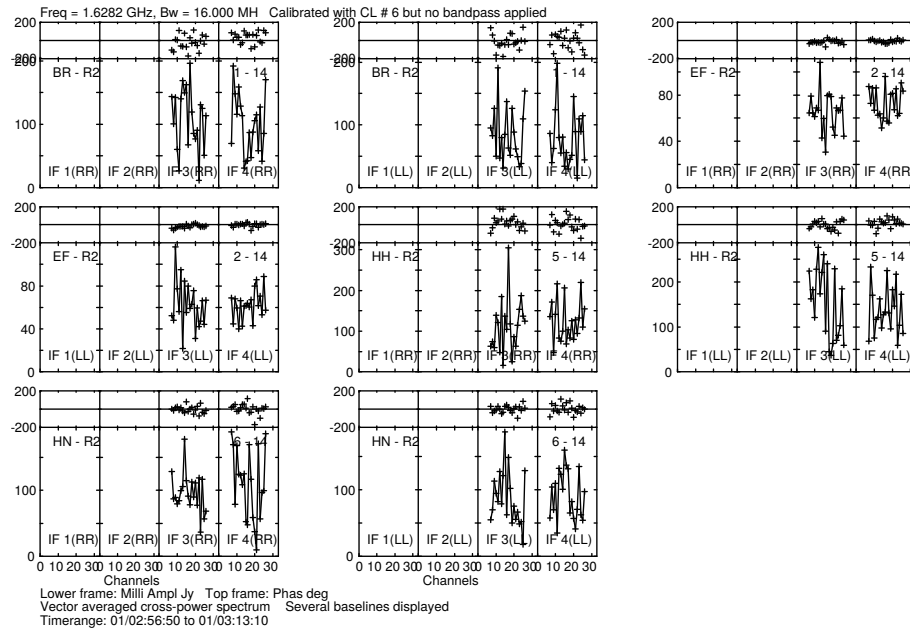


Figure 3.4: Frequency dependence of the amplitudes and phases (bottom and top panel of each individual plot, respectively) *after* fringe fitting for a few selected ground-space baselines, for the parallel hands. The phases are centred around zero, signifying a clear signal.

3.2.3 Bandpass calibration

Subsequently, the receiver bandpass response was calibrated with the BPASS task. In general, the bandpass response of the receiver is not flat over the covered frequency range, but falls off rapidly at the edges of each IF (cf. Fig. 3.5). Without correction, this will contaminate the recovered amplitudes after averaging the data in frequency.

The calibrator sources as well as 3C345 itself were examined as calibrators for the bandpass. The best results were obtained when using 3C286. First, the bandpass amplitudes were solved for, and then the more minor bandpass phase errors. All VLBA antennas were successfully calibrated this way, reaching a satisfactory removal of the bandpass response. For the other telescopes, no good solutions could be obtained, so the outer 5 of 32 channels on each side of the IF were flagged to reduce bandpass effects. The results can be examined in Fig. 3.6.

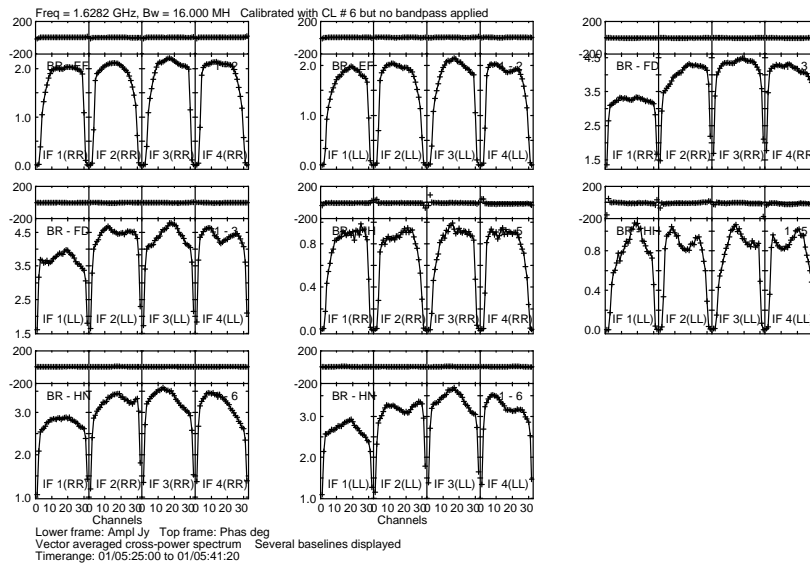


Figure 3.5: Amplitudes and phases as function of frequency *before* bandpass calibration. Compare with Fig. 3.6.

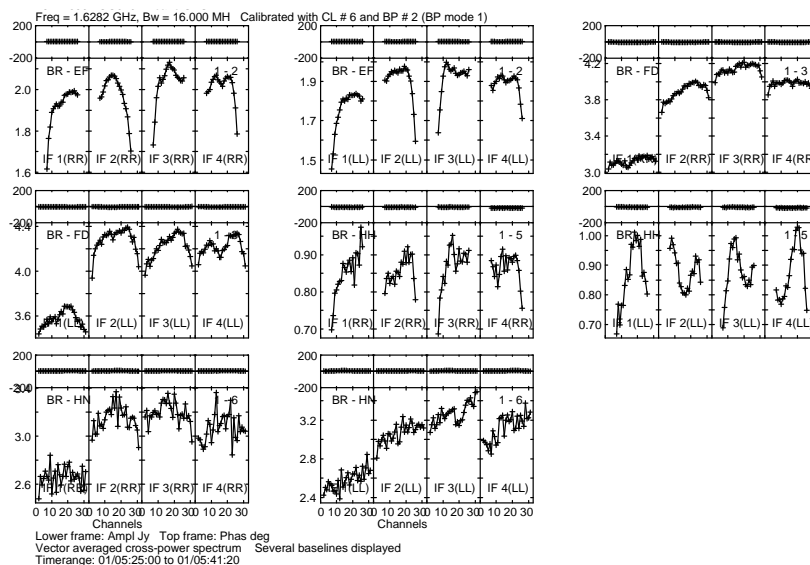


Figure 3.6: Amplitudes and phases as function of frequency *after* bandpass calibration. For VLBA stations, the bandpass response could be modelled satisfactorily, while for other stations, the channels at the edges of each IF were removed to mitigate the bandpass effects.

3.2.4 Data averaging

With the effects of phase offset, delay and rate removed from the data, and bandpass effects mitigated, one can average the data in frequency first. The data were exported while averaging all the frequency channels in each IF, but keeping the IFs distinct. This preserves some more information in the (u, v) -plane, and, as was already seen earlier during calibration, there might be IFs with data that is better behaved than others. In this case it is useful to be able to treat those IFs separately when it comes to flagging and self-calibration.

The data were then imaged in `Difmap`, which is explained in more detail in Sect. 4. After flagging, the time averaging is done there, which again greatly reduces the size of the data. Care has to be taken to not resolve out structure with too large averaging intervals, but ideally one improves the map SNR with larger intervals.

3.2.5 Polarisation calibration

The calibration so far concerned the calibration of the parallel hands, RR and LL. For imaging linear polarisation, the cross hands (RL and LR) have to be calibrated as well.

The first step is to compensate for remaining phase offsets between RCP and LCP with the AIPS task `RLDLY`. The resulting phases as a function of frequency will in principle be flat after the application of this offset. The remaining absolute phase offset is corrected at a later stage. This offset comes about because all phases are given relative to a reference antenna, whose phase difference between RCP and LCP is unknown. This phase term can be corrected with a rotation of the electric vector position angles in the final polarisation map made from Stokes Q and U , which will be discussed in Chapter 4. The corrections obtained with `RLDLY` have been applied, and for some SRT baselines, they can be examined in Fig. 3.7 and 3.8.

A property of radio receivers is the leakage of some signal from RCP to LCP and vice versa, which pollutes the signal in the cross hands (RL and LR). This is referred to as instrumental polarisation, or as D -terms, as I will refer to them in the following (see Sect. 2.9 for details). They are complex gains applied to the cross hands and thus have an amplitude and a phase.

Their correction is not straightforward, as some assumptions are made beforehand. The most important assumption is the self-similarity assumption: Assuming that the polarized intensity follows the total intensity distribution. With that prior, the AIPS task `LPCAL` can determine the D -terms for each telescope by using an image of the source in total intensity as input. Prior to that, the image is divided into sub-models with the task `CCEDT`. These sub-models help the task to deal with complex source structure, as the self-similarity assumption likely holds true for the submodels better than for the source brightness distribution as a whole. `CCEDT` can automatically select a specified number of submodels from the image. I tested different submodel representations of the image, but ultimately, the best D -term correction was achieved with the automatic model splitting.

For an accurate determination of a telescope's D -terms, one needs sufficient parallactic angle coverage on the source with the telescope. The parallactic angle is the angle between the receiver feed and the source, that will change as the Earth rotates. In principle, the D -terms are a purely instrumental effect and should not depend on the source that is used for their determination. However, given the sparse parallactic angle coverage of several telescopes on the calibrator sources, I deemed them not well-suited for D -term calibration. In addition, for the SRT, 3C 345 was the only source that was observed.

Figure 3.9 shows the D -terms in the complex plane for each telescope, and Table 3.2 lists their values. From experience over decades in VLBI, D -term amplitudes are expected to lie within 10 %, although values up to 20 % are not a rarity and can still be acceptable.

Values for all telescopes lie within that range, except for GB and SV, which show D -term amplitudes of the order of unity, which is unreasonable. For GB it is suspected that the origin of this lies in the uncertain amplitude calibration explained in Sect. 2.5, and in the small parallactic angle coverage (see Table 3.2 for the parallactic angle coverage of each telescope). The latter will decrease the accuracy of the D -term calibration considerably. Henceforth these two antennas were flagged in RL and LR. This was also done for RO, as the flagging of RCP and LCP in different IFs in each case (see Sect. 2.5) lead to RL and LR correlations being flagged effectively. These telescopes were henceforth flagged and are not shown in Fig. 3.9. The final iteration of LPCAL was done with the aforementioned telescopes flagged, as the bad data could also affect the D -term determination of the other antennas. Hence 16 antennas in total were used for imaging in polarized intensity.

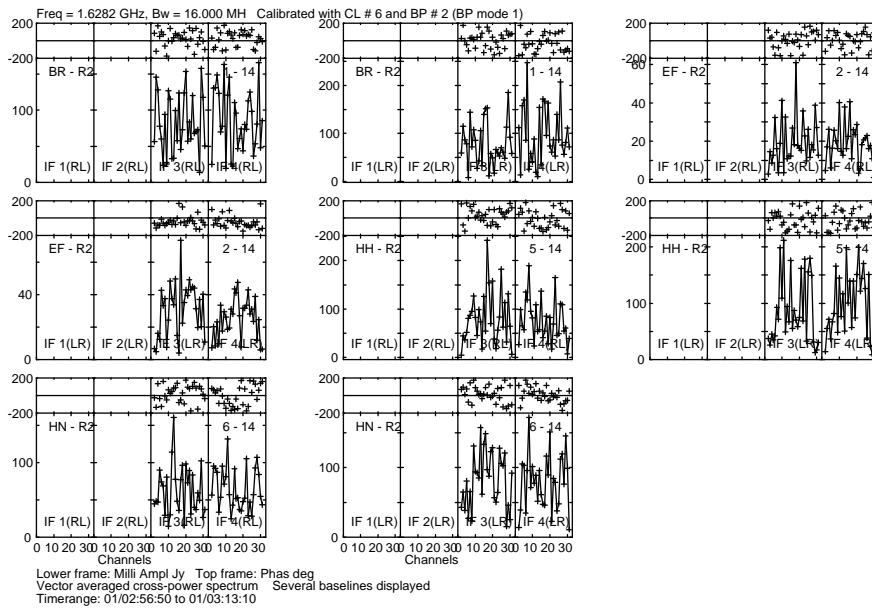


Figure 3.7: Phases of the baselines to the SRT in the cross-hand polarisations RL and LR *before* correction of the residual delay by RLDLY.

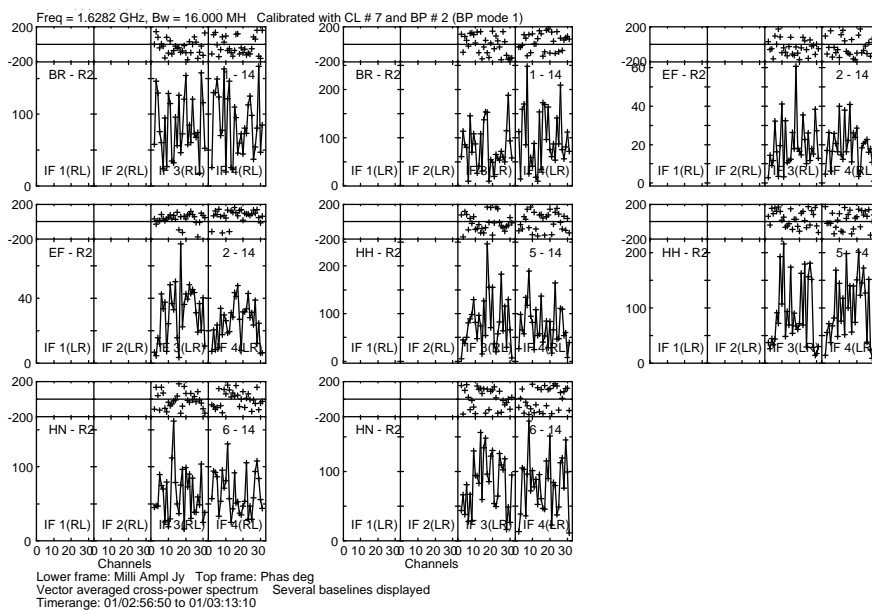


Figure 3.8: Phases of the baselines to the SRT in the cross-hand polarisations RL and LR *after* correction of the residual delay by RLDLY.

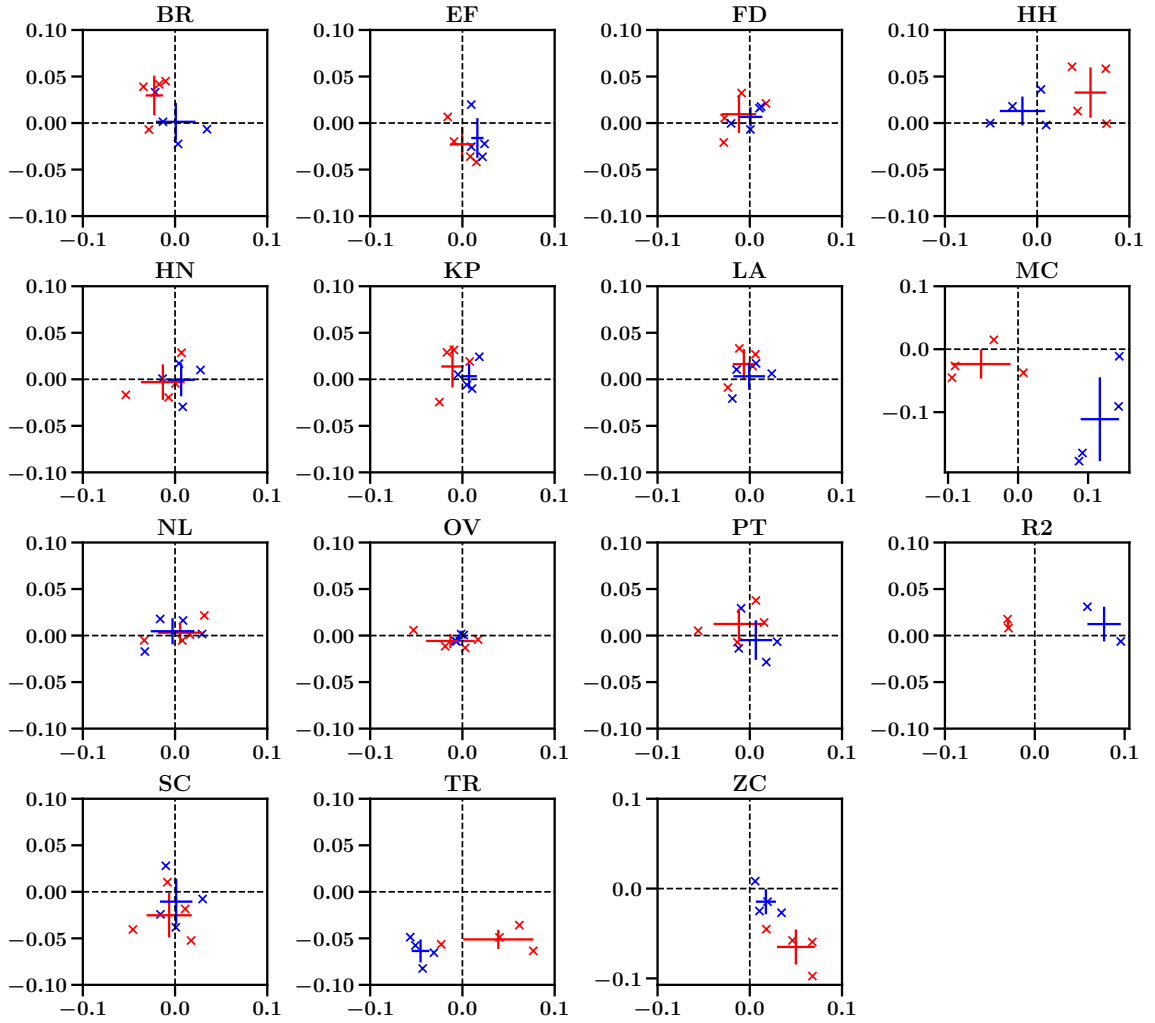


Figure 3.9: Visualisation of the instrumental polarisation (D -terms) for each of the 16 telescopes used for imaging in polarisation. Several issues with the data from Green Bank, Jodrell Bank and Svetloe led to the exclusion of these telescopes from the polarisation analysis (see text for details). The x -axes show the real part and the y -axes the imaginary part of the D -term amplitudes. The Red data points denote RCP and blue points LCP. Different data points in each subplot indicate results for different IFs. The data points with errorbars are the respective means of all IFs and their standard deviations.

Table 3.2: Parallactic angle coverage and D -terms for each telescope.

Antenna	Parallactic angle cov. [°]	RCP		LCP	
		m [%]	χ [°]	m [%]	χ [°]
BR	36.6	2.9	-166.3	3.5	-10.8
		5.2	131.4	2.3	-81.8
		4.5	112.5	1.3	174.2
		4.6	102.8	4.0	123.1
EF	112.3	1.7	157.5	2.2	64.2
		2.2	-114.6	3.3	-43.0
		3.7	-76.7	4.2	-59.0
		4.5	-70.1	2.7	-69.4
FD	120.6	2.8	50.2	2.0	-178.9
		2.8	169.0	1.9	56.7
		3.4	105.4	0.7	-84.6
		3.5	-143.5	2.2	55.4
GB	24.4
	
	
	
HH	0.0*	7.5	-0.5	5.1	-179.8
		9.5	38.1	3.2	146.1
		7.1	57.9	3.6	83.5
		4.6	16.4	1.0	-12.5
HN	145.5	2.9	76.3	3.1	-74.3
		0.5	-84.0	1.4	177.1
		2.1	-109.8	1.8	75.8
		5.6	-162.6	2.9	20.0
JB
	
	
	
KP	86.2	3.4	120.1	1.5	-43.7
		3.3	106.3	0.8	-51.1
		2.1	67.6	0.7	132.8
		3.5	-135.6	3.0	52.8
LA	99.4	3.5	108.8	2.8	-132.4
		2.8	77.2	1.8	144.0
		1.4	77.6	1.8	68.2
		2.5	-159.4	2.5	14.4

NOTE: The D -term amplitude is denoted by m and the phase by χ . The four rows for each antenna designate the results for each of the four IFs (or two IFs for the SRT). * Hartebeesthoek has an equatorial mount and thus formally has zero parallactic angle coverage. The SRT also has formal zero parallactic angle coverage as it observes in space and is not subject to Earth's rotation.

Table 3.3: Table 3.2 continued.

Antenna	Parallactic angle cov. [°]	RCP		LCP	
		m [%]	χ [°]	m [%]	χ [°]
MC	137.1	3.8	-78.5	14.5	-4.5
		10.5	-154.4	16.9	-32.3
		9.4	-163.5	19.8	-63.9
		3.8	156.7	18.9	-60.9
NL	151.3	3.8	34.2	3.7	-152.3
		1.6	3.4	2.4	132.0
		1.0	-34.0	1.8	62.0
		3.4	-171.5	2.9	3.3
OV	43.2	1.8	-14.2	0.9	-135.8
		1.4	-77.6	1.0	-144.6
		2.2	-148.4	0.2	19.8
		5.3	173.7	0.2	132.3
PT	94.6	3.8	80.1	3.0	-12.5
		2.1	42.3	3.4	-57.9
		1.5	-152.1	1.8	-131.0
		5.6	174.8	3.1	107.9
SRT	0.0*	3.0	164.7	6.6	27.9
		3.5	149.8	9.6	-3.8
RO
	
	
	
SC	174.2	1.3	128.9	3.8	-88.7
		2.1	-59.2	2.9	-123.2
		5.5	-71.7	3.0	109.7
		6.1	-138.5	3.1	-14.5
SV	80.0
	
	
	
TR	103.1	6.1	-112.2	7.7	-131.5
		6.3	-50.7	7.2	-115.3
		7.1	-30.1	7.5	-139.2
		10.0	-39.6	9.3	-117.6
ZC	140.8	4.9	-68.4	1.0	54.6
		7.4	-51.3	2.4	-37.2
		9.0	-41.3	2.7	-67.3
		11.9	-55.1	4.4	-38.1

Chapter 4

RadioAstron images of 3C 345 at 1.6 GHz

In this Chapter I will illustrate the imaging process of the *RadioAstron* data presented in Chapter 3. The obtained images, in both total (Sect. 4.2) and polarised intensity (Sect. 4.3), are shown and the image parameters are determined and presented here. A complete analysis of the *RadioAstron* images, in conjunction with multiwavelength data, will be presented in Chapter 5.

Parts of this Chapter have been published in Pötzl et al. (2018) and Pötzl et al. (2021).

4.1 Imaging

After the calibration described in Chapter 3, the data were ready for imaging. These data facilitate total intensity and linear polarisation images at the unprecedented angular resolution that is offered by *RadioAstron*. With this, the source structure and magnetic fields can be probed at the smallest scales.

For imaging, the software packages AIPS and Difmap (Shepherd 1997) were used. Difmap is a package developed at Caltech and widely used in VLBI for hybrid imaging, mainly due to its easy handling of data editing and the powerful visualisation options. Hybrid imaging consists of iterations of deconvolution and self-calibration runs. For deconvolution, a Clean algorithm is used. Difmap allows for very convenient interplay of clean and self-calibration procedures. For details, see Sect. 2.7.1 and 2.7.2.

First, the data were averaged in time in 90 s intervals. Prior to that, different averaging time intervals were tested, and this was chosen as compromise. Higher averaging times will yield higher *SNR* in the image, but if chosen too large, source structure could be averaged out. This holds especially true for fast changes in phase, that could be introduced by the fast-moving SRT when the acceleration is large close to the perigee.

The imaging process will depend greatly on how the visibilities are weighted when Fourier transforming them to get the actual image. In general, one differentiates between *natural* and *uniform* weighting.

For uniform weighting, the visibilities are averaged in bins of a given pixel size (gridding) prior to Fourier transforming, while weighting visibilities in each bin according to their associated errors by a specified degree. Uniform weighting thus puts more weight on regions in the (u, v) -plane where visibilities are less densely sampled, compared to when no gridding is applied. In contrast, for natural weighting, no gridding prior to the Fourier transform is done, in which case less densely sampled regions in the (u, v) -plane are sequentially weighted less. Choosing natural weighting increases sensitivity to larger scale

structure and reduces image noise, but also increases the restoring beam size compared to uniform weighting.

A uniform weighting scheme was chosen, without weighting of the visibility errors. This is done in `Difmap` with `uvweight 2,0`. For uniform weighting, the first parameter defines the visibility averaging bin size, weighted by the errors to a power according to the second parameter. So in this case, bins of two pixels were adopted without weighting the errors of the visibilities. In general, for *RadioAstron* observations, choosing natural weighting effectively puts so little weight to the SRT baselines that the beam size is almost as small as when flagging the SRT baselines.

In VLBI, `uvweight 2,-1` is commonly used, which weights the visibility errors to the power of -1. A weight of -2 would correspond to Gaussian errors. For *RadioAstron* observations, `uvweight 2,0` is preferred; because of the limited sensitivity of the SRT, the errors are larger. Choosing not to weight the errors increases the weight of baselines to the SRT, and thus improves the resolution of the final image. Additionally, the errors were remarkably small (and thus likely not well determined) on many baselines and probably do not reflect well the underlying uncertainties in the visibilities.

For imaging, the map size and pixel size were set upon following criteria. The map size should be at least 80 mas in declination and right ascension, as previous observations showed jet emission up to those scales at the observing wavelength. For the initial imaging, a canonical pixel size of 1/6 of the restoring beam width was chosen, resulting in a pixel size of 0.04 mas.

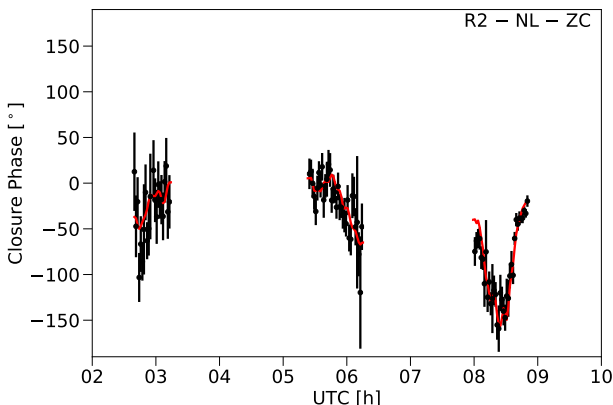


Figure 4.1: Closure phases of the triangle North Liberty (NL), Zelenchukskaya (ZC) and the SRT (R2). The source clean model is shown in red. The perigee of the SRT occurred during the last scans.

and then 3C 345 was imaged with the ground array only. The `Difmap` feature `modelfit` (see Sect. 4.2.1) was used, fitting a few Gaussian components to the data that reflect the source structure seen with the ground-array. This was followed by phase and amplitude self-calibration down to a few minutes solution interval to correct the ground station gains. For many of those stations, IF 1 showed much more scatter than the other IFs for reasons that could not be determined. A possible explanation is RFI, as this is most problematic at the lowest frequencies. This scatter has been removed with the above mentioned self-calibration procedure.

Going further, the SRT baselines were unflagged and the source subsequently imaged with careful clean and phase self-calibration. Different clean gains and phase self-calibration solution intervals were checked to ensure that no false structure is introduced

During imaging, it became clear that some ground stations had notably bad initial amplitude calibration, primarily SV and ZC. Amplitudes of baselines involving SV showed systematically lower amplitudes by a factor of a few than comparable other baselines. ZC showed increasing amplitudes up to tens of janskys for later scans, which could be due to miscalibration due to observing at very low elevation. The amount of atmosphere that the signal has to pass through before arriving at the telescope becomes exceedingly larger at low elevation, which makes the calibration of the telescope gains more difficult (see e.g., Eq. 6.6). To correct these issues, first the SRT was flagged in the data

in the image. In addition, different sets of clean windows, that limit the cleaning to the area in the image covered by them, were tested.

Imaging showed that there is emission eastwards of the brightness peak, that could not be calibrated out and is therefore likely real structure. For the final cleaning, amplitude and phase self-calibration down to the averaging time was applied for all ground stations, as well as phase self-calibration down to a three minutes solution interval and an overall gain factor for the SRT. The amplitude corrections applied to the SRT this way were +3% for IF 3 and -8% for IF 4. The visibilities corrected for gains from self-calibration as well as the source clean model are presented in Fig. 4.2 and Fig. 4.3. The obtained accuracy of the a-priori amplitude correction is in accordance with previous *RadioAstron* observations (see e.g. Kravchenko et al. 2020). In addition, Fig. 4.1 provides an example of the closure phases for one telescope triangle, where one can see that the model is visually a good fit to the data.

After correcting the D -terms of all stations with the Stokes I image obtained this way (see Sect. 3.2.5), a final clean run was conducted with the AIPS task `IMAGR` for the self-calibrated Stokes I , Q and U data, where the same parameters and clean windows were applied for each of them. Also a uniform weighting scheme comparable to `Difmap` was chosen, without making use of the robust parameter, that can in principle fine-tune the visibility weighting between full natural and full uniform weighting. The resulting images are presented in Fig. 4.5 and following, and will be discussed in Sect. 4.2.

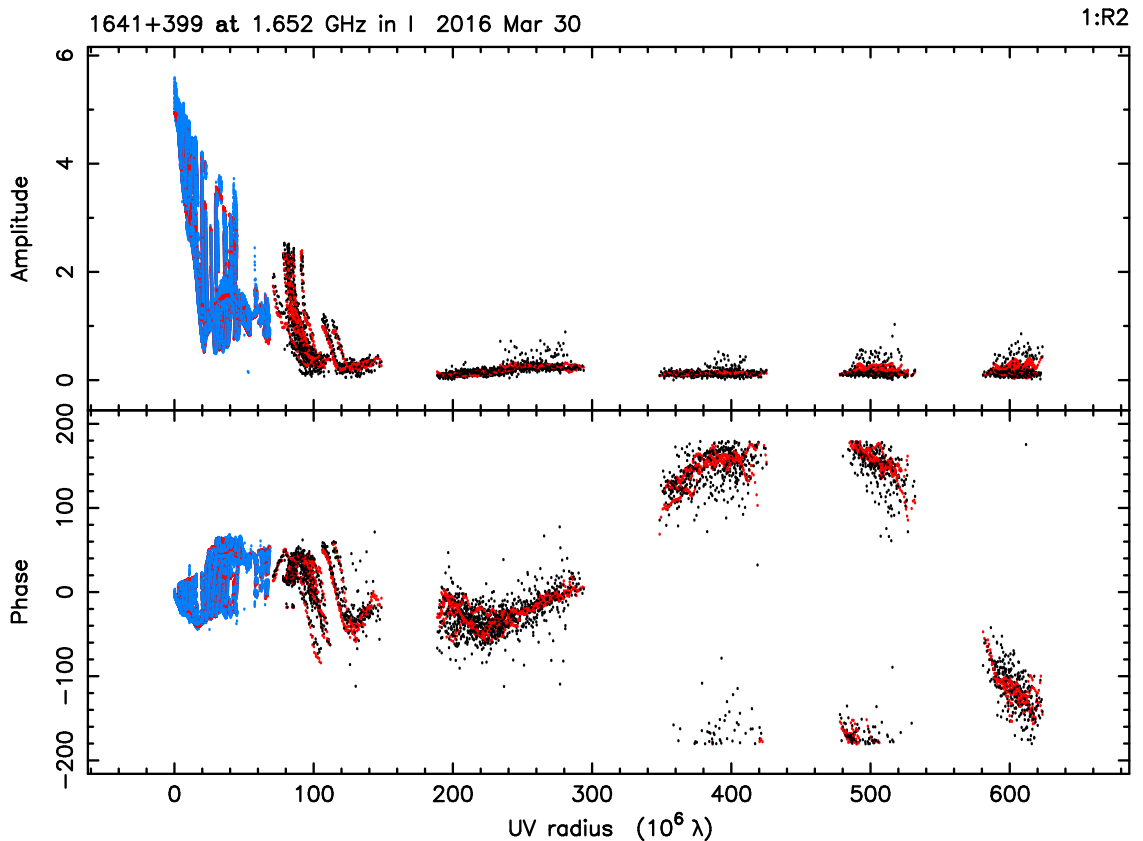


Figure 4.2: Visibility amplitudes (top) and phases (bottom) as a function of (u, v) -distance $\sqrt{u^2 + v^2}$. The blue data points correspond to the ground-array data, while the black data points correspond to the SRT baselines. The source clean model is shown in red. One can see the beating of spatial frequencies of the innermost jet features at baselines $> 300 M\lambda$.

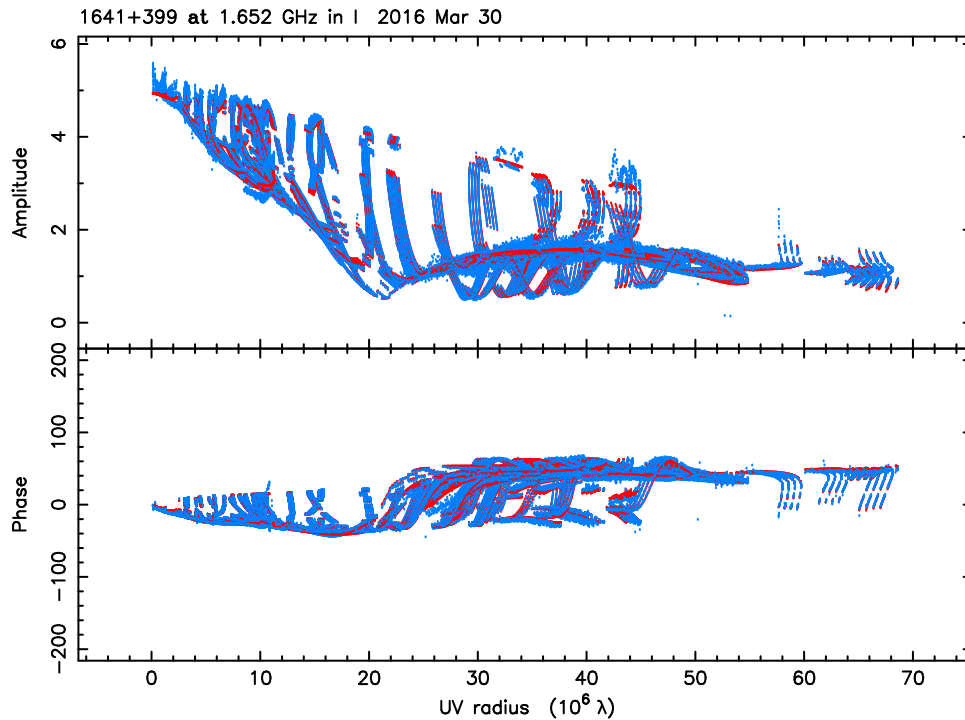


Figure 4.3: Visibility amplitudes (top) and phases (bottom) as a function of (u, v) -distance $\sqrt{(u^2 + v^2)}$ for the ground-array data only. The source clean model is shown in red.

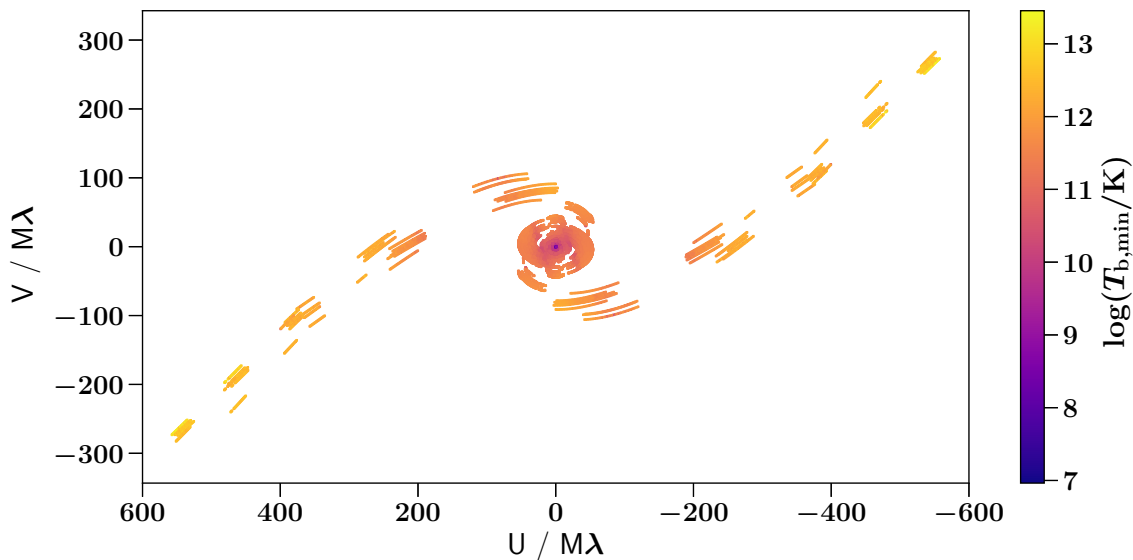


Figure 4.4: (u, v) -coverage of the 1.6 GHz observations with *RadioAstron*. The color scale shows the minimum brightness temperature $T_{b,\min}$ calculated from the visibilities according to Lobanov (2015) (see Sect. 5.2 for details).

4.2 Total intensity images

In the final images, the achieved resolution is $\sim 300 \mu\text{as}$ (minor axis FWHM, i.e. full width at half maximum, beam size), corresponding to a projected length of 2 pc or between ~ 2600 and $\sim 10000 r_G$ for a black hole mass ranging between $M_{\text{BH}} \sim 2 \times 10^9 M_\odot$ and $M_{\text{BH}} \sim 8 \times 10^9 M_\odot$ (Gu et al. 2001; Shen et al. 2011). With an assumed jet viewing angle of $\theta = 5^\circ$ (Schinzel et al. 2012), the deprojected length is 23 pc or between $\sim 3 \cdot 10^4$ and $\sim 10^5 r_G$.

The images reveal several components in the inner 10 mas of the jet, which could not be resolved with data from the ground array only. It is apparent that the eastern most feature, at the jet base, is not the brightest component, which is a characteristic already seen in 3C 345 with VSOP, the predecessor of *RadioAstron* (Klare et al. 2000, 2001, 2005). This feature likely corresponds to a partly synchrotron self-absorbed core, which is subsequently designated as the “core”. In addition, a visibly curved jet structure is observed in the few innermost mas of the jet, where the jet direction changes rapidly. The weak feature east of the core visible at the edge of Fig. 4.5 is considered to be rather an imaging artefact than an indication of a counter-jet, as it is only a few times the noise level. This is discussed in more detail in Sect. 5.9.

To quantify the observed jet direction, the structure along the jet is fitted with Gaussian profiles. The resulting jet ridge line is then plotted as the peak positions of the Gaussian profiles in Fig. 4.6. The curved jet structure is pronounced in this image. Two of the slices with Gaussian fit profiles are shown in Fig. 4.7.

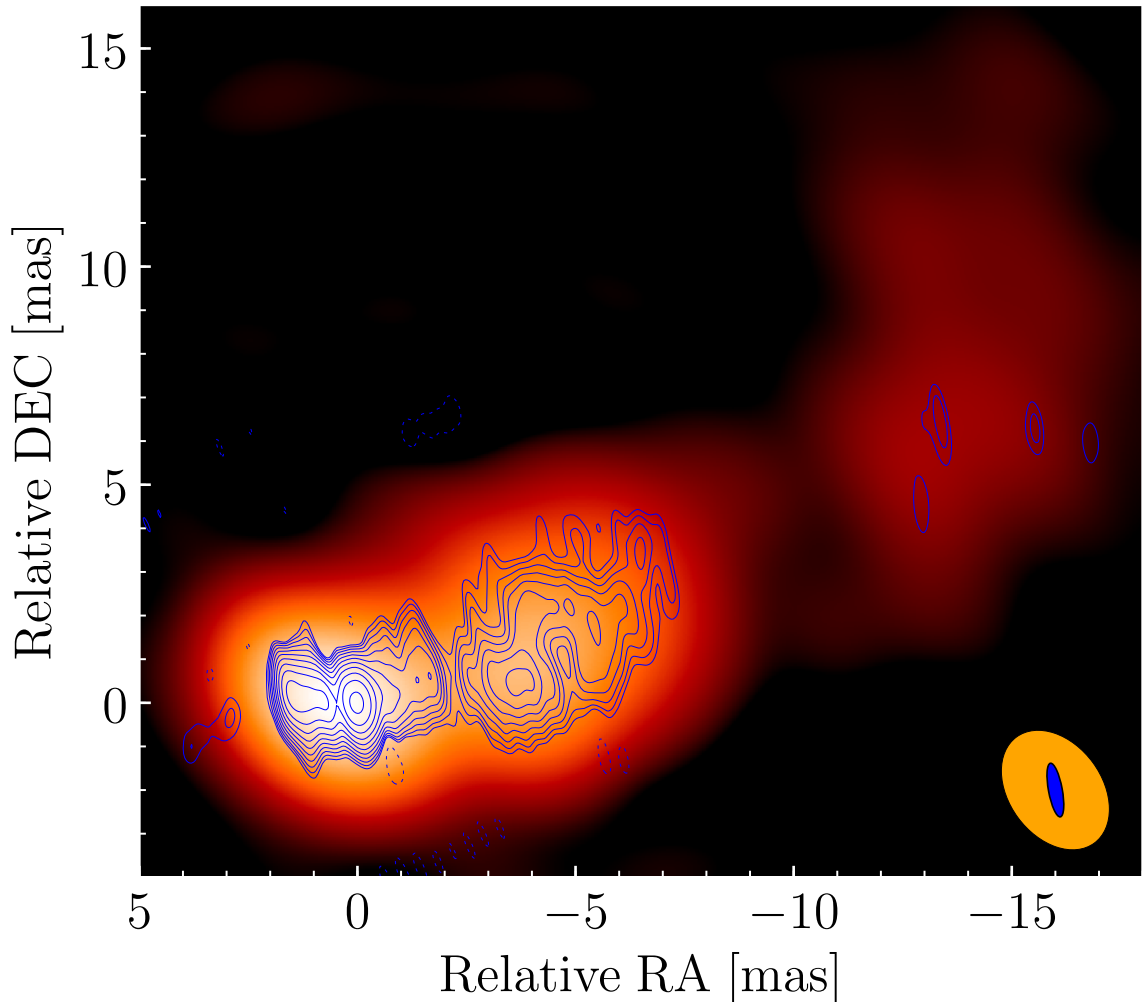


Figure 4.5: Total intensity image of 3C 345 at 1.6 GHz with the ground array data (orange scale) and all data including the space baselines (blue contours). The different beam sizes are displayed in the bottom right corner. A resolution of 1.25×0.32 mas at a P.A. of 10.50° is reached with *RadioAstron*. Contour levels are in percents of peak emission of 0.39 Jy/beam: $-2.83, 2.83, 4.0, 5.65, 8.0, 11.31, 16.0, 22.63, 32, 45.25, 64.0, 90.51$. For the ground array image, the resolution is 3.0×2.1 mas, and the colour-scale shows the total intensity in log-scale between 0.5 and 100% of the peak of 1.68 Jy.

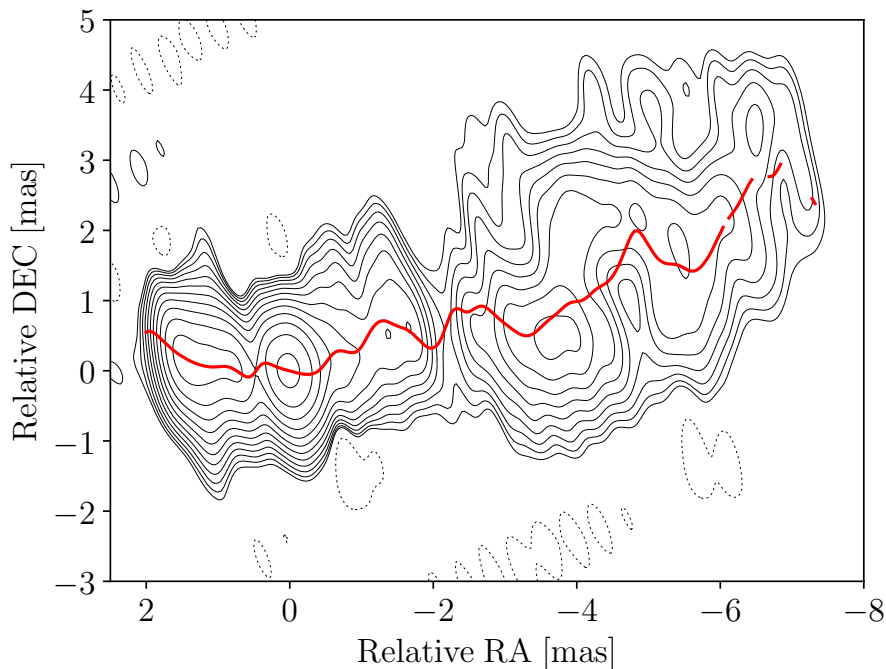


Figure 4.6: Total intensity image of 3C 345 at 1.6 GHz with *RadioAstron*, with jet ridge line overlaid. One-dimensional Gaussian profiles were fitted to the slices in North-South direction of the jet emission and defined the jet ridge line as their maxima along the jet. This illustrates the curved structure of the jet within the innermost few mas.

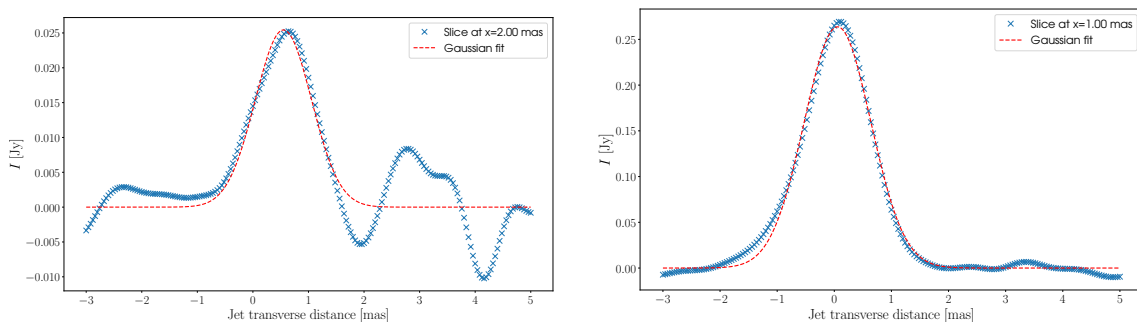


Figure 4.7: Total intensity data (blue points) and Gaussian fit (red dashed line) along slices in North-South direction at 1 mas (left) and 2 mas RA (right). The jet ridge line has been calculated with the positions of the maxima of the Gaussian fits and is displayed in Fig. 4.6.

4.2.1 Model fitting

The `modelfit` feature implemented in `Difmap` was used to model the visibilities directly with circular Gaussian components. The feature uses the Levenberg-Marquardt non-linear least squares minimisation technique (Levenberg 1944; Marquardt 1963). The free parameters of the Gaussian model fits are component total flux density S_{tot} , the Gaussian FWHM θ_{FWHM} , and the component position in polar coordinates with r and ϕ , with respect to the map phase centre. The axis ratio of the fitted elliptical Gaussians was fixed as to maintain the circular Gaussian condition. The errors of the `modelfit` parameters are calculated based on Schinzel (2011), where the formulas presented there are slightly re-written.

In addition to the fitted parameters, the peak flux density and the respective root mean square (RMS) error is measured, S_{peak} and σ_{RMS} , in the hybrid maps. Then

$$SNR = \frac{S_{\text{peak}}}{\sigma_{\text{RMS}}}, \quad (4.1)$$

$$\sigma_{\text{peak}} = \sigma_{\text{RMS}} \sqrt{1 + SNR}, \quad (4.2)$$

$$SNR_{\text{peak}} = \frac{S_{\text{peak}}}{\sigma_{\text{p}}}, \quad (4.3)$$

$$\sigma_{\text{tot}} = \sigma_{\text{peak}} \sqrt{1 + \left(\frac{S_{\text{tot}}}{S_{\text{peak}}} \right)^2}, \quad (4.4)$$

$$\sigma_{\theta} = \frac{\max(\theta, \theta_{\text{lim}})}{SNR_{\text{peak}}}, \quad \text{with } \theta_{\text{lim}} = \frac{4}{\pi} \sqrt{\pi \ln(2) \cdot b^2 \cdot \ln \left(\frac{SNR}{SNR - 1} \right)}, \quad (4.5)$$

$$\sigma_r = \frac{\sqrt{b^2 + \max(\theta, \theta_{\text{lim}})^2}}{SNR_{\text{peak}}} \quad \text{and} \quad (4.6)$$

$$\sigma_{\phi} = \arctan \left(\frac{\sigma_r}{r} \right) \cdot \frac{180^\circ}{\pi}. \quad (4.7)$$

The parameter θ_{lim} denotes the smallest component size to be resolved by an interferometer with beam size $b = \sqrt{b_{\text{maj}} \cdot b_{\text{min}}}$ with a given image SNR (Lobanov 2005). The max argument stands for the maximum of the two quantities in Eq. 4.5 and 4.6. Note that for Eq. 4.6, I follow a more conservative approach compared to Schinzel (2011), where there $\sigma_r = 0.5\sigma_{\theta}$ is assumed according to Fomalont (1999).

S_{peak} has been measured as follows: The component in question was removed from the clean map, and then the residual map was inspected where the peak flux density was taken at the component position. For σ_{RMS} , the RMS in the residual map (where nothing has been removed from the clean map) was obtained within 10×10 square pixels around the component position. The `modelfit` parameters are listed in Table 5.2.

For the *RadioAstron* data, all component sizes are above the limiting size calculated from Eq. 4.5 for map-averaged quantities. In the map, one finds $SNR \sim 150$ with an image noise of ~ 3 mJy, so $\theta_{\text{lim}} \approx 100 \mu\text{as}$. Note that Table 5.2 also lists the `modelfit` components from archival MOJAVE¹ data at 15 GHz that are used for comparison. The data will be described in more detail in Chapter 5.

For any model with a certain number of parameters used to describe a data set, one can choose an arbitrarily large number of parameters, as long as $n_{\text{params}} \leq n_{\text{data}}$. The number of degrees of freedom of the fit are then $n_{\text{DoF}} = n_{\text{data}} - n_{\text{params}}$. To find the minimum number of components that are needed to describe the data, while not overfitting the data, I use the criterion described in Schinzel et al. (2012):

$$0.68 = [\Gamma(n/2)]^{-1} \gamma(n/2, x_{0.68}/2), \quad (4.8)$$

where γ is the lower incomplete Euler-Gamma function, and Γ the complete Euler-Gamma function, $\gamma(a, z) = \int_0^z x^{a-1} e^{-x} dx$ and $\Gamma(z) = \int_0^\infty x^{z-1} e^{-x} dx$. Solving this cumulative distribution function of the χ^2 distribution yields $x_{0.68}$, and the equation was solved numerically for this analysis. Following Schinzel et al. (2012), I also employed a threshold of 0.68, corresponding to a 1σ improvement of model 2 over model 1 when

$$\frac{\chi_1^2}{\chi_2^2} \geq \frac{x_{0.68,2}}{x_{0.68,1}} \quad (4.9)$$

¹Monitoring of Jets in active galactic nuclei at very high energies

is fulfilled for model 1 with χ_1^2 and $n_{\text{DoF},1}$, and model 2 with χ_2^2 and $n_{\text{DoF},2}$. Several models with different numbers of circular Gaussian components were tested, and each time Eq. 4.9 was used to find the best model representation.

4.3 Linear polarisation images

For imaging Stokes Q and U , the task `IMAGR` in `AIPS` was used. The parameters were set in a way that a similar visibility weighting scheme as in `Difmap` was reached. The maps were cleaned for the same number of iterations as for Stokes I without any further self-calibration, as this was sufficiently done on the Stokes I data in `Difmap`.

As described in Sect. 1.4, the linear polarisation intensity P and the EVPAs (electric vector position angles, corresponding to χ in Sect. 1.4) are computed. An absolute phase offset after calibration still remains, that is, there is no absolute calibration for the EVPAs in the polarisation map. To correct this, one can use single-dish observations close in time to the VLBI observations. The Effelsberg telescope observed 3C 345 at the same epoch as the *RadioAstron* observations in polarisation. The results can be seen in Table 4.1.

Fist, the original VLBI map is convolved with a large beam, i.e. large enough to resolve out all the substructure in the map. One can then compare the overall EVPA direction to the single-dish data, and correct the EVPA offset accordingly. Since 3C 345 is markedly core dominated, with a core-to-extended flux ratio > 9 based off VLA observations at 5 GHz (Sambruna et al. 2004), I believe that the Effelsberg data reflect the EVPAs that are also probed by the VLBI observations.

Table 4.1: Results from Effelsberg single-dish measurements (U. Bach, private communication).

(1)	(2)	(3)	(4)	(5)	(6)	(7)
Epoch	λ [cm]	ν [GHz]	I [Jy]	P [Jy]	m [%]	χ [°]
Mar 30, 2016	18	1.66	6.77 ± 0.14	0.40 ± 0.01	5.92 ± 0.23	73.6 ± 1.2
June 2, 2016	2.2	13.0	5.72 ± 0.07
June 3, 2016	2.8	10.5	5.99 ± 0.08	0.218 ± 0.003	3.65 ± 0.07	43.4 ± 1.4

NOTE: Columns denote (1) observing epoch, (2) observing wavelength, (3) observing frequency, (4) total intensity flux, (5) polarized intensity flux, (6) fractional polarisation and (7) EVPA.

Multiple polarised components are observed, the brightest being roughly coincident with the total intensity peak (see Fig. 4.8). There is an offset visible between the two peaks, which was already observed with high-resolution VLBI observations in other AGN (e.g., Lobanov et al. 2015; Gómez et al. 2016). This could be due to the geometry of the jet or the magnetic field with variations in the pitch angle (Lyutikov et al. 2005). There is more polarised structure visible ~ 5 mas downstream of the jet. One can see an almost unpolarised core ($m = 1.56 \pm 0.67\%$), where synchrotron self-absorption likely also leads to significant depolarisation. An optically thick core region has been observed already between 8.1 GHz and 15.4 GHz by MOJAVE (Hovatta et al. 2014). I will go into more detail about the opacity in the jet in Sect. 5.5. Significant depolarisation can also happen if the magnetic field is disordered (Jorstad et al. 2007).

At the total intensity peak the fractional polarisation reaches $m = 5.29 \pm 0.51\%$, where at the location of component L6 it reaches $m = 6.69 \pm 1.40\%$. A degree of polarisation up to 60% ~ 5 mas is observed downstream of the jet, as depicted in Fig. 4.9. This value is very close to the theoretical limit of $\sim 70\%$. Kravchenko et al. (2020) also observed up to

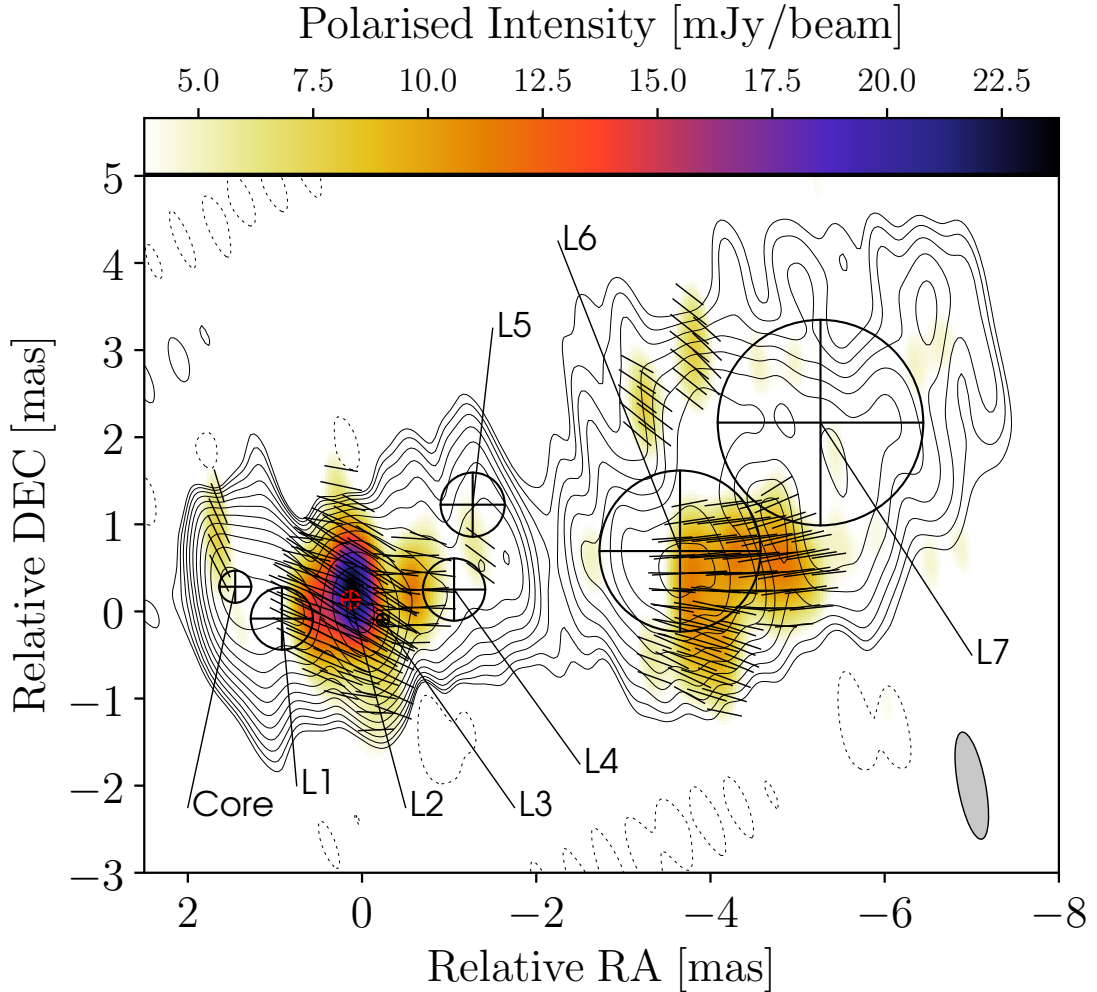


Figure 4.8: *RadioAstron* image of the total intensity and linearly polarised emission of 3C 345 at 1.6 GHz, observed on March 30, 2016. The map of the polarised intensity P is shown in colour-scale, overlaid with contours displaying the total intensity emission. The beam size is displayed on the bottom right with a resolution of 1.25×0.32 mas at a P.A. of 10.50° . The lines show the EVPAs the length of which is proportional to P . Contour levels are (% of peak emission of 0.39 Jy/beam): -2.0 , 2.0 , 2.83 , 4.0 , 5.65 , 8.0 , 11.31 , 16.0 , 22.63 , 32.0 , 45.25 , 64.0 , 90.51 . The crossed circles display the positions and sizes of the circular Gaussian components that were fitted to the data, and the parameters are listed with the respective component names in Table 5.2.

50 % degree of linear polarisation in the jet of 0716+714. However, since the flux density in the region of high m is low, the uncertainties are quite large, of the order of 20 %.

In general, both quasars and BL Lac objects showed the tendency of increasing fractional polarisation along the jet in an extensive MOJAVE survey of 484 sources (Pushkarev et al. 2017a). This may be due to magnetohydrodynamic turbulence becoming less important downstream of the jet as it expands, so the magnetic field becomes more ordered (Böttcher 2016). Compared to BL Lacs, quasars displayed overall less fractional polarisation and less stable EVPAs in the study. However, to assess the stability of the EVPAs in 3C 345, a dedicated multi-epoch study would be required, which is beyond the scope of this thesis. If this general trend holds true for 3C 345, deviations of the alignment of the EVPAs with the jet direction are not surprising. The trend seen in the MOJAVE survey of increasing fractional polarisation is also confirmed for the 3C 345 data, as can be examined in Fig. 4.9. The likely reason for that is that the jet emission layer is thinner at the edges, leading to less depolarisation due to the superposition of regions with different Faraday depths.

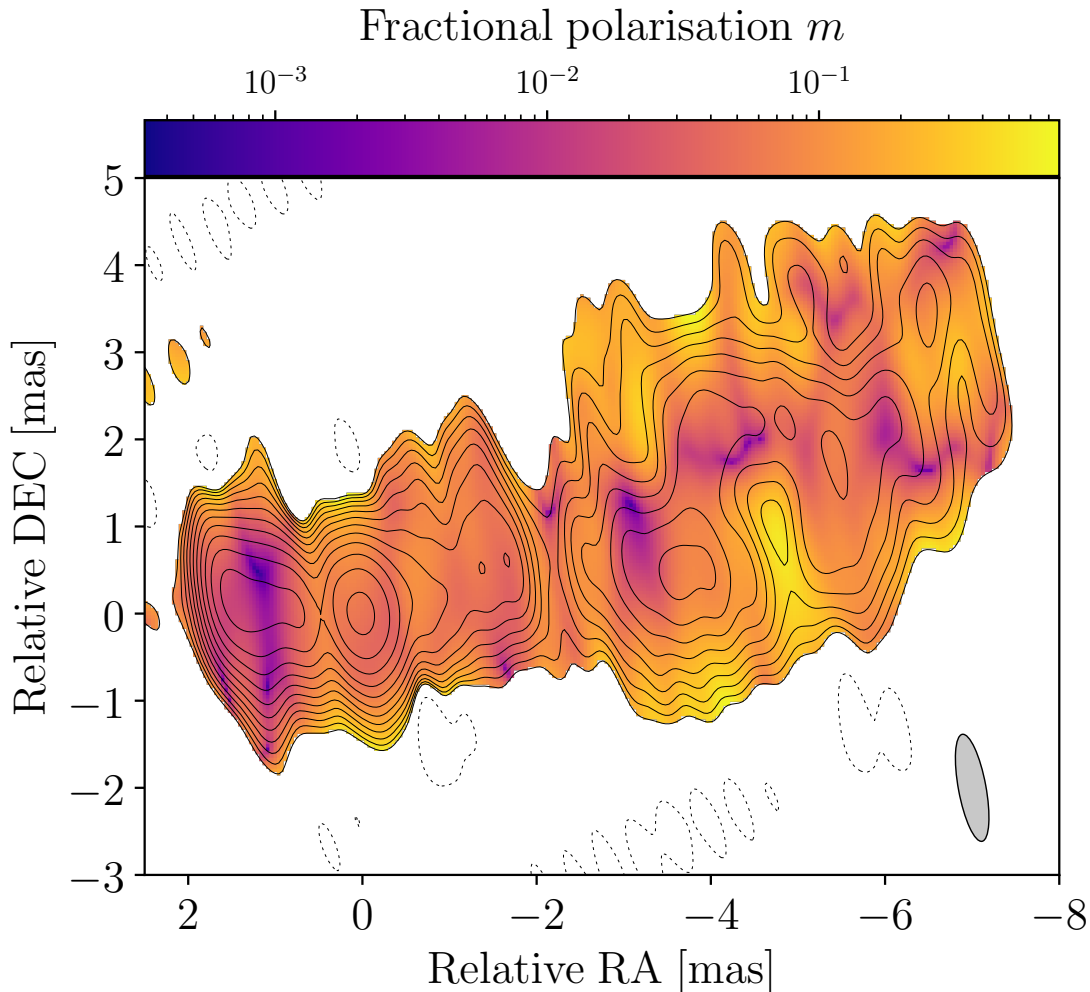


Figure 4.9: Same as Fig. 4.8, but displaying the fractional polarisation m in logarithmic colour scale. Values of $m \sim 5\%$ are observed along the jet, with notably high $m \sim 60\%$ at ~ 5 mas downstream of the jet.

Since many different iterations of D -term estimation have been considered in Sect. 3.2.5, the effect of uncertain instrumental polarisation on this fractional polarisation is likely small, but it can not be ruled out entirely that the high fractional polarisation is due to such uncertainties. To assess that, a Monte-Carlo imaging would be needed with a high number of different sets of D -terms and resulting polarisation images.

Overall the EVPAs seem to be quite well aligned with the local jet direction in the 1.6 GHz image, which was also observed for this source at 43 GHz by MacDonald et al. (2017). However, in the core, the EVPAs are oriented closer to the perpendicular orientation relative to the jet. This might be consistent with a possible rotation of the EVPAs by $\pi/2$ due to opacity effects (e.g., Gomez et al. 1994; Gabuzda and Gómez 2001), in the case of an optically thick core. This would indicate a B -field closer to the perpendicular relative to the jet direction also in the core. This will be discussed in more detail in Sect. 5.5 and 5.6. The motion of a shock on a helical path along the jet can explain the observed bright polarised features with the EVPAs aligned with the jet direction, where the magnetic field is quenched perpendicular to the jet direction (Wardle et al. 1994). Earlier multi-frequency, multi-epoch studies of 3C 345 have favoured this scenario (Ros et al. 2000). Lobanov and Zensus (1999) argued that shocks likely do not play a significant role in the dynamics and emission outside of the core region in 3C 345. In this case, the EVPAs ~ 5 mas downstream of the core could also be explained by a large-scale helical magnetic

field with a dominant toroidal component. There is an indication for a slight gradient in EVPA direction from the inner to the outer jet region, which is however not sufficient to confirm the presence of a helical magnetic field. This will be further tested with higher resolution *RadioAstron* observations at 22 GHz made in May 2016, close to my epoch at 1.6 GHz, that will be analysed for a future publication.

The discussion of the polarisation so far did not include possible Faraday rotation in the source. Faraday rotation might significantly rotate the EVPAs especially for the 1.6 GHz map, as their angular rotation $\Delta\chi \propto \lambda^2$, thus the Faraday rotation is stronger at lower frequencies. This is analysed and discussed in detail in Sect. 5.6.

Chapter 5

Analysis of the physical properties of the parsec-scale jet in 3C 345

In this Chapter I will address the physical properties of the parsec-scale jet in 3C 345 based on an analysis of the *RadioAstron* data presented in Chapter 3 and 4 in conjunction with a multifrequency VLBI dataset. I will mainly calculate and examine the brightness temperature, core shift, spectral index, and rotation measure in the source.

Parts of Sect. 5.2 and 5.3 have been published in Pötzl et al. (2021).

5.1 Complementary data

I obtained complementary data at other frequencies for the *RadioAstron* observations at 1.6 GHz, which are described in the following. An overview of the data sets is presented in Table 5.1.

5.1.1 VLBA data

During the observations with *RadioAstron*, the VLBA also observed 3C 345 at other frequencies during the times where the SRT was not observing. Data are available at 4.8 GHz (C-band), 8.4 GHz (X-band), and 15.3 GHz (U-band). All VLBA stations except Mauna Kea (MK) on Hawaii were observing. The lack of MK is unfortunate as it contributes to the longest baselines, which is why the resulting maps from these observations have a more limited resolution compared to observations with the full array. Close to the *RadioAstron* epoch, there are MOJAVE observations available at U-band, which are described in Sect. 5.1.2. I use these data instead of the smaller dataset obtained at my epoch.

The calibration of the data was done in a similar fashion as described in Chapter 3. The observed visibilities were parametrised with circular Gaussian components in the image plane, in the same manner as described in Sect. 4.2.1. The parameters of those Gaussian components are presented in Table 5.3.

5.1.2 MOJAVE data

The MOJAVE database was searched for observations close to the *RadioAstron* epoch. The MOJAVE survey monitors a large sample of AGN with the VLBA at 15.3 GHz (Lister et al. 2018). It is monitoring 3C 345 since 1995. Observations were performed close to my epoch on March 5th, 2016, less than a month apart from the *RadioAstron* observations, providing a good comparison. This is justified by the observed variability in the radio

light curves, and by the median velocity of jet components of $\sim 0.3 \text{ mas yr}^{-1}$. The 15 GHz data are available at the MOJAVE webpage¹.

As the MOJAVE survey presents images on their webpage with natural weighting, I took the calibrated MOJAVE data and imaged them again with uniform weighting and without any additional self-calibration. A uniform weighting scheme has been chosen here to increase the resolution and thus to get a closer comparison to the *RadioAstron* data.

Circular Gaussian model fits to the MOJAVE data set were conducted. A total of nine components were identified, while applying the same criterion as for the *RadioAstron* data to find the minimum number of components needed to describe the data. The resulting model parameters are different from those listed in the MOJAVE database, as there, they identify seven components with slightly different parameters from what I obtained. However, five of my fitted components are readily identified with the ones in the MOJAVE database, noticing that the components in the core-region are not easily cross-identified. The cross-identification can be seen in Table 5.2, where the MOJAVE components are designated by numbers, while my component designation follows a different scheme. In the MOJAVE survey, only components are identified that can be robustly tracked over at least five epochs (Lister et al. 2009). This may be a reason for the observed discrepancy in the results of the `modelfit`, as it was not tried to identify the Gaussian components obtained from model fitting across multiple epochs. In addition, in the MOJAVE survey, often times an elliptical Gaussian function is used to describe the core. In this case, the core identified in my component fitting could be merged with the component U1. In the following, the model fitting from my own analysis will be used, except for Sect. 5.8, where the aim is to track the evolution of components identified both in the MOJAVE database and the *RadioAstron* map.

5.1.3 BU blazar program data

In the framework of the Boston University blazar program² (Jorstad and Marscher 2016), 3C 345 is monitored among other sources at 43.1 GHz. The cadence of the observations is of the order of a month, and 3C 345 was observed very close to my epoch on March 18, 2016. As for the MOJAVE observations, a comparison seems reasonable, as the observing epochs are even closer to each other here. Circular Gaussians are fitted to the visibility data, and the resulting parameters are presented in Table 5.3.

Table 5.1: Data sets used for the analysis.

ν [GHz]	Band	Epoch	Array	N_{ant}
1.6	L	March 30, 2016	EVN + VLBA + SRT	19
4.8	C	March 30, 2016	VLBA	9
8.4	X	March 30, 2016	VLBA	9
15.3	U	March 5, 2016	VLBA	10
43.1	Q	March 18, 2016	VLBA	10

The resulting images, showing both total intensity and linear polarisation, for 4.8 GHz, 8.4 GHz, 15 GHz and 43 GHz are shown in Fig. 5.1, 5.2, 5.3 and 5.4.

¹<https://www.physics.purdue.edu/MOJAVE/sourcepages/1641+399.shtml>

²<https://www.bu.edu/blazars/VLBAproject.html>

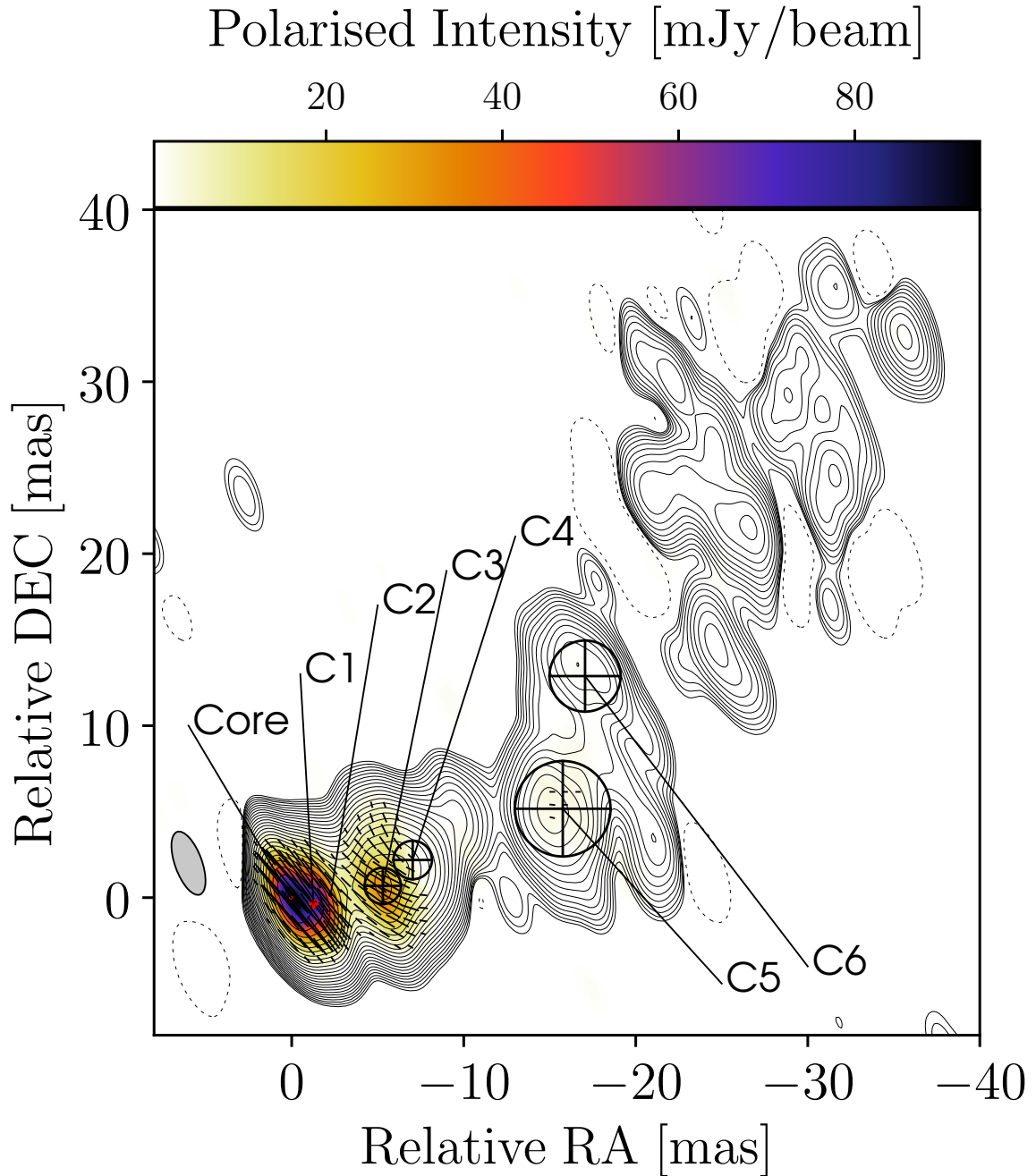


Figure 5.1: VLBA image of the total intensity and linearly polarised emission of 3C 345 at 4.8 GHz, observed on March 30, 2016. The map of the polarised intensity P is shown in colour-scale, overlaid with contours displaying the total intensity emission. The beam size is displayed on the left with a resolution of 1.57×3.88 mas at a P.A. of 19.95° . The lines show the EVPAs the length of which is proportional to P . Contour levels are (% of peak emission of 2.10 Jy/beam): $-0.016, 0.016, 0.031, 0.063, 0.125, 0.25, 0.5, 1.0, 2, 2.83, 4, 5.65, 8, 11.31, 16, 22.63, 32, 45.25, 64, 90.51$. The crossed circles display the positions and sizes of the circular Gaussian components that were fitted to the data, and the parameters are listed with the respective component names in Table 5.3.

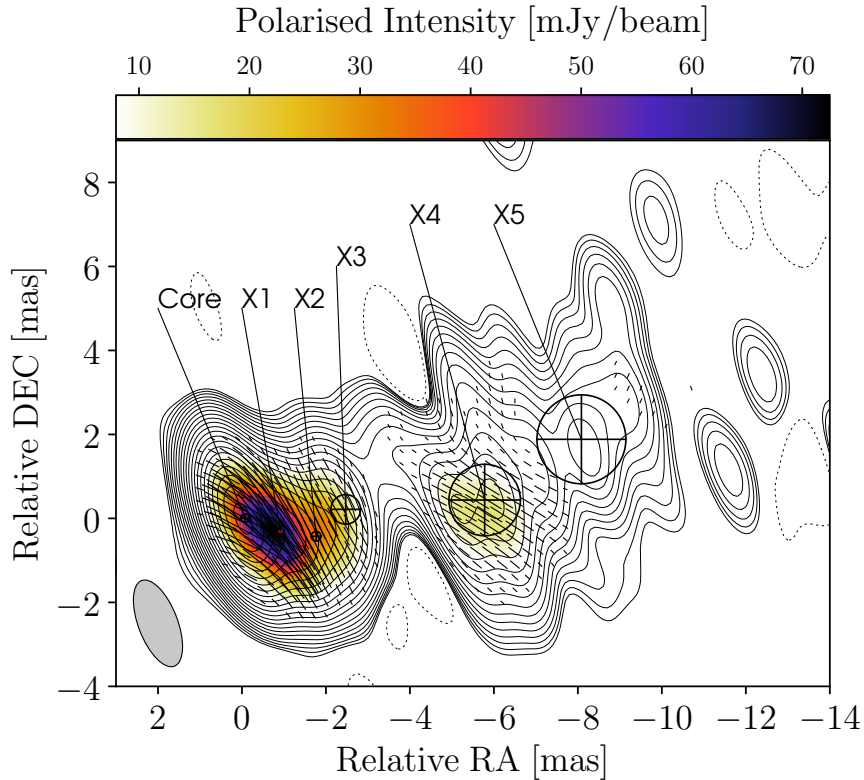


Figure 5.2: VLBA image of the total intensity and linearly polarised emission of 3C 345 at 8.4 GHz, observed on March 30, 2016. The map of the polarised intensity P is shown in colour-scale, overlaid with contours displaying the total intensity emission. The beam size is displayed on the bottom left with a resolution of 0.93×2.18 mas at a P.A. of 20.96° . The lines show the EVPAs the length of which is proportional to P . Contour levels are (% of peak emission of 2.54 Jy/beam): $-0.063, 0.063, 0.125, 0.25, 0.5, 1.0, 2, 2.83, 4, 5.65, 8, 11.31, 16, 22.63, 32, 45.25, 64, 90.51$. The crossed circles display the positions and sizes of the circular Gaussian components that were fitted to the data, and the parameters are listed with the respective component names in Table 5.3.

5.2 Brightness temperature

As described in Sect. 1.3, the brightness temperature of a source provides information about the involved emission mechanisms. measurements of the brightness temperature and the physical interpretation will be discussed for several regions in the jet in 3C 345.

The ability of an interferometer to measure the brightness temperature is in principle independent from the observing wavelength, and depends only on the projected interferometer baseline, measured as distance in metres (Kovalev et al. 2005). Accordingly, *RadioAstron* uniquely probes the highest brightness temperatures (e.g., Gómez et al. 2016; Kovalev et al. 2016; Kutkin et al. 2018; Pilipenko et al. 2018; Kovalev et al. 2020; Kravchenko et al. 2020).

The brightness temperature is calculated in two ways. First, the minimum brightness temperature $T_{b,\min}$ as well as the maximum brightness temperature $T_{b,\max}$ are estimated from the visibility data and the visibility errors according to Lobanov (2015). In addition to that, the brightness temperature is calculated from the fitted flux densities and FWHM of the `modelfit` components explained in Sect. 4.2.1. The values of the estimated brightness temperature from both methods are presented in Fig. 5.6, as well as in the (u, v) -coverage plot in Fig. 4.4 for the first method. The same methodology has been applied for the MOJAVE data presented in Sect. 5.1.2. I go into more detail about the comparison of the data sets in Sect. 5.2.2.

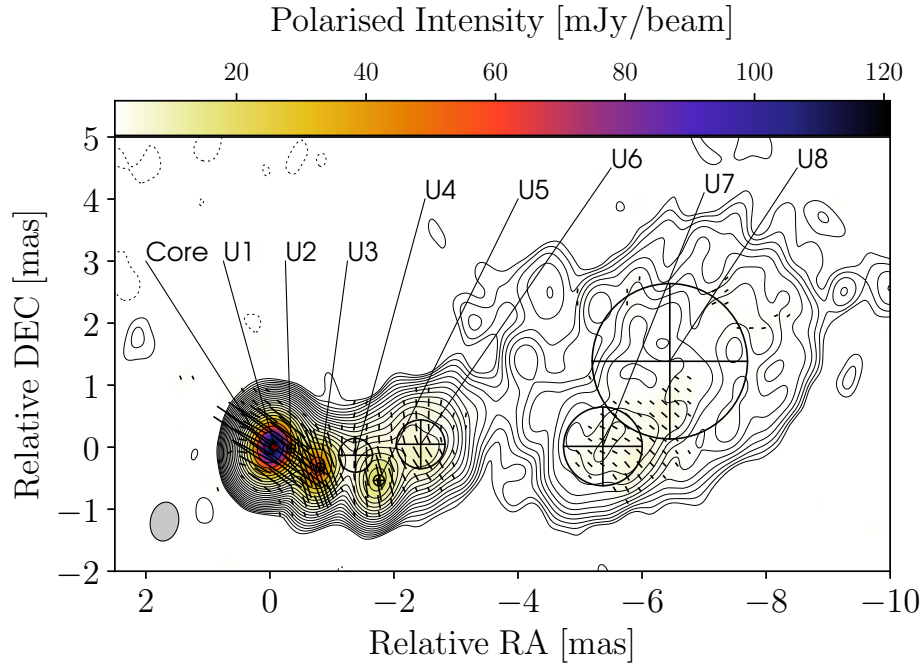


Figure 5.3: VLBA MOJAVE image of the total intensity and linearly polarised emission of 3C 345 at 15.3 GHz, observed on March 5, 2016. The map of the polarised intensity P is shown in colour-scale, overlaid with contours displaying the total intensity emission. The beam size is displayed on the bottom left with a resolution of 0.63×0.46 mas at a P.A. of -10.29° . The lines show the EVPAs the length of which is proportional to P . Contour levels are (% of peak emission of 3.44 Jy/beam): $-0.031, 0.031, 0.063, 0.125, 0.25, 0.5, 1.0, 2, 2.83, 4, 5.65, 8, 11.31, 16, 22.63, 32, 45.25, 64, 90.51$. The crossed circles display the positions and sizes of the circular Gaussian components that were fitted to the data, and the parameters are listed with the respective component names in Table 5.2.

For estimating the brightness temperature from the visibilities, one assumes a circular Gaussian distribution:

$$V = V_0 \exp\left(\frac{-\pi^2 \theta^2 q^2}{4 \ln 2}\right), \quad (5.1)$$

with θ being the size of the emitting region, q is the radial (u, v) -distance ($q = \sqrt{u^2 + v^2}$) in units of the wavelength λ , V_q is the visibility at the given distance q and V_0 the visibility at $q = 0$ (i.e., zero spacing, corresponding to the total flux density). Subsequently, it follows that

$$\theta = \frac{2 \ln 2}{\pi} \frac{\lambda}{B \sqrt{\ln(V_0/V_q)}}, \quad (5.2)$$

with $B = q \cdot \lambda$. Then the brightness temperature

$$T_b = \frac{\pi}{2k} \frac{B^2 V_0}{\ln(V_0/V_q)}. \quad (5.3)$$

For $V_0 = eV_q$, Eq. 5.3 has a minimum. Thus one can estimate the minimum brightness temperature as:

$$T_{b,\min} = \frac{\pi e}{2k} B^2 V_q, \quad (5.4)$$

where one only needs to assume a Gaussian brightness distribution. The maximum, or limiting brightness temperature can be obtained from Eq. 5.3 when adopting $V_0 = V_q + \sigma_q$

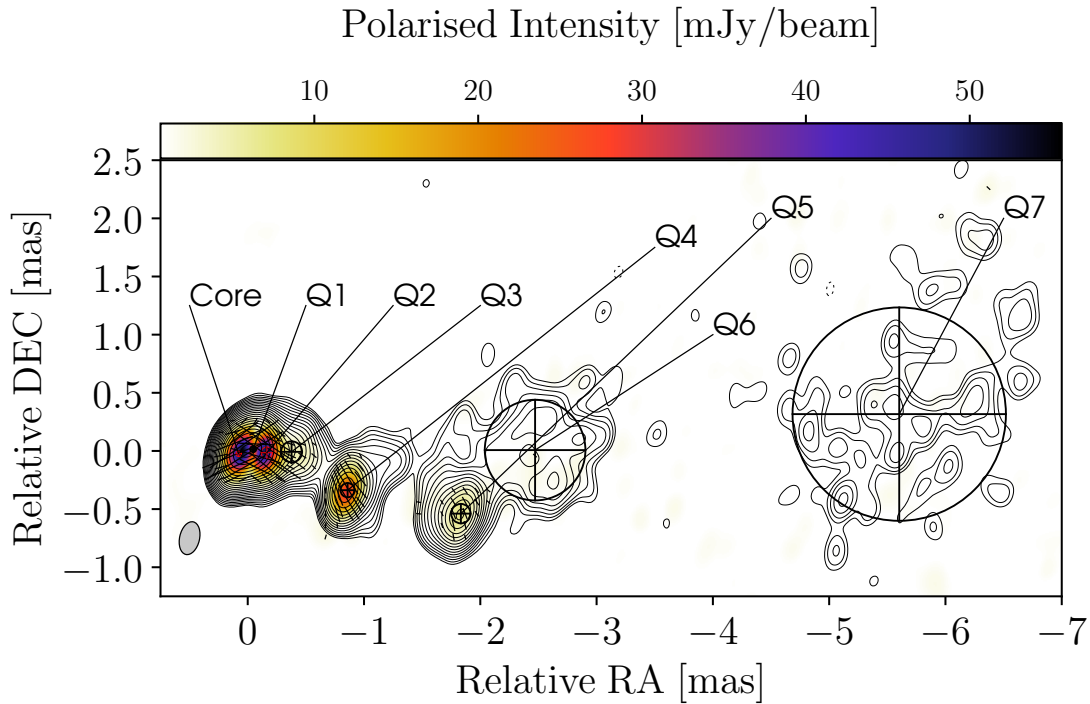


Figure 5.4: VLBA image of the total intensity and linearly polarised emission of 3C 345 at 43.1 GHz, observed on March 18, 2016 (BU blazar program). The map of the polarised intensity P is shown in colour-scale, overlaid with contours displaying the total intensity emission. The beam size is displayed on the bottom left with a resolution of 0.29×0.17 mas at a P.A. of -12.97° . The lines show the EVPAs the length of which is proportional to P . Contour levels are (% of peak emission of 1.68 Jy/beam): -0.063 , 0.063 , 0.125 , 0.25 , 0.5 , 1.0 , 2 , 2.83 , 4 , 5.65 , 8 , 11.31 , 16 , 22.63 , 32 , 45.25 , 64 , 90.51 . The crossed circles display the positions and sizes of the circular Gaussian components that were fitted to the data, and the parameters are listed with the respective component names in Table 5.3.

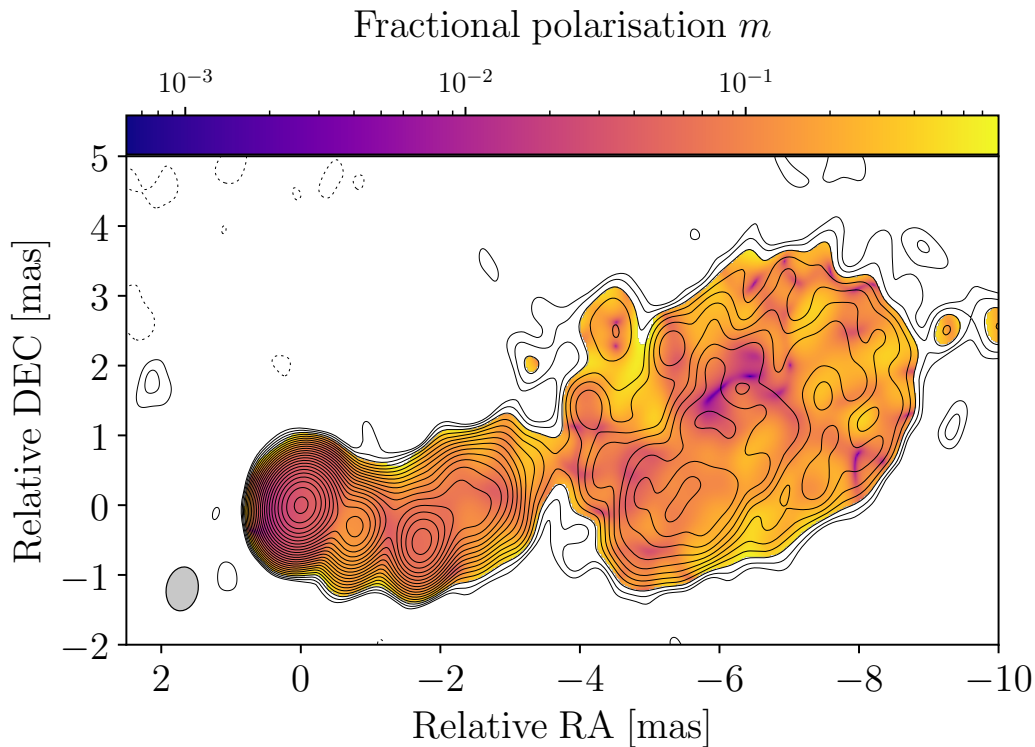


Figure 5.5: Same as Fig. 5.3, but displaying the fractional polarisation m in logarithmic colour scale.

as a lower limit. This effectively corresponds to the condition that the feature probed by the visibility V_q is marginally resolved. So this provides a reasonable limit for the longer baselines, especially for my *RadioAstron* data.

Generally, the estimates of the brightness temperature from the visibilities are most accurate for baselines $> 200 \text{ M}\lambda$, where $T_{b,\min}$ and $T_{b,\max}$ provide a reliable constraint on T_b (Lobanov 2015). As shown in Fig. 5.6, the data were binned into $10 \text{ M}\lambda$ bins, and for the bin at the largest (u, v) -distances, an average $T_{b,\min} = 6.46 \times 10^{12} \text{ K}$ and $T_{b,\max} = 1.90 \times 10^{13} \text{ K}$ has been calculated, which are the values that I will use in the following analysis.

From the Gaussian component fits, T_b is calculated as (see Eq. 1.6):

$$T_b = \frac{S_\nu c^2}{2 k_B \nu^2 \Omega}, \quad (5.5)$$

where S_ν denotes the flux density, c the speed of light, k_B the Boltzmann constant, ν the observing frequency, and Ω is the component solid angle. The highest T_b , that is calculated for component L3 (see Table 5.2), lies between $T_{b,\min}$ and $T_{b,\max}$ at $8.96 \times 10^{12} \text{ K}$, close to the maximum value. So the values obtained for $T_{b,\min}$ and $T_{b,\max}$ seem to provide a reasonable bracketing for the highest component brightness temperature.

It is generally thought that, for incoherent synchrotron sources such as AGN, if T_b increases to values larger than about 10^{12} K , the amount of energy released due to the Inverse Compton (IC) process becomes too large to be sustainable. This ‘‘IC catastrophe’’ reduces T_b again to values of about 10^{12} K on timescales of a day (Kellermann and Pauliny-Toth 1969). This is because of the strong dependence of the ratio of IC to synchrotron luminosities on the brightness temperature:

$$\frac{L_{\text{IC}}}{L_{\text{synch}}} \propto \left(\frac{T_b}{10^{12} \text{ K}} \right)^5 \left[1 + \left(\frac{T_b}{10^{12} \text{ K}} \right)^5 \right]. \quad (5.6)$$

This threshold is referred to as the IC limit. Readhead (1994) argued that the equipartition brightness temperature $T_{b,\text{eq}}$ might be a better constraint for the upper value of the brightness temperature, which is generally more of the order of 10^{11} K . It assumes an equipartition of the energy of particles and magnetic fields. For 3C 345, a value very close to 10^{11} K is estimated according to Readhead (1994):

$$T_{\text{eq}} = 1.6 \cdot 10^{12} \cdot h^{-2/17} F(\alpha)^{-2} \left[\frac{1 - (1+z)^{-1/2}}{1+z} \right] \cdot \left[\frac{1+z}{D} \right]^{(2\alpha-13)/17} S'_{\text{op}}{}^{1/17} (\nu'_{\text{op}})^{(1+2\alpha)/17}, \quad (5.7)$$

with $H_0 = h \cdot 100 \text{ km s}^{-1} \text{ Mpc}^{-1}$, with $h = 0.7$ for the assumed cosmology. Also, S'_{op} is the peak flux density and ν'_{op} is the turnover frequency in the observer’s frame (denoted as primed quantities). $F(\alpha)$ is defined as (Scott and Readhead 1977)

$$F(\alpha) = 1.6 \cdot C(\alpha) \left[\frac{\nu_{\text{low}}^{0.5-\alpha} - \nu_{\text{high}}^{0.5-\alpha}}{(2\alpha-1)f_1(\alpha)} \right]^{1/17} f_2(\alpha), \quad (5.8)$$

where $C(\alpha)$ is given in Shaffer et al. (1977), and $C(-0.2) = 2.25$ is adopted. Also (Scheuer and Williams 1968)

$$f_1(\alpha) = \frac{\alpha/2 + 2/3}{4\sqrt{3}(\alpha/2 + 1/2)(\alpha/2 + 11/12)} \cdot \frac{\hat{\Gamma}\left(\frac{3\alpha + 1}{6}\right) \hat{\Gamma}\left(\frac{3\alpha + 5}{6}\right)}{\hat{\Gamma}\left(\frac{6\alpha + 5}{12}\right) \hat{\Gamma}\left(\frac{6\alpha + 13}{12}\right)} \quad \text{and} \quad (5.9)$$

$$f_2(\alpha) = \frac{\alpha/2 + 11/2}{\alpha/2 + 2/3}, \quad (5.10)$$

where $\hat{\Gamma}$ is the complete Euler- Γ -function, which is used to replace the original factorial notation in Scheuer and Williams (1968) according to $(x-1)! = \hat{\Gamma}(x)$. The spectral index α is calculated as

$$\alpha = \frac{\log(S_{\nu_{\text{high}}}) - \log(S_{\nu_{\text{low}}})}{\log(\nu_{\text{high}}) - \log(\nu_{\text{low}})}, \quad (5.11)$$

and for Effelsberg measurements at $\nu_{\text{low}} = 10.5$ GHz and $\nu_{\text{high}} = 13.0$ GHz listed in Table 4.1, it yields $\alpha = -0.22 \pm 0.20$. This is in accordance with the value from Liu et al. (2018), who obtained $\alpha = -0.2$ with Effelsberg data from July 2014. It should be noted here that $T_{\text{b,eq}}$ depends only weakly on α . As a proxy for the peak flux density, the single-dish flux density at 1.6 GHz is used. Equation 5.7 gives an upper limit on $T_{\text{b,eq}}$ in case one is not using the actual peak flux density of the spectrum. With these values, $T_{\text{b,eq}} = 10^{10.7}$ is calculated.

The effect of the source redshift z and Doppler boosting (see Eq. 1.29 and 1.31) is considered according to:

$$T_{\text{b,obs}} = \delta \frac{T_{\text{b,int}}}{(1+z)}, \quad (5.12)$$

where $T_{\text{b,obs}}$ denotes the brightness temperature in the observer's frame and $T_{\text{b,int}}$ in the source frame. The jet Doppler factor is denoted by δ and θ is the jet viewing angle. In the following, a Doppler factor $\delta = 9.1 \pm 1.9$ is assumed as reported in Liodakis et al. (2017), calculated from variability arguments for the source. They also constrain the Doppler factor with assumptions on the IC emission (Ghisellini et al. 1993), yielding similar results. VLBI monitoring within the VLBA-BU-BLAZAR Program at 43 GHz also shows Doppler factors of the order of 10 (Jorstad et al. 2017). From these corrections one would expect the theoretical value not to exceed $T_{\text{b}} = 5.7 \times 10^{12}$ K in the source frame.

The visibility amplitudes imply the presence of emitting regions with observed brightness temperature in excess of the IC limit. This suggests either locally efficient injection or re-acceleration of particles in the jet to counter the inverse Compton cooling, or that the geometry of the jet creates significant changes in the Doppler factor, resulting in the sufficiently large Doppler boosting. Efficient particle re-acceleration could, for example, be achieved with turbulent plasma flowing down the jet and crossing a standing shock (Marscher 2014). Alternatively, magnetic reconnection events can efficiently accelerate particles (e.g. Sironi et al. 2015).

Doppler boosting due to changes in the viewing angle along the jet has been investigated by Qian et al. (1996) for 3C 345, who find that the position and flux variability of a component could be explained with helical motion. A similar well-pronounced case of a helical jet pattern is known in the source 1156+295 (Hong et al. 2004; Zhao et al. 2011). Variations in the jet orientation for the innermost 1 mas of the jet in 3C 345 within about 60° over 15 years also support such a scenario (Lister et al. 2013), and the helical motion could possibly be explained by precession of the accretion disc (Lobanov and Roland

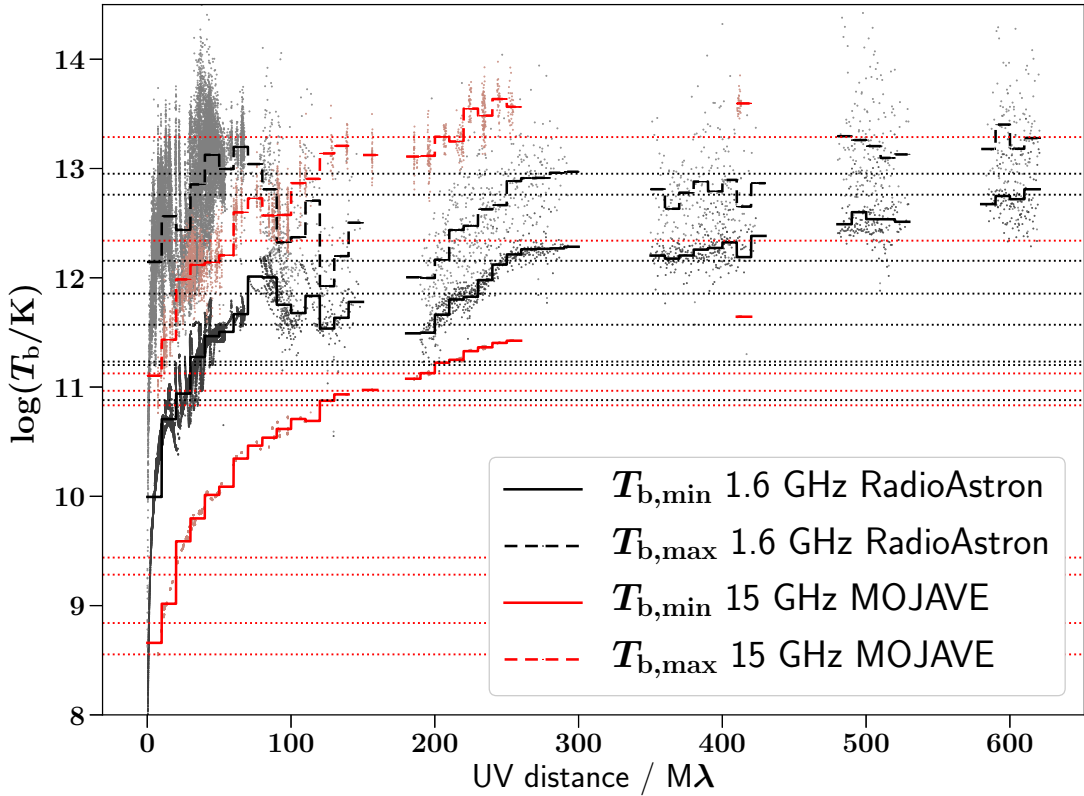


Figure 5.6: Minimum brightness temperature $T_{b,\min}$ and maximum brightness temperature $T_{b,\max}$ as a function of (u, v) -distance. The values were estimated from the visibilities following Lobanov (2015). The solid (dashed) lines show the average $T_{b,\min}$ ($T_{b,\max}$) in bins of $10 \text{ M}\lambda$ for *RadioAstron* (black) and MOJAVE (red), while the points show the individual data values with the same colour scheme. The dashed horizontal lines show T_b calculated from Gaussian component fits (see Table 5.2). $T_{b,\min}$ and $T_{b,\max}$ provide a reasonable bracketing for the brightness temperature at least for the *RadioAstron* data.

2005). Qian et al. (1996) find variability in the Doppler factor between 7 and 11, caused by the difference in viewing angle. This would be insufficient to explain the high $T_{b,\min}$ in my *RadioAstron* observations, where one would need $\delta > 11$. Schinzel et al. (2012) have investigated the Doppler factor for different components in 3C 345 observed between 2008 and 2010 at 43 GHz. They find Doppler factors as high as 23 for one component. Jorstad et al. (2017) also find maximum Doppler factors of about 17. Such high Doppler boosting could readily explain the high observed brightness temperatures, however I can not identify single components in the *RadioAstron* map with the components presented in these works.

Still, the inferred brightness temperatures from this work easily exceed the estimated $T_{b,\text{eq}}$ by an order of magnitude, suggesting that the jet in 3C 345 is, at least in part, not in equipartition. This indicates a flaring event, that is also supported by the radio light curve and the bright polarisation component that is observed at 1.5 mas (see Sect. 4.3).

5.2.1 Refractive substructure

More extreme values for the brightness temperature have been found in other sources observed by *RadioAstron*, e.g., in 3C 273 (Kovalev et al. 2016) and BL Lac (Gómez et al. 2016). Kovalev et al. (2016) suggest refractive substructure as a possible source of the high observed T_b , which has been investigated by Johnson et al. (2016). Following this, the possible effect of scattering on the estimated brightness temperature is also investigated

here. This effect is more prominent at longer wavelengths and starts contributing to the observed signal at $\lambda = 18$ cm at any baseline larger than $\sim 70,000$ km (~ 400 M λ), if the flux density at zero spacing is > 1 Jy and T_b is in the range of the values that are also obtained here (cf. Fig. 1 and 3 in Johnson et al. 2016).

To calculate $T_{b,\min}$, Eq. 3 in Johnson et al. (2016) is used, which accounts for both refractive substructure and angular broadening. The former will lead to an overestimate, the latter to an underestimate of $T_{b,\min}$:

$$T_{b,\min} = 1.2 \times 10^{12} \text{ K} \left(\frac{B}{10^5 \text{ km}} \right)^{5/6} \left(\frac{F_B}{20 \text{ mJy}} \right) \cdot \left(\frac{D}{1 \text{ kpc}} \right)^{1/6} \left(\frac{\lambda}{18 \text{ cm}} \right) \left(\frac{\theta_{\text{scatt}}}{300 \mu\text{as}} \right)^{-5/6}, \quad (5.13)$$

where B denotes the baseline length and F_B the measured flux density at this baseline. Adopting the NE2001 model (Cordes and Lazio 2002) for the Galactic distribution of free electrons, an angular broadening of $\theta_{\text{scatt}} = 0.28$ mas is estimated for the galactic coordinates of 3C 345 ($l = 63^\circ.45$, $b = 40^\circ.95$). At an assumed distance to the scattering screen of $D = 1$ kpc, $T_{b,\min} = 1.5 \times 10^{13}$ K is determined, which is even higher than the previous estimate without considering scattering. So I conclude that refractive substructure likely does not play a role for my *RadioAstron* observations. This is not surprising as 3C 345 lies at high galactic latitude, so there is likely not enough scattering material along the line of sight to cause significant refractive substructure.

Table 5.2: Circular Gaussian model fit parameters and inferred brightness temperature from the RadioAstron and MOJAVE data.

(1) Comp.	(2) Flux [mJy]	(3) Distance [mas]	(4) P.A. [°]	(5) Size [mas]	(6) T_b [K]	(7) m [%]	(8) χ [°]	(9) RM [rad m ⁻²]
<i>RadioAstron 1.6 GHz</i>								
Core	382±45	1.48±0.07	79.0±2.7	0.37±0.04	(1.43±0.32) × 10 ¹²	1.6±0.7	43±6	-17.9±12.7
L1	717±65	0.92±0.08	95.1±4.8	0.71±0.06	(7.16±1.33) × 10 ¹¹	0.9±0.8	68±1	15.2±9.7
L2	471±37	0.19±0.04	44.8±12.4	0.20±0.01	(5.76±0.85) × 10 ¹²	6.4±0.6	56±1	19.5±2.8
L3	334±29	0.25±0.04	-112.4±9.2	0.14±0.01	(8.96±1.38) × 10 ¹²	3.8±0.6	60±2	120.1±4.7
L4	373±30	1.09±0.07	-76.6±3.5	0.71±0.05	(3.72±0.60) × 10 ¹¹	4.7±2.4	55±7	123.1±2.0
L5	182±24	1.76±0.12	-46.0±4.0	0.73±0.09	(1.71±0.49) × 10 ¹¹	7.6±3.3	51±6	...
L6	1068±108	3.73±0.19	-79.3±2.9	1.85±0.18	(1.59±0.35) × 10 ¹¹	6.7±1.4	94±3	...
L7	831±144	5.69±0.42	-67.6±4.2	2.36±0.40	(7.59±2.87) × 10 ¹⁰	4.4±3.4	153±11	...
<i>MOJAVE 15 GHz</i>								
Core	1445±36	0.083±0.009	91.9±6.5	< 0.02	> 1.94 × 10 ¹³	2.87±0.04	55.0±0.1	...
U1	2200±44	0.077±0.008	-87.9±5.8	0.077±0.001	(2.19±0.08) × 10 ¹⁰	3.64±0.03	55.0±0.2	...
U2	312±17	0.34±0.02	-93.2±4.0	0.141±0.006	(9.24±1.01) × 10 ¹⁰	4.3±0.1	50.7±0.4	...
U3 (25)	455±22	0.87±0.02	-111.9±1.3	0.142±0.005	(1.33±0.11) × 10 ¹¹	13.1±0.3	19.1±0.3	...
U4	97±12	1.39±0.08	-95.4±3.4	0.55±0.06	(1.92±0.44) × 10 ⁹	6.5±1.6	-9.9±3.1	...
U5 (23)	353±19	1.84±0.02	-106.9±0.7	0.175±0.007	(6.81±0.67) × 10 ¹⁰	5.9±0.4	12.4±0.8	...
U6 (20)	286±20	2.43±0.06	-88.9±1.5	0.78±0.05	(2.75±0.47) × 10 ⁹	9.1±1.4	26.7±2.3	...
U7 (12)	188±19	5.37±0.14	-89.9±1.5	1.27±0.13	(6.92±1.78) × 10 ⁸	9.6±3.3	66.1±4.9	...
U8 (18)	379±51	6.59±0.35	-77.9±3.0	2.50±0.34	(3.58±1.12) × 10 ⁸	8.6±7.3	80.4±10.5	...

NOTE: Columns display the (1) component name, (2) flux density, (3) radial distance from the total intensity peak, (4) component position angle, (5) component FWHM size, (6) brightness temperature, (7) fractional polarisation, (8) Electric Vector Position Angle and (9) rotation measure, where applicable. Where the component size was smaller than the minimal resolvable source size in the map, a lower limit is provided (see Sect. 4.2.1 for details). Note that the errors are purely statistical errors and may be underestimated. For the components in the MOJAVE data, the names of the components in the MOJAVE database are added in brackets, if they could be cross-identified with my model fit.

Table 5.3: Circular Gaussian model fit parameters and inferred brightness temperature from the VLBA data at 4.8, 8.4 and 43.1 GHz.

(1) Comp.	(2) Flux [mJy]	(3) Distance [mas]	(4) P.A. [°]	(5) Size [mas]	(6) T_b [K]	(7) m [%]	(8) χ [°]
VLBA 4.8 GHz							
Core	1800±12	0.05±0.01	87.5±12.2	0.0594±0.0003	(3.06±0.03) × 10 ¹³	4.36±0.02	41.59±0.06
C1	1084±9	1.32±0.02	-105.6±0.7	0.425±0.003	(3.60±0.05) × 10 ¹¹	5.76±0.03	35.95±0.08
C2	334±5	2.27±0.03	-85.3±0.7	0.125±0.001	(1.29±0.04) × 10 ¹²	8.31±0.09	38.5±0.1
C3	671±9	5.34±0.04	-82.7±0.4	2.11±0.02	(9.03±0.24) × 10 ⁹	8.7±0.1	58.9±0.2
C4	347±6	7.37±0.06	-72.7±0.4	2.24±0.04	(4.15±0.16) × 10 ⁹	2.2±0.2	52.4±1.2
C5	201±7	16.58±0.22	-71.8±0.8	5.55±0.20	(3.92±0.32) × 10 ⁸	9.2±1.2	83.7±2.1
C6	66±3	21.37±0.21	-52.9±0.6	4.13±0.18	(2.33±0.23) × 10 ⁸	6.6±2.4	56.5±4.7
VLBA 8.4 GHz							
Core	2459±46	0.08±0.02	-86.3±13.8	0.207±0.003	(1.13±0.04) × 10 ¹²	1.87±0.01	59.1±0.1
X1	577±22	0.97±0.04	-108.5±2.3	0.050±0.002	> 2.13 × 10 ¹²	7.92±0.04	36.5±0.1
X2	417±19	1.82±0.05	-103.6±1.5	0.233±0.007	(1.51±0.12) × 10 ¹¹	7.26±0.08	26.3±0.1
X3	250±15	2.48±0.08	-85.0±1.7	0.70±0.03	(9.89±1.11) × 10 ⁹	8.9±0.2	30.5±0.3
X4	461±26	5.79±0.12	-85.7±1.2	1.70±0.09	(3.12±0.37) × 10 ⁹	10.7±0.2	58.4±0.4
X5	169±18	8.30±0.26	-76.9±1.8	2.12±0.21	(7.41±1.69) × 10 ⁸	2.5±0.7	-41.5±4.8
BU blazar program VLBA 43.1 GHz							
Core	1059±17	0.082±0.003	107.1±1.8	0.0475±0.0005	(3.51±0.10) × 10 ¹¹	3.54±0.05	-61.0±0.2
Q1	1255±17	0.050±0.002	-71.7±2.6	0.0512±0.0005	(3.56±0.08) × 10 ¹¹	1.69±0.04	-73.4±0.3
Q2	496±11	0.165±0.004	-95.3±1.4	0.099±0.002	(3.77±0.15) × 10 ¹⁰	6.98±0.09	55.8±0.2
Q3	115±6	0.37±0.01	-91.2±1.9	0.181±0.008	(2.62±0.27) × 10 ⁹	6.5±0.7	66.8±1.6
Q4	177±8	0.923±0.009	-111.4±0.6	0.122±0.004	(8.80±0.74) × 10 ⁹	21.8±0.5	28.8±0.3
Q5	163±8	1.91±0.01	-106.4±0.3	0.167±0.007	(4.35±0.42) × 10 ⁹	7.1±0.6	20.1±1.3
Q6	107±66	2.47±0.55	-89.8±12.6	0.87±0.54	(1.06±1.47) × 10 ⁸	45.0±15.8	43.7±4.9
Q7	141±66	5.61±0.86	-86.8±8.7	1.83±0.85	(3.13±3.26) × 10 ⁷	5.0±20.4	-47.4±57.4

NOTE: Columns display the (1) component name, (2) flux density, (3) radial distance from the total intensity peak, (4) component position angle, (5) component FWHM size, (6) brightness temperature, (7) fractional polarisation and (8) Electric Vector Position Angle. Where the component size was smaller than the minimal resolvable source size in the map, a lower limit is provided (see Sect. 4.2.1 for details). Note that the errors are purely statistical errors and may be underestimated.

5.2.2 Comparison with brightness temperatures from MOJAVE data

The brightness temperatures obtained from the 1.6 GHz space-VLBI data is compared with estimates obtained with the same methods using MOJAVE 15 GHz observations. To make a reasonable comparison of the two data sets, a filter is applied on the visibilities of the MOJAVE data, so that only data that occupy the same location (within 10 %) in the (u, v) -plane as the 1.6 GHz data are used for the MOJAVE brightness temperature estimate. I present $T_{b,\min}$ as a function of the (u, v) -radius in Fig. 5.6. As for the *RadioAstron* data, both the brightness temperatures obtained from the visibilities as well as those obtained from the Gaussian component fits are plotted (see again Fig. 5.6).

The range between $T_{b,\min}$ and $T_{b,\max}$ is larger for the MOJAVE data compared to the *RadioAstron* data. This could be due to the underestimated visibility errors in the former, so $T_{b,\max}$ might not be well defined, leading to a poor determination of $T_{b,\max}$. This may also indicate that the components in the inner jet are mostly unresolved. Nevertheless, the maximum brightness temperature from Gaussian component fits to the MOJAVE data still lies between the limits provided by $T_{b,\min}$ and $T_{b,\max}$. I will concentrate on the comparison between the different $T_{b,\min}$.

One can see significantly higher values for $T_{b,\min}$ in the 1.6 GHz *RadioAstron* data compared to the 15 GHz MOJAVE data. That is expected, as $T_b \propto \lambda^2$, and any differences in the ratio $T_{b,\min,RA}/T_{b,\min,MOJ}$ that differs from $(18 \text{ cm}/2 \text{ cm})^2$ as a function of UV distance seen in Fig. 5.6 can be interpreted as a non-zero spectral index. Indeed a trend of decreasing ratios for increasing (u, v) -distances is observed, which can be interpreted as a progressive change of the jet opacity from optically thin to thick with increasing baseline lengths in the innermost jet region. This is the case because the longest baselines primarily probe the bright, innermost part of the jet.

5.3 Variability timescale

Liu et al. (2018) have investigated the variability properties of a large samples of AGN observed with *RadioAstron* in terms of their modulation index at 5 GHz. The modulation index is defined as $m = \sigma_0/S_0$, where σ_0 and S_0 are the standard deviation and mean of a Gaussian distribution of flux density measurements.

3C 345 did not show any signs of intra-day variability (IDV), with m being consistent with zero, although the source is known to exhibit long-term (months to years) variability, as shown in observations at the Green Bank Interferometer at 2 GHz and 8 GHz (Rickett et al. 2006) and the VLA MASIV program (Lovell et al. 2008). Also at higher frequencies of up to 43 GHz, 3C 345 shows variability (e.g. Angelakis et al. 2019). The lack of IDV is not surprising considering the high Galactic latitude of 3C 345, as IDV is likely caused by scintillation due to the Galactic interstellar medium (Rickett et al. 2006). From the smallest component size in the *RadioAstron* data (for component L3), one can estimate the shortest variability timescale according to Jorstad et al. (2017):

$$\tau \sim \frac{25.3\theta D_L}{\delta(1+z)}. \quad (5.14)$$

Here τ is the variability timescale in years, θ is the component FWHM in mas (as given in Table 5.2), D_L is the luminosity distance and δ is the Doppler factor. Considering Doppler factors between 10 and 25 (see Sect. 5.2), the shortest variability timescale is estimated to be between 1 to 4 months, where only the lower estimate is broadly consistent with $\tau = 14.1 \text{ d}$, as found by (Rickett et al. 2006). This indicates that the component size is still slightly underestimated and not quite resolved.

The variability in 3C 345 has also been studied by Lähteenmäki et al. (1999) with data from the Metsähovi quasar monitoring program. They determine the variability timescale from flux density gradients, and calculate the variability brightness temperature. They report values of 10^{11} K, close to the equipartition value, which is significantly lower than the brightness temperatures obtained from the *RadioAstron* observations.

5.4 Core shift

For estimating the core shift between different frequencies, I use the GUI-based Python program developed by Laura Vega-García at the MPIfR, described in her PhD thesis (Vega García 2019). It employs the 2D cross-correlation algorithm as described in Lewis (1994). The procedure as used for astronomical images is explained in more detail in e.g., Croke and Gabuzda (2008) and Fromm (2012). The cross-correlation coefficient cc is given as:

$$cc = \frac{\sum_i \sum_j (I_{\nu_1}(i, j) - \overline{I_{\nu_1}})(I_{\nu_2}(i + \Delta i, j + \Delta j) - \overline{I_{\nu_2}})}{\sqrt{\sum_i \sum_j (I_{\nu_1}(i, j) - \overline{I_{\nu_1}})^2 \sum_i \sum_j (I_{\nu_2}(i + \Delta i, j + \Delta j) - \overline{I_{\nu_2}})^2}}, \quad (5.15)$$

where I_ν are the image intensities at the frequencies ν_1 and ν_2 at pixel coordinates i and j , and \overline{I} denotes the mean of an image. The algorithm searches for a maximum of cc for different shifts Δi and Δj . For the 2D cross-correlation, the optically thick core region should not be used as its position will change with frequency. The program of Vega García (2019) allows for a rectangular selection of a presumably optically thin region as an input for the correlation in both images.

For the 2D cross-correlation method one needs to convolve the maps that are to be aligned with the same beam, corresponding to the larger beam size. The maps need to have the same pixel size as well. Fromm et al. (2013) used a common pixel size of 1/20 of the beam size at the higher frequency (i.e., the smallest beam), so that no structural information is lost. For each pairwise alignment of two maps, I decided to use the pixel size from the map with the smallest pixel size, in most cases from the higher frequency map (except for the *RadioAstron* map). The formally best achievable accuracy of the 2D cross-correlation method is equal to the pixel size used (Vega García 2019). However, one can assess the quality of the obtained shift by inspecting the 2D distribution of correlation coefficients as a function of shifts in declination and right ascension, as displayed in Fig. A.1 to A.5 in the appendix A.

Another way to obtain the core shift is by using the features described by Gaussian model fits further downstream of the jet core that are optically thin, meaning their position does not change with frequency. If one can cross-identify one or more of such components in both data sets, one can align the multifrequency images with the positions of these components and obtain the core shift as the difference between the distance of the cores to the respective optically thin components.

Different alignments were tested with the components presented in Tab. 5.2 and 5.3. It proved difficult to cross-identify one specific component for all frequencies. For the lower frequencies at 1.6 and 4.8 GHz, the best alignment is obtained with components L6 and C3. At these low frequencies, the extended emission ~ 4 mas and further downstream of the jet is more reliably detected. At higher frequencies, aligning the maps with these components is challenging, yielding mostly unreasonable shifts between the maps. This may be due to the `clean` algorithm that is less sensitive to extended emission, and uncertainties in the cleaning in the process of hybrid imaging may have introduced uncertainties in the positions of the optically thin features.

So for higher frequencies, it was tried to align the maps with components that are situated more in the inner jet region. A cross-identification of components L5, C2, X3,

M6, and Q6 was attempted. With these components, one can reach an alignment similar to the result from the 2D cross-correlation. However, it became clear that the low-resolution observations at 4.8 and 8.4 GHz were not sufficient to resolve the components in the 1.6 and 15.3 GHz maps in the regions around components L4, L5, U5, and U6. Another issue is that, in general, components that are identified with `modelfit` may not correspond to real features in the image, but may be just mathematical constructs needed to reproduce a complex brightness distribution (Lister et al. 2009). Thus, to avoid these uncertainties with component identification, I decided to use the alignment obtained from the 2D cross-correlation.

In general, the maps are shifted so that their phase centre coincides with the total intensity peak. Therefore, the obtained shifts had to be re-referenced to the respective core position, which does not coincide with the total intensity peak in the maps, especially for the 1.6 GHz *RadioAstron* map. The core position was determined as the position of the Gaussian component most upstream in the jet.

To avoid uncertainties introduced by the different beam sizes, only the shifts between adjacent frequency maps in my dataset are calculated, and the core shifts were obtained from cumulative shifts (same procedure as in e.g., Fromm et al. 2013). The so obtained core shifts are displayed in Table 5.4.

Table 5.4: Core shifts with respect to the core position in the 15.3 GHz map.

(1)	(2)	(3)	(4)	(5)	(6)	(7)	(8)
ν	b_{maj}	b_{min}	θ_b	Δx	Δy	Δr	$\Delta\phi$
[GHz]	[mas]	[mas]	[$^\circ$]	[mas]	[mas]	[mas]	[$^\circ$]
1.6	1.249	0.316	10.50	-0.62 ± 0.13	-0.30 ± 0.08	0.688 ± 0.245	-116.2 ± 7.9
4.8	3.877	1.568	19.95	-0.22 ± 0.10	-0.33 ± 0.10	0.393 ± 0.206	-145.8 ± 15.0
8.4	0.934	2.183	20.96	-0.17 ± 0.03	-0.01 ± 0.03	0.17 ± 0.06	-94.1 ± 9.8
15.3	0.633	0.456	-10.29
43.1	0.287	0.171	-12.97	0.13 ± 0.01	0.03 ± 0.01	-0.13 ± 0.03	-104.1 ± 6.2

NOTE: Columns display the (1) observing frequency, (2) beam major axis, (3) beam minor axis, (4) beam position angle, (5) core shift in right ascension, (6) core shift in declination, (7) radial core shift (8) direction of the core shift.

One expects a frequency dependence of the core shift according to Eq. 1.67. The obtained core shifts are plotted vs. frequency and a fit to the data a function of the form

$$\Delta r = A \cdot \nu^{-1/k_r} + r_0 \quad (5.16)$$

is conducted. As the function has three parameters, A , k_r and r_0 , a minimum of four frequencies is needed to measure the core shift, as this will result in a minimum of three data points. A best-fit value of $k_r = 1.83 \pm 0.53$ with $\chi_{\text{red}}^2 = 1.142$ is obtained. Another fit is conducted with k_r fixed to 1, which results in $\chi_{\text{red}}^2 = 6.969$. Both fits are shown in Fig. 5.7. With these data, the fit clearly indicates a deviation from the equipartition case, where $k_r = 1$.

Schinzel (2011) studied the core shift in 3C 345 over 20 years between 1995 and 2005. They use data from the same frequencies, with the addition of 22 GHz measurements. They also reference the core shifts to 15 GHz, providing a suitable comparison. They find an average $k_r = 2.9$ across their epochs, and conclude that their poorly fitting data point at 1.6 GHz is likely strongly affected by blending with other features in the innermost jet region, which leads to an underestimation of the core shift. A fit excluding this data point yielded a k_r consistent with unity.

In principle, one expects blending effects to be less relevant for the high-resolution observations at 1.6 GHz with *RadioAstron*. However, other effects might play a role, so the same fit is run again without the data point at 1.6 GHz. The resulting fit yields $k_r = 1.04 \pm 0.10$ with $\chi_{\text{red}}^2 = 0.056$, slightly better than the fit where k_r is fixed to unity, with $\chi_{\text{red}}^2 = 0.063$. Within the errors, the fit is consistent with the $k_r = 1$ case. This corresponds to a 20-fold improvement in χ_{red}^2 , and the fit visually provides a better match for the data points. Based on the second fit, one would expect the value of the shift at 1.6 GHz to lie at 1.03 mas, an increase of ~ 0.3 mas, corresponding to about one beam size at 1.6 GHz. If k_r was indeed significantly above unity for the region of the 1.6 GHz core, it would imply that the distance of the core to the central engine is smaller than expected. This is difficult to explain in the framework of a self-absorbed jet. For the inner region of jets probed by observations at higher frequencies, a higher value of k_r could be expected due to free-free absorption in gaseous clouds surrounding the jet in the BLR. The BLR can extend up to 20 pc (Cassidy and Raine 1993), but is rather expected to extend up to about 1 pc or even lower from the central engine (Klein and Fletcher 2015). At the distance of the core region at 1.6 GHz, any absorption by gas of the BLR should be negligible. Also, such absorption would then be expected to have an even greater effect at higher frequencies, which is not observed.

From this I conclude that the core shift value measured with respect to the 1.6 GHz is indeed underestimated, although blending effects should play a minor role. The number of ground-SRT visibilities at the longest (u, v) -distances could be insufficient to reliably constrain the position of the core, as the compact core likely dominates the signal for the long (u, v) -distances. This systematic effect is not reflected in the purely statistical uncertainties given in Table 5.2. However, the most likely reason for the underestimated core shift is that, with the visibilities on space-ground baselines, one detects a weaker and compact feature upstream of the true core location compared to measurements by ground-ground baselines. This behaviour has been previously observed with VSOP (Gabuzda and Gómez 2001). In the following analysis, I will use the estimated $k_r = 1.04$ derived from the second fit without 1.6 GHz.

This result, which is in accordance with equipartition, may seem contradictory to the fact that in Sect. 5.2, it was found that the jet is likely not in equipartition. However, the highest brightness temperatures are in fact not observed in the core, but close to the jet component L2. To use Eq. 1.77 and 1.81, only equipartition in the core needs to be satisfied.

The frequency-independent core-shift measure $\Omega_{r\nu}$ and the core distance r_{core} are derived using Eq. 1.73 and 1.75, respectively. The obtained values can be inspected in Table 5.5. Pushkarev et al. (2012) found $\Omega_{r\nu} = 23.85 \text{ pc GHz}$ and $r_{\text{core}} = 29.94 \text{ pc}$ from core shift measurements to a reference frequency of 15 GHz, with measurements from frequencies between 8.1 and 12.1 GHz. Overall my values for r_{core} and $\Omega_{r\nu}$ are consistent with the values presented there. The position angles of the core shift derived there are around -90° . My values at 8.4 GHz are consistent with this, although the values at other frequencies, especially at the lower frequencies, deviate quite significantly from that. This trend is illustrated in Fig. 5.9, where the core shift in right ascension and declination for the different frequencies with respect to 15.3 GHz is plotted. Schinzel (2011) also noted a similar behaviour. In their study of the core shift in 3C 345 they obtain an average $\Omega_{r\nu} = (23.80 \pm 0.94) \text{ pc GHz}$, very close to my values. The position angle of the core shift at the lower frequencies, between 1.6 and 5.0 GHz, deviated by a similar amount from the one at higher frequencies. The transition point of the core shift direction lies between 4.8 and 8.4 GHz in my observations, so at slightly higher frequencies. This hints at changes of the jet direction in the innermost region, where components are thought to travel on helical paths (cf. Sect. 4.3).

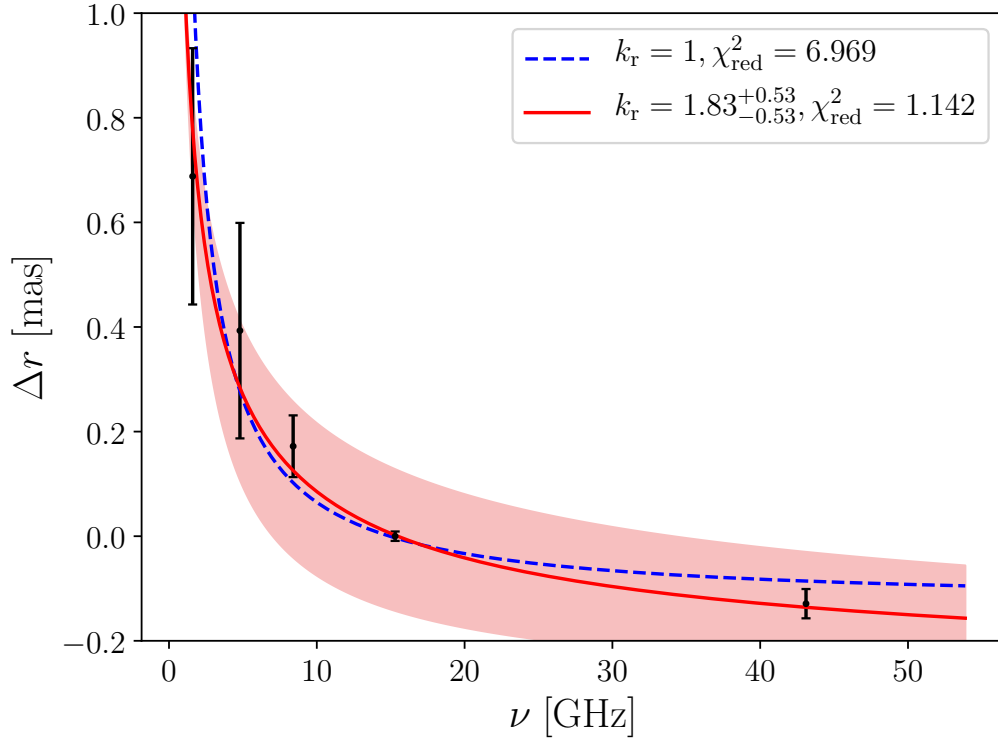


Figure 5.7: Core shift in 3C 345 based on shifts from four frequencies (1.6 GHz, 4.8 GHz, 8.4 GHz, and 43.1 GHz) relative to 15 GHz. The red line shows the best fit with $k_r = 1.83 \pm 0.53$, while the red shaded area shows the 1σ deviation. The blue dashed line shows the best fit when fixing $k_r = 1$.

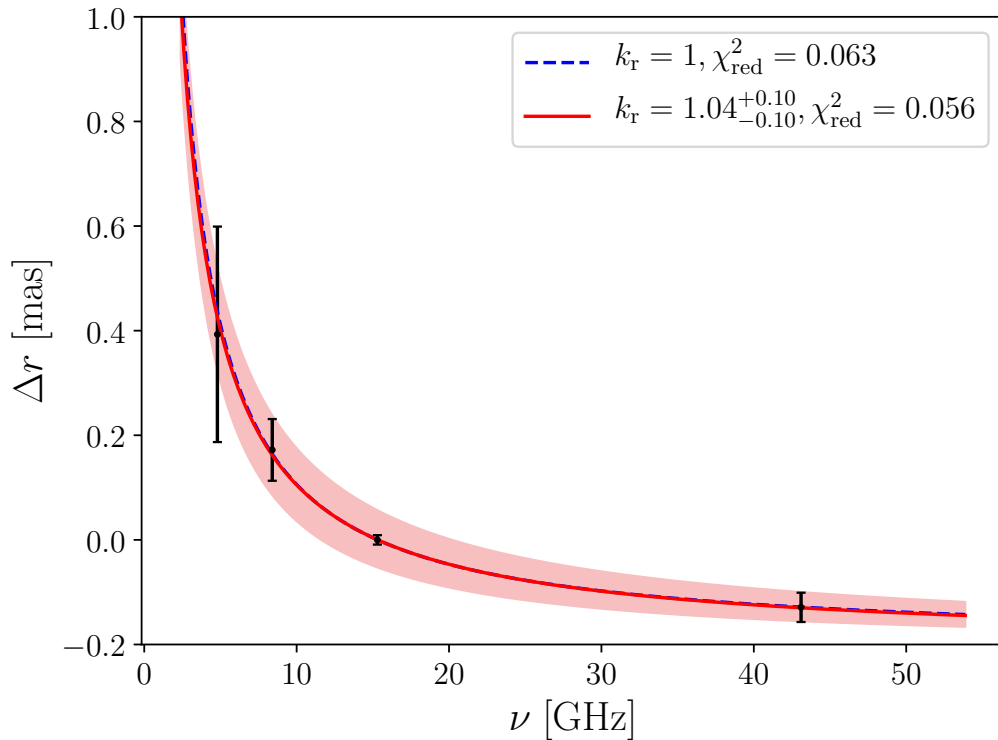


Figure 5.8: Core shift in 3C 345 based on shifts from three frequencies (4.8 GHz, 8.4 GHz, and 43.1 GHz) relative to 15 GHz. Because the shift to the lowest frequency at 1.6 GHz seems more poorly constrained (see Fig. 5.7), another fit without this frequency is performed. The red line shows the best fit with $k_r = 1.04 \pm 0.10$, while the red shaded area shows the 1σ deviation. The blue dashed line shows the best fit when fixing $k_r = 1$. Leaving out the 1.6 GHz data point yields a fit that is consistent with $k_r = 1$ within the errors.

It has been suggested that changes in the geometry of the jet can lead to a change in the observed $\Omega_{r\nu}$ with frequency, i.e. along the jet (Schinzel 2011). This can explain the somewhat lower $\Omega_{r\nu}$ observed at lower frequencies in my observations and the apparent change in position angle of the core shift at the same time. However, a change in $\Omega_{r\nu}$ can also be caused by deviations of the magnetic field or particle density along the jet, where the jet might not be in equipartition, as suggested for the region around the L2 component in the 1.6 GHz map.

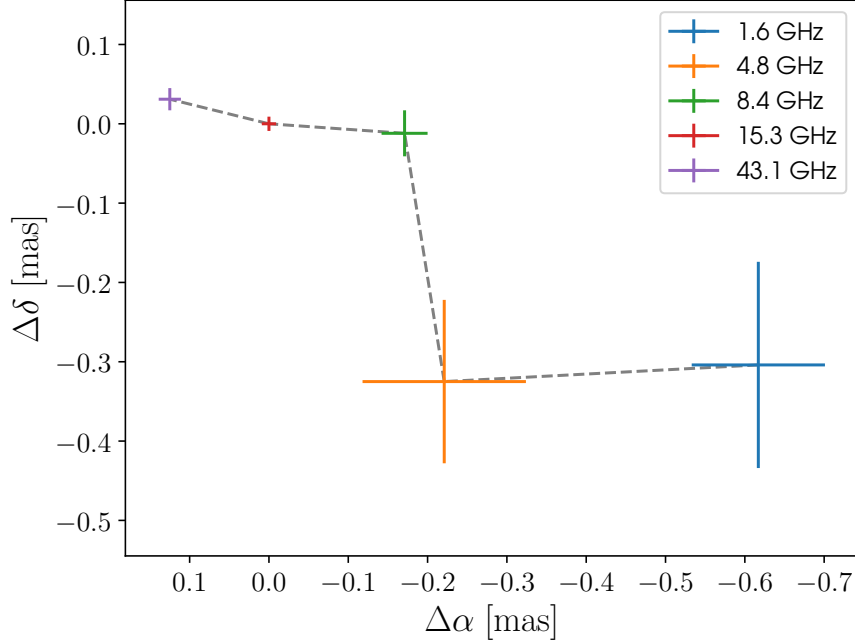


Figure 5.9: Core shifts in right ascension (x -axis) and declination (y -axis) with respect to 15.3 GHz (the 15.3 GHz data point lies at the origin). The respective values can be read off in Table 5.4. The change in direction of the core shift between higher (43.1, 15.3 and 8.4 GHz) to lower (4.8 and 1.6 GHz) is clearly visible.

Table 5.5: Quantities derived from the core shifts presented in Table 5.4.

(1) ν [GHz]	(2) $\Omega_{r\nu}$ [pc GHz]	(3) r_{core} [pc]	(4) B_1 † [G]	(5) B_{core} † [G]	(6) B_1 ‡ [G]	(7) B_{core} ‡ [G]
1.6	8.1 ± 2.9	59.2 ± 21.1	2.6 ± 0.7	0.04 ± 0.02	0.58 ± 0.15	0.010 ± 0.004
4.8	17.6 ± 9.2	44.5 ± 23.3	4.6 ± 1.8	0.10 ± 0.07	1.04 ± 0.41	0.02 ± 0.02
8.4	20.3 ± 7.0	29.8 ± 10.2	5.2 ± 1.3	0.17 ± 0.07	1.15 ± 0.30	0.04 ± 0.02
15.3
43.1	18.9 ± 4.1	5.7 ± 1.2	4.9 ± 0.8	0.85 ± 0.23	1.09 ± 0.18	0.19 ± 0.05

NOTE: Columns display the (1) frequency, (2) core shift measure, (3) distance of the core to the central engine, (4)+(6) magnetic field at 1 pc from the central engine and (5)+(7) the magnetic field in the core. † Values calculated according to Eq. 1.77 (Lobanov 1998), ‡ values calculated according to Eq. 1.81 (Hirotani 2005).

Since the result of the core shift analysis is consistent with $k_r = 1$, one can make use of Eq. 1.77 and 1.81 to calculate the magnetic field at 1 pc from the central engine, B_1 , as well as the magnetic field in the respective core, B_{core} . Both equations are derived

from slightly different approaches by (Lobanov 1998) and (Hirovani 2005), respectively, and yield somewhat different values.

For the calculation the jet Doppler factor δ is fixed to 9.1 (Liodakis et al. 2017) and the jet viewing angle $\theta = 5^\circ$ (Schinzel et al. 2012). The jet opening angle is calculated using the jet widths within the first 1 mas in the 1.6 GHz *RadioAstron* map from the jet ridge line fit (see Sect. 4.2). This yields an apparent opening angle of $\phi_0 \approx 4.9^\circ$. The deprojected jet opening angle $\phi = \phi_0 \cdot \sin \theta \approx 0.4^\circ$. The determined values can be found in Table 5.5. My values obtained with Eq. 1.81 are consistent with previous results from Pushkarev et al. (2012), who report $B_{\text{core}} = 0.04 \text{ G}$ and $B_1 = 1.2 \text{ G}$. Thus I decide to continue with these values.

5.5 Spectral index

With the alignment between the maps at different frequencies obtained from Sect. 1.5, enables the construction of spectral index maps between all adjacent frequencies. This functionality is also provided in the Python program by Vega García (2019). Again, the spectral index α is defined as $S_\nu \propto \nu^\alpha$, and α is calculated according to Eq. 5.11. The reliability of the spectral index maps was tested while determining the best map alignment (Sect. 5.4). Since the jet is not transversely resolved, one does not expect large transverse gradients in α , which are also not observed in the final maps. An exception is the spectral index distribution between 4.8 and 8.4 GHz (Fig. 5.16), where the core region shows an gradient from north to south. At the same time, a gradient is visible at $\sim 8 \text{ mas}$ in the opposite direction. Overall, the asymmetry is likely partly caused by the insufficient data quality at these frequencies. It could however also reflect the changes of the jet direction in the innermost jet region, as discussed in Sect. 5.4.

All the resulting maps are displayed in Fig. 5.10 to 5.22, where also the spectral index profile along two selected slices along the jet for each map is plotted. One slice is horizontal, and the other is chosen to reflect the overall jet direction. In addition to the adjacent frequencies, the spectral index between the 1.6 and 15.3 GHz map is calculated, as they have a comparable resolution.

Typically, an optically thick core is seen in all maps, with the spectral index declining along the jet direction. This behaviour is expected for a self-absorbed jet. Interestingly, an increase in the spectral index at $\sim 1.5 - 2 \text{ mas}$ is observed in Fig. 5.10. It almost coincides with the total intensity peak, and coincides well with the peak in polarised intensity, which is slightly offset from the peak in total intensity. This can more clearly be seen in Fig. 5.11, where both spectral index as well as total and polarized intensity are plotted along the jet. A similar feature is seen at $\sim 3 \text{ mas}$. This supports the idea that the feature around L2 corresponds to a shock front, possibly propagating down the jet.

Hovatta et al. (2014) calculated spectral index maps between 8.1 GHz and 15.4 GHz for many sources in the MOJAVE sample, including 3C 345. They found an optically thick core with $\alpha \approx 2.5$ and α declining along the jet ridge line. In earlier observations between 1995 and 1996, Ros et al. (2000) studied the spectral index between 5, 8, 15 and 22 GHz. They find the core region to be optically thick as well, with a more visible gradient where the spectral index first increases at the jet apex before reaching its maximum. This may be due to the difference in beam size, where they chose to resolve all their maps with a circular beam of 1.2 mas radius. The maps at 5 GHz were over-resolved in the direction parallel to the jet with that beam, which could lead to uncertainties in the spectral index in this direction. The difference in the observed spectral index profile could also reflect an increase in opacity due to enhanced particle density as shocks start to travel down the jet from the core region. However, this should be reflected in an increase in the core flux density at the *RadioAstron* epoch compared to the observations in Ros et al. (2000),

which is not observed (see Fig. 5.34, where the core flux density from the MOJAVE survey is plotted from 1995 to 2020). On the other hand, it is visible in those data that a new feature (C26) is ejected from the core around the *RadioAstron* epoch, with a rise in core flux density in late 2015 of about 1 Jy compared to the neighbouring epochs in the data. So likely the aftermath of a newly ejected component is observed in my *RadioAstron* data, manifesting itself in increased particle density and opacity in the core region.

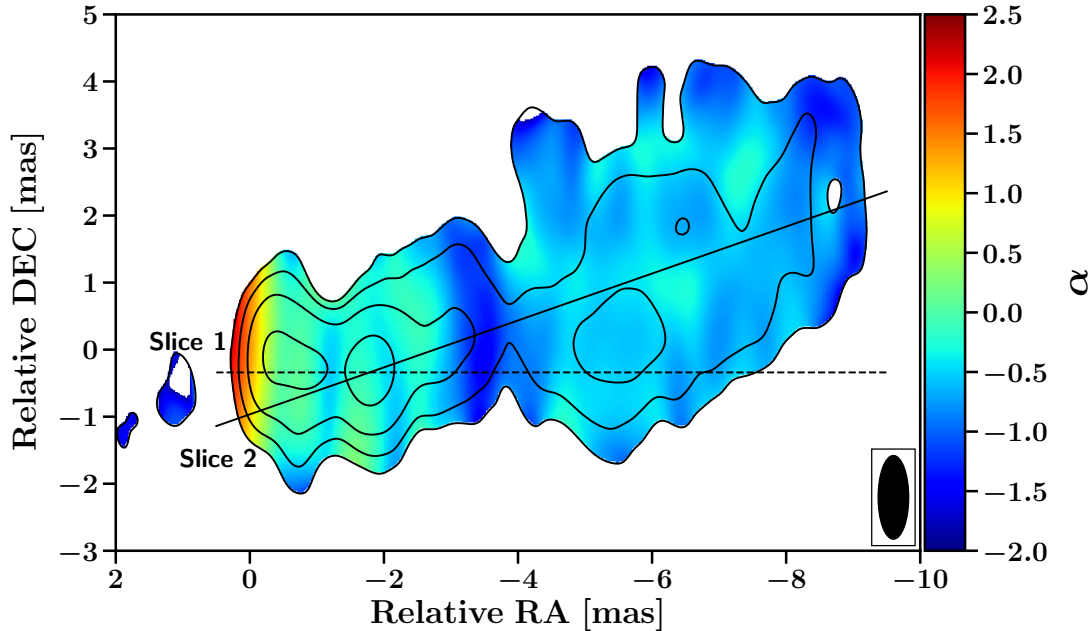


Figure 5.10: Spectral index map between the 1.6 GHz *RadioAstron* and the 15.3 GHz MOJAVE observations, after correcting for the core shift. An optically thick core is visible to the east, and the jet turns gradually optically thin along the jet flow. An increase in the spectral index is observed at positions with enhanced total and polarised intensity, indicating a shock front. Two slices along the jet are displayed, one horizontal one (dotted line) and one along the jet direction (dashed line). The spectral index profile along those slices is displayed in Fig. 5.11 and 5.12.

5.6 Rotation Measure

With the linear polarisation maps presented in Sect. 5.1 and the *RadioAstron* polarisation map, the rotation measure in 3C 345 can be studied. As argued in Sect. 1.4, a minimum of three frequencies is needed for a reliable fitting of the *RM*. A compromise is chosen between angular resolution and the number of frequencies by using the 1.6 GHz, 4.8 GHz, 8.4 GHz and 15.3 GHz data and convolving all maps with the beam of the 8.4 GHz map. In this way the map at 4.8 GHz is overresolved by a factor of ~ 1.75 , which is reasonable given the *SNR* in that map. By choosing this beam size, I want to make the best use of the high-resolution *RadioAstron* data, while not over-resolving the maps below the *SNR*-based limit (see Eq. 4.5, cf. Martí-Vidal et al. 2012). At the same time, the frequency coverage in the fit has to be sufficient to constrain the possible $n\pi$ ambiguities in the observed EVPAs. I decided to exclude the 43 GHz map for this analysis, as the difference in frequency would become exceedingly large between the lowest and highest frequency (a factor of ~ 27), giving rise to more uncertainties.

Subsequently, the four maps are convolved with the 8.4 GHz beam as presented in Table 5.4. The smallest pixel size of 0.02 mas is chosen from the 15 GHz MOJAVE map for all frequencies. It has been argued that this yields the best results when comparing

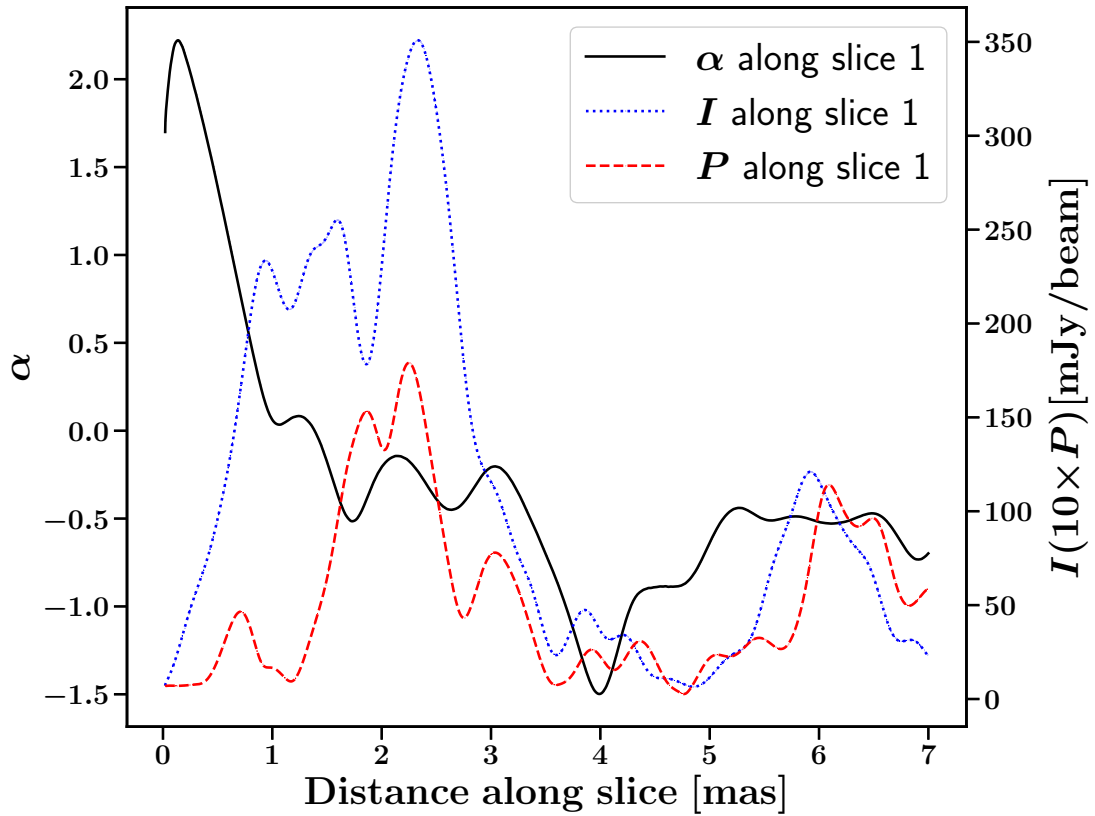


Figure 5.11: Spectral index profile along slice 1 in Fig. 5.10. The spectral index α is displayed as the black solid line, the total intensity I as the blue dotted line and the polarised intensity P , upscaled by a factor of 10 for better visibility, as the dashed red line. Regions of enhanced polarised emission at ~ 2 and ~ 3 mas are co-located with a rise in α .

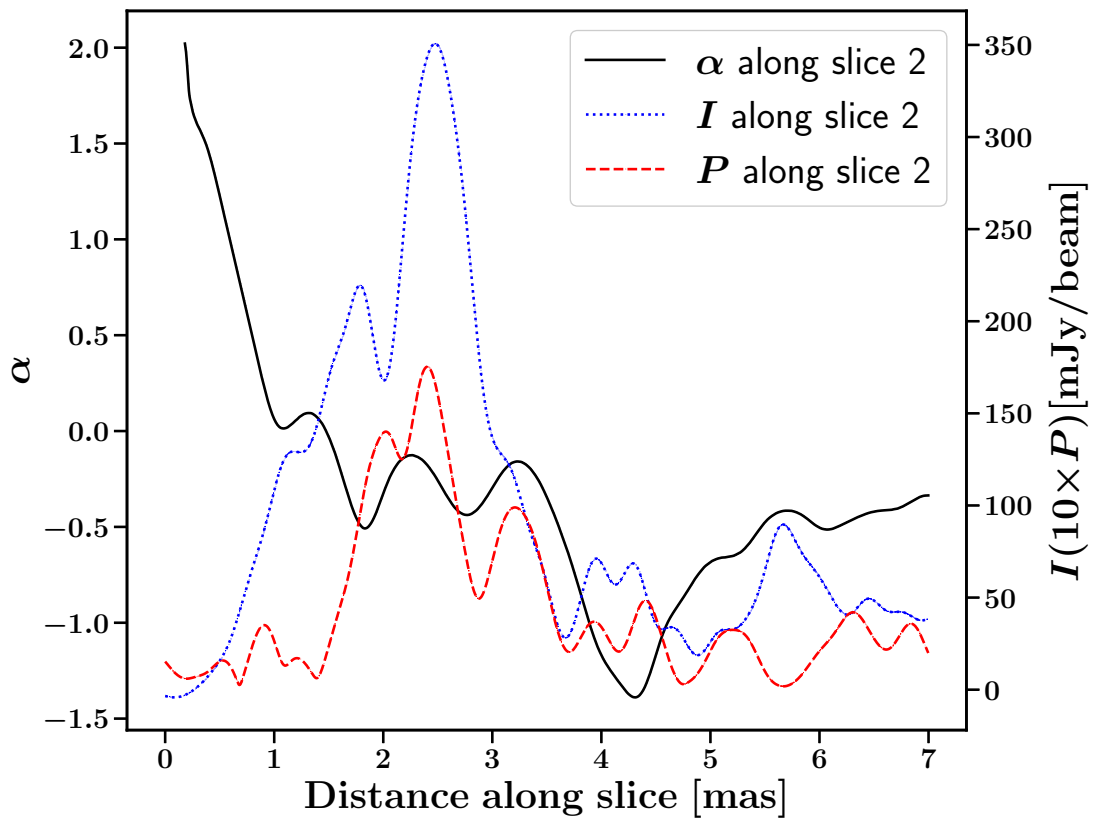


Figure 5.12: Spectral index profile along slice 2 in Fig. 5.10. See Fig. 5.11 for description.

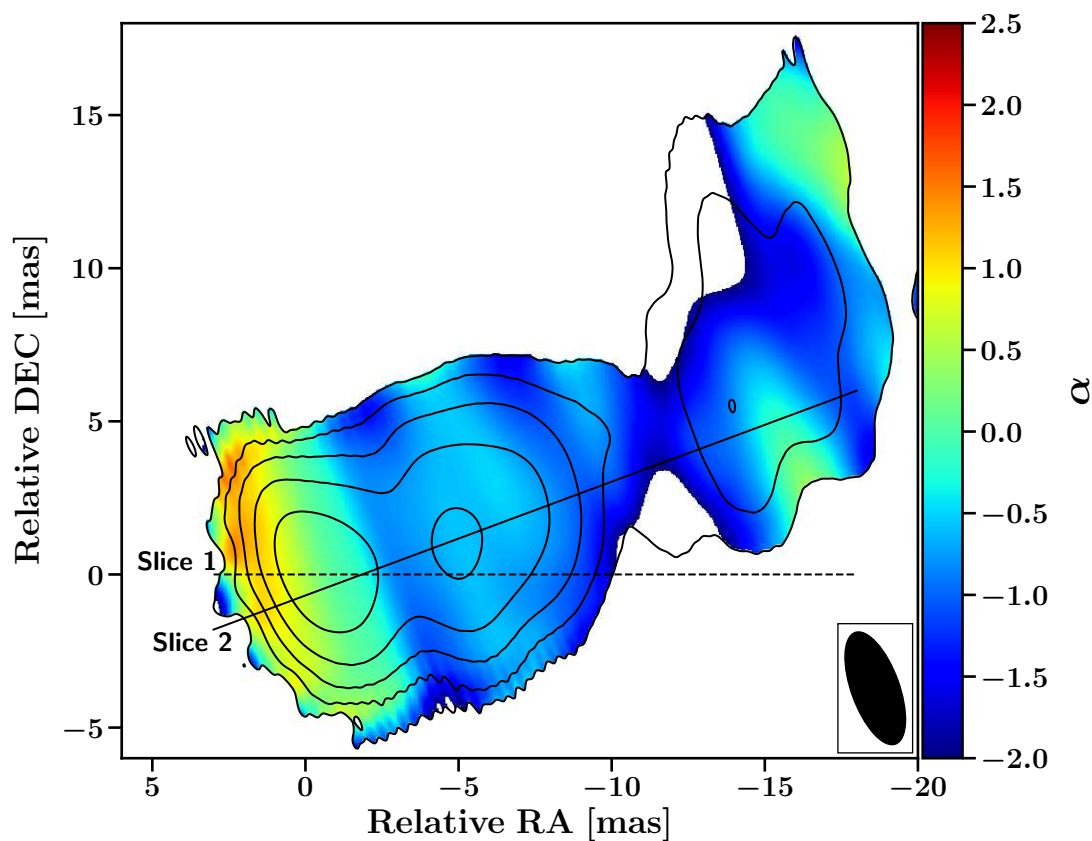


Figure 5.13: Spectral index map between the 1.6 GHz *RadioAstron* and the 4.8 GHz VLBA observations, after correcting for the core shift. Two slices along the jet are displayed, one horizontal one (dotted line) and one along the jet direction (dashed line). The spectral index profile along those slices is displayed in Fig. 5.14 and 5.15. The wiggly structures at the lower contour levels are artefacts in the 1.6 GHz map introduced by oversampling of the visibilities with residual calibration errors when convolved with the much larger beam at 4.8 GHz.

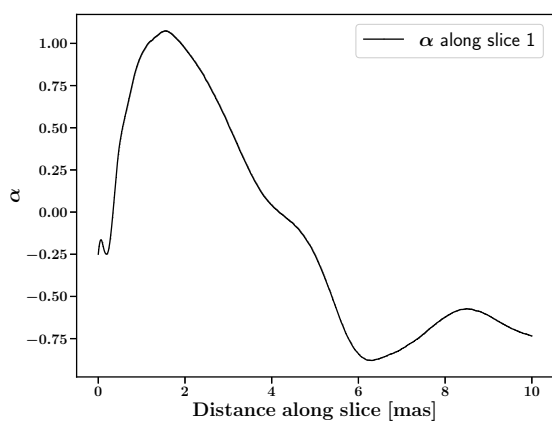


Figure 5.14: Spectral index profile along slice 1 in Fig. 5.13.

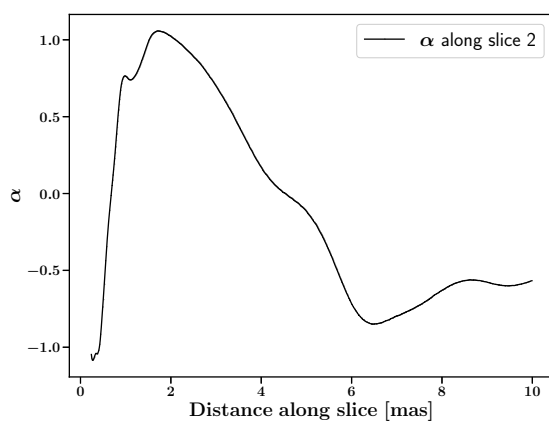


Figure 5.15: Spectral index profile along slice 2 in Fig. 5.13.

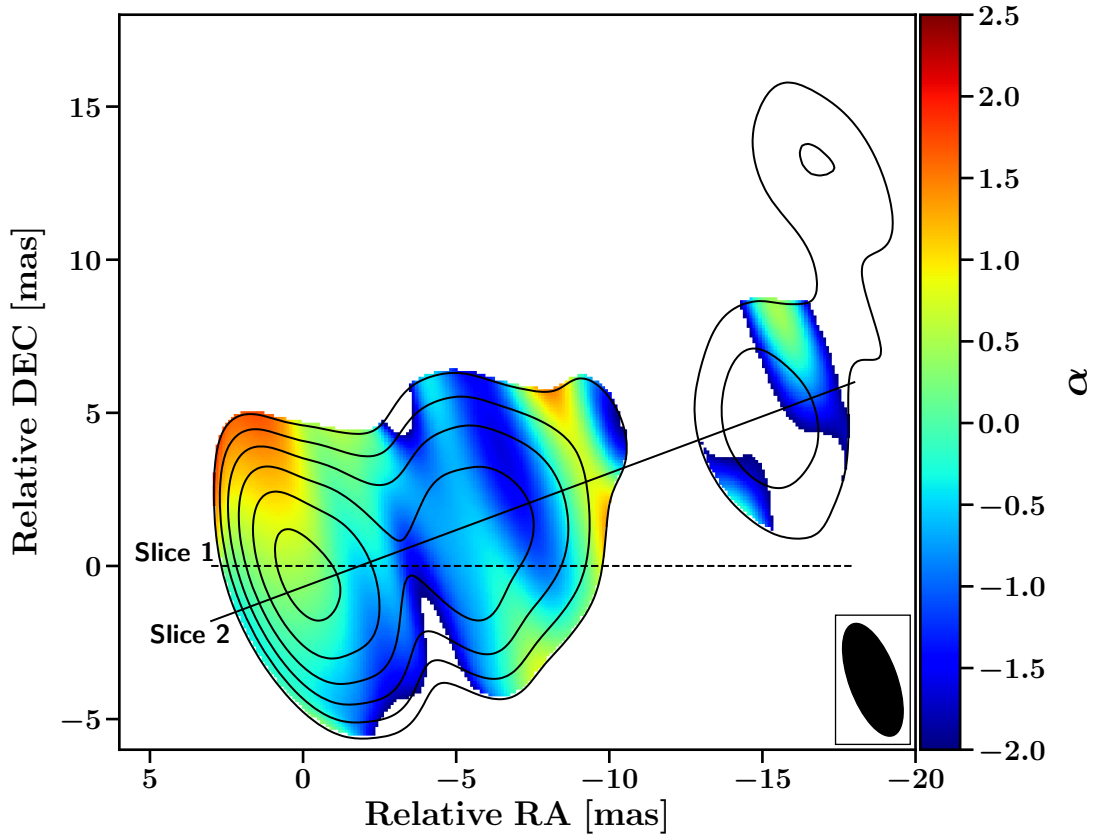


Figure 5.16: Spectral index map between the 4.8 GHz VLBA and the 8.4 GHz VLBA observations, after correcting for the core shift. Two slices along the jet are displayed, one horizontal one (dotted line) and one along the jet direction (dashed line). The spectral index profile along those slices is displayed in Fig. 5.17 and 5.18.

maps with different beam and pixel sizes (Fromm et al. 2013). The shifts obtained from the 2D cross-correlation discussed in Sect. 5.4 are applied to the images.

The errors in the Q and U maps, σ_Q and σ_U are calculated following Hovatta et al. (2012). Firstly, the RMS errors in the maps are estimated by computing the off-source RMS in the Q and U maps over squares of a few hundred pixels. Then the error contribution of the D -term estimation is determined as

$$\sigma_{D\text{term}} = \frac{0.002}{\sqrt{N_{\text{ant}} \cdot N_{\text{IF}} \cdot N_{\text{scan}}}} \sqrt{I^2 + (0.3 \cdot I_{\text{peak}})^2}, \quad (5.17)$$

where N_{ant} is the number of antennas, N_{IF} the number of IFs and N_{scan} the number of scans with independent parallactic angle. I is the total intensity and I_{peak} the respective peak flux density in the map. Hovatta et al. (2012) calculate the factor 0.002 from the scatter in their D -terms. Their observations were done with the VLBA, a homogeneous VLBI array. Since in my data the antennas have very different properties, this scatter can not be estimated in a meaningful way. Thus the same factor in the error determination is used, pointing to the fact that the scatter might be underestimated. The resulting σ_P are then:

$$\sigma_P = \sqrt{\sigma_{\text{RMS}}^2 + \sigma_{D\text{term}}^2 + (1.5 \cdot \sigma_{\text{RMS}})^2}, \quad (5.18)$$

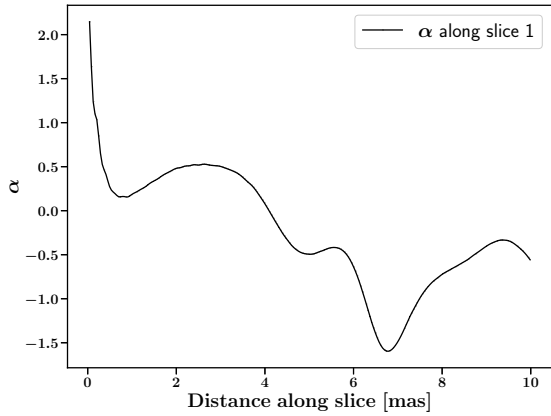


Figure 5.17: Spectral index profile along slice 1 in Fig. 5.16.

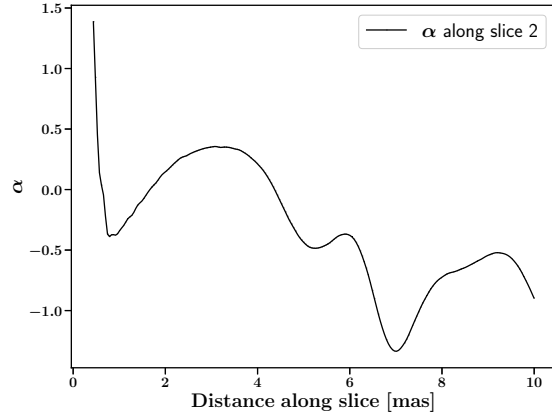


Figure 5.18: Spectral index profile along slice 2 in Fig. 5.16.

which also includes an uncertainty due to the clean deconvolution. Now the EVPA errors are calculated as

$$\sigma_\chi = \sqrt{\left(\frac{180^\circ}{\pi} \cdot 0.5 \cdot \frac{Q \cdot \sigma_U}{Q^2 + U^2}\right)^2 + \left(\frac{180^\circ}{\pi} \cdot 0.5 \cdot \frac{U \cdot \sigma_Q}{Q^2 + U^2}\right)^2 + \sigma_{\chi_0}^2}, \quad (5.19)$$

where σ_{χ_0} is an additional uncertainty in the absolute EVPA calibration in degrees, which is mostly due to the uncertainties of the EVPA measurements in the single-dish observations as presented in Table 4.1. The error for each pixel in the maps is calculated. Following that, a linear χ^2 fit to Eq. 1.58 is performed for each pixel with pixel coordinates i, j that fulfils the following condition: for each map, $SNR_{ij}^P > 3$, where $SNR^P = P/\sigma_P$ is defined. In addition, a map with less conservative conditions is produced, i.e. only with pixels with $SNR_{ij}^{P,\nu} > 1$. The χ^2 is calculated as

$$\chi^2 = \sum_i \frac{y_i^{\text{obs}} - y_i^{\text{mod}}}{\sigma_i}, \quad (5.20)$$

with y^{obs} being the observed data points with associated errors σ_i and y^{mod} being the model values. Subsequently, the errors in the fit parameters are determined from the covariance matrices. The whole procedure described above involving the application of map alignment, *RM* fitting and plotting the results is performed by a `Python` script I wrote for that purpose. The script was tested on archival data from Hovatta et al. (2012), yielding broadly consistent results. For constructing the rotation measure, only pixels with total intensity above the lowest contour level displayed in the images in Fig. 4.8, 5.1, 5.2, and 5.3 have been used. This corresponds to SNR cutoffs of ~ 5.6 , ~ 5 , ~ 3.7 and ~ 2.6 for the L-band, C-band, X-band, and U-band maps, respectively.

The resulting fits for three selected pixels in the *RM* map are displayed in Fig. 5.29, 5.30 and 5.31. The complete *RM* maps are shown in Fig. 5.25 for a SNR cutoff in P of three and in Fig. 5.27 for a SNR cutoff in P of one. Fig. 5.26 and Fig. 5.28 show the respective *RM* 1- σ error maps.

EVPAs are prone to a $n\pi$ degeneracy (see Sect. 1.4.3), requiring a careful investigation of the obtained linear fits. So the individual fits are inspected and evaluated if they could be improved with $n\pi$ rotations of the observed EVPAs. To quantify this, rotations of π of the EVPAs at 1.6 GHz are allowed, as that seems to influence the fit the most. Then the program looks for improvements of the achieved χ^2 with the allowed rotations that fulfil $\chi_1^2/\chi_2^2 > 1.25$. χ_i^2 are the reduced χ^2 values for fit 1 without and fit 2 with additional EVPA

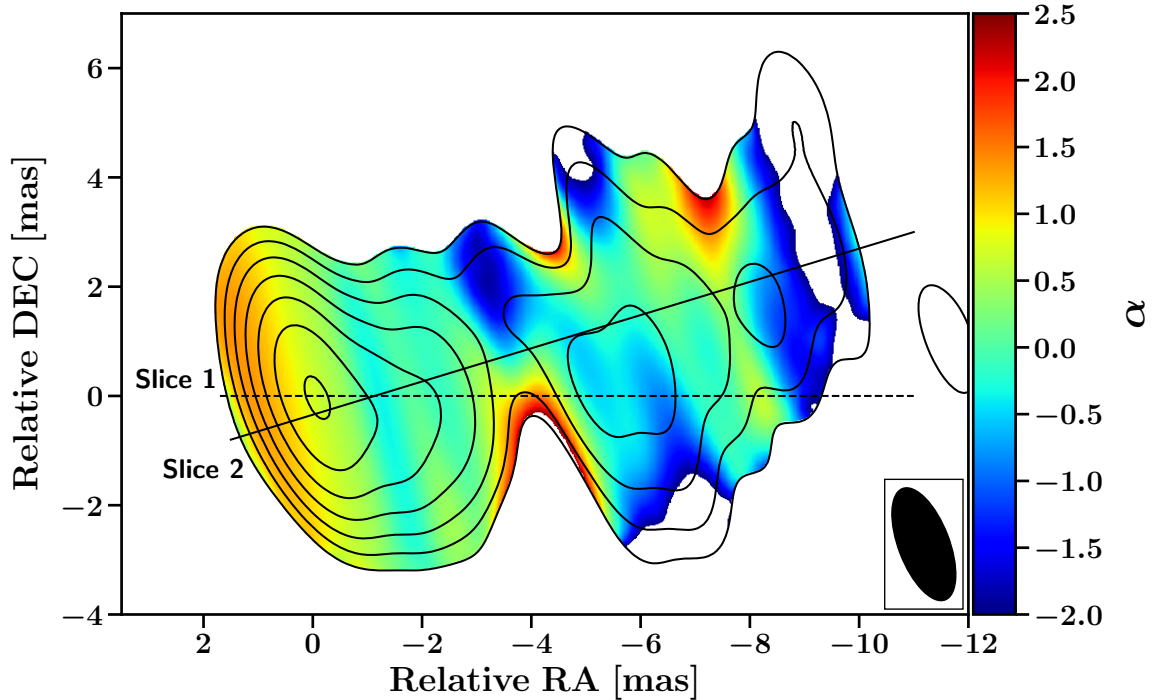


Figure 5.19: Spectral index map between the 8.4 GHz VLBA and the 15.3 GHz MOJAVE observations, after correcting for the core shift. Two slices along the jet are displayed, one horizontal one (dotted line) and one along the jet direction (dashed line). The spectral index profile along those slices is displayed in Fig. 5.20 and 5.21.

rotations. That threshold has been chosen by making use of Eq. 4.8, as one is effectively adding a parameter to the fit. In most cases, no rotations were necessary. As an example, the red data point in Fig. 5.29 or 5.31 indicates the the EVPA has been rotated. It shall be noted that the allowance of rotations by larger multitudes of π would lead to much higher values of RM , which is not expected given previous VLBI observations.

In Fig. 5.27, mostly RM values of the order of tens of rad m^{-2} are observed. At 1.6 GHz, this is already enough to rotate the observed EVPAs in the 1.6 GHz polarisation map in Fig. 4.8 significantly, by several tens of degrees. Regions of higher RM of the order of 100 are identified in the vicinity of L3 and in the core. Interestingly, there is a gradient along the jet, with higher RM in the core region, where the sign is actually flipped. This indicates a change in magnetic field direction *along* the jet, which means there exists a poloidal magnetic field component. This could indeed imply the presence of a helical magnetic field, as a purely toroidal one could not produce these changes. However, as noted in Sect. 4.3, one might miss a rotation of the EVPAs by 90 degrees due to relativistic aberration in the core, if $\tau > 1$. In that case, one could expect the observed RM to be lower, and possibly positive (see Fig. 5.30). It has to be noted that the RM in core region is more uncertain due to the inclusion of lower SNR pixels, so care has to be taken when interpreting the RM in this region. This is mostly reflected in the larger errors on the RM in this region. For that, see Fig. 5.26 and the RM at the positions of the Gaussian components displayed in Table 5.2. Future observations with higher SNR could shed more light on this.

The obtained RM values are compared with earlier observations. Hovatta et al. (2012) have studied the RM in many AGN jets, with observations at four frequencies between 8 and 15 GHz. The results showed two distinct regions in 3C 345, one with $RM = 156.4 \pm 72.0 \text{ rad m}^{-2}$ in the core region and another one with $RM = -50.3 \pm 72.0 \text{ rad m}^{-2}$ at $\sim 1.5 \text{ mas}$ downstream of the jet. Given the measurement errors, the RM in the second

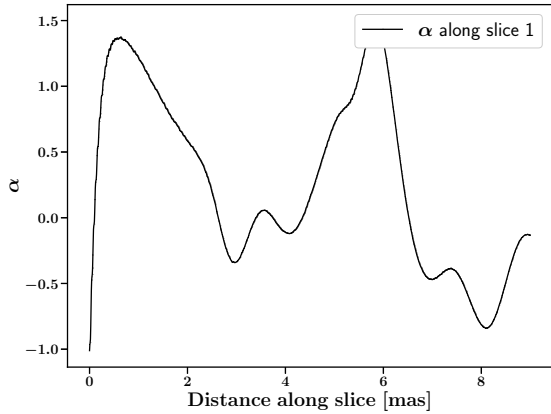


Figure 5.20: Spectral index profile along slice 1 in Fig. 5.19.

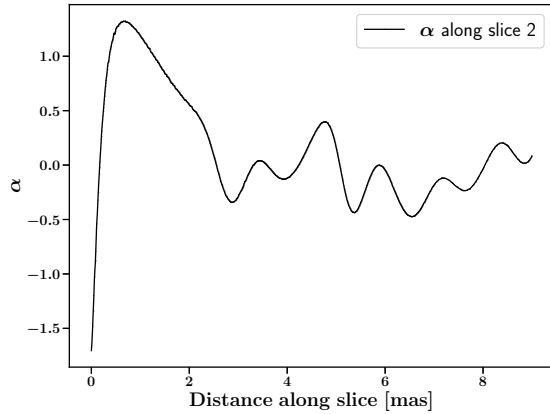


Figure 5.21: Spectral index profile along slice 2 in Fig. 5.19.

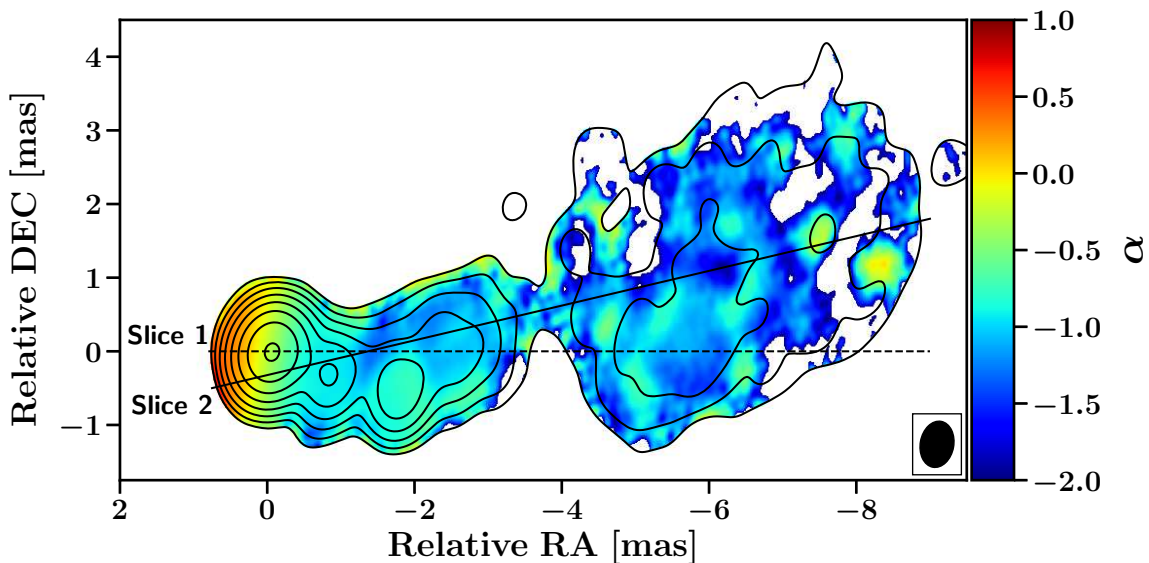


Figure 5.22: Spectral index map between the 15.3 GHz MOJAVE and the 43.1 GHz VLBA observations from the BU blazar program, after correcting for the core shift. Two slices along the jet are displayed, one horizontal one (dotted line) and one along the jet direction (dashed line). The spectral index profile along those slices is displayed in Fig. 5.23 and 5.24.

region is consistent with zero, while for the core-region one could expect a significant rotation of the EVPAs in the core. For a better comparison, the RM fit was also performed without the 1.6 GHz map, yielding a similar frequency coverage as in Hovatta et al. (2012). In the case of internal Faraday rotation, where regions with different Faraday depths contribute to the observed RM , there might not be an exact dependence on λ^2 of the EVPA rotation. Over the large frequency range that is covered in my observations, one could expect some changes of the λ^2 dependence. However, the obtained RM are very similar in that case as well.

Motter and Gabuzda (2017) also studied the RM at four frequencies around 1.6 GHz in six AGN, one of which was 3C 345 in March of 2010. They found RM in the range between -30 and $+30$ rad m^{-2} , and report a statistically significant (2.5σ) RM gradient transverse to the jet direction. This supports the presence of a toroidal magnetic field that may be part of a helical one. However, the difference in beam size compared to the *RadioAstron* observations is about a factor 20 in the east-west and a factor ten in north-south direction. In addition, my observations only focus on the innermost ~ 10 mas of the jet, while Motter and Gabuzda (2017) find the RM gradient farther downstream. In

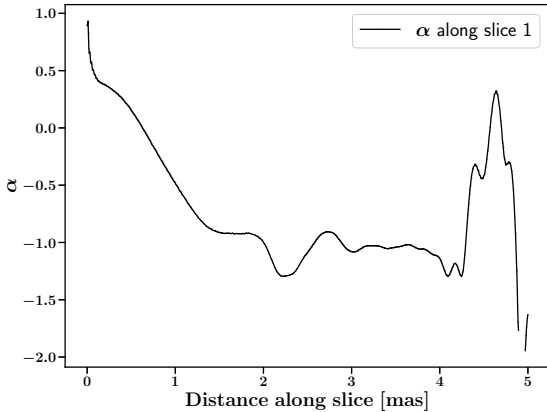


Figure 5.23: Spectral index profile along slice 1 in Fig. 5.22.

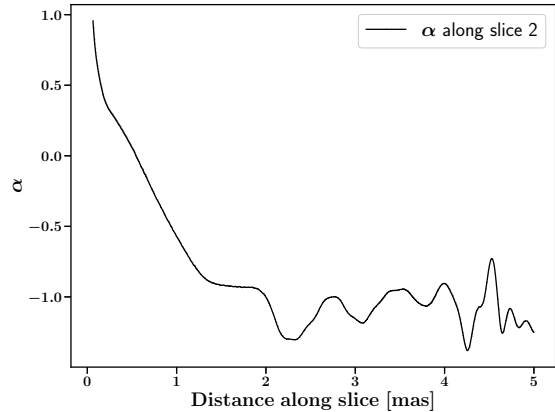


Figure 5.24: Spectral index profile along slice 2 in Fig. 5.22.

comparison, there seems to be no evidence for a transverse gradient of the RM in Fig. 5.25. This is expected to some degree, as all the datasets do not resolve the jet transversely. Especially at 1.6 GHz, the beam shape is highly elliptical due to the limited (u, v) -coverage with *RadioAstron*. Overall, the values are consistent with the other measurements at low frequencies. The higher frequency RM measurements generally show higher RM values. Beam depolarisation in my observations is not a likely reason for this, as the limiting resolution in both my data and the one in Hovatta et al. (2012) comes from the map at ~ 8 GHz.

RadioAstron data have previously been used to calculate the RM at high angular resolution. For BL Lac, Gómez et al. (2016) find a RM between -3000 and 3000 rad m^{-2} between 15 GHz, 22 GHz with *RadioAstron* and 43 GHz, with a clear transverse RM gradient. Kravchenko et al. (2020) also find a high RM up to $-10000 \text{ rad m}^{-2}$ between 22 GHz with *RadioAstron* and 43 GHz, in the blazar 0716+714. So far, there are no other studies published which investigate the RM in an AGN at both high resolution and low frequencies, which is unique for space-VLBI observations like *RadioAstron*.

In addition, one can estimate the amount of bandwidth polarisation that should be expected at 1.6 GHz according to Eq. 1.65. With that, it can be seen that the observed RM will not yield any significant bandwidth depolarisation over the total bandwidth of 64 MHz in the 1.6 GHz data. For example, a reduction of the degree of polarisation by $\sim 25\%$ could be expected for RM as high as 1000, which is unlikely given my data. So the depolarisation that is observed especially in the core at 1.6 GHz, is likely internal depolarisation, or depolarisation by an unresolved foreground Faraday screen (see Sect. 1.4.4). The possibility of beam depolarisation can not be ruled out entirely, but it is rather unlikely to be significant as the jet components identified in the 1.6 GHz map start to be resolved by *RadioAstron*. This can be seen from the accurate bracketing of the Gaussian model fit T_b by the estimates of $T_{b,\text{min}}$ and $T_{b,\text{max}}$ from visibilities alone. This is because for $T_{b,\text{max}}$ to give a good estimate of T_b , the emitting region has to be at least slightly resolved (cf. Sect. 5.2). Also the variability timescale from the Gaussian component sizes was consistent with previous observations (see Sect. 5.3).

The RM corrected polarised intensity map at 1.6 GHz is shown in Fig. 5.32. Only EVPAs that have been rotated are shown in the image to avoid confusion. EVPA corrected maps at the other frequencies are not shown for brevity, as no significant change of the EVPAs is expected due to the λ^2 dependence.

There is significant rotation of the EVPAs visible at 1.6 GHz. While it was stated in Sect. 4.3 that the EVPAs are predominantly parallel to the jet direction, it is apparent that Faraday rotation somewhat changes that conclusion. To illustrate this, the difference

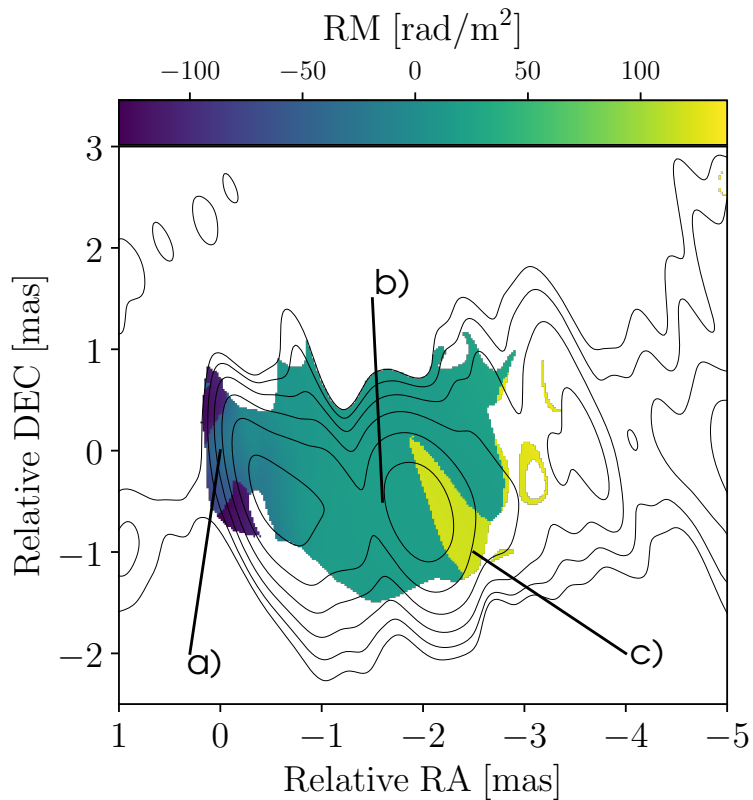


Figure 5.25: *RM* map constructed with linear fits to the EVPAs at 1.6, 4.8, 8.4, and 15.3 GHz. A cutoff in polarisation of $SNR^P = P/\sigma_P > 1$ has been applied. The contours display the total intensity at 1.6 GHz, with the contour levels being in percents of the peak emission of 0.39 Jy/beam: 2.83, 4, 5.65, 8, 11.31, 16, 22.63, 32, 45.25, 64, 90.51. Three different regions are identified, the fit for which is shown in Fig. 5.29, 5.30 and 5.31 for region a), b) and c), respectively.

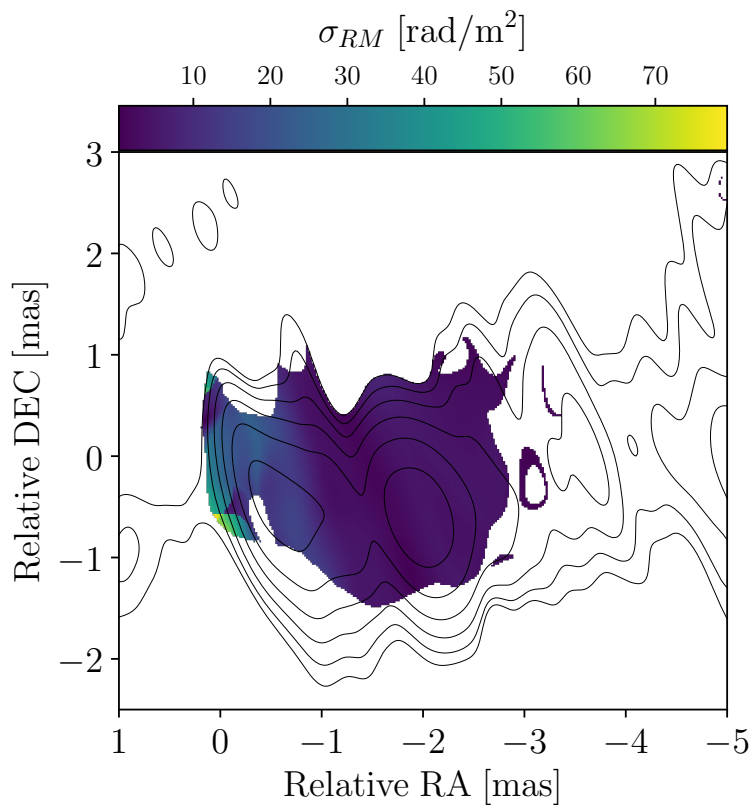


Figure 5.26: Map of the *RM* 1- σ errors for Fig. 5.25.

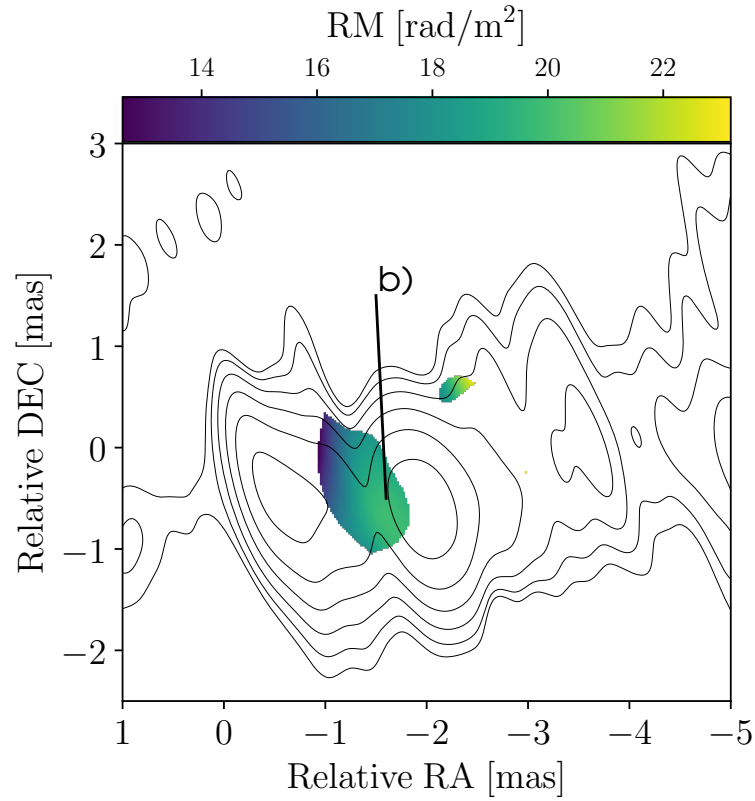


Figure 5.27: *RM* map constructed with linear fits to the EVPAs at 1.6, 4.8, 8.4, and 15.3 GHz. A cutoff in polarisation of $SNR^P = P/\sigma_P > 3$ has been applied. The contours display the total intensity at 1.6 GHz, with the contour levels being in percents of the peak emission of 0.39 Jy/beam: 2.83, 4, 5.65, 8, 11.31, 16, 22.63, 32, 45.25, 64, 90.51. The fit for region b) is displayed in Fig. 5.30.

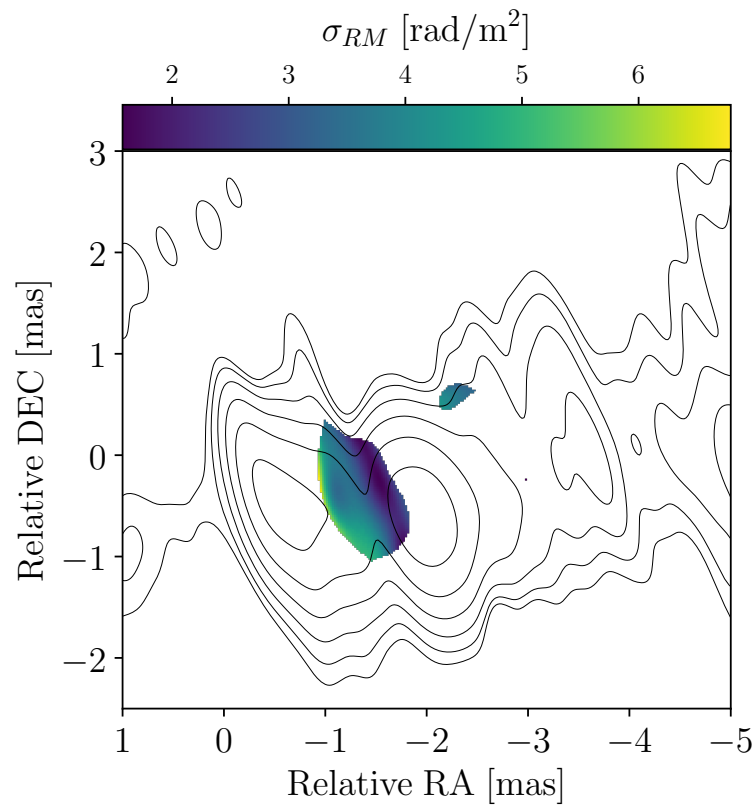


Figure 5.28: Map of the *RM* 1- σ errors for Fig. 5.27.

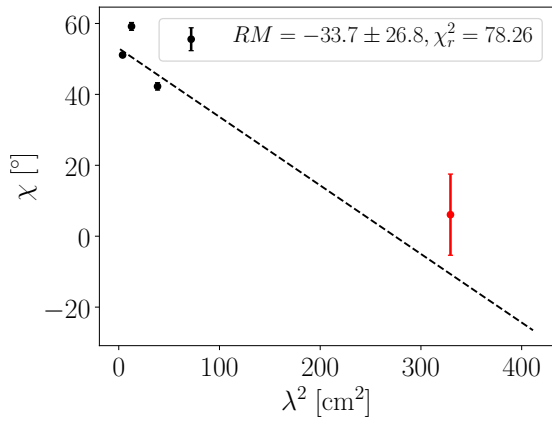


Figure 5.29: *RM* fit for the central pixel at (0|0) mas in the map in Fig. 5.25 (region a)).

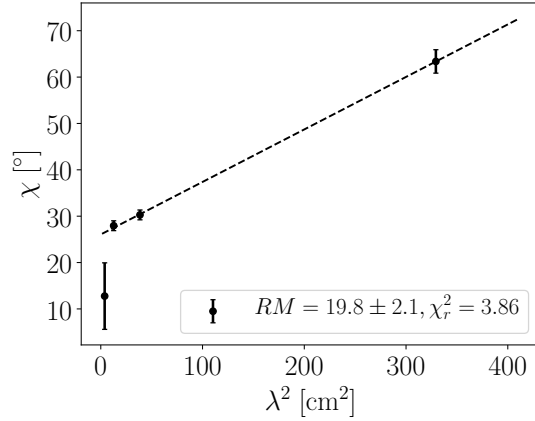


Figure 5.30: *RM* fit at the pixel at (-1.6| -0.5) mas in the map in Fig. 5.25 (region b)).

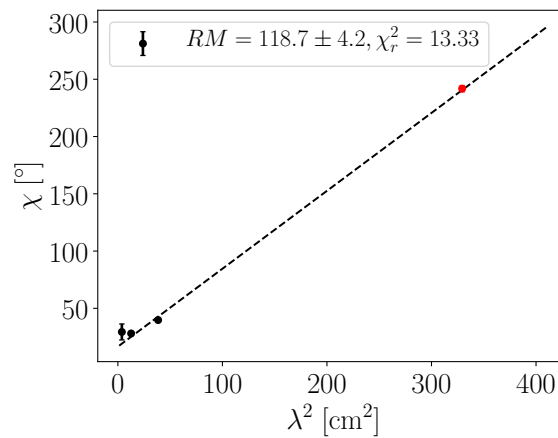


Figure 5.31: *RM* fit at the pixel at (-2.5| -1.0) mas in the map in Fig. 5.25 (region c)).

between the jet position angle and EVPA is plotted in Fig. 5.33. To avoid uncertainties in the calculation of the local jet direction by using single pixels, a moving average has been computed for each pixel. That means for each value of the P.A., the surrounding 20 pixels have been averaged. The same procedure was followed for the EVPAs. Figure 5.33 clearly demonstrates that without the *RM* correction, the EVPAs followed quite closely, within $\sim 40^\circ$, the local jet direction. With the *RM* correction, the EVPAs are less aligned with the jet direction, and in the region between L2 and L3, at ~ 1 mas, they even tend to be more perpendicular. A similar behaviour of the EVPAs was also noted in Ros et al. (2000). Shocks can possibly compress magnetic fields and make the EVPAs perpendicular to the shock front (e.g. Laing 1980). In many AGN, the EVPAs tend to be either parallel or perpendicular to the jet flow (e.g. Lyutikov et al. 2005), where in quasars, the alignment is less stable and less preferred to be aligned with the jet direction (see also Pushkarev et al. 2017a).

The EVPAs seem to be a bit closer aligned to the jet direction with the considered Faraday rotation in the core. It has been suggested that in optically thick jet regions such as the core at 1.6 GHz, the EVPAs are oriented parallel to the magnetic field due to relativistic aberration effects (e.g., Gomez et al. 1994; Gabuzda and Gómez 2001). However, (Wardle 2018) argues that higher optical depths of between 6 and 7 are needed for this apparent $\pi/2$ flip in the EVPAs. Such high opacities are not observed (see Sect. 5.5). It can not be conclusively said how the magnetic field in the core region is oriented from the observed EVPAs.

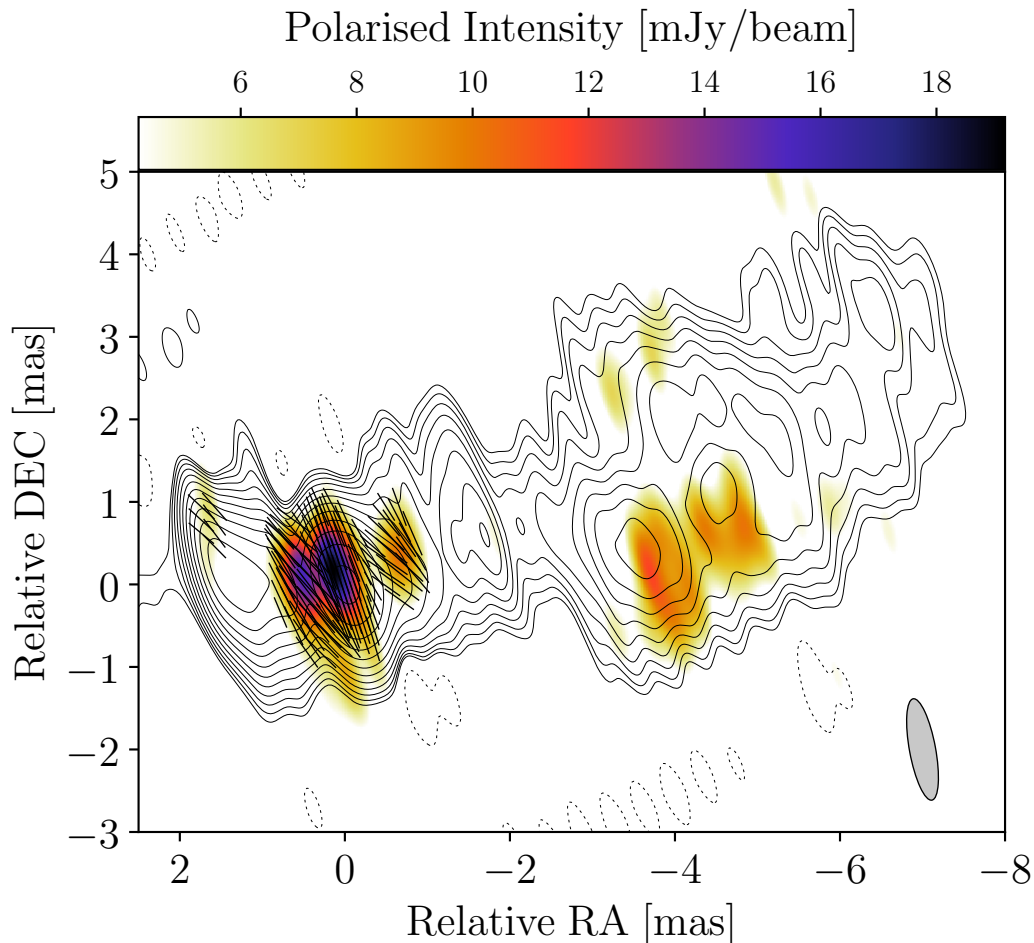


Figure 5.32: *RadioAstron* image of the total and linearly polarised intensity of 3C 345 at 1.6 GHz, with overlaid *RM corrected* EVPAs. Only the EVPAs that have been rotated are shown for clarity. The map of the polarised intensity P is shown in colour-scale, overlaid with contours displaying the total intensity emission. The beam size is displayed on the bottom right with a resolution of 1.25×0.32 mas at a P.A. of 10.50° . Contour levels are (% of peak emission of 0.39 Jy/beam): -2.0 , 2.0 , 2.83 , 4.0 , 5.65 , 8.0 , 11.31 , 16.0 , 22.63 , 32.0 , 45.25 , 64.0 , 90.51 . Compare to Fig. 4.8.

The observed rotation of the EVPAs could in principle be due to internal or external Faraday rotation. An internal rotation is unlikely if the jet consists of a pair plasma, as suggested by Hirovani (2005). This is because electrons and positrons gyrate in opposite directions, effectively cancelling out any Faraday rotation. In this scenario the Faraday rotation thus is likely produced by electrons in an external Faraday screen, as e.g. suggested in Kravchenko et al. (2020). The discrimination between those two scenarios is discussed in more detail in Sect. 5.7.

5.7 Estimating the electron density

Both the core shift and the Faraday rotation depend on the electron density and the magnetic field. To compare both effects and derive the electron density, one has to make some simplifying assumptions. I will discuss the implications of these assumptions later in this section.

1. The Faraday rotation is produced internally in the jet. Although external Faraday rotation may be favoured for my observations (see previous section), this assumption needs to be made here.

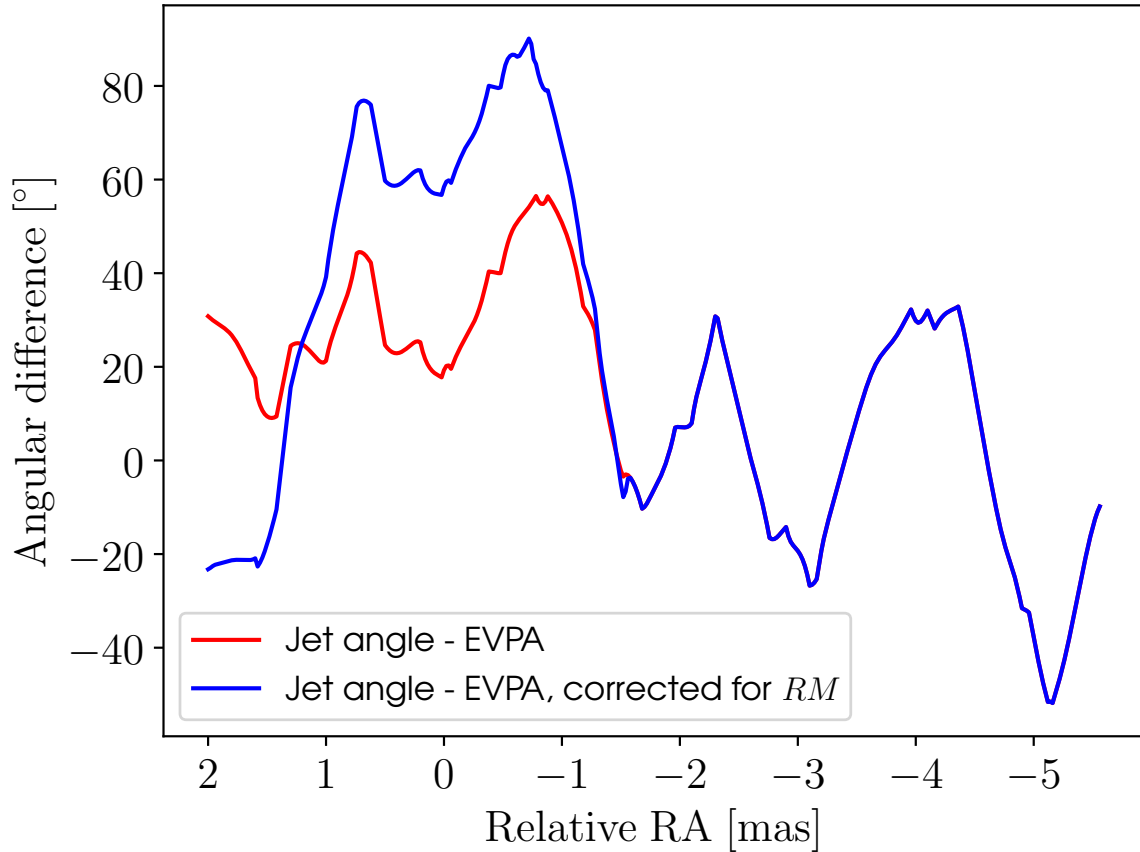


Figure 5.33: Difference between jet position angle and EVPAs along the jet ridge line (see Fig. 4.6) for the 1.6 GHz *RadioAstron* map. The plot shows two lines, the blue one with, and the red one without RM correction. Both jet PA and EVPAs have been calculated as a moving average (see text for details). It is apparent that there is a change from the EVPAs being parallel to being perpendicular to the local jet direction when accounting for Faraday rotation in the source.

2. The magnetic field probed by the core shift and the Faraday rotation are approximately the same. With the core shift, one measures the jet axial magnetic field, while Faraday rotation probes the magnetic field component along the line of sight.
3. The Faraday rotation comes from a region where the magnetic field and the electron density are uniform, so the integration along the line of sight is trivial.
4. The region in which the Faraday rotation takes place fulfils the condition of equipartition of particle and magnetic energy density. The results from Sect. 5.4 support this scenario for the core region.

With these assumptions in mind, one can use Eq. 1.58 and 1.76 to obtain either the magnetic field or the electron density in the core region. One can solve Eq. 1.58 for the magnetic field and equal that to the magnetic field derived from the core shift, for the case of equipartition (assumption 4) (Eq. 1.77):

$$n_{\text{core}} = \frac{2\pi m^2 c^4}{e^3} \cdot \frac{RM}{B_{\text{core}} \cdot l} \quad (5.21)$$

$$n_1 = \frac{2\pi m^2 c^4}{e^3} \cdot \frac{RM}{B_1 \cdot l} \cdot \left(\frac{r_{\text{core}}}{\text{pc}} \right)^3. \quad (5.22)$$

One can put Eq. 5.21 and 5.22 in a more tangible form according to Eq. 1.59:

$$\frac{n_{\text{core}}}{\text{cm}^{-3}} = 1.2 \cdot 10^{-6} \left(\frac{RM}{\text{rad m}^{-2}} \right) \cdot \left(\frac{B_{\text{core}}}{\text{G}} \right)^{-1} \cdot \left(\frac{l}{\text{pc}} \right)^{-1} \quad (5.23)$$

$$\frac{n_1}{\text{cm}^{-3}} = 1.2 \cdot 10^{-6} \left(\frac{RM}{\text{rad m}^{-2}} \right) \cdot \left(\frac{B_1}{\text{G}} \right)^{-1} \cdot \left(\frac{l}{\text{pc}} \right)^{-1} \cdot \left(\frac{r_{\text{core}}}{\text{pc}} \right)^3. \quad (5.24)$$

At this point, assumption 2) has been used implicitly, by assuming a uniform emitting region of size l . The size is calculated as the FWHM of the jet width from the jet ridge line fit in the 1.6 GHz *RadioAstron* map, corrected for the viewing angle. For the rotation measure, the RM is averaged over the core region, which yields an $RM \approx -27 \text{ rad m}^{-2}$.

For Eq. 5.21 and 5.22, $n_1 \approx 0.3 \text{ cm}^{-3}$ and $n_{\text{core}} \approx 9 \cdot 10^{-5} \text{ cm}^{-3}$ is obtained for $B_{\text{core}} = 0.010 \text{ G}$, taken from Table 5.5.

For comparison, one can also derive the particle density from Eq. 1.82, which yields $n_1 = 23 \text{ cm}^{-3}$ and $n_{\text{core}} = 7 \cdot 10^{-3} \text{ cm}^{-3}$ for an assumed $\gamma_{\text{min}} = 10^2$ and $\gamma_{\text{max}}/\gamma_{\text{min}} = 10^3$ (Hirotani 2005). Note that Eq. 1.82 does not strongly depend on the ratio $\gamma_{\text{max}}/\gamma_{\text{min}}$.

The obtained values differ by about two orders of magnitude. Given the assumptions, in order to reconcile the values, either the RM or γ_{min} has to be substantially higher. However, if the assumption of internal Faraday rotation is correct, one would in fact expect γ_{min} to be even lower than what was assumed here. Faraday rotation is caused by relatively low-energy electrons. Thus for internal Faraday rotation, either the spectrum of relativistic electrons has to extend to low energies, or the relativistic plasma is mixed with a population of thermal electrons (Hovatta et al. 2012). Since the RM would have to be about two order of magnitude larger, which is not expected from the analysis in Sect. 5.6, I conclude that the assumptions made above are indeed too simplified, and the Faraday rotation likely does not occur in the inner jet.

5.8 Component evolution

To better evaluate if travelling shocks can be responsible for the bright polarised emission observed with *RadioAstron*, MOJAVE data (Lister et al. 2019) are compiled, where the database was searched for the component model fits. The information of all components that are identified in the *RadioAstron* epoch (see Table 5.2) are extracted from that data set. For each component, the brightness temperature is calculated according to Eq. 5.5. A similar analysis has been done by Lisakov et al. (2017) for 3C 273, who saw a rise in brightness temperature during a γ -ray flare.

In the MOJAVE epoch on March 5, a new component became visible (labelled as component 26 according to Lister et al. (2019)). At the same time, a local maximum in the OVRO flux density is visible, which is likely caused primarily by the rise in flux density in the core. The core flux increase might well be related to the ejection of component 26 at the same time, as other studies have also shown (e.g., Klare 2003; Schinzel 2011). There is no apparent increase in the flux densities or brightness temperatures of the other components at that time, although component 25 shows an increase in T_b some months after the *RadioAstron* epoch.

The spatial coincidence of the components with the polarised emission in the 1.6 GHz *RadioAstron* map is investigated. From the map alignment described in Sect. 5.4, it is found that the highly polarised component L2 likely corresponds to component U5 at 15.3 GHz. This component is identified as component 23 in the MOJAVE survey. Indeed, the brightness temperature of this component drops by about an order of magnitude shortly after my epoch. This indicates that the feature corresponds to a shock travelling

down the jet, which weakens as the jet expands further downstream where a drop of T_b is evident in this component.

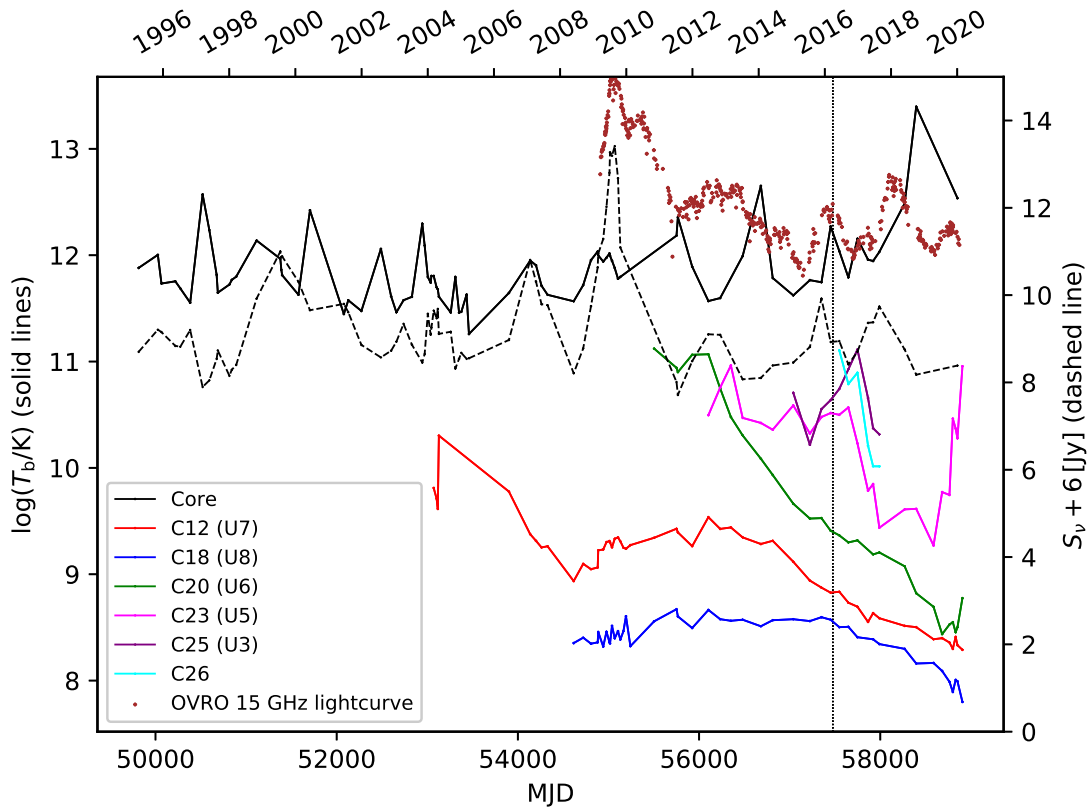


Figure 5.34: Evolution of the brightness temperature in the components identified at the MO-JAVE epoch. Solid lines denote the brightness temperature and the dashed line the flux density for the core component. For comparison, the OVRO light curve at 15 GHz is shown as brown data points. The flux density has been upscaled for clarity.

5.9 Possible counter-jet emission

The large scale jet of 3C 345 shows a strong jet to the northwest as seen in Fig. 1.21, and Kollgaard et al. (1989) report a feature to the northeast at 5 GHz that could be interpreted as a weaker counter-jet. It is up to date unclear how the possible counter-jet would be connected to the parsec-scale jet. They found that this counter-jet lies within 10° of an ejected VLBI component, which could hint at the counter-jet being less affected by bending as the approaching jet. Vega García (2019) found hints for a counter-jet in a map from 5 GHz *RadioAstron* observations. More likely, it corresponds to the easternmost feature that is identified as the self-absorbed core in this work. From similar high-resolution observations, at 5 GHz with VSOP (Klare et al. 2001), at 43 GHz (Jorstad et al. 2017)³, and at 86 GHz (Nair et al. 2019)⁴, no evidence for a counter-jet has emerged so far. In addition to the Doppler deboosting, free-free absorption from an absorbing torus around the SMBH might obscure the counter-jet (as in NGC 1052, see e.g., Kadler et al. 2004; Baczkó et al. 2019), even if the angular resolution was sufficient at higher frequencies.

A weak feature to the east of the core is noticeable, which I attribute most likely to an imaging artefact. With a viewing angle of $\sim 5^\circ$, one would expect that the Doppler beaming renders the counter-jet almost, if not completely, invisible. With $\Gamma = 10$ and

³https://www.bu.edu/blazars/VLBA_GLAST/3c345.html

⁴<https://www3.mpifr-bonn.mpg.de/div/3mmsurvey/>

$\theta = 5^\circ$, $\delta_{\text{jet}} \approx 11$, while $\delta_{\text{counter-jet}} \approx 0.05$. This would make the counter-jet appear more than 200 times fainter than the approaching jet.

In principle, one can calculate the jet speed β or the viewing angle θ from the jet-to-counter-jet flux ratio R , if one of the variables is known, from (see Eq. 1.33)

$$R = \frac{S_\nu^{\text{jet}}}{S_\nu^{\text{counter-jet}}} = \left(\frac{\delta_{\text{jet}}}{\delta_{\text{counter-jet}}} \right)^{3-\alpha} = \left(\frac{1 + \beta \cos \theta}{1 - \beta \cos \theta} \right)^{3-\alpha}. \quad (5.25)$$

If the feature belongs to a possible counter-jet, one measures $S_\nu^{\text{counter-jet}} = 16.7 \text{ mJy}$, and $S_\nu^{\text{jet}} = 299.8 \text{ mJy}$. Both values are taken as the peak intensities in the image in the region of interest. With that, $R \approx 18$. For realistic values of β between 0.995 and 0.9995 (Γ between 10 and 30), the viewing angle would lie between 55° and 65° . This is in conflict with the vast majority of viewing angles reported in the literature, and I conclude that it is unrealistic to identify the feature with a counter-jet. It is more likely an imaging artefact (i.e., sidelobe).

Chapter 6

Core-shift studies with long-baseline source-frequency phase referencing

To estimate the magnetic field strength along the relativistic plasma outflows in AGN, one can utilize the measure of the positional shift of the VLBI core with frequency (see Sect. 1.5 and 5.4). However, measuring the core shift is difficult, as the absolute position of the source is lost in conventional VLBI self-calibration. In these cases, the core shift is typically determined by referencing the core position to optically thin jet features whose positions should not change with frequency (the self-referencing method; cf., Lobanov 1998; Kovalev et al. 2008; Sokolovsky et al. 2011). Using this self-referencing method, the shifts can be detected reliably only in about 10% of compact radio sources (Kovalev et al. 2008). In the remaining fraction, the core shift can only be measured by phase-referencing (PR) their positions to nearby calibrator sources (relative astrometry). The basics of this method and its extension to mm wavelengths will be explained in Sect. 6.1 and 6.2.

6.1 Phase referencing

For the PR technique, one uses a calibrator near on the sky to the source of interest. This way, each telescope observes similar atmospheric fluctuations for both sources. One can then transfer the phase gains from the calibrator to the target source, and remove the phase fluctuations introduced by the atmosphere (see e.g. Beasley and Conway 1995).

If one observes the target source at time t_2 in between observations of a bright calibrator at t_1 and t_3 , the phases at each time will be:

$$\phi_{\text{cal}}(t_1) = \phi_{\text{c}}(t_1) + \phi_{\text{inst}}^{\text{c}}(t_1) + \phi_{\text{pos}}^{\text{c}}(t_1) + \phi_{\text{ant}}^{\text{c}}(t_1) + \phi_{\text{atmo}}^{\text{c}}(t_1) + \phi_{\text{iono}}^{\text{c}}(t_1), \quad (6.1)$$

$$\phi_{\text{tar}}(t_2) = \phi_{\text{t}}(t_2) + \phi_{\text{inst}}^{\text{t}}(t_2) + \phi_{\text{pos}}^{\text{t}}(t_2) + \phi_{\text{ant}}^{\text{t}}(t_2) + \phi_{\text{atmo}}^{\text{t}}(t_2) + \phi_{\text{iono}}^{\text{t}}(t_2) \quad \text{and} \quad (6.2)$$

$$\phi_{\text{cal}}(t_3) = \phi_{\text{c}}(t_3) + \phi_{\text{inst}}^{\text{c}}(t_3) + \phi_{\text{pos}}^{\text{c}}(t_3) + \phi_{\text{ant}}^{\text{c}}(t_3) + \phi_{\text{atmo}}^{\text{c}}(t_3) + \phi_{\text{iono}}^{\text{c}}(t_3), \quad (6.3)$$

where ϕ_{inst} refers to the phase induced by the instrumentation (like clock errors or electrical path delay effects), ϕ_{pos} refers to the source position error, ϕ_{ant} to the error in antenna position, and ϕ_{atmo} and ϕ_{iono} to the atmospheric and ionospheric errors, respectively. One can now interpolate the phase solutions (delay and rate) of the bright calibrator obtained by fringe fitting at times t_1 and t_3 to t_2 , and apply those absolute phase offsets, delays, and rates to the calibrator data. One can then average the target source data in time and frequency.

This will still leave the phase uncertainties described in Eq. 6.2, which are normally resolved with phase self-calibration during imaging. This time, one can image and self-calibrate the phases of the calibrator ϕ_{cal} at times t_1 and t_3 , and interpolate them to t_2 . Then, one can take the difference of the target source and calibrator phases:

$$\begin{aligned} \phi_{\text{tar}}(t_2) - \phi_{\text{cal}}(t_2) = & \phi_{\text{t}}(t_2) - \phi_{\text{c}}(t_2) + (\phi_{\text{inst}}^{\text{t}} - \phi_{\text{inst}}^{\text{c}}(t_2)) + (\phi_{\text{pos}}^{\text{t}}(t_2) - \phi_{\text{pos}}^{\text{c}}(t_2)) \\ & + (\phi_{\text{ant}}^{\text{t}}(t_2) - \phi_{\text{ant}}^{\text{c}}(t_2)) + (\phi_{\text{atmo}}^{\text{t}}(t_2) - \phi_{\text{atmo}}^{\text{c}}(t_2)) + (\phi_{\text{iono}}^{\text{t}}(t_2) - \phi_{\text{iono}}^{\text{c}}(t_2)). \end{aligned} \quad (6.4)$$

It is now reasonable to assume that the phase errors due to the instrumentation, antenna position and, given the sources have a small separation on the sky, the phase errors due to the atmosphere and ionosphere are very similar for both sources. In this case, their differences will be negligible in Eq. 6.4, leaving

$$\phi_{\text{tar}} - \phi_{\text{cal}} \approx \phi_{\text{t}} + (\phi_{\text{pos}}^{\text{t}} - \phi_{\text{pos}}^{\text{c}}) \quad (6.5)$$

in the case of $\phi_{\text{c}} = 0$, i.e. if the calibrator is compact. The t_2 dependence was dropped in this equation. If the calibrator has significant substructure, one can image the calibrator and account for the structural phase from the non-point-like structure. Concluding, one is left with information about the target source structure and its relative position to the calibrator source.

The PR technique has been successfully applied for several decades in cm-VLBI (e.g., Marcaide and Shapiro 1983; Alef 1988). With this, positional accuracies of hundreds of μs could be achieved (Guirado et al. 1995; Ros et al. 1998). In recent years, the development of VLBI at mm wavelengths has seen a surge (see Boccardi et al. 2017). The resolution with mm-VLBI is even approaching scales of a few r_{g} as of now (Issaoun et al. 2019; Event Horizon Telescope Collaboration et al. 2019a). Since the resolution of an interferometer is proportional to the wavelength, one aims for smaller observing wavelengths to decrease the beam size and thus increasing resolution. Observing at mm wavelengths would naturally also improve the precision of PR observations, but there are limitations.

In cm-VLBI PR, the main contribution of atmospheric fluctuations comes from the ionosphere, which introduces the dispersive errors that one wishes to compensate. At mm wavelengths, a primarily non-dispersive phase error is introduced in the troposphere, that also has to be corrected for. These tropospheric phase fluctuations are faster at mm wavelengths, requiring faster telescope source switching. Additional factors are the intrinsically weaker source flux densities at higher wavelengths, reduced telescope sensitivity, and higher opacity of the atmosphere (see also Fig. 2.2).

6.2 Source-frequency phase referencing (SFPR)

The need to overcome the aforementioned limitations for mm-VLBI PR lead to the development of source-frequency phase referencing (SFPR) (Rioja and Dodson 2009; Rioja et al. 2014, 2015)). This technique combines the established phase-referencing with calibrator sources with phase transfer of lower frequency to higher frequency observations (see also Middelberg et al. 2005).

At mm-wavelengths, the dominant contribution to ϕ_{atm} in Eq. 6.2 comes from the troposphere. Finding a suitable calibrator at these wavelengths is difficult. Martí-Vidal et al. (2010) investigated the effect of limited coherence in PR observations at 8.4 GHz and 15 GHz, and found that the limiting dynamic range in the recovered images is inversely proportional to the sine of the calibrator-to-target separation. Even for separations of $< 5^\circ$, the loss in coherence can already mitigate the recovered flux densities by 20% in comparison to self-calibrated images. At higher frequencies, this puts even stronger limitations on PR observations.

The aim is to correct the rapid phase fluctuations that limit the coherence with measurements of the same source at lower frequencies. This is done by transferring those phase solutions to the higher frequency observations, since the tropospheric phase errors are non-dispersive.

Consider the contributions to the phase of one of the sources displayed in Eq. 6.2. The contribution ϕ_{atm} , which corresponds to the tropospheric fluctuations at high frequencies, is, for the frequency ν_{high} (Rioja and Dodson 2009)

$$\phi_{\text{atm}}^{\text{high}} = 2\pi\nu_{\text{high}}(z_1 f_1 - z_2 f_2)/c, \quad (6.6)$$

where z corresponds to the excess zenith path length and f to the mapping function of the source direction. The subscripts 1 and 2 denote the two different antennas. If one scales the phase solutions at ν_{low} by the frequency ratio $R = \nu_{\text{high}}/\nu_{\text{low}}$, the difference between the phase contributions by the troposphere vanishes:

$$\phi_{\text{tro}}^{\text{high}} - R \cdot \phi_{\text{tro}}^{\text{low}} = 0. \quad (6.7)$$

Considering an arbitrary phase term of $2\pi n$ that can be added in Eq. 6.2, with $n \in \mathbb{Z}$, choosing R as an integer frequency ratio will naturally compensate for those terms. Overall, this step, termed frequency phase transfer (FPT), effectively accounts for all non-dispersive errors at the target frequency ν_{high} . In concordance with a second step of PR, the procedure is termed SFPR.

Rioja et al. (2014) tested SFPR with nearly contemporaneous VLBA and KVN (Korean VLBI network, Kim et al. 2004; Lee et al. 2014) observations at 22 GHz and 43 GHz. The KVN was equipped with multi-channel receivers (see, e.g. Han et al. 2013) that observed at two frequencies simultaneously, while the VLBA used more conventional fast frequency switching. It has to be assumed that the duty cycle of this frequency switching is shorter than the coherence time imposed by the fast tropospheric fluctuations. However, observing at multiple frequencies simultaneously is expected to perform even better in tracking the phase fluctuations. And indeed, in their work they showed that the multi-channel receivers offer superior compensation for the atmospheric errors.

Additionally, Rioja et al. (2015) tested the SFPR technique for the KVN at all four observing bands at 22, 43, 87, and 130 GHz. Compensating for the atmospheric errors that normally limit the coherence time showed that the data can be integrated over much longer timescales up to several hours. This makes detections of much weaker sources possible.

Observations at multiple frequencies also offer an additional benefit: without the need of self-calibration, these observations offer high-precision relative position measurements between several frequencies, allowing us to measure the core shift directly. Given that observations always need a calibrator, these shifts in the core-position are always relative shifts between the sources. For the calibrator, a putative core shift also has to be accounted for.

However, with the maximum baselines of the KVN spanning about ~ 500 km, a factor ~ 20 smaller than intercontinental VLBI, blending effects of different jet features likely pose a limit to the astrometric accuracy of the measurements. Rioja et al. (2014) found this effect to dominate the difference in agreement between the KVN and VLBA observations and conclude that these have to be corrected for.

The Yebes 40-m telescope in Spain now is also equipped with a new set of multi-channel receivers. As of the writing of this thesis, simultaneous observations at 22 and 43 GHz are possible, with the addition of 86 GHz in the future. This provides a unique opportunity to test SFPR with simultaneous multi-frequency observations for very long baselines and could compensate for the blending effect introduced by the limited KVN resolution.

6.3 Observations

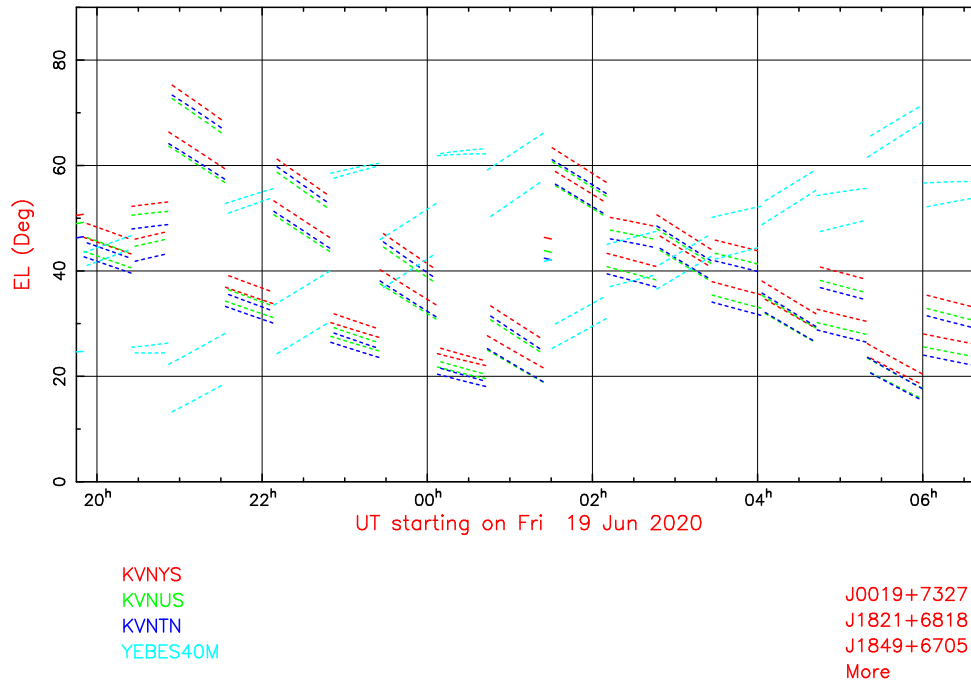


Figure 6.1: Example observation schedule for my proposed observations. The sources are organised in four groups of two sources consisting of a calibrator and the science target (both can be calibrators and science targets at the same time). The scans were distributed across the whole observing time to get the best possible (u, v) -coverage.

In 2018 I proposed, together with a small team of collaborators, observations with the KVN and the Yebes 40-m telescope. I selected a sample of AGN from the VERA Fringe survey¹ at 22 GHz and the QCAL-1 KVN 43 GHz calibrator survey². The sample was constrained to contain sources with declination of $> 40^\circ$ to make sure to obtain sufficient (u, v) -coverage with the widely separated, limited number of telescopes. This also assured that enough common sky coverage (≥ 5 h) could be obtained for all telescopes, as they are situated in East Asia and Europe.

To make sure all the sources could be detected, the source flux densities from the VERA survey at 22 GHz and the KVN calibrator survey at 43 GHz were used to extrapolate them to the long baselines between the KVN and Yebes. From the VERA survey, there are flux densities for baselines $B < 70 \text{ M}\lambda$, $70 \text{ M}\lambda < B < 100 \text{ M}\lambda$, and $B > 100 \text{ M}\lambda$. For the KVN survey, there are flux densities for baselines $B < 21 \text{ M}\lambda$, $21 \text{ M}\lambda < B < 42 \text{ M}\lambda$, and $B > 42 \text{ M}\lambda$. With this information, only sufficiently compact sources can be selected. To ensure this, I calculated the ratio of flux densities at the longest to the shortest baselines in the available datasets, and selected sources with a ratio ≥ 0.8 .

Since the targets are selected to be compact, a power-law falloff is assumed from low to high (u, v) -distances, so one can extrapolate the flux densities logarithmically. In case the sources had flux densities at longer baselines that exceeded the short-baseline flux density, a mean of flux densities was calculated as an estimate.

The baseline sensitivities (1σ) are 4.7 mJy for the intra-KVN baselines, and 1.9 mJy for the KVN-Yebes baselines at 22 GHz. At 43 GHz, they are 7.0 mJy and 3.5 mJy, respectively. This makes a detection threshold for the longest baselines of 13 mJy at 22 GHz and 25 mJy at 43 GHz. My target sources are all above this limit, where some are quite bright

¹http://astrogeo.org/fss/fss_det.txt

²<http://astrogeo.org/qcal1/datafile1.txt>

(several Jy), and others are estimated to be just barely detectable, like J0217+7349 (see Table 6.1). Thus I will be able to truly test the limits of the SFPR technique at these long baselines.

With the estimated flux densities, the source sample was further filtered to contain only sources that have a positional accuracy on the sky θ_{pos} , defined as

$$\theta_{\text{pos}} = \theta_{\text{beam}} \frac{\pi \theta_{\phi}}{180^{\circ}} \frac{S_{\text{mean}}}{S_{\text{source}}}, \quad (6.8)$$

that is of the order of a few $1000 r_{\text{G}}$. Here θ_{ϕ} is the estimated phase accuracy and S_{mean} the mean flux density from the sample of Rioja et al. (2015). To assess the angular size in r_{G} , one needs an estimate of the black hole mass M_{bh} and the source viewing angle θ_{j} to be able to calculate the de-projected distance in which one is interested. For six (marked in boldface) out of 28 sources listed in Table 6.1 estimates for both quantities could be found in the literature. For the other sources conservative assumptions of $M_{\text{bh}} \sim 5 \times 10^8 M_{\odot}$ and $\theta_{\text{j}} \sim 10^{\circ}$ were made. For the typical magnetic field strength of 0.3 G at 22 GHz obtained from the core shifts (Lobanov 1998), I estimate that the nuclear opacity in my sample will enable us to probe linear scales of $2900 R_{\text{G}}$ at 22 GHz and reaching down to $500 R_{\text{G}}$ at 129 GHz.

For the observations, the sources were paired in a way that two sources will always have an angular distance of $< 10^{\circ}$ (see Table 6.2). For the sources for which there was no other suitable target source usable as a calibrator, I searched for calibrators in the VLBA Calibrator³ and ASTROGEO⁴ databases as well as in the GMVA survey of ultracompact extragalactic radio sources at 86 GHz (Nair et al. 2019)⁵.

For J1849+6705, I found J1821+6818, which has 0.33 Jy single dish flux and 0.315 Jy at $62 \text{ M}\lambda$ at 86 GHz (05/2011, Nair et al. 2019), 2.9° apart. For BL Lac (J2202+4216), I found J2114+4634, which has 0.07 Jy single dish flux and 0.471 Jy at $55 \text{ M}\lambda$ at 86 GHz (10/2010, Nair et al. 2019), which are 9.6° apart (see Table 6.2). These calibrators were deemed bright enough and close enough to the targets. Overall I aimed for pairs with a brighter and a weaker source, to test whether the transfer of the phase calibration from the stronger source will make the weaker one detectable.

The proposal was accepted on Jan 9, 2019 by the KVN and on Jan 25, 2019 by Yebes. In the planning stage, I had to make sure to have the correct frequency setup at all stations, so fringe test observations were necessary. In total it took several iterations for successful fringe test observations, and the actual proposed observations are still in the scheduling status. This was due to a multitude of factors, including organisational problems as well as technical problems with the frequency and overall receiver setup. I will outline in the following the challenges that I faced in scheduling and observing.

I initially proposed single-polarisation (RCP or LCP) observations at 22 GHz and 43 GHz, recording at a data rate of 1 Gb/s per frequency band, split into 16 sub-bands (or intermediate frequencies, IFs) with a bandwidth of 16 MHz per sub-band, using 2-bit sampling in single polarisation. This makes a total bandwidth of 512 MHz per band. In addition, I wanted to observe at the KVN at 86 and 129 GHz with the same setup, which would be KVN only.

At the beginning, the problem arose that for the new Yebes multi-channel receivers there was not yet a polariser installed. A $\lambda/4$ plate was installed for that purpose in April 2019 to be able to observe LCP or RCP, which are the common observables in VLBI and also for the KVN.

³<http://www.vlba.nrao.edu/astro/calib/>

⁴http://astrogeo.org/gaps/gaps_names.tab

⁵<https://www3.mpifr-bonn.mpg.de/div/3mmsurvey/>

Table 6.1: Source sample for the proposed observations with the KVN and Yebes.

Name (1)	z (2)	V_{pred} (3) [Jy]	θ_{pos} (4) [mas]	θ_{pos} (5) [$10^3 R_G$]	M_{bh} (6) [$10^8 M_{\odot}$]	ref (7)	θ_j (8) [$^{\circ}$]	ref (9)
J0019+7327*	1.781	1.275	0.029	4.20	8.5	[1]	7.3	[2]
J0102+5824*	0.644	3.080	0.011	1.56			4.0	[3]
J0110+680*	0.290	0.170	0.223	20.40				
J0113+4948*	0.389	0.620	0.061	3.87	10.1	[4]	8.7	[5]
J0128+6306*	0.018	0.089	0.127	0.98				
J0136+4751*	0.859	0.157	0.033	1.14	20.4	[4]	11.4	[5]
J0217+7349*	2.367	0.048	0.026	3.11	3.0	[1]	23.8	[5]
J0228+6721*	0.523	0.016	0.067	8.77			6.6	[3]
J0303+4716*	0.475	0.460	0.079	9.87				
J0349+4609*	1.853	0.031	0.123	21.86				
J0359+6005*	0.455	0.235	0.158	19.28				
J0415+4452*	0.485	0.905	0.040	5.10				
J0503+6600*	1.695	0.150	0.253	45.39				
J0517+4537*	0.839	0.020	0.067	10.72				
J0610+7248*	3.530	0.115	0.316	49.05				
J0714+7408*	0.371	0.220	0.165	17.78				
J0731+6718*	0.170	0.140	0.237	14.43				
J1849+6705*	0.657	1.255	0.029	0.41	41.5	[6]	12.3	[5]
J2007+4029*	1.736	1.512	0.023	4.02			4.02	[3]
J2022+7611*	0.594	0.305	0.115	16.11				
J2038+5119*	1.686	0.046	0.021	3.69				
J2202+4216* (BL Lac)	0.069	2.525	0.015	0.18	14.5	[7]	7.50	[2]
J0154+4743 [†]	1.026	0.050	0.126	21.40				
J0230+4032 [†]	1.019	0.085	0.090	15.34	17.3	[4]		
J0253+5102 [†]	1.732	0.059	0.277	49.68	12.9	[7]		
J0313+4120 [†]	0.134	0.595	0.035	1.73				
J0655+4100 [†]	0.022	0.091	0.145	1.33			6.9	[5]
J0733+5022 [†]	0.720	0.096	0.117	17.80	8.1	[4]		

NOTE: Column denote (1) source name (J2000); (2) source redshift; (3) V_{pred} – predicted flux density extrapolated to the KVN-Yebes baselines from the flux densities from the VERA Fringe survey at 22 GHz (denoted with *) and the QCAL-1 KVN 43 GHz calibrator survey (denoted with [†]); (4)+(5) θ_{pos} – estimated positional accuracies from the same surveys (see text for details); (6) M_{bh} – black hole mass estimate available from literature; (8) θ_j – jet viewing angle estimates available from literature. The target sources for the observations are shown in boldface. References: [1] Zhou and Cao (2009), [2] Pushkarev et al. (2009), [3] Hovatta et al. (2009), [4] Cao and Jiang (2002), [5] Britzen et al. (2007), [6] Gu et al. (2001), [7] Ghisellini et al. (2014).

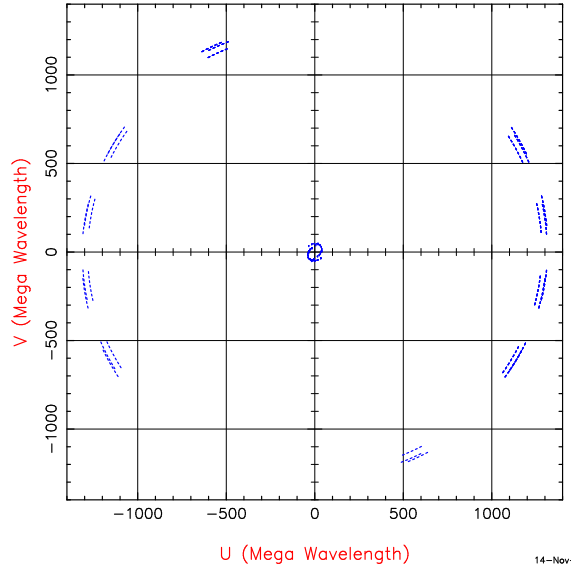


Figure 6.2: Exemplar (u, v) -coverage for J0217+7349. The maximum (u, v) -distance shown is 1400 M λ . The restriction for sources with declination $> 40^\circ$ improves the (u, v) -coverage on all telescopes owing to more common visibility, especially for the long baselines to the Yebes telescope.

Table 6.2: Observation schedule with four source pairs. The angular separation is always less than 10° .

Group	Source	Calibrator	$\theta_{\text{sep}} [^\circ]$
A	J1849+6705	J1821+6818	2.9
B	J0217+7349	J0019+7327	8.2
C	J2202+4216 (BL Lac)	J2114+4634	9.6
D	J0136+4751	J0113+4948	4.3

For the fringe test, generally a strong SiO Maser line was observed. The first fringe test was done on May 8, 2019, and the first observations were scheduled three days later. The fringe test did not yield fringes to Yebes for unknown reasons, and so the observations were postponed. Fringes were found among the KVN stations.

During the planning of the observations I decided to use all four telescopes at the two lowest frequencies and to observe in dual-polarisation mode to increase the sensitivity at these bands. This was only made possible after it was confirmed that Yebes could observe with a data rate of 4 Gb/s.

On May 22 a second fringe test was scheduled, but was not successful because of a bad recorder configuration. It was repeated on May 24, after a prior failure of KVN station Tanma (KT) was fixed. Due to a data format mismatch, the fringe test did not yield fringes again. KVN recorded in a mode with two channels with 512 MHz each, while Yebes seemingly recorded with 32 channels of 32 MHz each. It was suspected that the sample ordering was incorrect, and after some corrections to the data, fringes were found. The data were made available on August 26, as well as the data from the KVN for which fringes were detected for the observations on May 26.

Since still there were no successful observations, I proposed re-observations on October 31, 2019. Another fringe test was scheduled for Nov 20, this time for both the 1 Gb/s as well as the 4 Gb/s mode, to see if both have issues or only one of them. Both failed, and while problems with the channel ordering in the final schedule file were proposed as reason for failure of the 1 Gb/s observations, it was still unclear what led to the issues with the

4 Gb/s mode. The initially scheduled re-observations on Nov 27 were cancelled because of the unsuccessful fringe test and rain at two KVN stations.

In the next months it was tried to determine why no fringes were found in the fringe tests; for instance, it was tested if Yebes in single-dish mode detected the SiO maser lines, and despite that being successful, the reason for the unsuccessful fringe test remained unknown.

A new fringe test was conducted on May 11, 2020. With no success initially, fringes were found after correcting some reversed-sideband effect, that shifted the maser line for Yebes. The successful fringe test observations are shown in Fig. 6.3. Following this, new observations were scheduled for June 19, 2020. Fig. 6.1 shows an example of the planned observation schedule for eight selected sources, that was originally to be observed on this date. The source pairings are also displayed in Table 6.2. These observations were cancelled due to malfunction of the receiver at Yebes, reported on June 17. Further rescheduling was delayed due to the KVN being in summer maintenance mode until September 2020. As of the writing of this thesis, no successful observations for all four stations can be reported, and results are expected to be reported in a forthcoming publication.

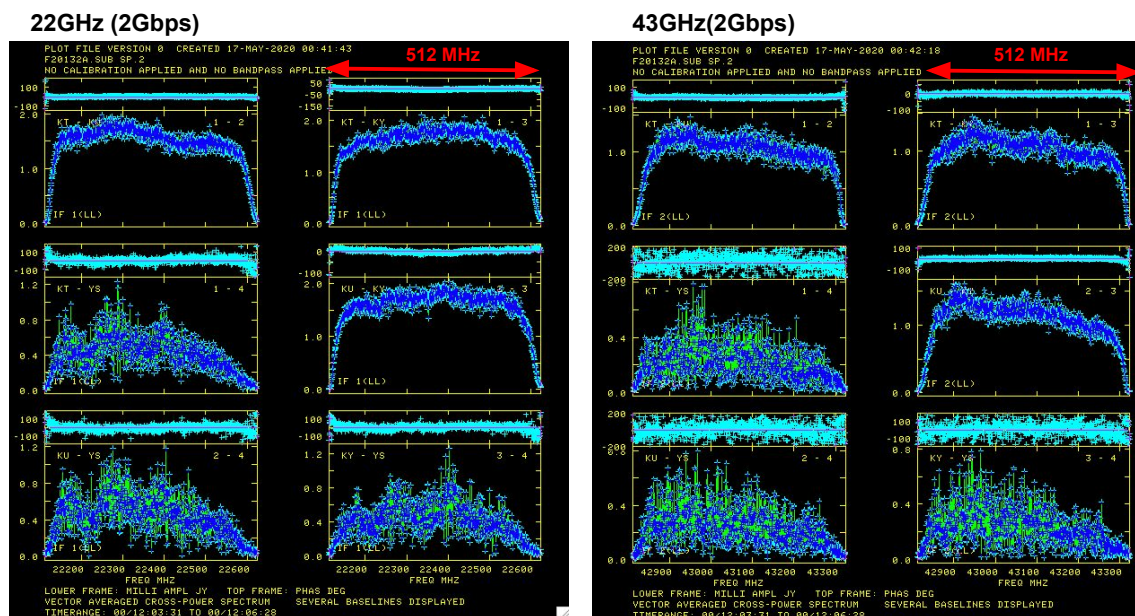


Figure 6.3: Successful fringe test on May 11, 2020 at 4 Gb/s between all 4 stations (from T. Jung, priv. comm.)

SFPR observations consist of alternate observations of the source and the calibrator with a slow duty cycle of a few minutes. Frequency switching is not necessary as one observes at all frequencies simultaneously. I decided on a ~ 4 min cycle time (i.e., calibrator-target-calibrator). The exact time will depend on the telescope slewing time. This may be different between the Yebes 40-m telescope and the KVN telescope for two reasons. First, the 40-m telescope is much larger than the KVN antennas, increasing its slewing time in general. Secondly, due to the large distance between the telescopes in Europe and East Asia, they observe the source at different elevations at the same time. Due to this, their slewing times might differ when observing the source.

In principle, slower switching time is more time-efficient but more risky, as detections are less likely within a smaller integration time. Faster switching time is, in contrast, less risky, but also less efficient. I considered the option including different switching cycles in the observations to reduce the overall risk, but in the end decided that it is not very

promising in the given observing time of 11 h. In both Rioja et al. (2014, 2015), a ~ 3 min cycle time was chosen. I opted for a slightly larger cycle time to make detections more likely, as the expected correlated flux density is lower for the longer baselines.

6.4 Outlook

Judging from the baseline sensitivity, of the four source pairs, I expect to detect all sources even without SFPR, with conventional VLBI self-calibration. Then the performance of SFPR can be compared with hybrid maps. There are sources with predicted flux densities between a few tens of mJy (close to the detection limit) up to several Jy, which will enable us to explore the limitations of SFPR.

When SFPR has been applied to the data, one can infer relative core shifts between the respective calibrator and target source with high precision. Rioja et al. (2015) calculated that the registration errors of their images are if the order of a few tens of μas , depending on the source and the frequency pair used. They estimate that the increase in maximum baseline of 8000 km would result in a 20-fold decrease of the astrometric error, which I should be able to achieve with my proposal. This accuracy will allow us to infer the core shifts to very high precision, of a few microarcseconds.

With the SFPR method one measures relative core shifts between the source pairs. Breaking the degeneracy requires the analysis of a source with multiple calibrator sources situated in different direction from the source on the sky. In a future study I plan to do such an analysis. For this study, a literature search could put some constraints on expected core shifts for some of the observed sources. In addition, for the brighter sources, one can try to align the self-calibrated maps at the two frequencies with some optically thin structure (see Sect. 5.4), and infer the core shift from there.

Being able to calculate the magnetic field and its radial dependence, as described in Sect. 1.5, at $10^3 - 10^4 r_g$, which is my goal with the observations, will enable me to constrain the jet launching in AGN jets. A radial dependence in the jet of $B(r) \propto r^{-1}$ and a maximum field strength $B_{\text{max}} \approx 10^4 \text{ G}$ are expected for an accretion disk dominated magnetic field (Field and Rogers 1993), while the field should fall off more rapidly for the other scenarios and may reach a much stronger maximum value in the case of a magnetic rotator (Kardashev 1995), see also Lobanov (1998).

Chapter 7

Concluding remarks and outlook

With this thesis, I aimed to improve the understanding of the AGN jet launching, collimation and propagation, as well as their physical properties on parsec-scales, with detailed studies of flat spectrum radio quasar 3C 345.

In this work, I presented the data reduction and analysis of space-VLBI data obtained with *RadioAstron* for 3C 345. With the constructed full-polarisation space-VLBI images at 1.6 GHz it was possible to probe the magnetic field structure of the source, revealing an almost completely depolarised core region and electric vector position angles aligned with the jet direction. The brightest feature in the jet at 1.5 mas is also highly polarised. In conjunction with the obtained spectral index maps, obtained from a multi-frequency VLBI dataset, a shock scenario is favoured for this region, as the spectrum steepens at this position. Overall, the core is optically thick between the observed wavelengths of 1.6, 4.8, 8.4, 15.3, and 43.1 GHz. The features farther downstream of the peak brightness in the 1.6 GHz *RadioAstron* map could be identified with shocks, but it is also possible that they probe a toroidal magnetic field independently of shocks, that could in principle be part of a helical magnetic field. The achieved resolution transverse to the jet direction is insufficient to probe potential transverse changes in the EVPA direction, although there are hints at that. This could be further investigated with space-VLBI at higher frequencies and mm-VLBI data.

In conjunction with VLBA data at 4.8, 8.4, and 15 GHz, I constructed the distribution of the rotation measure in the source, at unprecedented resolution for the probed wavelengths. This reveals a modest and mostly homogeneous RM in the source, in concordance with previous VLBI observations at lower resolution or higher frequencies. Depending on the chosen pixel SNR threshold, there are hints at a higher RM region close to the total intensity peak at 1.6 GHz, and even a flip in the sign of the RM along the jet. The latter would require a poloidal magnetic field component in the source. The RM -corrected image at 1.6 GHz changes the orientation of the EVPAs around the peak brightness position from parallel to almost perpendicular to the local jet direction. This behaviour is in accordance with previous VLBI observations at higher frequencies and supports the idea that a shock propagating down the jet dominates the emission in the region. An order-of-magnitude comparison of the electron density derived from core-shift measurements and RM analysis hints at an external Faraday screen being responsible for the observed rotation of the EVPAs. A detailed future analysis of the depolarisation properties will shed light onto the nature of the Faraday rotation. In addition, a comprehensive study of the synchrotron spectrum across all wavelengths in the jet will give further constraints on the magnetic field properties in the framework of synchrotron self-absorption.

These results can be solidified with more data, for which I will analyse *RadioAstron* data at 22 GHz in conjunction with GMVA data at 86 GHz. These data will provide additional constraints for the core shift analysis in this work. Polarisation data could also

potentially reveal RM gradients perpendicular to the jet direction, which would support the existence of a helical magnetic field. The brightness temperature as a function of the (u, v) -distance can also be studied, complementing my analysis in Chapter 5.

In the second part of the thesis, I presented the concept of applying source frequency phase referencing (SFPR) observations, which make it possible to accurately probe the core shifts in AGN. They do not rely on image alignment at different frequencies, after the absolute position of the source is lost during self-calibration. The advent of multi-channel receivers, which observe at several wavelengths simultaneously, enable the phase referencing technique to higher frequencies. This allows us to obtain reliable estimates of the core shift at high frequencies, which in turn makes it possible to probe the magnetic field profile along the jet close to the central engine. An observing program was designed for a small sample of compact AGN. They were selected in a way as to probe regions of several 1000 gravitational radii with the achieved positional accuracy. These observations, planned for the end of 2020, will extend the SFPR technique to longer baselines compared to previous studies, minimising blending effects and thus improving the accuracy. This project will be an important pathfinder in this emerging field, where other telescopes begin to implement multi-channel receivers.

Appendix A

Map alignment

Here the distributions of the 2D cross-correlation coefficients for the alignment between the maps presented in Chapter 5 are shown.

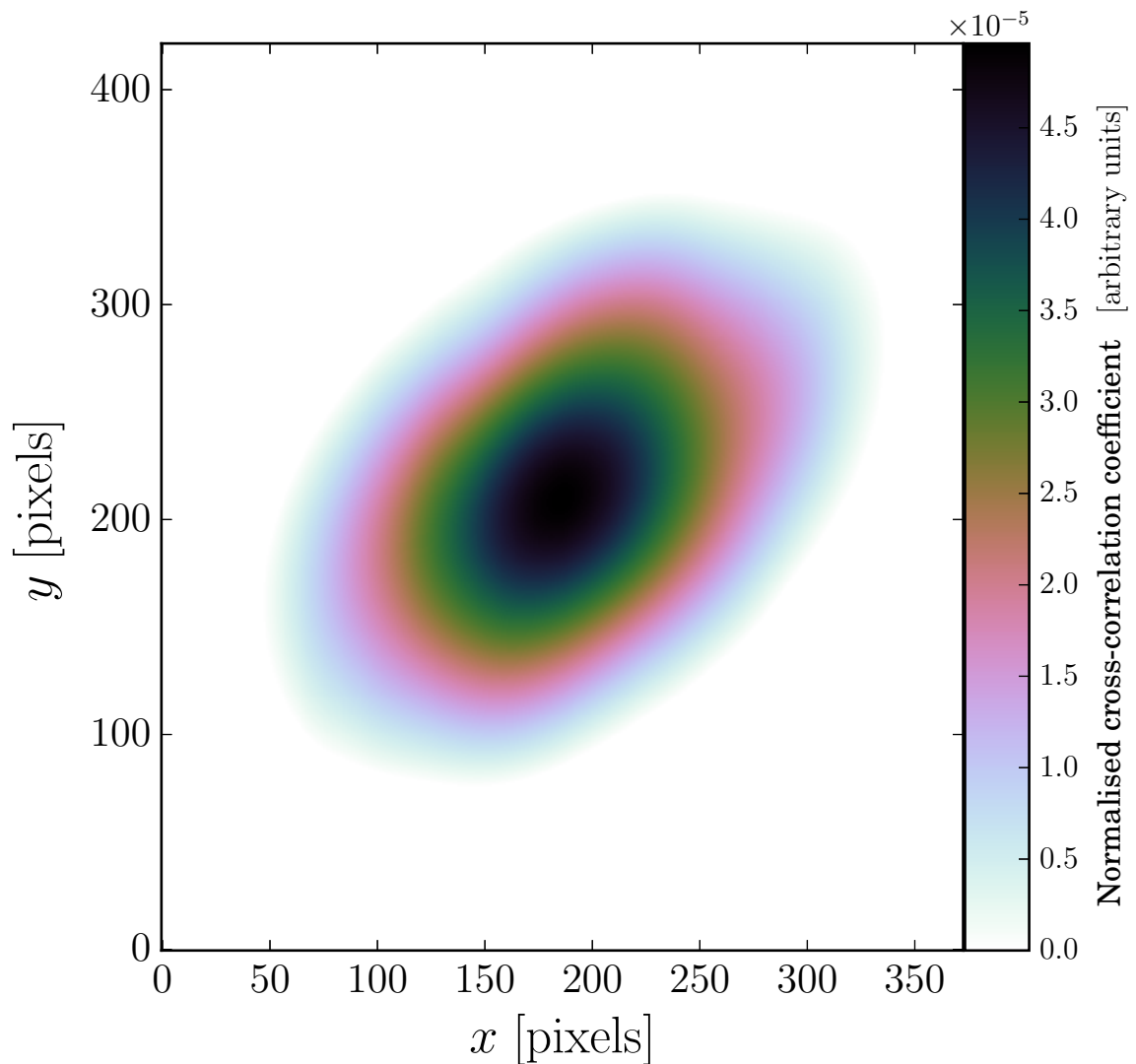


Figure A.1: Distribution of the 2D-cross-correlation coefficient from the alignment of the 1.6 GHz RadioAstron and the 15.3 GHz MOJAVE observations (cf. Fig. 5.10). One pixel corresponds to 0.02 mas.

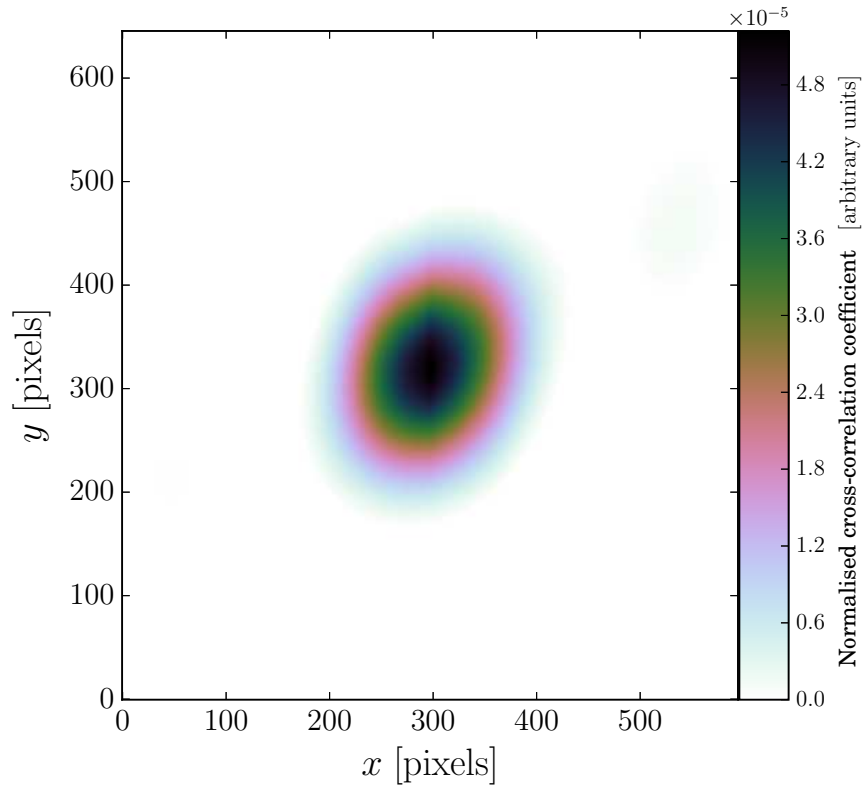


Figure A.2: Distribution of the 2D-cross-correlation coefficient from the alignment of the 1.6 GHz RadioAstron and the 4.8 GHz VLBA observations (cf. Fig. 5.13). One pixel corresponds to 0.15 mas.

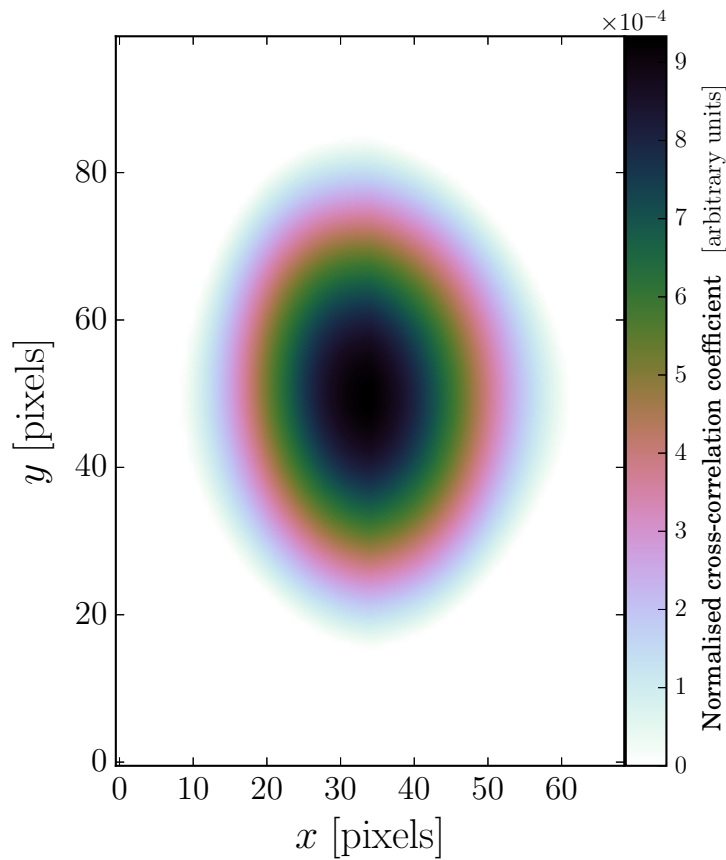


Figure A.3: Distribution of the 2D-cross-correlation coefficient from the alignment of the 4.8 GHz and the 8.4 GHz VLBA observations (cf. Fig. 5.16). One pixel corresponds to 0.1 mas.

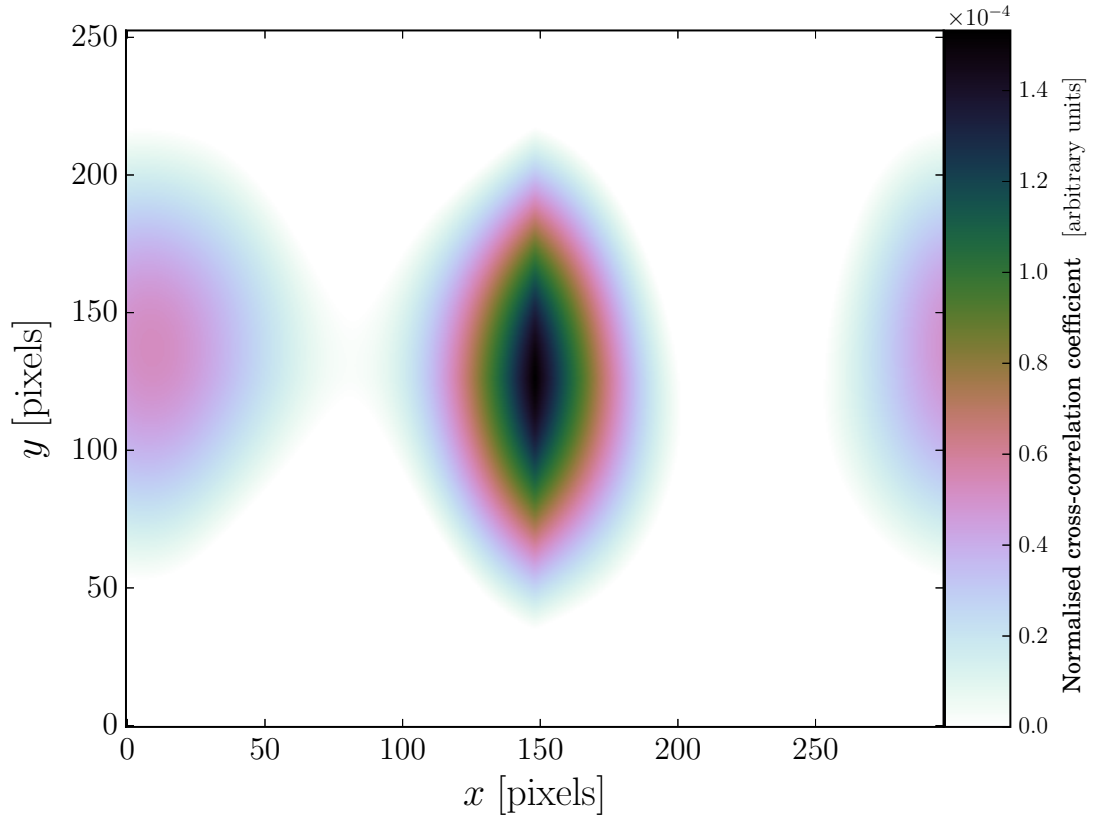


Figure A.4: Distribution of the 2D-cross-correlation coefficient from the alignment of the 8.4 GHz VLBA and the 15.3 GHz MOJAVE observations (cf. Fig. 5.19). One pixel corresponds to 0.02 mas.

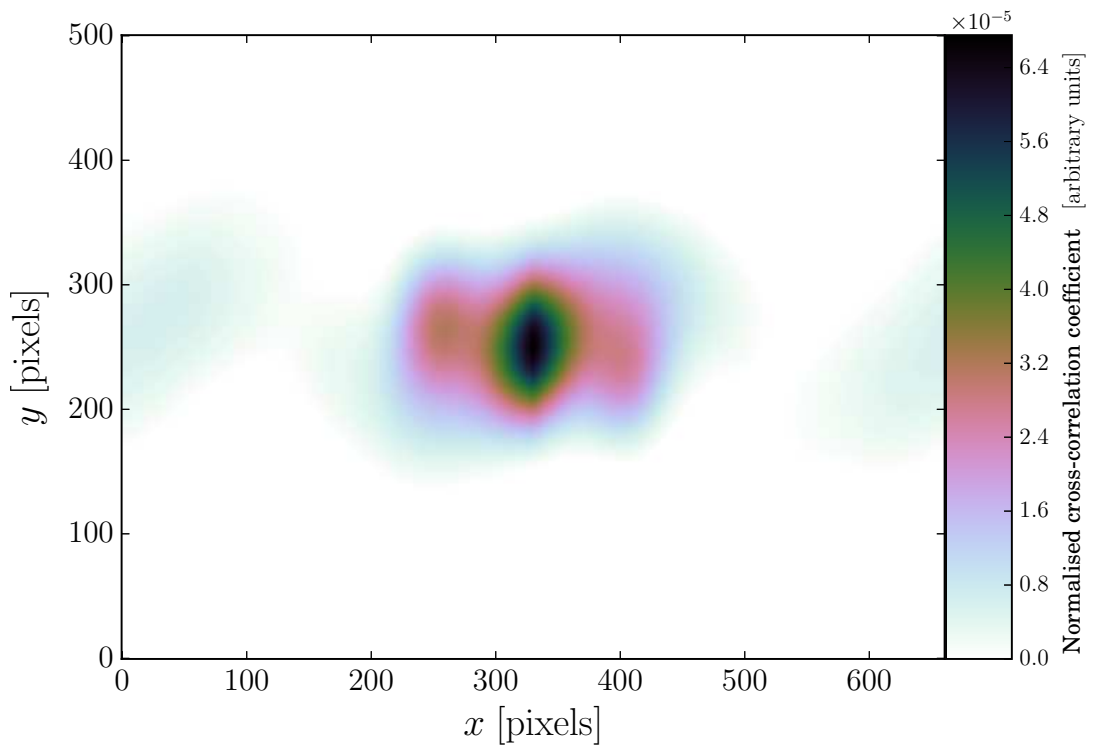


Figure A.5: Distribution of the 2D-cross-correlation coefficient from the alignment of the 15.3 GHz MOJAVE and the 43.1 GHz VLBA observations from the BU blazar program (cf. Fig. 5.22). One pixel corresponds to 0.01 mas.

Bibliography

- Alef, W. (1988). “Test of Phase-Reference Mapping for Switched Observations”. In: *The Impact of VLBI on Astrophysics and Geophysics*. Ed. by M. J. Reid and J. M. Moran. Vol. 129. IAU Symposium. URL: <https://ui.adsabs.harvard.edu/abs/1988IAUS..129..523A>.
- Aller, H. D. and Haddock, F. T. (1967). “Time Variations of the Radio Polarization of Quasi-Stellar Sources at 8000 Mc/s”. In: *ApJ* 147, 833. DOI: 10.1086/149067.
- Angelakis, E., Fuhrmann, L., Myserlis, I., et al. (2019). “F-GAMMA: Multi-frequency radio monitoring of Fermi blazars. The 2.64 to 43 GHz Effelsberg light curves from 2007-2015”. In: *A&A* 626, A60. DOI: 10.1051/0004-6361/201834363. arXiv: 1902.04404 [astro-ph.HE].
- Angioni, R. (2018). “VLBI and gamma-ray studies of radio galaxies in the TANAMI monitoring program”. PhD thesis. Universität zu Köln. URL: <https://kups.ub.uni-koeln.de/9380/>.
- Ansoldi, S., Antonelli, L. A., Arcaro, C., et al. (2018). “The Blazar TXS 0506+056 Associated with a High-energy Neutrino: Insights into Extragalactic Jets and Cosmic-Ray Acceleration”. In: *ApJL* 863, L10. DOI: 10.3847/2041-8213/aad083. arXiv: 1807.04300 [astro-ph.HE].
- Baade, W. (1956). “Polarization in the Jet of Messier 87.” In: *ApJ* 123, 550. DOI: 10.1086/146194.
- Baczko, A. K., Schulz, R., Kadler, M., et al. (2019). “Asymmetric jet production in the active galactic nucleus of NGC 1052”. In: *A&A* 623, A27. DOI: 10.1051/0004-6361/201833828. arXiv: 1901.02639 [astro-ph.GA].
- Bardeen, J. M. and Petterson, J. A. (1975). “The Lense-Thirring Effect and Accretion Disks around Kerr Black Holes”. In: *ApJL* 195, L65. DOI: 10.1086/181711.
- Beasley, A. J. and Conway, J. E. (1995). “VLBI Phase-Referencing”. In: *Very Long Baseline Interferometry and the VLBA*. Ed. by J. A. Zensus, P. J. Diamond, and P. J. Napier. Vol. 82. Astronomical Society of the Pacific Conference Series.
- Blandford, R. D. and Znajek, R. L. (1977). “Electromagnetic extraction of energy from Kerr black holes.” In: *MNRAS* 179, 433. DOI: 10.1093/mnras/179.3.433.
- Blandford, R. D. and Rees, M. J. (1978). “Extended and compact extragalactic radio sources: interpretation and theory.” In: *Physica Scripta* 17, 265. DOI: 10.1088/0031-8949/17/3/020.
- Blandford, R. D. and Königl, A. (1979). “Relativistic jets as compact radio sources.” In: *ApJ* 232, 34. DOI: 10.1086/157262.
- Blandford, R. D. and Payne, D. G. (1982). “Hydromagnetic flows from accretion disks and the production of radio jets.” In: *MNRAS* 199, 883. DOI: 10.1093/mnras/199.4.883.

- Blandford, R., Meier, D., and Readhead, A. (2019). “Relativistic Jets from Active Galactic Nuclei”. In: *ARA&A* 57, 467. DOI: 10.1146/annurev-astro-081817-051948. arXiv: 1812.06025 [astro-ph.HE].
- Blumenthal, G. R. and Gould, R. J. (1970). “Bremsstrahlung, Synchrotron Radiation, and Compton Scattering of High-Energy Electrons Traversing Dilute Gases”. In: *Reviews of Modern Physics* 42, 237. DOI: 10.1103/RevModPhys.42.237.
- Boccardi, B. (2015). “The two-sided relativistic outflow in Cygnus A: extragalactic jet physics at extreme spatial resolution”. PhD thesis. Universität zu Köln. URL: <https://kups.ub.uni-koeln.de/7026/>.
- Boccardi, B., Krichbaum, T. P., Ros, E., et al. (2017). “Radio observations of active galactic nuclei with mm-VLBI”. In: *A&AR* 25, 4. DOI: 10.1007/s00159-017-0105-6. arXiv: 1711.07548 [astro-ph.HE].
- Bolton, J. G. and Slee, O. B. (1953). “Galactic Radiation at Radio Frequencies. V. The Sea Interferometer”. In: *Australian Journal of Physics* 6, 420. DOI: 10.1071/PH530420.
- Böttcher, M. (2016). “Spectral and Polarization Signatures of Relativistic Shocks in Blazars”. In: *Galaxies* 4, 22. DOI: 10.3390/galaxies4030022. arXiv: 1609.01167 [astro-ph.HE].
- Britzen, S., Roland, J., Laskar, J., et al. (2001). “On the origin of compact radio sources. The binary black hole model applied to the gamma-bright quasar PKS 0420-014”. In: *A&A* 374, 784. DOI: 10.1051/0004-6361:20010685.
- Britzen, S., Brinkmann, W., Campbell, R. M., et al. (2007). “The soft X-ray properties of AGN from the CJF sample. A correlation analysis between soft X-ray and VLBI properties”. In: *A&A* 476, 759. DOI: 10.1051/0004-6361:20042439. arXiv: 0802.4347 [astro-ph].
- Britzen, S., Fendt, C., Böttcher, M., et al. (2019). “A cosmic collider: Was the IceCube neutrino generated in a precessing jet-jet interaction in TXS 0506+056?” In: *A&A* 630, A103. DOI: 10.1051/0004-6361/201935422.
- Bruni, G., Anderson, J., Alef, W., et al. (2016). “The RadioAstron Dedicated DiFX Distribution”. In: *Galaxies* 4, 55. DOI: 10.3390/galaxies4040055.
- Bruni, G., Savolainen, T., Gómez, J. L., et al. (2020). “Active galactic nuclei imaging programs of the RadioAstron mission”. In: *Advances in Space Research* 65, 712. DOI: 10.1016/j.asr.2019.03.044. arXiv: 1904.00814 [astro-ph.GA].
- Burn, B. J. (1966). “On the depolarization of discrete radio sources by Faraday dispersion”. In: *MNRAS* 133, 67. DOI: 10.1093/mnras/133.1.67.
- Campbell, W. W. and Moore, J. H. (1918). “The spectrographic velocities of the bright-line nebulae.” In: *Publications of Lick Observatory* 13, 75. URL: <https://ui.adsabs.harvard.edu/abs/1918PLic0..13...75C>.
- Cao, X. and Jiang, D. R. (2002). “Relation between radio core length and black hole mass for active galactic nuclei”. In: *MNRAS* 331, 111. DOI: 10.1046/j.1365-8711.2002.05185.x. arXiv: astro-ph/0110541 [astro-ph].
- Cassidy, I. and Raine, D. J. (1993). “The broad-line regions of active galaxies.” In: *MNRAS* 260, 385. DOI: 10.1093/mnras/260.2.385.
- Cheung, C. C., Harris, D. E., and Stawarz, L. (2007). “Superluminal Radio Features in the M87 Jet and the Site of Flaring TeV Gamma-Ray Emission”. In: *ApJL* 663, L65. DOI: 10.1086/520510. arXiv: 0705.2448 [astro-ph].

- Clark, B. G. (1980). “An efficient implementation of the algorithm ’CLEAN’”. In: *A&A* 89, 377. URL: <https://ui.adsabs.harvard.edu/abs/1980A&A...89..377C>.
- Cordes, J. M. and Lazio, T. J. W. (2002). “NE2001.I. A New Model for the Galactic Distribution of Free Electrons and its Fluctuations”. In: *arXiv e-prints*, astro-ph/0207156. arXiv: astro-ph/0207156 [astro-ph].
- Croke, S. M. and Gabuzda, D. C. (2008). “Aligning VLBI images of active galactic nuclei at different frequencies”. In: *MNRAS* 386, 619. DOI: 10.1111/j.1365-2966.2008.13087.x. arXiv: 0809.3313 [astro-ph].
- Curtis, H. D. (1918). “Descriptions of 762 Nebulae and Clusters Photographed with the Crossley Reflector”. In: *Publications of Lick Observatory* 13, 9. URL: <https://ui.adsabs.harvard.edu/abs/1918PLic0..13....9C>.
- Deller, A. T., Brisken, W. F., Phillips, C. J., et al. (2011). “DiFX-2: A More Flexible, Efficient, Robust, and Powerful Software Correlator”. In: *PASP* 123, 275. DOI: 10.1086/658907. arXiv: 1101.0885 [astro-ph.IM].
- Edge, D. O., Shakeshaft, J. R., McAdam, W. B., et al. (1959). “A survey of radio sources at a frequency of 159 Mc/s.” In: *MmRAS* 68, 37. URL: <https://ui.adsabs.harvard.edu/abs/1959MmRAS...68...37E>.
- Elitzur, M. (2007). “Unification Issues and the AGN Torus”. In: *The Central Engine of Active Galactic Nuclei*. Ed. by L. C. Ho and J. W. Wang. Vol. 373. Astronomical Society of the Pacific Conference Series. arXiv: astro-ph/0612458 [astro-ph].
- Event Horizon Telescope Collaboration, Akiyama, K., Alberdi, A., et al. (2019a). “First M87 Event Horizon Telescope Results. I. The Shadow of the Supermassive Black Hole”. In: *ApJL* 875, L1. DOI: 10.3847/2041-8213/ab0ec7. arXiv: 1906.11238 [astro-ph.GA].
- (2019b). “First M87 Event Horizon Telescope Results. V. Physical Origin of the Asymmetric Ring”. In: *ApJL* 875, L5. DOI: 10.3847/2041-8213/ab0f43. arXiv: 1906.11242 [astro-ph.GA].
- Fanaroff, B. L. and Riley, J. M. (1974). “The morphology of extragalactic radio sources of high and low luminosity”. In: *MNRAS* 167, 31. DOI: 10.1093/mnras/167.1.31P.
- Fanti, C., Fanti, R., Ficarra, A., et al. (1981). “Low frequency variable sources 5 year monitoring program at 408 MHz”. In: *A&AS* 45, 61. URL: <https://ui.adsabs.harvard.edu/abs/1981A&AS...45...61F>.
- Fath, E. A. (1909). “The Spectra of Some Spiral Nebulae and Globular Star Clusters”. In: *Popular Astronomy* 17, 504. URL: <https://ui.adsabs.harvard.edu/abs/1909PA....17..504F>.
- Felli, M. and Spencer, R. E., eds. (1989). *Very Long Baseline Interferometry: Techniques and Applications*. Vol. 283. NATO Advanced Science Institutes (ASI) Series C. DOI: 10.1007/978-94-009-2428-4.
- Field, G. B. and Rogers, R. D. (1993). “Radiation from Magnetized Accretion Disks in Active Galactic Nuclei”. In: *ApJ* 403, 94. DOI: 10.1086/172185.
- Fomalont, E. B. (1999). “Image Analysis”. In: *Synthesis Imaging in Radio Astronomy II*. Ed. by G. B. Taylor, C. L. Carilli, and R. A. Perley. Vol. 180. Astronomical Society of the Pacific Conference Series.

- Fossati, G., Maraschi, L., Celotti, A., et al. (1998). “A unifying view of the spectral energy distributions of blazars”. In: *MNRAS* 299, 433. DOI: 10.1046/j.1365-8711.1998.01828.x. arXiv: astro-ph/9804103 [astro-ph].
- Fromm, C. (2012). “Spectral Evolution in Blazars: The case of CTA 102”. PhD thesis. Rheinische Friedrich-Wilhelms-Universität Bonn. URL: <https://link.springer.com/book/10.1007/978-3-319-10768-4>.
- Fromm, C. M., Ros, E., Perucho, M., et al. (2013). “Catching the radio flare in CTA 102. III. Core-shift and spectral analysis”. In: *A&A* 557, A105. DOI: 10.1051/0004-6361/201321784. arXiv: 1306.6208 [astro-ph.CO].
- Gabuzda, D. C. and Gómez, J. L. (2001). “VSOP polarization observations of the BL Lacertae object OJ 287”. In: *MNRAS* 320, L49. DOI: 10.1046/j.1365-8711.2001.04147.x.
- Ghisellini, G., Padovani, P., Celotti, A., et al. (1993). “Relativistic Bulk Motion in Active Galactic Nuclei”. In: *ApJ* 407, 65. DOI: 10.1086/172493.
- Ghisellini, G., Tavecchio, F., Maraschi, L., et al. (2014). “The power of relativistic jets is larger than the luminosity of their accretion disks”. In: *Nature* 515, 376. DOI: 10.1038/nature13856. arXiv: 1411.5368 [astro-ph.HE].
- Giovannini, G., Savolainen, T., Orienti, M., et al. (2018). “A wide and collimated radio jet in 3C84 on the scale of a few hundred gravitational radii”. In: *Nature Astronomy* 2, 472. DOI: 10.1038/s41550-018-0431-2. arXiv: 1804.02198 [astro-ph.GA].
- Gomez, J. L., Alberdi, A., Marcaide, J. M., et al. (1994). “Synchrotron emission from bent shocked relativistic jets. III. Aberration of light and time delay effects.” In: *A&A* 292, 33.
- Gómez, J. L., Lobanov, A. P., Bruni, G., et al. (2016). “Probing the Innermost Regions of AGN Jets and Their Magnetic Fields with RadioAstron. I. Imaging BL Lacertae at 21 Microarcsecond Resolution”. In: *ApJ* 817, 96. DOI: 10.3847/0004-637X/817/2/96. arXiv: 1512.04690 [astro-ph.HE].
- Greisen, E. W. (2003). “AIPS, the VLA, and the VLBA”. In: *Information Handling in Astronomy - Historical Vistas*. Ed. by A. Heck. Vol. 285. Astrophysics and Space Science Library. DOI: 10.1007/0-306-48080-8_7.
- Gu, M., Cao, X., and Jiang, D. R. (2001). “On the masses of black holes in radio-loud quasars”. In: *MNRAS* 327, 1111. DOI: 10.1046/j.1365-8711.2001.04795.x. arXiv: astro-ph/0104383 [astro-ph].
- Guirado, J. C., Marcaide, J. M., Elosegui, P., et al. (1995). “VLBI differential astrometry of the radio sources 1928+738 and 2007+777 at 5 GHz.” In: *A&A* 293, 613. URL: <https://ui.adsabs.harvard.edu/abs/1995A&A...293..613G>.
- Han, S.-T., Lee, J.-W., Kang, J., et al. (2013). “Korean VLBI Network Receiver Optics for Simultaneous Multifrequency Observation: Evaluation”. In: *PASP* 125, 539. DOI: 10.1086/671125.
- Hirabayashi, H., Hirose, H., Kobayashi, H., et al. (1998). “Overview and Initial Results of the Very Long Baseline Interferometry Space Observatory Programme”. In: *Science* 281, 1825. DOI: 10.1126/science.281.5384.1825.

- Hirabayashi, H., Hirosawa, H., Kobayashi, H., et al. (2000). “The VLBI Space Observatory Programme and the Radio-Astronomical Satellite HALCA”. In: *PASJ* 52, 955. DOI: 10.1093/pasj/52.6.955.
- Hirotoni, K. (2005). “Kinetic Luminosity and Composition of Active Galactic Nuclei Jets”. In: *ApJ* 619, 73. DOI: 10.1086/426497. arXiv: astro-ph/0411087 [astro-ph].
- Högbom, J. A. (1974). “Aperture Synthesis with a Non-Regular Distribution of Interferometer Baselines”. In: *A&AS* 15, 417. URL: <https://ui.adsabs.harvard.edu/abs/1974A&AS...15..417H>.
- Hong, X. Y., Jiang, D. R., Gurvits, L. I., et al. (2004). “A relativistic helical jet in the γ -ray AGN 1156+295”. In: *A&A* 417, 887. DOI: 10.1051/0004-6361:20031784. arXiv: astro-ph/0401627 [astro-ph].
- Hovatta, T., Valtaoja, E., Tornikoski, M., et al. (2009). “Doppler factors, Lorentz factors and viewing angles for quasars, BL Lacertae objects and radio galaxies”. In: *A&A* 494, 527. DOI: 10.1051/0004-6361:200811150. arXiv: 0811.4278 [astro-ph].
- Hovatta, T., Lister, M. L., Aller, M. F., et al. (2012). “MOJAVE: Monitoring of Jets in Active Galactic Nuclei with VLBA Experiments. VIII. Faraday Rotation in Parsec-scale AGN Jets”. In: *AJ* 144, 105. DOI: 10.1088/0004-6256/144/4/105. arXiv: 1205.6746 [astro-ph.CO].
- Hovatta, T., Aller, M. F., Aller, H. D., et al. (2014). “MOJAVE: Monitoring of Jets in Active Galactic Nuclei with VLBA Experiments. XI. Spectral Distributions”. In: *AJ* 147, 143. DOI: 10.1088/0004-6256/147/6/143. arXiv: 1404.0014 [astro-ph.GA].
- Hubble, E. P. (1925). “NGC 6822, a remote stellar system.” In: *ApJ* 62, 409. DOI: 10.1086/142943.
- (1926). “Extragalactic nebulae.” In: *ApJ* 64, 321. DOI: 10.1086/143018.
- Hubble, E. (1929). “A Relation between Distance and Radial Velocity among Extragalactic Nebulae”. In: *Proceedings of the National Academy of Science* 15, 168. DOI: 10.1073/pnas.15.3.168.
- Issaoun, S., Johnson, M. D., Blackburn, L., et al. (2019). “The Size, Shape, and Scattering of Sagittarius A* at 86 GHz: First VLBI with ALMA”. In: *ApJ* 871, 30. DOI: 10.3847/1538-4357/aaf732. arXiv: 1901.06226 [astro-ph.HE].
- Jackson, J. D. (1999). *Classical Electrodynamics*. 3rd ed. John Wiley & Sons. ISBN: 9780471309321.
- Johnson, M. D., Kovalev, Y. Y., Gwinn, C. R., et al. (2016). “Extreme Brightness Temperatures and Refractive Substructure in 3C273 with RadioAstron”. In: *ApJL* 820, L10. DOI: 10.3847/2041-8205/820/1/L10. arXiv: 1601.05810 [astro-ph.HE].
- Jorstad, S. G., Marscher, A. P., Stevens, J. A., et al. (2007). “Multiwaveband Polarimetric Observations of 15 Active Galactic Nuclei at High Frequencies: Correlated Polarization Behavior”. In: *AJ* 134, 799. DOI: 10.1086/519996. arXiv: 0705.4273 [astro-ph].
- Jorstad, S. and Marscher, A. (2016). “The VLBA-BU-BLAZAR Multi-Wavelength Monitoring Program”. In: *Galaxies* 4, 47. DOI: 10.3390/galaxies4040047.
- Jorstad, S. G., Marscher, A. P., Morozova, D. A., et al. (2017). “Kinematics of Parsec-scale Jets of Gamma-Ray Blazars at 43 GHz within the VLBA-BU-BLAZAR Program”. In: *ApJ* 846, 98. DOI: 10.3847/1538-4357/aa8407. arXiv: 1711.03983 [astro-ph.GA].

- Kadler, M., Ros, E., Lobanov, A. P., et al. (2004). “The twin-jet system in NGC 1052: VLBI-scrutiny of the obscuring torus”. In: *A&A* 426, 481. DOI: 10.1051/0004-6361:20041051. arXiv: astro-ph/0407283 [astro-ph].
- Kadler, M., Krauß, F., Mannheim, K., et al. (2016). “Coincidence of a high-fluence blazar outburst with a PeV-energy neutrino event”. In: *Nature Physics* 12, 807. DOI: 10.1038/nphys3715. arXiv: 1602.02012 [astro-ph.HE].
- Kardashev, N. S. (1995). “Cosmic supercollider”. In: *MNRAS* 276, 515. DOI: 10.1093/mnras/276.2.515.
- Kellermann, K. I. and Pauliny-Toth, I. I. K. (1969). “The Spectra of Opaque Radio Sources”. In: *ApJl* 155, L71. DOI: 10.1086/180305.
- Kim, H. G., Han, S. T., Sohn, B. W., et al. (2004). “Construction of the Korean VLBI Network (KVN)”. In: *European VLBI Network on New Developments in VLBI Science and Technology*. arXiv: astro-ph/0412689 [astro-ph].
- Kim, J. Y., Krichbaum, T. P., Lu, R. S., et al. (2018). “The limb-brightened jet of M87 down to the 7 Schwarzschild radii scale”. In: *A&A* 616, A188. DOI: 10.1051/0004-6361/201832921. arXiv: 1805.02478 [astro-ph.GA].
- Klare, J., Zensus, J. A., Ros, E., et al. (2000). “A Sharper View into the Parsec-Scale Jet of 3C345”. In: *Astrophysical Phenomena Revealed by Space VLBI*. Ed. by H. Hirabayashi, P. G. Edwards, and D. W. Murphy. URL: <https://ui.adsabs.harvard.edu/abs/2000aprs.conf...21K>.
- Klare, J., Zensus, J. A., Krichbaum, T. P., et al. (2001). “The quasar 3C 345 at the highest resolution with mm-VLBI and space-VLBI”. In: *Galaxies and their Constituents at the Highest Angular Resolutions*. Ed. by R. T. Schilizzi. Vol. 205. arXiv: astro-ph/0101433 [astro-ph].
- Klare, J. (2003). “Quasi-Periodicity in the Parsec-Scale Jet of the Quasar 3C 345 - A high resolution Study using VSOP and VLBA”. PhD thesis. Rheinische Friedrich-Wilhelms-Universität Bonn. URL: <https://kups.ub.uni-koeln.de/9380/>.
- Klare, J., Zensus, J. A., Lobanov, A. P., et al. (2005). “Quasi-Periodic Changes in the Parsec-Scale Jet of 3C 345”. In: *Future Directions in High Resolution Astronomy*. Ed. by J. Romney and M. Reid. Vol. 340. Astronomical Society of the Pacific Conference Series. arXiv: astro-ph/0311182 [astro-ph].
- Klein, U. (2014). *Lecture notes from course on Radio Astronomy, held at the University of Bonn in the winter term 2014/2015*.
- Klein, U. and Fletcher, A. (2015). *Galactic and Intergalactic Magnetic Fields*. Springer, Cham. DOI: 10.1007/978-3-319-08942-3.
- Kollgaard, R. I., Wardle, J. F. C., and Roberts, D. H. (1989). “High-Dynamic-Range VLA Observations of the Quasar 3C 345”. In: *AJ* 97, 1550. DOI: 10.1086/115095.
- Königl, A. (1981). “Relativistic jets as X-ray and gamma-ray sources.” In: *ApJ* 243, 700. DOI: 10.1086/158638.
- Kovalev, Y. Y., Kellermann, K. I., Lister, M. L., et al. (2005). “Sub-Milliarcsecond Imaging of Quasars and Active Galactic Nuclei. IV. Fine-Scale Structure”. In: *AJ* 130, 2473. DOI: 10.1086/497430. arXiv: astro-ph/0505536 [astro-ph].

- Kovalev, Y. Y., Lobanov, A. P., Pushkarev, A. B., et al. (2008). “Opacity in compact extragalactic radio sources and its effect on astrophysical and astrometric studies”. In: *A&A* 483, 759. DOI: 10.1051/0004-6361:20078679. arXiv: 0802.2970 [astro-ph].
- Kovalev, Y. Y., Kardashev, N. S., Kellermann, K. I., et al. (2016). “RadioAstron Observations of the Quasar 3C273: A Challenge to the Brightness Temperature Limit”. In: *ApJL* 820, L9. DOI: 10.3847/2041-8205/820/1/L9. arXiv: 1601.05806 [astro-ph.HE].
- Kovalev, Y. Y., Kardashev, N. S., Sokolovsky, K. V., et al. (2020). “Detection statistics of the RadioAstron AGN survey”. In: *Advances in Space Research* 65, 705. DOI: 10.1016/j.asr.2019.08.035. arXiv: 1909.00785 [astro-ph.GA].
- Kravchenko, E. V., Gómez, J. L., Kovalev, Y. Y., et al. (2020). “Probing the Innermost Regions of AGN Jets and Their Magnetic Fields with RadioAstron. III. Blazar S5 0716+71 at Microarcsecond Resolution”. In: *ApJ* 893, 68. DOI: 10.3847/1538-4357/ab7dae. arXiv: 2003.08776 [astro-ph.HE].
- Kutkin, A. M., Pashchenko, I. N., Lisakov, M. M., et al. (2018). “The extreme blazar AO 0235+164 as seen by extensive ground and space radio observations”. In: *MNRAS* 475, 4994. DOI: 10.1093/mnras/sty144. arXiv: 1801.04892 [astro-ph.GA].
- Lähteenmäki, A., Valtaoja, E., and Wiik, K. (1999). “Total Flux Density Variations in Extragalactic Radio Sources. II. Determining the Limiting Brightness Temperature for Synchrotron Sources”. In: *ApJ* 511, 112. DOI: 10.1086/306649.
- Laing, R. A. (1980). “A model for the magnetic-field structure in extended radio sources.” In: *MNRAS* 193, 439. DOI: 10.1093/mnras/193.3.439.
- Lee, S.-S., Petrov, L., Byun, D.-Y., et al. (2014). “Early Science with the Korean VLBI Network: Evaluation of System Performance”. In: *AJ* 147, 77. DOI: 10.1088/0004-6256/147/4/77.
- Levenberg, K. (1944). “A method for the solution of certain non-linear problems in least squares”. In: *Quart. Appl. Math.* 2, 164. DOI: 10.1090/qam/10666.
- Lewis, J. (1994). “Fast Template Matching”. In: *Vis. Interface* 95, 120. URL: http://scribblethink.org/Work/nvisionInterface/vi95_lewis.pdf.
- Liodakis, I., Zezas, A., Angelakis, E., et al. (2017). “Reconciling inverse-Compton Doppler factors with variability Doppler factors in blazar jets”. In: *A&A* 602, A104. DOI: 10.1051/0004-6361/201629902. arXiv: 1503.04780 [astro-ph.HE].
- Lisakov, M. M., Kovalev, Y. Y., Savolainen, T., et al. (2017). “A connection between γ -ray and parsec-scale radio flares in the blazar 3C 273”. In: *MNRAS* 468, 4478. DOI: 10.1093/mnras/stx710. arXiv: 1703.07976 [astro-ph.GA].
- Lister, M. L., Cohen, M. H., Homan, D. C., et al. (2009). “MOJAVE: Monitoring of Jets in Active Galactic Nuclei with VLBA Experiments. VI. Kinematics Analysis of a Complete Sample of Blazar Jets”. In: *AJ* 138, 1874. DOI: 10.1088/0004-6256/138/6/1874. arXiv: 0909.5100 [astro-ph.CO].
- Lister, M. L., Aller, M. F., Aller, H. D., et al. (2013). “MOJAVE. X. Parsec-scale Jet Orientation Variations and Superluminal Motion in Active Galactic Nuclei”. In: *AJ* 146, 120. DOI: 10.1088/0004-6256/146/5/120. arXiv: 1308.2713 [astro-ph.CO].
- Lister, M. L., Aller, M. F., Aller, H. D., et al. (2018). “MOJAVE. XV. VLBA 15 GHz Total Intensity and Polarization Maps of 437 Parsec-scale AGN Jets from 1996 to 2017”. In: *ApJS* 234, 12. DOI: 10.3847/1538-4365/aa9c44. arXiv: 1711.07802 [astro-ph.GA].

- Lister, M. L., Homan, D. C., Hovatta, T., et al. (2019). “MOJAVE. XVII. Jet Kinematics and Parent Population Properties of Relativistically Beamed Radio-loud Blazars”. In: *ApJ* 874, 43. DOI: 10.3847/1538-4357/ab08ee. arXiv: 1902.09591 [astro-ph.GA].
- Liu, J., Bignall, H., Krichbaum, T., et al. (2018). “Effelsberg Monitoring of a Sample of RadioAstron Blazars: Analysis of Intra-Day Variability”. In: *Galaxies* 6, 49. DOI: 10.3390/galaxies6020049. arXiv: 1804.09289 [astro-ph.GA].
- Lobanov, A. P. (1996). “Physics of the Parsec-Scale Structures in the Quasar 3C 345”. PhD thesis. New Mexico Institute of Mining and Technology. URL: <https://www3.mpifr-bonn.mpg.de/staff/alobanov/research/thesis.html>.
- Lobanov, A. P. (1998). “Ultracompact jets in active galactic nuclei”. In: *A&A* 330, 79. arXiv: astro-ph/9712132 [astro-ph].
- Lobanov, A. P. and Zensus, J. A. (1999). “Spectral Evolution of the Parsec-Scale Jet in the Quasar 3C 345”. In: *ApJ* 521, 509. DOI: 10.1086/307555. arXiv: astro-ph/9903318 [astro-ph].
- Lobanov, A. P. and Roland, J. (2005). “A supermassive binary black hole in the quasar 3C 345”. In: *A&A* 431, 831. DOI: 10.1051/0004-6361:20041831. arXiv: astro-ph/0411417 [astro-ph].
- Lobanov, A. P. (2005). “Resolution limits in astronomical images”. In: *arXiv e-prints*, astro-ph/0503225. arXiv: astro-ph/0503225 [astro-ph].
- Lobanov, A. (2007). “Compact radio jets and nuclear regions in active galaxies”. In: *arXiv e-prints*. arXiv: 0708.4280 [astro-ph].
- (2015). “Brightness temperature constraints from interferometric visibilities”. In: *A&A* 574, A84. DOI: 10.1051/0004-6361/201425084. arXiv: 1412.2121 [astro-ph.IM].
- Lobanov, A. P., Gómez, J. L., Bruni, G., et al. (2015). “RadioAstron space VLBI imaging of polarized radio emission in the high-redshift quasar 0642+449 at 1.6 GHz”. In: *A&A* 583, A100. DOI: 10.1051/0004-6361/201526335. arXiv: 1504.04273 [astro-ph.GA].
- Longair, M. S. (2011). *High Energy Astrophysics*. Cambridge University Press.
- Lovell, J. E. J., Rickett, B. J., Macquart, J. P., et al. (2008). “The Micro-Arcsecond Scintillation-Induced Variability (MASIV) Survey. II. The First Four Epochs”. In: *ApJ* 689, 108. DOI: 10.1086/592485. arXiv: 0808.1140 [astro-ph].
- Lyutikov, M., Pariev, V. I., and Gabuzda, D. C. (2005). “Polarization and structure of relativistic parsec-scale AGN jets”. In: *MNRAS* 360, 869. DOI: 10.1111/j.1365-2966.2005.08954.x. arXiv: astro-ph/0406144 [astro-ph].
- MacDonald, N. R., Jorstad, S. G., and Marscher, A. P. (2017). “‘Orphan’ γ -Ray Flares and Stationary Sheaths of Blazar Jets”. In: *ApJ* 850, 87. DOI: 10.3847/1538-4357/aa92c8. arXiv: 1611.09953 [astro-ph.HE].
- Marcaide, J. M. and Shapiro, I. I. (1983). “High precision astrometry via very-long-baseline radio interferometry : estimate of the angular separation between the quasars 1038+528A and B.” In: *AJ* 88, 1133. DOI: 10.1086/113402.
- (1984). “VLBI study of 1038+528A and B : discovery of wavelength dependence of peak brightness location.” In: *ApJ* 276, 56. DOI: 10.1086/161592.

- Marquardt, D. W. (1963). “An Algorithm for Least-Squares Estimation of Nonlinear Parameters”. In: *Journal of the Society for Industrial and Applied Mathematics* 11, 431. DOI: 10.1137/0111030.
- Marscher, A. P. (1996). “The Inner Jets of Blazars”. In: *Energy Transport in Radio Galaxies and Quasars*. Ed. by P. E. Hardee, A. H. Bridle, and J. A. Zensus. Vol. 100. Astronomical Society of the Pacific Conference Series. URL: <https://ui.adsabs.harvard.edu/abs/1996ASPC..100...45M>.
- (2014). “Turbulent, Extreme Multi-zone Model for Simulating Flux and Polarization Variability in Blazars”. In: *ApJ* 780, 87. DOI: 10.1088/0004-637X/780/1/87. arXiv: 1311.7665 [astro-ph.HE].
- Martí-Vidal, I., Ros, E., Pérez-Torres, M. A., et al. (2010). “Coherence loss in phase-referenced VLBI observations”. In: *A&A* 515, A53. DOI: 10.1051/0004-6361/201014203. arXiv: 1003.2368 [astro-ph.IM].
- Martí-Vidal, I., Pérez-Torres, M. A., and Lobanov, A. P. (2012). “Over-resolution of compact sources in interferometric observations”. In: *A&A* 541, A135. DOI: 10.1051/0004-6361/201118334. arXiv: 1203.2071 [astro-ph.IM].
- Marziani, P., Sulentic, J. W., Dultzin-Hacyan, D., et al. (1996). “Comparative Analysis of the High- and Low-Ionization Lines in the Broad-Line Region of Active Galactic Nuclei”. In: *ApJS* 104, 37. DOI: 10.1086/192291.
- Meier, D. L., Koide, S., and Uchida, Y. (2001). “Magnetohydrodynamic Production of Relativistic Jets”. In: *Science* 291, 84. DOI: 10.1126/science.291.5501.84.
- Michelson, A. A. and Pease, F. G. (1921). “Measurement of the Diameter of α Orionis with the Interferometer.” In: *ApJ* 53, 249. DOI: 10.1086/142603.
- Middelberg, E., Roy, A. L., Walker, R. C., et al. (2005). “VLBI observations of weak sources using fast frequency switching”. In: *A&A* 433, 897. DOI: 10.1051/0004-6361:20042078. arXiv: astro-ph/0412564 [astro-ph].
- Motter, J. C. and Gabuzda, D. C. (2017). “18-22 cm VLBA Faraday rotation studies of six AGN jets”. In: *MNRAS* 467, 2648. DOI: 10.1093/mnras/stx256. arXiv: 1702.06659 [astro-ph.GA].
- Nair, D. G., Lobanov, A. P., Krichbaum, T. P., et al. (2019). “Global millimeter VLBI array survey of ultracompact extragalactic radio sources at 86 GHz”. In: *A&A* 622, A92. DOI: 10.1051/0004-6361/201833122. arXiv: 1808.09243 [astro-ph.GA].
- Nakamura, M. and Asada, K. (2013). “The Parabolic Jet Structure in M87 as a Magnetohydrodynamic Nozzle”. In: *ApJ* 775, 118. DOI: 10.1088/0004-637X/775/2/118. arXiv: 1308.1436 [astro-ph.HE].
- Padovani, P. (2017). “On the two main classes of active galactic nuclei”. In: *Nature Astronomy* 1, 0194. DOI: 10.1038/s41550-017-0194. arXiv: 1707.08069 [astro-ph.GA].
- Penrose, R. and Floyd, R. M. (1971). “Extraction of Rotational Energy from a Black Hole”. In: *Nature Physical Science* 229, 177. DOI: 10.1038/physci229177a0.
- Perley, R. A., Dreher, J. W., and Cowan, J. J. (1984). “The jet and filaments in Cygnus A.” In: *ApJL* 285, L35. DOI: 10.1086/184360.
- Pilipenko, S. V., Kovalev, Y. Y., Andrianov, A. S., et al. (2018). “The high brightness temperature of B0529+483 revealed by RadioAstron and implications for interstellar

- scattering”. In: *MNRAS* 474, 3523. DOI: 10.1093/mnras/stx2991. arXiv: 1711.06713 [astro-ph.HE].
- Planck Collaboration, Ade, P. A. R., Aghanim, N., et al. (2014). “Planck 2013 results. XVI. Cosmological parameters”. In: *A&A* 571, A16. DOI: 10.1051/0004-6361/201321591. arXiv: 1303.5076 [astro-ph.CO].
- Plavin, A. V., Kovalev, Y. Y., Kovalev, Y. A., et al. (2021). “Directional Association of TeV to PeV Astrophysical Neutrinos with Radio Blazars”. In: *ApJ* 908, 157. DOI: 10.3847/1538-4357/abceb8. arXiv: 2009.08914 [astro-ph.HE].
- Plavin, A. V., Kovalev, Y. Y., Kovalev, Y. A., et al. (2020). “Observational Evidence for the Origin of High-energy Neutrinos in Parsec-scale Nuclei of Radio-bright Active Galaxies”. In: *ApJ* 894, 101. DOI: 10.3847/1538-4357/ab86bd. arXiv: 2001.00930 [astro-ph.HE].
- Pötzl, F. M., Lobanov, A. P., Ros, E., et al. (2018). “RadioAstron observations of 3C 345”. In: *14th European VLBI Network Symposium & Users Meeting (EVN 2018)*. URL: <https://pos.sissa.it/344/118/pdf>.
- Pötzl, F. M., Lobanov, A. P., Ros, E., et al. (2021). “Probing the innermost regions of AGN jets and their magnetic fields with RadioAstron. IV. The quasar 3C 345 at 18 cm: Magnetic field structure and brightness temperature”. In: *A&A* 648, A82. DOI: 10.1051/0004-6361/202039493. arXiv: 2102.04441 [astro-ph.HE].
- Pushkarev, A. B., Kovalev, Y. Y., Lister, M. L., et al. (2009). “Jet opening angles and gamma-ray brightness of AGN”. In: *A&A* 507, L33. DOI: 10.1051/0004-6361/200913422. arXiv: 0910.1813 [astro-ph.CO].
- Pushkarev, A. B., Hovatta, T., Kovalev, Y. Y., et al. (2012). “MOJAVE: Monitoring of Jets in Active galactic nuclei with VLBA Experiments. IX. Nuclear opacity”. In: *A&A* 545, A113. DOI: 10.1051/0004-6361/201219173. arXiv: 1207.5457 [astro-ph.HE].
- Pushkarev, A., Kovalev, Y., Lister, M., et al. (2017a). “Linear Polarization Properties of Parsec-Scale AGN Jets”. In: *Galaxies* 5, 93. DOI: 10.3390/galaxies5040093. arXiv: 1712.03025 [astro-ph.HE].
- Pushkarev, A. B., Kovalev, Y. Y., Lister, M. L., et al. (2017b). “MOJAVE - XIV. Shapes and opening angles of AGN jets”. In: *MNRAS* 468, 4992. DOI: 10.1093/mnras/stx854. arXiv: 1705.02888 [astro-ph.HE].
- Qian, S. J., Krichbaum, T. P., Zensus, J. A., et al. (1996). “Intrinsic evolution of a superluminal knot in 3C345.” In: *A&A* 308, 395. URL: <https://ui.adsabs.harvard.edu/abs/1996A&A...308..395Q>.
- Readhead, A. C. S. (1994). “Equipartition Brightness Temperature and the Inverse Compton Catastrophe”. In: *ApJ* 426, 51. DOI: 10.1086/174038.
- Richards, J. L., Hovatta, T., Max-Moerbeck, W., et al. (2014). “Connecting radio variability to the characteristics of gamma-ray blazars”. In: *MNRAS* 438, 3058. DOI: 10.1093/mnras/stt2412. arXiv: 1312.3634 [astro-ph.HE].
- Rickett, B. J., Lazio, T. J. W., and Ghigo, F. D. (2006). “Interstellar Scintillation Observations of 146 Extragalactic Radio Sources”. In: *ApJs* 165, 439. DOI: 10.1086/504897. arXiv: astro-ph/0509030 [astro-ph].

- Rioja, M. J. and Dodson, R. (2009). “VLBA Scientific Memorandum n. 32 - Multi-frequency Astrometry with VSOP-2: An application of Source/Frequency Phase Referencing techniques”. In: *arXiv e-prints*, arXiv:0910.1161. arXiv: 0910.1161 [astro-ph.IM].
- Rioja, M. J., Dodson, R., Jung, T., et al. (2014). “Verification of the Astrometric Performance of the Korean VLBI Network, Using Comparative SFPR Studies with the VLBA at 14/7 mm”. In: *AJ* 148, 84. DOI: 10.1088/0004-6256/148/5/84. arXiv: 1407.4604 [astro-ph.IM].
- Rioja, M. J., Dodson, R., Jung, T., et al. (2015). “The Power of Simultaneous Multifrequency Observations for mm-VLBI: Astrometry up to 130 GHz with the KVN”. In: *AJ* 150, 202. DOI: 10.1088/0004-6256/150/6/202. arXiv: 1509.02621 [astro-ph.IM].
- Ros, E., Marcaide, J. M., Guirado, J. C., et al. (1998). “High Precision Astrometry with VLBI”. In: *Ap&SS* 263, 319. DOI: 10.1023/A:1002131116188. arXiv: astro-ph/9901276 [astro-ph].
- Ros, E., Zensus, J. A., and Lobanov, A. P. (2000). “Total intensity and polarized emission of the parsec-scale jet in 3C 345”. In: *A&A* 354, 55. arXiv: astro-ph/9911454 [astro-ph].
- Ros, E., Kadler, M., Perucho, M., et al. (2020). “Apparent superluminal core expansion and limb brightening in the candidate neutrino blazar TXS 0506+056”. In: *A&A* 633, L1. DOI: 10.1051/0004-6361/201937206. arXiv: 1912.01743 [astro-ph.GA].
- Rybicki, G. B. and Lightman, A. P. (1979). *Radiative processes in astrophysics*. Wiley-VCH Verlag.
- Ryle, M. and Vonberg, D. D. (1946). “Solar Radiation on 175 Mc./s.” In: *Nature* 158, 339. DOI: 10.1038/158339b0.
- Ryle, M. and Hewish, A. (1960). “The synthesis of large radio telescopes”. In: *MNRAS* 120, 220. DOI: 10.1093/mnras/120.3.220.
- Ryle, M. (1962). “The New Cambridge Radio Telescope”. In: *Nature* 194, 517. DOI: 10.1038/194517a0.
- Sambruna, R. M., Gambill, J. K., Maraschi, L., et al. (2004). “A Survey of Extended Radio Jets with Chandra and the Hubble Space Telescope”. In: *ApJ* 608, 698. DOI: 10.1086/383124. arXiv: astro-ph/0401475 [astro-ph].
- Scheuer, P. A. G. and Williams, P. J. S. (1968). “Radio Spectra”. In: *ARA&A* 6, 321. DOI: 10.1146/annurev.aa.06.090168.001541.
- Schinzl, F. (2011). “Physics and Kinematics of the Parsec Scale Jet of the Quasar 3C345”. PhD thesis. Universität zu Köln. URL: <https://kups.ub.uni-koeln.de/4400/>.
- Schinzl, F. K., Lobanov, A. P., Taylor, G. B., et al. (2012). “Relativistic outflow drives γ -ray emission in 3C 345”. In: *A&A* 537, A70. DOI: 10.1051/0004-6361/201117705. arXiv: 1111.2045 [astro-ph.CO].
- Schmidt, M. (1963). “3C 273 : A Star-Like Object with Large Red-Shift”. In: *Nature* 197, 1040. DOI: 10.1038/1971040a0.
- Schwab, F. R. and Cotton, W. D. (1983). “Global fringe search techniques for VLBI”. In: *AJ* 88, 688. DOI: 10.1086/113360.

- Scott, M. A. and Readhead, A. C. S. (1977). “The low-frequency structure of powerful radio sources and limits to departures from equipartition.” In: *MNRAS* 180, 539. DOI: 10.1093/mnras/180.4.539.
- Seyfert, C. K. (1943). “Nuclear Emission in Spiral Nebulae.” In: *ApJ* 97, 28. DOI: 10.1086/144488.
- Shaffer, D. B., Kellermann, K. I., Purcell, G. H., et al. (1977). “The compact radio sources in 4C 39. 25 and 3C 345.” In: *ApJ* 218, 353. DOI: 10.1086/155689.
- Shen, Y., Richards, G. T., Strauss, M. A., et al. (2011). “A Catalog of Quasar Properties from Sloan Digital Sky Survey Data Release 7”. In: *ApJS* 194, 45. DOI: 10.1088/0067-0049/194/2/45. arXiv: 1006.5178 [astro-ph.CO].
- Shepherd, M. C. (1997). “Difmap: an Interactive Program for Synthesis Imaging”. In: *Astronomical Data Analysis Software and Systems VI*. Ed. by G. Hunt and H. Payne. Vol. 125. Astronomical Society of the Pacific Conference Series. URL: <https://ui.adsabs.harvard.edu/abs/1997ASPC..125...77S>.
- Sironi, L., Petropoulou, M., and Giannios, D. (2015). “Relativistic jets shine through shocks or magnetic reconnection?” In: *MNRAS* 450, 183. DOI: 10.1093/mnras/stv641. arXiv: 1502.01021 [astro-ph.HE].
- Slipher, V. M. (1917). “The spectrum and velocity of the nebula N.G.C. 1068 (M 77)”. In: *Lowell Observatory Bulletin* 3, 59. URL: <https://ui.adsabs.harvard.edu/abs/1917LowOB...3...59S>.
- Smirnov, O. M. (2011). “Revisiting the radio interferometer measurement equation. I. A full-sky Jones formalism”. In: *A&A* 527, A106. DOI: 10.1051/0004-6361/201016082. arXiv: 1101.1764 [astro-ph.IM].
- Sokolovsky, K. V., Kovalev, Y. Y., Pushkarev, A. B., et al. (2011). “A VLBA survey of the core shift effect in AGN jets. I. Evidence of dominating synchrotron opacity”. In: *A&A* 532, A38. DOI: 10.1051/0004-6361/201016072. arXiv: 1103.6032 [astro-ph.CO].
- Sol, H., Pelletier, G., and Asseo, E. (1989). “Two-flow model for extragalactic radio jets.” In: *MNRAS* 237, 411. DOI: 10.1093/mnras/237.2.411.
- Taylor, G., Carilli, C. L., and Perley, R. A., eds. (1999). *Synthesis Imaging in Radio Astronomy II*. Vol. 180. Astronomical Society of the Pacific Conference Series.
- Thompson, A. R., Moran, J. M., and Swenson George W., J. (2017). *Interferometry and Synthesis in Radio Astronomy, 3rd Edition*. Springer. DOI: 10.1007/978-3-319-44431-4.
- Thum, C., Agudo, I., Molina, S. N., et al. (2018). “POLAMI: Polarimetric Monitoring of Active Galactic Nuclei at Millimetre Wavelengths - II. Widespread circular polarization”. In: *MNRAS* 473, 2506. DOI: 10.1093/mnras/stx2436. arXiv: 1709.08743 [astro-ph.GA].
- Ulaby, F., Long, D., Blackwell, W., et al. (2014). *Microwave radar and radiometric remote sensing*. University of Michigan Press.
- Unwin, S. C., Wehrle, A. E., Lobanov, A. P., et al. (1997). “Variability in the Inverse-Compton X-Ray Flux from the Jet in Quasar 3C 345”. In: *ApJ* 480, 596. DOI: 10.1086/303988.

- Urry, C. M. and Padovani, P. (1995). “Unified Schemes for Radio-Loud Active Galactic Nuclei”. In: *PASP* 107, 803. DOI: 10.1086/133630. arXiv: astro-ph/9506063 [astro-ph].
- Valtonen, M. J., Lehto, H. J., Nilsson, K., et al. (2008). “A massive binary black-hole system in OJ287 and a test of general relativity”. In: *Nature* 452, 851. DOI: 10.1038/nature06896. arXiv: 0809.1280 [astro-ph].
- Vega García, L. (2019). “Space VLBI studies of internal structure and physical processes in extragalactic relativistic jets”. PhD thesis. Universität zu Köln. URL: <https://kups.ub.uni-koeln.de/9379/>.
- Vega-García, L., Lobanov, A. P., Perucho, M., et al. (2020). “Multiband RadioAstron space VLBI imaging of the jet in quasar S5 0836+710”. In: *A&A* 641, A40. DOI: 10.1051/0004-6361/201935168. arXiv: 1912.00925 [astro-ph.GA].
- Walker, R. C., Hardee, P. E., Davies, F. B., et al. (2018). “The Structure and Dynamics of the Subparsec Jet in M87 Based on 50 VLBA Observations over 17 Years at 43 GHz”. In: *ApJ* 855, 128. DOI: 10.3847/1538-4357/aaafcc. arXiv: 1802.06166 [astro-ph.HE].
- Wardle, J. F. C., Cawthorne, T. V., Roberts, D. H., et al. (1994). “Interpretation of VLBI Kinematic and Polarization Data: Application to 3C 345”. In: *ApJ* 437, 122. DOI: 10.1086/174980.
- Wardle, J. F. C., Homan, D. C., Ojha, R., et al. (1998). “Electron-positron jets associated with the quasar 3C279”. In: *Nature* 395, 457. DOI: 10.1038/26675.
- Wardle, J. (2018). “The Variable Rotation Measure Distribution in 3C 273 on Parsec Scales”. In: *Galaxies* 6, 5. DOI: 10.3390/galaxies6010005.
- Zamaninasab, M., Clausen-Brown, E., Savolainen, T., et al. (2014). “Dynamically important magnetic fields near accreting supermassive black holes”. In: *Nature* 510, 126. DOI: 10.1038/nature13399.
- Zensus, J. A., Cohen, M. H., and Unwin, S. C. (1995). “The Parsec-Scale Jet in Quasar 3C 345”. In: *ApJ* 443, 35. DOI: 10.1086/175501.
- Zhao, W., Hong, X. Y., An, T., et al. (2011). “Radio structure of the blazar 1156+295 with sub-pc resolution”. In: *A&A* 529, A113. DOI: 10.1051/0004-6361/201016192. arXiv: 1102.3046 [astro-ph.CO].
- Zhou, M. and Cao, X.-W. (2009). “The relation between black hole masses and Lorentz factors of the jet components in blazars”. In: *Research in Astronomy and Astrophysics* 9, 293. DOI: 10.1088/1674-4527/9/3/003. arXiv: 0806.2435 [astro-ph].

Special thanks

Three years pass by much faster than I anticipated, and here I am writing these acknowledgements. I want to stress that none of the work done within these years would have been possible without the help and support of several people, who I want to thank here. These include more people than I can mention here, and my deep apologies to those that I am missing.

First I would like to thank Prof. Anton Zensus for giving me the opportunity to do a PhD project in this exciting field of research and the continued support. The future and the possibilities in this field are certainly bright and exciting. Thank you also to Prof. Andreas Eckart for being my second supervisor and supporting me in the TAC meetings. In addition I want to thank the IMPRS for Astronomy and Astrophysics with its coordinator Dr. Rainer Mauersberger for funding and also for creating a vivid environment for doctoral researchers. I really enjoyed my time as both internal and external representative of the PhD researchers within IMPRS, where I had the opportunity to contribute to the efforts of the research school. I got to know many great people and learned a great deal along the way.

I want to express my deepest gratitude to my advisors Dr. Andrei Lobanov and Prof. Eduardo Ros, who helped me both scientifically as well as mentally through my time as a doctoral researcher. Having had two advisors always increased the possibility that one of them is available for answering my questions - and both did a splendid job while doing so. They always lent an ear to my concerns, and their proofreading of this thesis certainly improved it by a lot. Overall, this work never would have made it to the finish line without them.

Thanks go also to Dr. Nicholas MacDonald, who participated in my TAC meeting and provided helpful insights there and on other occasions along the way.

Special thanks go to the other doctoral researchers in my group, that shared some or the better part of my way as a doctoral researcher. They include: Laura Vega-García, Roberto Angioni, Celine Chidiac, Pedro Humire, Dongjin Kim, Jae-Young Kim, and Thalia Traianou. With many of you I shared the renowned student office E2.05 for at least some time, and the atmosphere there was always great. Thank you very much for the warm welcome in the group when I started, for the scientific input, the nice casual talks, and overall making my time as a doctoral researcher even more enjoyable.

I want to thank all my family and friends that supported me during this endeavour. *Ich will mich außerdem bei meiner Schwester bedanken, mit der ich so viel zusammen durchlebt habe und die immer eine Quelle der Inspiration für mich war. Und zum Schluss möchte ich mich speziell bei meiner Mutter bedanken. Schon in meinen frühen Kindheitstagen hat sie meine Neugier und meinen Wissensdurst mit allen verfügbaren Mitteln unterstützt und*

versucht, mir alle Fragen so gut es ging zu beantworten. Ohne ihre Ausdauer würde ich sicherlich nicht gerade diese Worte schreiben - du bist die Beste!

Acknowledgements

This research has made use of data obtained with the Global Millimeter VLBI Array (GMVA), which consists of telescopes operated by the MPIfR, IRAM, Onsala, Metsahovi, Yebes, and the VLBA. The VLBA is an instrument of the National Radio Astronomy Observatory. The National Radio Observatory is a facility of the National Science Foundation operated under the cooperative agreement by Associated Universities. The data were correlated at the MPIfR in Bonn, Germany.

The *RadioAstron* project is led by the Astro Space Center of the Lebedev Physical Institute of the Russian Academy of Sciences and the Lavochkin Scientific and Production Association under a contract with the State Space Corporation ROSCOSMOS, in collaboration with partner organizations in Russia and other countries.

This study makes use of 43 GHz VLBA data from the VLBA-BU Blazar Monitoring Program (VLBA-BU-BLAZAR; <http://www.bu.edu/blazars/VLBAproject.html>), funded by NASA through the Fermi Guest Investigator Program. The VLBA is an instrument of the National Radio Astronomy Observatory. The National Radio Astronomy Observatory is a facility of the National Science Foundation operated by Associated Universities, Inc.

Partly based on observations performed with radio telescopes of IAA RAS (Federal State Budget Scientific Organization Institute of Applied Astronomy of Russian Academy of Sciences).

The European VLBI Network is a joint facility of independent European, African, Asian, and North American radio astronomy institutes. Scientific results from data presented in this publication are derived from the following EVN project code(s): GG079A.

The National Radio Astronomy Observatory and the Green Bank Observatory are facilities of the National Science Foundation operated under cooperative agreement by Associated Universities, Inc.

This research has made use of data from the MOJAVE database that is maintained by the MOJAVE team (Lister et al. 2018).

Partly based on observations with the 100-m telescope of the MPIfR (Max-Planck-Institut für Radioastronomie) at Effelsberg. The data were correlated at the DiFX correlator (Deller et al. 2011; Bruni et al. 2016) of the MPIfR at Bonn.

This research has made use of NASA's Astrophysics Data System. This research has made use of *adstex* (<https://github.com/yymao/adstex>). This research has made use of the NASA/IPAC Extragalactic Database (NED), which is operated by the Jet Propulsion Laboratory, California Institute of Technology, under contract with the National Aeronautics and Space Administration.

I thank Laura Vega-García for providing me with her software developed at the MPIfR (Vega García 2019) and instructing me on its usage.

Erklärung

Hiermit versichere ich an Eides statt, dass ich die vorliegende Dissertation selbstständig und ohne die Benutzung anderer als der angegebenen Hilfsmittel und Literatur angefertigt habe. Alle Stellen, die wörtlich oder sinngemäß aus veröffentlichten und nicht veröffentlichten Werken dem Wortlaut oder dem Sinn nach entnommen wurden, sind als solche kenntlich gemacht. Ich versichere an Eides statt, dass diese Dissertation noch keiner anderen Fakultät oder Universität zur Prüfung vorgelegen hat; dass sie - abgesehen von unten angegebenen Teilpublikationen und eingebundenen Artikeln und Manuskripten - noch nicht veröffentlicht worden ist sowie, dass ich eine Veröffentlichung der Dissertation vor Abschluss der Promotion nicht ohne Genehmigung des Promotionsausschusses vornehmen werde. Die Bestimmungen dieser Ordnung sind mir bekannt. Darüber hinaus erkläre ich hiermit, dass ich die Ordnung zur Sicherung guter wissenschaftlicher Praxis und zum Umgang mit wissenschaftlichem Fehlverhalten der Universität zu Köln gelesen und sie bei der Durchführung der Dissertation zugrundeliegenden Arbeiten und der schriftlich verfassten Dissertation beachtet habe und verpflichte mich hiermit, die dort genannten Vorgaben bei allen wissenschaftlichen Tätigkeiten zu beachten und umzusetzen. Ich versichere, dass die eingereichte elektronische Fassung der eingereichten Druckfassung vollständig entspricht.

Teilpublikationen:

F. M. Pötzl et al. (2021). “Probing the innermost regions of AGN jets and their magnetic fields with RadioAstron. IV. The quasar 3C 345 at 18 cm: Magnetic field structure and brightness temperature”. In: *A&A* 648, A82. DOI: 10.1051/0004-6361/202039493. arXiv: 2102.04441 [astro-ph.HE]

F. M. Pötzl et al. (2018). “RadioAstron observations of 3C 345”. In: *14th European VLBI Network Symposium & Users Meeting (EVN 2018)*. URL: <https://pos.sissa.it/344/118/pdf>

07.07.2021, Felix Pötzl 

Datum, Name und Unterschrift

Felix Pötzl

Blücherstr. 1a
53115 Bonn
Germany
E-Mail: fpoetzl@mail.de
Phone: +491781337263



Particulars

Date and place of birth: November 7, 1991, Bonn
Citizenship: German
Family status: Unmarried

Education and qualifications

11/17 – present University of Cologne, PhD student in physics
Master thesis: Comparison of CO line and dust continuum emission as tracers of molecular gas masses through cosmic time, under supervision of Prof. Dr. Karl Menten and Dr. Axel Weiß at the Max-Planck-Institut für Radioastronomie (MPIfR)
10/14 – 12/16 University of Bonn, astrophysics degree course, finished 2016 with master of science degree (Ø 1,5)
Bachelor thesis: Submillimeter observations of lensed quasar host galaxies, under supervision of Prof. Dr. Frank Bertoldi and Dr. Markus Albrecht at the Argelander-Institut für Astronomie (AlfA) of the university of Bonn
10/10 – 09/14 University of Bonn, physics degree course, finished 2014 with bachelor of science degree (Ø 2,1)
08/02 – 06/10 Rhein-Sieg-Gymnasium Sankt Augustin, Abitur (Ø 2,1)
08/98 – 07/02 Evangelische Grundschule, Sankt Augustin-Hangelar

Employment

11/17 – present Doctoral researcher in the VLBI group at the Max-Planck-Institut für Radioastronomie (MPIfR)
03/17 – 10/17 Working in the research group of Prof. Dr. Frank Bertoldi at the Argelander-Institut für Astronomie (AlfA)
01/16 – 02/17 Scientific employee at the MPIfR during master thesis
10/14 – 02/15 Tutor at the university of Bonn for optics lecture
03/14 – 07/14 Tutor at the university of Bonn for optics lab course
10/13 – 02/14 Tutor at the university of Bonn for optics lecture

Bonn, 07.07.2021 *Felix Pötzl*